

UNIVERSITY OF CALIFORNIA, MERCED

Tropical cyclone impacts in the eastern tropical North Pacific oxygen minimum zone:  
Novel findings from subsurface measurements

A dissertation submitted in partial satisfaction of the  
requirements for the degree of  
Doctor of Philosophy  
in  
Environmental Systems  
in the  
Graduate Division  
of the  
University of California, Merced  
By

Brandon Michael Genco

Committee in charge:  
Professor Adeyemi Adebiyi, Chair  
Professor J. Michael Beman, Advisor  
Professor Justin D. Yeakel  
Professor Michael N. Dawson

Fall 2023

Tropical cyclone impacts in the eastern tropical North Pacific oxygen minimum zone:  
Novel findings from subsurface measurements

Copyright

Brandon Michael Genco, 2023

All rights reserved

The dissertation of Brandon Michael Genco, titled Tropical cyclone impacts in the eastern tropical North Pacific oxygen minimum zone: Novel findings from subsurface measurements, is approved:



---

Professor Adeyemi Adebisi (Chair)



---

Professor J. Michael Beman (Advisor)



---

Professor Justin D. Yeakel



---

Professor Michael N Dawson

University of California, Merced  
2023

## Vita

### **EDUCATION**

---

- 2007 BA** Boston University, Boston, MA. Biology, Specialization in Marine Science  
**2017 MA** University of Hawai'i at Manoa, Honolulu, HI. Geography

### **RESEARCH AND PROFESSIONAL EXPERIENCE**

---

- 2018 – 2022 Graduate Student Researcher:** *University of California, Merced*
- 2017 – 2018 Cartographer:** *Civil Maps. San Francisco, CA*
- 2017 – 2018 Fisheries Biologist:** *ICF Jones & Stokes. San Francisco, CA*
- 2017 Fisheries Observer / Biologist:** *Saltwater Inc. / NOAA. San Francisco, CA*
- 2013 – 2015 Graduate Research Assistant:** *University of Hawai'i at Manoa*
- 2012 Research Intern:** *Monterey Bay Aquarium Research Institute. Moss Landing, CA*
- 2011 – 2018 Vice President:** *Christina Clarke Genco Foundation. Boston, MA*
- 2008 – 2011 Fisheries Observer / Biologist:** *A.I.S Inc. / NOAA / NMFS. Gloucester, MA*
- 2007 Scientific Diver:** *Conservation International & Boston University/ Belize*
- 2004 – 2005 Research Assistant:** *Boston University. Boston, MA*
- 2001 Laboratory Assistant:** *CityLab. Boston Medical Center. Boston, MA*

### **TEACHING**

---

- 2019 & 2023 Teaching Assistant:** *UC Merced. School of Natural Sciences*
- 2018 – 2019 Laboratory Teaching Assistant:** *UC Merced. Environmental Systems program*
- 2012 – 2018 General or Biology/Math Tutor:** *Multiple tutoring companies, Berkeley, CA*
- 2015 Elementary School Outreach:** *Environmental Science. Honolulu*
- 2011 Biology/Math Tutor:** *MATCH Charter Public High School, Boston MA*
- 2001 – 2003 Teaching Assistant:** *CityLab, Boston University & Beaver Country Day School*

### **PUBLICATIONS**

---

Mora C, Caldwell IR, Caldwell JM, Fisher MR, **Genco BM**, Running SW. (2015) Suitable Days for Plant Growth Disappear under Projected Climate Change: Potential Human and Biotic Vulnerability. *PLoS Biol* 13(6): e1002167

Reitzel AM, Sullivan JC, Brown BK, Chin DW, Cira EK, Edquist SK, **Genco BM**, Joseph OC, Kaufman CA, Kovitvongsa K, Muñoz MM, Negri TL, Taffel JR, Zuehlke RT, Finnerty JR. (2007). Ecological and developmental dynamics of a host-parasite system involving a sea anemone and two ctenophores. *J. Parasitology* 93, 1392-1402

# Preface

Chapters 1-3 are the focus of this dissertation and related to tropical cyclones (hurricanes) and understanding their impact on the biology of a unique ocean biome in the Pacific abutting the coast of North America, this work was completed in Dr. J. Michael Beman's lab by the author during his tenure from Fall 2020 to the end of 2023. Prior to joining that lab, the author completed an initial lab rotation in Dr. Erin Hestir's Earth Observation and Remote Sensing lab, from Fall 2018 to Spring 2020, the work started there, was cut short due to the pandemic, but is presented in the Appendix. The topic is developing methods to use light emitted by ocean biota for future understanding of ocean ecology.

## Layout

The structure of this dissertation is as follows: In chapters 1-3 various approaches are taken to understand some lesser-known phenomena in the ocean. Chapter 4 provides synthesis. The Appendix is the development of a new method to improve our understanding of biota in the ocean based on more well known ecological and oceanographic phenomena at a particular study site. Chapters and sections are outlined below:

**Introduction:** of the main topics and questions of the dissertation. The background section is a well-cited 'pocket' reference that outlines key concepts and relevant literature. It encompasses some sub disciplines of this multisystem dissertation, and is supplementary.

**Chapter One, and supplement:** are the results of a research cruise, which sampled under Hurricane Bud, in June 2018, in the ETNP OMZ. In this chapter, various data provide context for the subsurface measurements during that opportunistic event. This manuscript currently in preparation was a team project where I present findings from my and colleagues' investigations. We provide solid confirmation of a plankton bloom over an OMZ microbial community, and a unique shoaling of the OMZ. Included is a simple time series analysis using modeled satellite derived exported carbon, co-occurring with past TC overpass in a representative area of ocean. It should be noted that organic matter analysis, conducted by co-authors, is at the forefront of its field.

**Chapter Two:** expands upon the data collected during the unique opportunistic process cruise, primarily additional analysis of CTD/sensor profiles, and ADCP water current data for Stations 3, 3.5, and 4. Additional CTD/sensor profiles provide valuable information about the time evolution and the biological response to the physical disturbance. Comparing the cruise track ADCP data with CTD profiles provides evidence for a better ecological-oceanographic understanding of resultant observations following Hurricane Bud. Reexamining the subsurface profiles coupled with remote sensing and *in situ* water sampling provides a more comprehensive and integrated place for hypothesis development and future work, of this complex multidimensional phenomenon.

**Chapter Three:** builds upon ideas and findings in first two chapters using a robotic subsurface profiling array in the ocean to: (1) look at case study of a TC Olaf, which in late summer of 2021, was similar to Bud, and passed over a similar region of the ETNP. (2) A simple evaluation of this multi robot array to capture TC subsurface oxygen changes in the central and eastern Pacific TC overpass region.

**Chapter Four:** provides a brief conclusion and synthesis of the dissertation.

The **Appendix:** uses knowledge of very well-known phenomena in the ocean to develop new methods. Results demonstrate that off the shelf, passive, radiometric sensors can be used to measure bioluminescence leaving the water surface, likely produced by Dinoflagellates in a bay in Central California. Passive radiometers are a mainstay of sensing biota in the ocean. Bioluminescence is an important biological phenomenon in the ocean. It is original research, unrelated to TCs and OMZs, conducted by the author in pursuit of a Ph.D.

## Motivation and merit

**Motivation,** of this work was to investigate novel observations and the more general *Whys* that stem from a *that's interesting* moment of discovery. Study questions become *Whats* and *Hows*, as this format is more appropriate for the heuristic methods of scientific inquiry. Hopefully, some of the ideas expressed here help approximate some truths and may contribute to the scientific community.

**Merit** and **findings** of this work: include several multidimensional analyses of impacts under a TC in the ETNP OMZ, which is new for this region of ocean. Results include, documenting shoaling of an OMZ, extrapolating the scale of impacts in this region using models and multiple remote sensing tools, and developing an integrative ecological oceanographic theory that has implications for all oligotrophic TC impact regions of the ocean. Finally using the ocean array demonstrates that TC oxygen changes can be further studied at a biogeographic scale. Unrelated to TCs and OMZs, presented, is an initial proof of concept that may be used to develop a new method to better measure biology in the ocean. New methods to measure biology in the ocean are always needed.

## Acknowledgements

In my academic career I have been privileged to be mentored and supported by a great many wonderful and exceptional scientists, whilst at the same time sustained by loving family and friends. Here I would like to explicitly acknowledge the graduate students of UC Merced and especially those in the Environment Systems program. Finally, I appreciate very much the behind the scenes support by faculty of the ES program.

# Contents

<b>Contents .....</b>	<b>vi</b>
List of Figures .....	viii
List of Tables .....	xvi
<b>Abstract.....</b>	<b>1</b>
<b>Introduction.....</b>	<b>2</b>
Background .....	3
References.....	9
<b>Chapter One: Tropical cyclones drive simultaneous oxygen minimum zone shoaling and enhanced organic matter supply .....</b>	<b>13</b>
Abstract.....	14
Introduction.....	14
Methods .....	16
Results.....	20
Discussion.....	31
Acknowledgments.....	34
References.....	34
Chapter One Supplement .....	38
<b>Chapter Two: Fine scale temporal subsurface oceanographic dynamics and a resultant ecological model from the 2018 process cruise and Hurricane Bud .....</b>	<b>48</b>
Abstract.....	48
Introduction.....	48
Methods .....	50
Results.....	52
Discussion .....	75
References.....	78
<b>Chapter Three: Capturing tropical cyclone subsurface impacts using the BGC-Argo float array in the eastern North Pacific.....</b>	<b>80</b>
Abstract.....	80
Introduction.....	80
Methods .....	83
Results and Discussion .....	85

Conclusions.....	100
References.....	101
<b>Chapter Four: Conclusions for tropical cyclones and OMZs.....</b>	<b>103</b>
<b>Appendix: Remote sensing of bioluminescent radiance: exploring the potential for increased biological information in an understudied signal .....</b>	<b>105</b>
Abstract.....	105
Introduction.....	105
Background.....	106
Methods .....	109
Results and Discussion .....	111
Future Work.....	120
Acknowledgments: .....	122
References.....	122

## List of Figures

<b>Ch 1 - Figure 1 .....</b>	<b>21</b>
Maps of (a) hurricane and cruise tracks, (b) long-term average OMZ depth, and shipboard flowthrough (c) SST and (d) chlorophyll in the ENTP. In panel (a), color-shaded dots show maximum sustained wind speeds <sup>22</sup> every six hours along Hurricane Bud's track, with the daily hurricane eye position during June 2018 labeled by purple numbers. The black line with dates in June 2018 (black numbers ranging from June 10-25) shows the cruise track. Panel (b) displays the long-term average depth of the OMZ (defined by 20 µM DO) based on the World Ocean Atlas climatology <sup>23</sup> . OMZ depth is indicated by 50 m contours and shading. Ship-board flowthrough (c) SST and (d) chlorophyll-a concentrations are shown by color shading. In panels b, c, and d, black circles with numbers indicate sampling stations.	
<b>Ch 1 - Figure 2 .....</b>	<b>22</b>
Remotely sensed [Chl a] images ( $\text{mg m}^{-3}$ ) prior to (June 4 <sup>th</sup> -10 <sup>th</sup> 2018), during (June 11 <sup>th</sup> -15 <sup>th</sup> ), and following (June 16 <sup>th</sup> -23 <sup>rd</sup> ) Hurricane Bud demonstrate the presence and influence of the tropical cyclone. [Chl a] values are shown on the color scale, with values above 5 $\text{mg m}^{-3}$ shown in red. Overlayed true-color imagery shows cloud cover, land cover, and areas with no available [Chl a] values. Eye position is shown for tropical cyclones Bud (storm symbol) and Aletta (triangle), and the red circle (200 km diameter) is centered on station 3.5. See text for dates and specific storm strength designation. Images are ca. local solar noon.	
<b>Ch 1 – Figure 3 .....</b>	<b>25</b>
Water column profiles at Station 4 demonstrate hurricane-driven shifts in (a) temperature, (b) dissolved oxygen, (c) chlorophyll, and (d) dissolved organic carbon (DOC) concentrations between 2017 (dark blue profiles) and 2018 (light blue profiles). The dashed line in panel b indicates 20 µM DO.	
<b>Ch 1 - Figure 4 .....</b>	<b>27</b>
Post hurricane profiles from Station 3.5 show substantial differences with data from other cruises, floats, and stations in (a) temperature, (b) dissolved oxygen concentrations, (c) chlorophyll, (d) nitrite concentrations, (e) DOC, and (f) particulate organic carbon (POC) concentrations. In panels a-c, Station 3.5 data (orange) are shown in comparison to earlier cruises and recent float data (blue and green profiles) collected nearby (see text). In panels d-f, Station 3.5 data (orange) show distinct patterns in comparison to all other data collected on our cruises (gray). The dashed line in panel c indicates 20 µM DO.	
<b>Ch 1 - Figure 5 .....</b>	<b>28</b>
Hurricane occurrence in the ENTP. Color scale shows hurricane eye observations per $0.5^\circ \times 0.5^\circ$ cell from 1942 to 2021 in the NOAA HURDAT database. Hurricanes outside of the ENTP (~5-33°N, and 150-90°W) and within 200 km distance from land (including islands located off the Pacific coast of Mexico) were excluded.	
<b>Ch 1 - Figure 6 .....</b>	<b>30</b>
Organic matter and microbial communities show unique compositions and variations at Station 3.5. The heatmap displays the relative abundance (color scale at left) of molecular features at different sampling depths (right axis). Two way hierarchical clustering of abundant molecular features is shown at the bottom of the heatmap, with clusters of features unique to or enriched in surface samples highlighted in orange (n=353). ‘Sunburst’ plot at left displays the chemical composition of the surface-enriched or -unique features at the Superclass, Class, and Subclass (progressing from innermost to outermost circle). Chemical structures of key surface-enriched or -unique features are shown at right. 16S rRNA data show active microbial groups at 10 m and 80 m depth at Station 3.5, with key microbial phyla indicated.	

<b>Ch 1 - Supplementary Figure 1 .....</b>	<b>40</b>
Continuous flowthrough data of Sea Surface Temperature (SST; red line) and chlorophyll- <i>a</i> concentration (in $\mu\text{g/L}$ ; green line) from the 2018 <i>R/V Oceanus</i> cruise. Chlorophyll increases coincide with decreases in SST near stations 2, 3.5, and 4 in wake of Hurricane Bud. Gray bars denote periods on station when water profile measurements and biogeochemical casts were collected (see Figures 1 & 3). Date/times are local (MDT/UTC-6). Data are available on the R2R repository.	
<b>Ch 1 - Supplementary Figure 2 .....</b>	<b>41</b>
Select daily remotely sensed [Chl a] composites ( $\text{mg m}^{-3}$ ) from June 6-27th 2018, with true-color cloud imagery overlayed, demonstrate the presence and influence of Hurricane Bud. [Chl a] values above $5 \text{ mg m}^{-3}$ are shown as red, while RGB imagery is shown for areas with no available [Chl a] values. The red circle (100 km radius) in all images is centered on Station 3.5. Eye position is shown for tropical cyclones Bud, and Aletta. See text for dates and specific storm strength designation. Images are ca. local solar noon. Larger area, and alternate days from Figure 2 main text.	
<b>Ch 1 - Supplementary Figure 3 .....</b>	<b>42</b>
Water column profiles of combined nitrate + nitrite concentrations at Station 3.5 (green; 2018 only) and Station 4 (blue; 2017 and 2018). For Station 4, 2017 data are shown in dark blue, and 2018 data collected following the hurricane are shown in light blue.	
<b>Ch 1 - Supplementary Figure 4 .....</b>	<b>42</b>
Dissolved oxygen profiles, CTDs from 2018 cruise with reference cruise measurements closest to (a) Station 3.5, and (b) Station 4. Reference cruises have course depth resolution. Colored lines indicate each cruise. Multiple profiles are shown for the 2018 cruise in gray. Dates listed for reference cruises indicate the start month of the cruise.	
<b>Ch 1 - Supplementary Figure 5 .....</b>	<b>43</b>
8-day resolution: Non-lagged export flux (proportion of modeled VGPM). Derived from 8-day remotely sensed Chl-a & SST input variables. Values are mean computed for the 200km box around Station 3.5 ( $\text{m}^{-2} \text{ day}^{-1}$ ) for each variable (a) Export flux left axis (mg C). Positive anomalies only (above or equal to mean). Colored vertical lines are individual tropical disturbances that pass within the export 200 km flux box around Station 3.5. Orange = Hurricane strength, Blue = less than ". Height of each line is the median eye pressure per individual storm, which corresponds to the inverted right axis. Gray dashed horizontal line is 1 SD ( $\sigma$ ) above mean export flux for time series, and corresponds to 1013.25 mb, standard atmospheric pressure at sea level for reference. (b) MODIS derived Chl-a [ $\mu\text{L}$ ] in green/right axis, and export flux in black/left axis. Dashed horizontal lines are 1 SD ( $\sigma$ ) above mean for time series (EF = gray, Chl-a = green). (c) MODIS derived Chl-a [ $\mu\text{L}$ ] in green/left axis, and sea surface temperature ( $^{\circ}\text{C}$ ) in red/right axis. Dashed lines are 1 SD ( $\sigma$ ) above/below mean for time series (Chl-a = green, SST = red).	
<b>Ch 1 - Supplementary Figure 6 .....</b>	<b>44</b>
To be supplied by collaborators. Listed for congruence with the main text of manuscript in preparation.	
<b>Ch 2 - Figure 1 .....</b>	<b>54</b>
Ocean current profiles from shipboard ADCP sensors. 2-hour averaged, depth integrated (10-50m) horizontal vector (m/s) components with colors indicating temperature using Wh300 hz bb surface ADCP. Track on map corresponds to the three panels in Figure 2.	

<b>Ch 2 - Figure 2 .....</b>	<b>54</b>
Ocean current profiles from shipboard ADCP sensor. Corresponds to the cruise track in Figure 1. Top panel is zonal velocity, u, ( $\text{m s}^{-1}$ ). Middle panel is meridional, v, “ ”. Bottom panel vertical velocity, w, ( $\text{mm s}^{-1}$ ). Gray indicates no data, or data removed due to ship movement induced noise. Red is positive (East, North, Up). Blue is negative (West, South, Down). Left axis is depth to 1000m. Times in decimal yr-day UTC-0. Panels are velocity components from the 75 kHz near-band sensor.	
<b>Ch 2 - Figure 3 .....</b>	<b>57</b>
Station 3.5 surface ADCP. Ocean current profiles from shipboard ADCP surface sensor over station 3.5. Time window corresponds to vessel sampling at Station 3.5. Top panel is zonal velocity, u, ( $\text{m s}^{-1}$ ). Bottom panel is meridional, v, “ ”. Red is positive (East, North). Blue is negative (West, South). Times in decimal yr-day (168.8 ~ 2018-06-19 19:13 UTC-0). Green overlay/right axis is ship velocity ( $\text{m s}^{-1}$ ). Left axis is depth to 150m. Panels are velocity components from the 300 kHz sensor.	
<b>Ch 2 - Figure 4 .....</b>	<b>57</b>
Station 3.5 deep. Ocean current profiles from shipboard ADCP sensor over station 3.5. Time window corresponds to vessel sampling at Station 3.5. Top panel is zonal velocity, u, ( $\text{m s}^{-1}$ ). Middle panel is meridional, v, “ ”. Bottom panel is vertical velocity, w, ( $\text{mm s}^{-1}$ ). Gray indicates no data, or data removed due to ship movement induced noise. Red is positive (East, North, Up). Blue is negative (West, South, Down). Times in decimal yr-day (169.80 ~ 2018-06-19 19:13 UTC-0). Left axis is depth to 1000m. Panels are velocity components from the 75 kHz near-band sensor.	
<b>Ch 2 - Figure 5 .....</b>	<b>58</b>
Station 3.5 CTD sections. Time is listed as hrs in UTC-0 in panels on x-axis, for 06-20. Sections are interpolated between CTD casts as indicated by dashed lines at top of each panel. Four panels clockwise from top left are, oxygen [ $\mu\text{mol/kg}$ ], beam attenuation [1/m], fluorescence [ $\text{mg/m}^3$ ], and density as Sigma-t [ $\text{kg/m}^3$ ]. Variables on right y-axis, depth to 80m on left y-axis.	
<b>Ch 2 - Figure 6 .....</b>	<b>59</b>
Station 3.5 CTD profiles for the second cast, 19 - 21:04 UTC-0. (a) oxygen [ $\mu\text{mol/kg}$ ], (b) beam attenuation [1/m], (c) fluorescence [ $\text{mg/m}^3$ ], (d) percentage of photosynthetically active radiation [%] (e) density as Sigma-theta [ $\text{kg/m}^3$ ], and (f) temperature in Celsius. The y-axis is increasing depth in meters.	
<b>Ch 2 - Figure 7 .....</b>	<b>60</b>
Station 3.5 CTD profiles for the second cast, 19 - 21:04 UTC-0, by isopycnal surfaces. (a) oxygen [ $\mu\text{mol/kg}$ ], (b) beam attenuation [1/m], (c) fluorescence [ $\text{mg/m}^3$ ], and (d) percentage of available photosynthetically active radiation in purple [%]. y-axis being Sigma-0, potential density anomaly [ $\text{kg/m}^3$ ], as opposed to depth.	
<b>Ch 2 - Figure 8 .....</b>	<b>61</b>
Station 3.5 descriptive oceanographic CTD profiles for the second cast, 19 - 21:04 UTC-0. (a) potential density anomaly Sigma-0 [ $\text{kg/m}^3$ ] top x-axis in blue, with the square of the buoyancy frequency in brown [ $\text{N}^2[\text{s}^{-2}]$ ], bottom x-axis. (b) Temperature in Celsius in red top x-axis, Salinity in PSUs in green bottom x-axis. (c) Spice, ratio of (warm + salty)/ (cold+fresh) of water mass [ $\text{kg/m}^3$ ]. (d) Rrho = change in f' of salinity/temperature over depth as described in methods. Diffusivity implementation.	
<b>Ch 2 - Figure 9 .....</b>	<b>62</b>
Station 3.5 CTD profiles by depth. Each column is an individual cast plotted in sequential order corresponding to Table 1 (e.g., cast 1 {a,f,k}). (a-e) oxygen [ $\mu\text{mol/kg}$ ], (f-j) beam attenuation [1/m], (k-o) fluorescence [ $\text{mg/m}^3$ ]. The y-axis is increasing depth in meters.	

<b>Ch 2 - Figure 10 .....</b>	<b>63</b>
Station 3.5 CTD profiles by isopycnal surfaces. Each column is a unique cast plotted in sequential order corresponding to Table 1 (e.g., cast 1 {a,f,k}). (a-e) oxygen [ $\mu\text{mol/kg}$ ], (f-j) beam attenuation [1/m], (k-o) fluorescence [ $\text{mg/m}^3$ ]. y-axis being Sigma-0, potential density anomaly [ $\text{kg/m}^3$ ], as opposed to depth.	
<b>Ch 2 - Figure 11 .....</b>	<b>64</b>
Station 4 surface ADCP. Ocean current profiles from shipboard ADCP surface sensor over station 4. Time window corresponds to vessel sampling at Station 4. Top panel is zonal velocity, $u$ , ( $\text{m s}^{-1}$ ) . Bottom panel is meridional, $v$ , “ ”. Red is positive (East, North). Blue is negative (West, South). Times in decimal yr-day (171.5 ~ 2018-06-21 11:59 UTC-0). Green overlay/right axis is ship velocity ( $\text{m s}^{-1}$ ). Left axis is depth to 150m. Panels are velocity components from the 300 kHz sensor.	
<b>Ch 2 - Figure 12 .....</b>	<b>65</b>
Station 4 deep. Ocean current profiles from shipboard ADCP sensor over Station 4. Time window corresponds to vessel sampling at Station 3. Top panel zonal velocity, $u$ , ( $\text{m s}^{-1}$ ) . Middle panel is meridional, $v$ , “ ”. Bottom panel is vertical velocity, $w$ , ( $\text{mm s}^{-1}$ ). Gray indicates no data, or data removed due to ship movement induced noise. Red is positive (East, North, Up). Blue is negative (West, South, Down). Times in decimal yr-day (171.5 ~ 2018-06-21 11:59 UTC-0). Left axis is depth to 1000m. Panels are velocity components from the 75 kHz near-band sensor.	
<b>Ch 2 - Figure 13 .....</b>	<b>65</b>
Station 3 CTD sections. Time is listed as hrs in UTC-0 in panels, for 06-17/18. Sections are interpolated between CTD casts as indicated by dashed lines at top of each panel. Four panels clockwise from top left are, oxygen [ $\mu\text{mol/kg}$ ], beam attenuation [1/m], fluorescence [ $\text{mg/m}^3$ ], and density as Sigma-t [ $\text{kg/m}^3$ ]. Variables on right y-axis, depth to 70m on left y-axis.	
<b>Ch 2 - Figure 14 .....</b>	<b>66</b>
Station 4 CTD profiles by depth. Each column is an individual cast plotted in sequential order corresponding to Table 2 (e.g., cast 1 {a,g,m}). (a-f) oxygen [ $\mu\text{mol/kg}$ ], (g-l) beam attenuation [1/m], (m-r) fluorescence [ $\text{mg/m}^3$ ]. The y-axis is increasing depth in meters.	
<b>Ch 2 - Figure 15 .....</b>	<b>67</b>
Station 4 oceanographic plots, (a) four subplots for cast 3, clockwise from top left: {1} potential density anomaly Sigma-0 [ $\text{kg/m}^3$ ] top x-axis in blue, with the square of the buoyancy frequency in brown [ $\text{N}^2[\text{s}^{-2}]$ ] , bottom x-axis. {2} Temperature in Celsius in red top x-axis, Salinity in PSUs in green bottom x-axis. {3} Spice, ratio of (warm + salty)/ (cold+fresh) of water mass [ $\text{kg/m}^3$ ]. {4} Rrho = change in $f'$ of salinity/temperature over depth as described in methods. Salt finger implementation. (b) same sub plots for cast 4. (c) is casts: 1-6 of density as Sigma-theta [ $\text{kg/m}^3$ ], as opposed to depth.	
<b>Ch 2 - Figure 16 .....</b>	<b>69</b>
Station 3 surface ADCP. Ocean current profiles from shipboard ADCP surface sensor over Station 3. Time window corresponds to vessel sampling at Station 3. Top panel is zonal velocity, $u$ , ( $\text{m s}^{-1}$ ) . Bottom panel is meridional, $v$ , “ ”. Red is positive (East, North). Blue is negative (West, South). Times in decimal yr-day (167.25 ~ 2018-06-17 06:02 UTC-0). Green overlay/right axis is ship velocity ( $\text{m s}^{-1}$ ). Left axis is depth to 150m. Panels are velocity components from the 300 kHz sensor	

<b>Ch 2 - Figure 17 .....</b>	<b>69</b>
Station 3 deep. Ocean current profiles from shipboard ADCP sensor over Station 3. Time window corresponds to vessel sampling at Station 3. Top panel zonal velocity, u, ( $\text{m s}^{-1}$ ). Middle panel is meridional, v, “ ”. Bottom panel is vertical velocity, w, ( $\text{mm s}^{-1}$ ). Gray indicates no data, or data removed due to ship movement induced noise. Red is positive (East, North, Up). Blue is negative (West, South, Down). Times in decimal yr-day (167.25 ~ 2018-06-17 06:02 UTC-0). Left axis is depth to 1000m. Panels are velocity components from the 75 kHz near-band sensor.	
<b>Ch 2 - Figure 18 .....</b>	<b>70</b>
Station 3 CTD sections. Time is listed as hrs in UTC-0 in panels, for 06-17/18. Sections are interpolated between CTD casts as indicated by dashed lines at top of each panel. Four panels clockwise from top left are, oxygen [ $\mu\text{mol/kg}$ ], beam attenuation [1/m], fluorescence [ $\text{mg/m}^3$ ], and density as Sigma-t [ $\text{kg/m}^3$ ]. Variables on right y-axis, depth to 175m on left y-axis.	
<b>Ch 2 - Figure 19 .....</b>	<b>71</b>
Station 3. CTD profiles by depth. Each column is an individual cast plotted in sequential order corresponding to Table 2, casts were chosen to be ~ 24 hours apart. (e.g., cast 1 {a,d,g,j}). (a-c) oxygen [ $\mu\text{mol/kg}$ ], (d-f) beam attenuation [1/m], (g-i) fluorescence [ $\text{mg/m}^3$ ], and (j-l) density as Sigma-theta [ $\text{kg/m}^3$ ]. The y-axis is increasing depth in meters.	
<b>Ch 2 - Figure 20 .....</b>	<b>72</b>
Station 3 CTD profiles by isopycnal surfaces. Each column is a unique cast plotted in sequential order corresponding to Table 2. Casts were chosen to be ~ 24 hours apart. (e.g., cast 1 {a,d,g}). (a-c) oxygen [ $\mu\text{mol/kg}$ ], (d-f) beam attenuation [1/m], (g-i) fluorescence [ $\text{mg/m}^3$ ]. y-axis being Sigma-0, potential density anomaly [ $\text{kg/m}^3$ ], as opposed to depth.	
<b>Ch 2 - Figure 21 .....</b>	<b>73</b>
Station 3 descriptive oceanographic CTD profiles for the sixth cast, 18 - 01:01 UTC-0. (a) potential density anomaly Sigma-0 [ $\text{kg/m}^3$ ] top x-axis in blue, with the square of the buoyancy frequency in brown [ $\text{N}^2[\text{s}^{-2}]$ ], bottom x-axis. (b) Temperature in Celsius in red top x-axis, Salinity in PSUs in green bottom x-axis. (c) Spice, ratio of (warm + salty)/(cold+fresh) of water mass [ $\text{kg/m}^3$ ]. (d) Rrho = change in f' of salinity/temperature over depth as described in methods. Diffusivity implementation.	
<b>Ch 2 - Figure 22 .....</b>	<b>74</b>
ADCP station 3.5 deep, casts 1 & 2. Ocean current profiles from shipboard ADCP sensor over station 3.5. Time window corresponds to CTD casts 1 and 2 (Table 1). Top panel is meridional velocity, v, ( $\text{m s}^{-1}$ ). Middle panel is vertical velocity, w, ( $\text{mm s}^{-1}$ ). Bottom panel is error velocity in the vertical velocity panel. Gray indicates no data, or data removed due to ship movement induced noise. Red is positive (North, Up). Blue is negative (South, Down). Times in UTC-0 for 06-19. Left axis is depth to 1000m. Panels are velocity components from the 75 kHz near-band sensor.	
<b>Ch 2 - Figure 23 .....</b>	<b>74</b>
ADCP station 3.5 shallow, casts 1 & 2. Ocean current profiles from shipboard ADCP surface sensor over station 3.5. Time window corresponds to CTD casts 1 and 2 (Table 1). First panel is zonal velocity, u, ( $\text{m s}^{-1}$ ). Second panel is meridional, v, “ ”. Third panel is vertical velocity, w, ( $\text{mm s}^{-1}$ ) a depth in meters. Gray indicates no data, or data removed due to ship movement induced noise. Bottom panel is error velocity in the vertical velocity panel. Gray indicates no data, or data removed due to ship movement induced noise. Red is positive (East, North, Up). Blue is negative (West, South, Down). Times in UTC-0 for 06-19. Green overlay/right axis is ship velocity. Pink dots/right axis is ship heading in cardinal direction. Left axis is depth to 1000m. Panels are velocity components from the 300 kHz sensor.	

<b>Ch 3 - Figure 1 .....</b>	<b>91</b>
Map of overlays of tropical cyclones and BGC-Argo profiles with oxygen sensors. Within the time and space selection window, see methods, Table 1. (a) All six hour positions for TC's in the database, blue dots, with profiles of a float that fell within 500 kms, black dots. (b) Hurricane tracks, blue lines, and associated profiles falling within 200km, black dots. (c) Major hurricane tracks, blue lines, and associated profiles falling within 100km, black dots. Time window is from 30 days prior to or 45 days after TC overpass.	
<b>Ch 3 - Figure 2 .....</b>	<b>92</b>
Spatial overlay of Hurricanes Bud (Ch 1 & 2), with cruise sampling stations (numbered circles), as well as Hurricane Olaf. Three different dashed lines are tracks of associated BGC-Argo floats with identifier numbers. Floats 6903093 and 6903094 were used for reference data for Station 3.5 (Ch 1 Fig. 4a). Color-shaded dots show maximum sustained wind speeds every six hours along Hurricane Olaf's track.	
<b>Ch 3 - Figure 3 .....</b>	<b>93</b>
Float 6903093 track under Olaf. Dates for before, during and after profiles used in following figures. Float track and dates in green. Six hour position of Hurricane Olaf with corresponding winds speeds, date and times in black. UTC-0. color-shaded dots show maximum sustained wind speeds every six hours along Hurricane Olaf's track.	
<b>Ch 3 - Figure 4 .....</b>	<b>93</b>
Chl-a map on 2023-09-12. Olaf overpass. Multiple sensors for composite image (see Ch-1 Fig 2, and methods Ch-1) image from <a href="https://worldview.earthdata.nasa.gov">https://worldview.earthdata.nasa.gov</a>	
<b>Ch 3 - Figure 5 .....</b>	<b>94</b>
Multiple floats and TC Olaf. Dates in the title give the window of six hour eye position for Olaf on the map. Three sets of dots are profiles for floats 6903094, 6903093, 5905068, from North to South, respectively. Positive and negative numbers are days after or before from closest overpass to the TC track for individual profiles. Scale is wind speed for TC at the six hour position.	
<b>Ch 3 - Figure 6 .....</b>	<b>95</b>
Multiple floats and TC Nora. Dates in the title give the window of six hour eye position for Nora on the map. Nora in the map. Three sets of dots are profiles for floats 6903094, 6903093, 5905068, from North to South, respectively. Positive and negative numbers are days after or before from closest overpass to the TC track for individual profiles. Scale is wind speed for TC at the six hour position.	
<b>Ch 3 - Figure 7 .....</b>	<b>96</b>
Profiles of oxygen [ $\mu\text{mol/kg}$ ] (a:c), and temperature in Celsius (d:f) for float 6903093 under Olaf. Three columns (a,d; b,e; c,f), are profile groupings: prior, immediately following, and post disturbance, following sequential order corresponding time relative to TC overpass. Lines in each panel are dashed, dotted, solid in sequential order, within groupings. Days relative are: -20, -16, -10, 0, 4, 10, 20, 24.	
<b>Ch 3 - Figure 8 .....</b>	<b>97</b>
Profiles of Chl-a [ $\mu\text{g L}^{-1}$ ] (a:c), and CDOM (d:f) for float 6903093 under Olaf. Three columns (a,d; b,e; c,f), are profile groupings: prior, immediately following, and post disturbance, following sequential order corresponding time relative to TC overpass. Lines in each panel are dashed, dotted, solid in sequential order, within groupings. Days relative are: -20, -16, -10, 0, 4, 10, 20, 24.	

<b>Ch 3 - Figure 9 .....</b>	<b>98</b>
Density profiles of oxygen [ $\mu\text{mol/kg}$ ] (a:c), and Chl-a [ $\mu\text{g L}^{-1}$ ] (d:f) for float 6903093 under Olaf. Three columns (a,d; b,e; c,f), are profile groupings: prior, immediately following, and post disturbance, following sequential order corresponding time relative to TC overpass. Lines in each panel are dashed, dotted, solid in sequential order, within groupings. Days relative are: -20, -16, -10, 0, 4, 10, 20, 24. y-axis being Sigma-0 , potential density anomaly [ $\text{kg/m}^3$ ], as opposed to depth.	
<b>Ch 3 - Figure 10 .....</b>	<b>99</b>
Density profiles of cp660, beam attenuation at 660 nm [ $\text{m}^{-1}$ ] (a:c) for float 6903093 under Olaf. Three columns are profile groupings: prior, immediately following, and post disturbance, following sequential order corresponding time relative to TC overpass. Lines in each panel are dashed, dotted, solid in sequential order, within groupings. Days relative are: -20, -16, -10, 0, 4, 10, 20, 24. y-axis being Sigma-0 , potential density anomaly [ $\text{kg/m}^3$ ], as opposed to depth.	
<b>Ch 3 - Figure 11 .....</b>	<b>99</b>
Interpolated time series section of Float 69003094 from 2021-2023. Not the same float as proceeding figures of profiles. Black line is Mixed depth red lines are density isopycnals.	
<b>Ch 3 - Figure 12 .....</b>	<b>100</b>
Interpolated section of Float 69003094 for Olaf and Nora overpasses. Not the same float as proceeding figures of profiles. For Olaf Passover date (09/10), was -1 and 5 days to the closest profiles. Black line is the mixed layer depth red lines are density isopycnals.	
<b>App. – Figure 1 .....</b>	<b>114</b>
Map of stations and repeat sampling, O indicates ocean, with inside the bay as either D deep (>15m) or, S shallow. High resolution lidar bathymetry was used to map the depth inside the bay, with a coarser gridded dataset for the ocean stations. Both are freely available from NOAA's Coastal Management Office. Yellow dots "Sample Stations" are averaged GPS of actual measurements. Green triangles are static station markers.	
<b>App. – Figure 2 .....</b>	<b>115</b>
Subset map from Figure 1 of stations and repeat sampling. Red arrows indicate stations D1 & D2, the most important for this study. Note sampling at B1 was added in June 2019 as it is close to a moored subsurface science buoy, operated by the Bodega Bay Marine Lab. Hog Island is the ca. center of image for reference. Gray to black in image indicates increasing depth from Lidar data used in Figure 1 (scale the same).	
<b>App. – Figure 3 .....</b>	<b>116</b>
Full moon indicated by solid lines, new moon dashed. Lines are mean for all sites per sampling night. Top panel is downwelling irradiance, incoming moonlight a meter above water (magenta). Middle panel is water leaving/upwelling radiance (green). Units differ. Bottom panel is reflectance (black), the ratio of upwelling energy to incoming energy ( $\pi * \text{radiance/irradiance}$ ). Does not take into account the moon angle, assuming all angles are nadir. Reflectance values over one were excluded. X-axis is wavelength.	
<b>App. – Figure 4 .....</b>	<b>117</b>
Integrated nighttime subsurface radiometric profiles, upwelling radiance - downward facing probe, for June 2019 full moon sampling. Trends are means for integrated values (points) for 0-5m for all profiles per station. Y-axis is intensity, x axis is wavelength. From top panel:: Station D5, D1, S2, B1 (see Figure 1).	

**App. – Figure 5 ..... 118**

Single nighttime subsurface radiometric profiles, upwelling radiance - downward facing probe, for June 2019 full moon sampling. Y-axis is intensity, x axis is wavelength. Panels are specific depths at three stations. From top panel: Station D1 6m, Station D1 1m, Station S2 1m, Station D4 1m. Intensities at known bioluminescent wavelengths are present, but noise cannot be excluded. The strong signal @ 466nm in the upper left panel is a common wavelength for bioluminescent producing marine taxa.

## List of Tables

<b>Ch 1 - Supplementary Table 1 .....</b>	<b>44</b>
Storm position (eye), translational speed, and wind speeds for Hurricane Bud every 6 hours. Times are UTC-0 and coordinates are given for the position of the storm center/eye. Translational speed is calculated for distance traveled from the previous six hour position. Wind speed is maximum sustained for that position. The ratio (WS/TS) is wind speed (WS) over translational speed (TS). It is also given for the cubed wind speed (WS <sup>3</sup> /TS). Higher numbers indicate more wind energy imparted to a section of ocean per unit time. The simple ratio is reported for congruence with other studies, the cubed wind speed ratio provides an accurate indication of kinetic energy transferred from wind to the ocean. Bolded rows correspond to Supplementary Table 2. The last time point is prior to landfall near San Jose del Cabo, Mexico. Position and wind speed data are from NOAA.	
<b>Ch 1 - Supplementary Table 2 .....</b>	<b>45</b>
Storm position (eye), time, translational speed, and wind speeds for Hurricane Bud corresponding to closest spatial pass to each station. Times are UTC-0. Distance is eye position distance to cruise station. Hours after indicates time after an overpass when cruise subsurface sampling (multiple casts) was at the mean point in time at the specific station. Data and methods are the same as Supplementary Table 1.	
<b>Ch 1 - Supplementary Table 3 .....</b>	<b>45</b>
To be supplied by collaborators. Listed for congruence with the main text of manuscript in preparation.	
<b>Ch 1 - Supplementary Table 4 .....</b>	<b>45</b>
To be supplied by collaborators. Listed for congruence with the main text of manuscript in preparation.	
<b>Ch 2 - Table 1 .....</b>	<b>56</b>
Station 3.5 CTD individual cast times. UTC-0, and with local time for diurnal context.	
<b>Ch 2 - Table 2 .....</b>	<b>64</b>
Station 4 CTD individual cast times. UTC-0, and with local time for diurnal context.	
<b>Ch 2 - Table 3 .....</b>	<b>68</b>
Station 3 CTD individual cast times. UTC-0, and with local time for diurnal context.	
<b>Ch 3 - Table 1 .....</b>	<b>88</b>
Total BGC-Argo floats within ETNP OMZ-Hurricane zone. Spatial temporally as defined in Methods. Floats interacting and profiles interacting are for the largest selection, All tropical cyclones, 500 km and from 30 days prior to or 45 days after TC overpass. As defined in methods, the area for BGC-Argo profile selection was 38.5N, 3.5S, 180W, 78W. TCs were selected from within a 7 degree buffer within this spatial domain. Applies to all Tables.	
<b>Ch 3 - Table 2 .....</b>	<b>88</b>
Number of TCs intersecting BGC-Argo floats. * For floats within 30 days prior to or 45 days after TC overpass. ** indicates the highest category over TCs full track. Hurricanes cat 1-5, Major = Cat 4 & 5. Tropical Cyclones category is inclusive of all non-hurricane and hurricane strength storms. Hurricanes are inclusive of major and non-major hurricanes. Designations apply to all following tables 1-3. Range indicates that an individual TC will change designation/strength over its lifetime.	
<b>Ch 3 - Table 3 (a) .....</b>	<b>89</b>
Floats and profiles <b>Tropical Storms</b> . As table 2, for tropical cyclones only, classified as below hurricane strength.	

<b>Ch 3 - Table 3 (b) .....</b>	<b>89</b>
Floats and profiles <b>Hurricanes**</b> . As table 2, for hurricanes only, classified as below hurricane strength, but not Major.	
<b>Ch 3 - Table 3 (c) .....</b>	<b>89</b>
Floats and profiles <b>for Major Hurricanes**</b> . As table 2, for major hurricanes	
<b>Ch 3 - Table 4 .....</b>	<b>01</b>
MANOVA table of significance for independent variables, column one. Columns two and three are the two dependent variables. For profiles after a TC overpass. “Absolute depth of OMZ” is the value of the top of the OMZ. “Change from Pre-Strom Depth” based on the change between prior and post TC overpass for the TC-Float interactions. “Pre-storm condition profiles” indicates summary statistics for prior profiles absolute depth of the OMZ. P values are given by: *** 99%, ** 95%, * 90%.	
<b>App. – Table 1 .....</b>	<b>119</b>
Identified dinoflagellate genera from May 2023 sampling at Station D2. * Slash indicates either one of the two genera, or species whose taxonomic classification have changed from the first to the second genera. HAB species indicates harmful bloom species, an inclusive term for single species, whose blooms coincide with production of toxins <sup>53</sup> . Known to be bioluminescent is largely from ref <sup>24</sup> , but also from main identification reference <sup>53</sup> .	

## Abstract

Tropical cyclones (TCs) are a regular feature of the eastern tropical North Pacific (ETNP) oxygen minimum zone (OMZ). Oxygen minimum zones are ocean biomes, which are defined by consistently low oxygen at depth. Yet, no subsurface studies in the ETNP OMZ have explored TC impacts.

Presented are findings from a Category 4 Hurricane (Bud) in the ETNP OMZ during a research cruise. Sampling beneath Bud's wake revealed storm-induced alterations in the upper water column, leading to heightened concentrations of particulate organic carbon and chlorophyll, signaling an active phytoplankton bloom. Comparisons to reference data indicate a shoaling of the OMZ by 29-50 m. Simultaneously, molecular analysis of organic matter documented phytoplankton-derived compounds. 16S rRNA transcripts indicated a dominance of phytoplankton, and labile organic matter degraders near the surface, with known OMZ anoxic microbes below the OMZ depth.

A follow up study employed subsurface oceanographic techniques from the same cruise. Methods include (1) analysis of multiple profiles using Conductivity Temperature Depth instruments coupled with optical sensors for biogeochemical variables and (2) continuous subsurface current velocities measured by an Acoustic Doppler Current Profiler array (ADCP). The profiles provided insights into subsurface water properties, while shipboard ADCP data confirmed the presence of near-inertial waves, a TC-induced mixing mechanism. By synthesizing observations, a novel ecological-oceanographic model was developed.

In the final TC OMZ study, the Biogeochemical Argo (BGC-Argo) float array was used to examine TC induced subsurface biological parameters and oxygen fluctuations. (1) Hurricane Olaf was used as a case study; In similarity to Bud, OMZ shoaling, and the creation of a subsurface deep chlorophyll feature was observed. (2) Statistical analyses were conducted to assess the array's potential in understanding TCs and OMZ shoaling across the Eastern Pacific. Results echo studies on plankton blooms and inter-storm variability.

A pilot study, unrelated to TCs and OMZs, was conducted in Tomales Bay, California. Nocturnal radiometric data was collected, during two different lunar phases, in conjunction with optimal plankton bloom conditions. The study successfully distinguished between water leaving radiance derived from subsurface emission and lunar reflectance. Microscopic analysis confirmed the presence of known genera of bioluminescent dinoflagellates at the site.

## Introduction

Tropical cyclones (TCs) are a regular feature of the eastern tropical North Pacific (ETNP) oxygen minimum zone (OMZ), which is the ocean's largest subsurface OMZ, but are typically less common above the other major oxygen minimum zones. OMZs occur where physical and biological processes deplete dissolved oxygen (DO) concentrations below  $20 \mu\text{M}^{1,2}$ , making DO levels a primary state, and structuring, variable in these systems. OMZs are important regions of biogeochemical cycling<sup>3,4</sup> due to anaerobic biological activity. As a result, changes<sup>5</sup> in the volume and intensity of OMZ regions can have global biogeochemical ramifications<sup>6-8</sup>.

Cyclones are known to fuel phytoplankton blooms through mixing and upwelling of nutrients into the upper water column<sup>9,10</sup>, resulting in an overall increase in primary productivity throughout the ocean<sup>9,11,12</sup>. Cyclone intensity is predicted to increase globally with climate change<sup>13</sup>. However, differences exist at the scale of individual storms and between ocean basins<sup>9</sup>. Multiple interacting factors must align to result in increased productivity<sup>9,14,15</sup>. Coarse remotely sensed global analyses of chlorophyll-a concentrations, (Chl-a), following TC overpasses in the ETNP OMZ indicate a potentially strong biological response<sup>9,12</sup>. However, the biological models forced by TCs used to predict Chl-a response show a mismatch with observations<sup>9</sup>, suggesting a lack of understanding in exactly how biota respond to hurricanes. In the ETNP and globally, cyclone impacts are predominantly studied using satellite data, without subsurface *in situ* measurements, we lack a complete understanding of what happens below the surface. ***In situ* research of TCs impacts on the subsurface biology in this unique biogeochemical system is needed.**

Hurricanes could alter DO distributions in the ETNP OMZ by disrupting the structure of the water column through mixing and storm induced upwelling, as well as entrainment of oxygen from the air-sea interface caused by high energy winds. Hurricanes may increase surface water gas saturation through decreases in temperature, and gas exchange from the breaking of turbulent waves. Hurricanes ultimately may have varying dynamic effects on DO<sup>16</sup> if they induce a biological response that consumes oxygen beyond initial high input<sup>17</sup>. This could lead to shoaling of the OMZ and affect associated biogeochemical processes<sup>3</sup>. Knowledge of OMZ microbial communities and biogeochemical processes suggest a highly efficient response to increases in available oxidants and fresh organic matter<sup>18-20</sup>, indicating the possibility of biological ‘priming<sup>21</sup>, by hurricanes and net oxygen consumption. However, the scale at which hurricanes affect the subsurface biogeochemistry of the ETNP is not well resolved. **Given multiple dynamic pathways, analysis of observational data following hurricanes in the ETNP OMZ would improve our understanding of the biological response to hurricane disturbances.**

This **dissertation** is fundamentally centered on novel observations following an oceanographic research cruise that sampled the subsurface ocean following a hurricane in the ENTP OMZ. Science questions stem from placing biogeochemical observations in context. The three chapters are formatted to be standalone studies, but they are best read in sequence as the first chapter documents phenomena that may be new to science and the two subsequent chapters build upon those findings. There is a progression from

documenting the first order *Whats* related to primary observations, to then developing more scalable general theories, *Hows*, by taking a multidimensional view of the environmental system, and finally to investigating the occurrence of observations and theory at scale over the hurricane domain of the eastern Pacific.

**Chapter One** documents the findings from a research cruise that sampled after the overpass of a Category 4 hurricane (Bud) in the eastern tropical North Pacific Ocean, oxygen minimum zone. The study addresses: *What* is the impact of a strong tropical cyclone on the biological and biogeochemical state of the ETNP OMZ, *How* does the biological response explain a shoaling of the OMZ observed? An overarching general question is, *How* do hurricanes affect this important region of the ocean?

**Chapter Two** investigates mechanistic underpinnings in the observed variance of subsurface profiles across and within sampling stations, from the same cruise. Here questions are: *What* is the connection between physical oceanographic mechanisms and the biological response to TC disturbances, *How* do specific subsurface TC-mixing phenomena impact deep microbial communities under this storm? A general model is discussed that attempts to integrate the new biological observations, with more mature physical oceanographic work.

**Chapter Three** attempts to explore the main findings of Chapters One and Two, a shoaling of the OMZ and the concentration of biomass associated with subsurface chlorophyll features, within the ETNP using a robotic subsurface sampling array and additional tropical cyclone overpasses. Questions of repeatable and testable are more implicit, with the general questions of: *How* do the initial findings scale, *Can* those primary observations be captured at a larger scale using a different methodology? The final statistical analysis addresses, *How* does OMZ shoaling variability align with the community's understanding of TC-induced plankton blooms?

## Background

*This section is provided for optional use as a reference.*

### OMZs

Oxygen minimum zones are coastal and open ocean habitats that account for approximately 8% of the surface area of the global ocean<sup>2</sup>. They are defined by consistently low oxygen at depth. The eastern tropical North Pacific (ETNP) is the largest, by area, of the five major discrete oxygen minimum zones. With an areal extent of  $\sim 12.4 * 10^6 \text{ km}^2$ , it is approximately 2.5 times larger than the contiguous United States, and accounts for 40% of the area of the five major OMZ's, and 12% by volume<sup>2</sup>.

OMZs differ from classical oxygen minima locations found throughout the ocean, in that OMZs are shallower and more oxygen depleted<sup>2</sup>. Where global minima may be found at depths of 1000m -1500m, OMZs often impinge into the photic zone (upper 200m). Additionally, OMZs may have 2% less DO than values used to define global minima. The depth profiles of OMZs and minima differ in shape. In global minima, DO

decreases with depth with an approximately linear curve, to a relative minima, and then increases slowly with increasing depth. OMZs, however, show a more complex pattern: (1) starting at the surface there is a rapid decrease of DO with increasing depth, following a power function, to extremely low values. (2) The values reach a low, with a derivative of zero with increasing depth, until (3) they begin to increase again at the bottom of the OMZ core, (4) where they finally reach a deep maximum, (5) then decrease with depth to a deep minima before (6) they increase again<sup>2,3,20</sup>. While the pattern below the OMZ core differs from classic minima, it's the location of the top of an OMZ and its core that may be most important for exchange with the atmosphere and impactful for primary production, given the surface skewed biomass distribution of the ocean.

A DO concentration less than or equal to 20 micromolar of O<sub>2</sub> per kg of seawater (0.5 ml/L of seawater), is a value often used to delineate OMZs in the Pacific and the ENTP<sup>3</sup>. This represents ~ 10 % of surface DO. This value coincides to where anaerobic microbial processes become active, and is severely hypoxic for most larger metazoans. In comparison global minima have DO values ranging from 50 - 200 micromolar, meaning they are not fully anaerobic or severely hypoxic. While large organisms are absent from the core of the OMZ, migratory animals may be found above or below the OMZ<sup>3</sup>. DO levels structure OMZ ecosystems. Changes in the depth of the OMZ are overlaid over other structuring depth profiles such as photosynthetically available radiation<sup>19</sup>.

OMZs are found where input of DO is low and consumption through biological respiration is high. As climatic, biogeographic, and oceanographic volumes, OMZs may be parameterized at a steady state, with low surface ventilation, and with deep DO input low due to sluggish circulation<sup>1</sup>. High export of production from the euphotic zone to depth, associated with eastern boundary current upwelling in the ETNP, initiates microbial respiration that consumes oxygen; causing it to decline. The canonical work of Klaus Wyrtki<sup>1</sup> simplifies the differential equations used to define OMZs at steady state to show biological consumption causes the existence of local vertical oxygen minima, with the depth of occurrence dictated by ocean circulation. Steady state can only be assumed when integrating over appropriate space and time scales. For example, recent changes in decadal fluxes of CO<sub>2</sub> are linked to changes in ocean circulation<sup>5</sup>.

OMZs and their internal structure<sup>22</sup> fluctuate from seasonal<sup>2,22</sup> to geological scales<sup>3</sup>. Geological evidence from the eastern boundary shelf region of the ENTP OMZ suggests its size, intensity, and existence oscillates at millennial time scales over the last 60,000 years, possibly weakening during cool periods and strengthening during warm periods<sup>23</sup>. Our knowledge of modern OMZs indicates decadal and seasonal variability. Observations of decadal variation in oxidant driven biogeochemical processes fit models built on ENSO variability well in the ETNP<sup>24</sup>. This is congruent with the multitude of oceanographic and biological processes that are impacted by ENSO fluctuations in the eastern Pacific basin.

The ecosystems of OMZs are largely dominated by microbes<sup>20,25</sup>. Microbial seasonal and vertical distributions<sup>26</sup> follow patterns seen globally in oligotrophic regions, yet are unique communities in of themselves<sup>3,27–29</sup>. In OMZs the divide between anaerobic and aerobic biological processes is fundamentally important, yet complex and dynamic<sup>3,19,20,30</sup>.

Oxygen producing photosynthetic cyanobacteria are responsible for primary production and biological oxygen input in OMZs<sup>30,31</sup>. Respiration of detrital matter initiated through new cyanobacteria production<sup>30</sup>, often through complex carbon pathways<sup>32</sup>, depletes oxygen. However other pathways<sup>33</sup> are fundamentally important, with aerobic nitrite oxidation significantly contributing to DO consumption in OMZs<sup>2,3,18–20,30,34</sup>. Other biogeochemical cycles of import include novel nitrogen, and sulfur, pathways<sup>3</sup>. Surface production is not the only input to heterotrophic respiration, with terrestrially derived carbon likely having a significant impact<sup>35</sup>. High microbial mortality in OMZs likely contributes to carbon cycling, via the viral shunt<sup>36</sup>, and subsequent oxygen consumption—yet more viral studies in the OMZ are needed<sup>29</sup>.

The complex three dimensional structure of oxygen<sup>22</sup> within the ENTP OMZ provides spatially variable stoichiometric limitations for biological consumption. It also provides an important scaffolding for structuring the ENTP OMZ as a distinct ocean biogeographic ecoregion<sup>37</sup>. The frequency<sup>38</sup> of subsurface intrusions of oxygen varies spatially. This pattern could be incorporated into efforts at spatial biogeographical hierarchical delineations in the ocean<sup>37,39,40</sup> to supplement those founded on using surface ocean parameters<sup>41,42</sup>. Intrusion zones could be considered habitat types and studied through the lens of landscape ecology.

The edge of the OMZ is not solely a physical structuring variable but also the location and result of a particular biological community. With unique species, and communities found at this interface, and importantly they actively define it via biogeochemical processes<sup>20,28,43,44</sup>. That is, The OMZ boundary and the biological associated communities are a non independent (non-linear) phenomenon that co- occur.

Biogeographic theory in the ocean suggests the boundaries of spatial units are unique subregions, and that they should be defined by oceanographic currents<sup>42</sup>. The boundaries of the ETNP are impacted by intrusions of DO from geostrophic currents. Intrusions of DO into the equatorial edge of the OMZ are the most significant, due to the Northern Subsurface Countercurrent. The northern boundary experiences zonal subsurface jets, but they account for a smaller net DO flux. At its eastern boundary, the seasonal cycle of upwelling/downwelling introduces low/high DO waters into the OMZ core<sup>22</sup>. It has been suggested that the microbes in OMZ are evolutionarily adapted to these intrusion regimes<sup>18</sup>.

Hurricanes, TC's with high intensity winds, may be an intrusion mechanism<sup>45</sup> that is important for the ETNP OMZ, given TC's high frequency of occurrences is spatially in-sync with its boundaries and core<sup>2,46</sup>. Gas exchange across the air-sea interface follows a positive relationship with wind speed. The exact model defining that relationship is a variable step function; linear to cubic<sup>47</sup>. Additionally, hurricanes are an earth system feature that have existed over the ETNP OMZ for sufficient geological time<sup>48,49</sup>, and as such they might be of evolutionarily significance.

## Tropical cyclones and biological effects

It is well established through observations that TC-induced ocean mixing caused by cyclonic storms can increase primary productivity in the ocean. The cause of the increased productivity is attributed to increased nutrient input to surface waters through

mixing, entrainment and upwelling<sup>10,15,50</sup>. However, shoaling and or mixing of the existent deep chlorophyll maximum, can produce false positives in satellite derived bloom estimates<sup>51</sup>. The potential energy of mixing comes from the high winds of TCs.

In general, TC-induced mixing intensity varies with the cube of the wind speed and varies inversely with storm translation speed<sup>52</sup>. Additionally, the radius of maximum SST cooling (an indicator of spatial extent of mixing) increases linearly for low to mean values of translational speeds<sup>52</sup>. Medium sized, slow moving, storms can have as much as a 30 fold increase in productivity as compared to background levels<sup>53</sup>. Decadal global analysis suggests increases in Chl-a in oligotrophic regions due to increases in the intensity and frequency of the strongest TCs<sup>12</sup>.

However, differences exist at the scale of individual storms<sup>54</sup>, and between ocean basins. Not all storms cause Chl-a increases. Work by Lin *et. al.*<sup>55</sup>, suggests that a simple increased mixing and increased productivity model does not fit observed patterns of several typhoons in the Western Central Pacific. In their analysis of eleven storms only two induced significant phytoplankton blooms, and the largest storm did not produce a bloom. Storm size, storm translational speed, sustained wind speeds, and the interaction of ocean eddies must all align in order to observe increasing productivity, as measured by the proxy surface derived Chlorophyll-a concentration<sup>14</sup>.

Hurricanes are dynamic and complex meteorological events<sup>56</sup>. Their formation, subsequent progression, and characteristics are fundamentally tied to the section of ocean they interact with. Enthalpy changes, via heat transferred from the ocean to the atmosphere, is the fuel that drives hurricanes. Importantly it is a highly dynamic interaction. Indeed, modeling hurricane formation was the genesis for the “butterfly effect” concept, where end conditions in a nonlinear deterministic system can differ significantly based on slight variations in its initial boundary conditions<sup>57</sup>. Biological activity following TC overpasses may be viewed as a one way forcing and response function, yet the physical dynamics of wind input and ocean overturning involves ongoing exchange of heat between the atmospheric phenomenon and the underlying ocean<sup>58</sup>. Or, put another way, TCs are both endogenous and exogenous disturbances to the surface ocean system.

Hurricanes can impact the upper 200-300 meters of the ocean.<sup>15</sup> A storm's ability to induce productivity increases is dependent on the precondition of the underlying ocean, which dictates mixing extent<sup>55</sup>. Precondition factors include: the depth of the mixed layer (MLD), density stratification, salinity, sea surface temperature (SST), or transient ocean eddies. The deeper the MLD the greater the volume of water to be overturned, requiring more energy to overturn it. A greater temperature difference between the bottom of MLD and underlying ocean also requires more work to mix. SST prior to a storm can add or subtract to a storm's energy. Decreases in salinity induced through TC precipitation acts as a negative feedback to mixing via increased stratification<sup>15</sup>. Density stratification, the pycnocline, inhibits mixing. Seawater density is a product of its salinity and temperature as dictated by the equation of state for seawater.

The consistently deep MLD of the western North Pacific subtropical ocean, where many detailed hurricane studies have been conducted, is thought to explain many TC overpasses that have not caused blooms<sup>55</sup>. Pre-storm warm eddies act as an energetic barrier to mixing and explain low productivity increases in many large storms<sup>55</sup>. Eddy

vorticity may interact constructively or destructively with TC mixing energy<sup>15</sup>. Additionally, the presence of warm ocean eddies increases the depth of the nutricline, which is what is mixed, and transported, to the surface by winds, initiating increases in primary production<sup>15</sup>. Cold eddies may have the opposite effect.

Cyclonic, cold core eddies in the eastern Pacific have been shown to increase localized productivity through upwelling of nutrients, as well as an enhanced deep chlorophyll maxima (DCM), congruent with eddy Ekman pumping, in all seas<sup>51</sup>. In general, anticyclonic warm core eddies have the opposite effect because of downwelling. Prior productivity levels, including the depth, or existence, of the DCM<sup>51</sup>, is a precondition for TC overpasses that impacts the biological response<sup>55</sup>.

The mixing induced by TCs is dependent on multiple variables of the precondition because the mixing itself is complex<sup>15</sup>. Simplified, it is the net effect of two intertwined categories of mixing: (1) vertical entrainment and (2) geostrophic mixing. Entrainment is the localized overturning and mixing of the surface layer of the ocean due to turbulence caused by wind, waves, and surface currents that results in a colder thicker MLD. The biological impacts may be considered a sort of localized ‘spring bloom’ as is seen in temperate systems<sup>59</sup>.

Geostrophic mixing, upwelling (Ekman suction), and downwelling (Ekman pumping) is due to the TC interacting with the ocean and resultant geostrophic advective currents. Near-inertial waves are a second type of non-independent geostrophic mixing that interacts with Ekman transport<sup>60</sup>. Near-inertial waves are transverse mechanical waves that propagate through the interior of the upper ocean. Variable wind induced forcing initiates their formation while the Coriolis force acts as the restoring force<sup>61</sup>. They are a mechanism responsible for upwelling and horizontal mixing post-TC<sup>10,62</sup>; but do not always form for every storm. Tropical cyclones with translational speeds below 4 m/s may be assumed<sup>10,53,55</sup> to form inertial waves. Inertial waves emerge in slab models of the surface ocean following a TC overpass<sup>63</sup>. In these models: Winds cause horizontal shear, the shear of the surface slab over the underlying stationary slab, creates an inertial driven harmonic oscillation of the two slabs as the earth rotates<sup>64</sup>. The net effect of these oscillations may be upwelling, but they oscillate between upwelling and downwelling limbs, with periods determined by energy input and latitude. The periods of inertial waves are in the order of multiple hours to days. These oceanographic phenomena are non-intuitive in structure, and are more difficult to measure than wind induced entrainment.

Remote sensing studies of TC’s biological response and SST changes<sup>11-13</sup>, without *in situ* measurements<sup>53</sup>, cannot distinguish between these multiple mixing mechanisms that act synergistically<sup>61</sup>. Both act together to produce cold wakes following a TC, where inertia wave propagation is tied to density and thermal stratification. Most global studies use TC cold wake as a proxy for mixing. However, cold suction (temperature changes due to conduction as opposed to advection)<sup>61</sup>, and dimensionality issues (surface temperature as opposed to depth complexity/integration) are factors that make SST an imperfect proxy for mixing.

Entertainment and upwelling will occur at different spatial temporal scales following a TC. In general, entrainment may be more localized in space and constrained in time, with upwelling lasting longer and propagating outwards from a storm’s center.

Upwelling may be more important for maintaining a sustained response, especially for persistence of blooms, as inertial waves may persist for weeks after a storm as they are weakly dispersive. Conversely most authors suggest entrainment explains the majority of cold wake temperature changes.

There is good agreement in spatial patterns of chlorophyll, SST, wind, and currents to TC track. Blooms are stronger on the right side of a cyclone track in the northern hemisphere. That corresponds to strong cold wakes on that side, which is due to the storm's wind rotation direction (counterclockwise) causing better wind-current resonance<sup>15</sup>. Spatial patterns are often more complex when TCs pass close to land, because of associated confounding factors introduced through interaction with the shelf<sup>35,65,66</sup>. Importantly, biological responses to TCs have not been specifically examined in the ETNP OMZ.

## Dissolved oxygen and hurricanes

Given the importance of DO in the ETNP OMZ (and globally), and the potential for hurricanes to affect this fundamental element, examining DO and TCs in the ETNP OMZ is pertinent. Yet there have been few studies either globally or in ENTP that have explored this in depth.

Based on first principles it would be assumed DO in the ETNP OMZ is dependent on O<sub>2</sub> input through physical means, with both loss and gain through biological means. Net effects could mask various feedback loops. Hurricanes can cause increases in DO through entrainment and secondary induced photosynthesis. Any new production may also induce increased consumption due to heterotrophic respiration. Oxygen levels may increase if biological responses are weak given increased input due to the geometric increase of gas uptake due to wind forcing.

A study<sup>17</sup> from a research cruise in the South China sea following a typhoon found increases in surface DO. The authors hypothesized that this finding was due to input of DO from TC caused air-sea entrainment, intrusion from a subsurface current, and production from photosynthesis due to an observed plankton bloom. A separate study<sup>16</sup> looking at five TCs in the Bay of Bengal OMZ using Argo floats found mixed results. The author's bin their results into three categories based solely on strength of upwelling/downwelling of surface waters and its impact on vertical distribution of DO. Given their small sample size and the high number of confounding variables and variance (spatial position relative to storm, time of measurement, plankton level, seasonal differences, storm strength differences, and position within the basin), it is difficult to extrapolate conclusions. Additionally, the temporal sampling profiling frequency of a single Argo float (average = 10 days) is too coarse to capture the alternating period of inertia waves. The authors acknowledge that biogeochemical processes could affect DO but do not attempt analysis on their limited data, despite the fact they have Chl-a values.

Physical input of O<sub>2</sub> across the air-sea interface due to TC input is expected to follow a cubic relationship at wind speeds above 35m/s. Derived from both experimental evidence<sup>67,68</sup>, and in situ studies<sup>47</sup>. Additional super saturation of DO occurs due to bubble injection in TCs<sup>47</sup>. The air-sea gas exchange literature is dominated by CO<sub>2</sub>

flux<sup>69,70</sup> estimates, and care must be taken in using<sup>71</sup> soluble (CO<sub>2</sub>) fluxes to estimate non soluble (O<sub>2</sub>) gas fluxes. Temperature dependent models must be used.

## References

1. Wyrtki, K. The oxygen minima in relation to ocean circulation. in *Deep Sea Research and Oceanographic Abstracts* vol. 9 11–23 (Elsevier, 1962).
2. Paulmier, A. & Ruiz-Pino, D. Oxygen minimum zones (OMZs) in the modern ocean. *Progress in Oceanography* **80**, 113–128 (2009).
3. Gilly, W. F., Michael Beman, J., Litvin, S. Y. & Robison, B. H. Oceanographic and biological effects of shoaling of the oxygen minimum zone. *Annual Review of Marine Science* **5**, 393–420 (2013).
4. Pavia, F. J. *et al.* Shallow particulate organic carbon regeneration in the South Pacific Ocean. *Proc Natl Acad Sci USA* **116**, 9753–9758 (2019).
5. DeVries, T., Holzer, M. & Primeau, F. Recent increase in oceanic carbon uptake driven by weaker upper-ocean overturning. *Nature* **542**, 215–218 (2017).
6. Deutsch, C., Brix, H., Ito, T., Frenzel, H. & Thompson, L. Climate-Forced Variability of Ocean Hypoxia. *Science* **333**, 336–339 (2011).
7. Long, M. C., Deutsch, C. & Ito, T. Finding forced trends in oceanic oxygen. *Global Biogeochemical Cycles* **30**, 381–397 (2016).
8. Hutchins, D. A. & Fu, F. Microorganisms and ocean global change. *Nat Microbiol* **2**, 17058 (2017).
9. Menkes, C. E. *et al.* Global impact of tropical cyclones on primary production. *Global Biogeochemical Cycles* **30**, 767–786 (2016).
10. Price, J. F. Upper ocean response to a hurricane. *Journal of Physical Oceanography* **11**, 153–175 (1981).
11. Foltz, G. R., Balaguru, K. & Leung, L. R. A reassessment of the integrated impact of tropical cyclones on surface chlorophyll in the western subtropical North Atlantic. *Geophysical Research Letters* **42**, 1158–1164 (2015).
12. Da, N. D., Foltz, G. R. & Balaguru, K. Observed Global Increases in Tropical Cyclone-Induced Ocean Cooling and Primary Production. *Geophys Res Lett* **48**, (2021).
13. Bhatia, K. T. *et al.* Recent increases in tropical cyclone intensification rates. *Nature communications* **10**, 1–9 (2019).
14. Hu, C., Lee, Z. & Franz, B. Chlorophyll a algorithms for oligotrophic oceans: A novel approach based on three-band reflectance difference. *Journal of Geophysical Research: Oceans* **117**, 1–25 (2012).
15. Zhang, H., He, H., Zhang, W. Z. & Tian, D. Upper ocean response to tropical cyclones: a review. *Geoscience Letters* **8**, 1–12 (2021).
16. Xu, H., Tang, D., Sheng, J., Liu, Y. & Sui, Y. Study of dissolved oxygen responses to tropical cyclones in the Bay of Bengal based on Argo and satellite observations. *Science of The Total Environment* **659**, 912–922 (2019).
17. Lin, J., Tang, D., Alpers, W. & Wang, S. Response of dissolved oxygen and related marine ecological parameters to a tropical cyclone in the South China Sea. *Advances in Space Research* **53**, 1081–1091 (2014).
18. Kalvelage, T. *et al.* Aerobic Microbial Respiration In Oceanic Oxygen Minimum Zones. *PLoS ONE* **10**, e0133526 (2015).
19. Beman, J. M. *et al.* Substantial oxygen consumption by aerobic nitrite oxidation in oceanic oxygen minimum zones. *Nat Commun* **12**, 7043 (2021).

20. Ulloa, O., Canfield, D. E., DeLong, E. F., Letelier, R. M. & Stewart, F. J. Microbial oceanography of anoxic oxygen minimum zones. *Proc. Natl. Acad. Sci. U.S.A.* **109**, 15996–16003 (2012).
21. Bingeman, C. W., Varner, J. E. & Martin, W. P. The Effect of the Addition of Organic Materials on the Decomposition of an Organic Soil. *Soil Science Society of America Journal* **17**, 34–38 (1953).
22. Margolskee, A., Frenzel, H., Emerson, S. & Deutsch, C. Ventilation Pathways for the North Pacific Oxygen Deficient Zone. *Global Biogeochemical Cycles* **33**, 875–890 (2019).
23. Cannariato, K. G. & Kennett, J. P. Climatically related millennial-scale fluctuations in strength of California margin oxygen-minimum zone during the past 60 k.y. *Geology* **27**, 975–978 (1999).
24. Yang, S., Gruber, N., Long, M. C. & Vogt, M. ENSO-Driven Variability of Denitrification and Suboxia in the Eastern Tropical Pacific Ocean. *Global Biogeochem. Cycles* **31**, 1470–1487 (2017).
25. Moran, M. A. The global ocean microbiome. *Science* **350**, aac8455 (2015).
26. Giovannoni, S. J. & Vergin, K. L. Seasonality in Ocean Microbial Communities. *Science* **335**, 671–676 (2012).
27. Saunders, J. K., Fuchsman, C. A., McKay, C. & Rocap, G. Complete arsenic-based respiratory cycle in the marine microbial communities of pelagic oxygen-deficient zones. *Proc. Natl. Acad. Sci. U.S.A.* **116**, 9925–9930 (2019).
28. Beman, J. M. & Carolan, M. T. Deoxygenation alters bacterial diversity and community composition in the ocean’s largest oxygen minimum zone. *Nature Communications* **4**, (2013).
29. Long, A. M., Jurgensen, S. K., Petchel, A. R., Savoie, E. R. & Brum, J. R. Microbial Ecology of Oxygen Minimum Zones Amidst Ocean Deoxygenation. *Front. Microbiol.* **12**, 748961 (2021).
30. Fuchsman, C. A. *et al.* Cyanobacteria and cyanophage contributions to carbon and nitrogen cycling in an oligotrophic oxygen-deficient zone. *ISME J* **13**, 2714–2726 (2019).
31. Garcia-Robledo, E. *et al.* Cryptic oxygen cycling in anoxic marine zones. *Proc. Natl. Acad. Sci. U.S.A.* **114**, 8319–8324 (2017).
32. Brewin, R. J. W. *et al.* Sensing the ocean biological carbon pump from space: A review of capabilities, concepts, research gaps and future developments. *Earth-Science Reviews* **217**, 103604 (2021).
33. Falkowski, P. G., Fenchel, T. & Delong, E. F. The Microbial Engines That Drive Earth’s Biogeochemical Cycles. *Science* **320**, 1034–1039 (2008).
34. Francis, C. A., Beman, J. M. & Kuypers, M. M. M. New processes and players in the nitrogen cycle: The microbial ecology of anaerobic and archaeal ammonia oxidation. *ISME Journal* **1**, 19–27 (2007).
35. Ragavan, P. & Kumar, S. Potential role of priming effect in the open ocean oxygen minimum zones: an outlook. *Hydrobiologia* **848**, 2437–2448 (2021).
36. Weinbauer, M. G., Chen, F. & Wilhelm, S. W. Virus-mediated redistribution and partitioning of carbon in the global oceans. *Microbial carbon pump in the ocean* 54–56 (2011).
37. Sutton, T. T. *et al.* A global biogeographic classification of the mesopelagic zone. *Deep Sea Research Part I: Oceanographic Research Papers* **126**, 85–102 (2017).
38. Kwiecinski, J. V. & Babbin, A. R. A High-Resolution Atlas of the Eastern Tropical Pacific Oxygen Deficient Zones. *Global Biogeochemical Cycles* **35**, (2021).
39. Spalding, M. D. *et al.* Marine ecoregions of the world: A bioregionalization of coastal and shelf areas. *BioScience* **57**, 573–583 (2007).
40. Briones, E. E., Rice, J. & Ardon, J. Global open oceans and deep seabed (GOODS)

- biogeographic classification. *UNESCO, IOC* **54**, (2009).
41. Longhurst, A. R. *Ecological geography of the sea*. (Academic Press, 2010).
  42. Priede, I. G. Biogeography of the oceans: a review of development of knowledge of currents, fronts and regional boundaries from sailing ships in the sixteenth century to satellite remote sensing. *Pure and Applied Geophysics* **171**, 1013–1027 (2014).
  43. Cox, I. *et al.* Distinct habitat and biogeochemical properties of low-oxygen-adapted tropical oceanic phytoplankton. *Limnology & Oceanography* **68**, 2022–2039 (2023).
  44. Bryant, J. A., Stewart, F. J., Eppley, J. M. & DeLong, E. F. Microbial community phylogenetic and trait diversity declines with depth in a marine oxygen minimum zone. *Ecology* **93**, 1659–1673 (2012).
  45. Atamanchuk, D., Koelling, J., Send, U. & Wallace, D. W. R. Rapid transfer of oxygen to the deep ocean mediated by bubbles. *Nat. Geosci.* **13**, 232–237 (2020).
  46. Murakami, H. *et al.* Simulation and prediction of category 4 and 5 hurricanes in the high-resolution GFDL HiFLOR coupled climate model. *Journal of Climate* **28**, 9058–9079 (2015).
  47. McNeil, C. & D’Asaro, E. Parameterization of air-sea gas fluxes at extreme wind speeds. *Journal of Marine Systems* **66**, 110–121 (2007).
  48. Marsaglia, K. M. & Klein, G. D. The paleogeography of paleozoic and mesozoic storm depositional systems. *The Journal of Geology* **91**, 117–142 (1983).
  49. Fedorov, A. V., Brierley, C. M. & Emanuel, K. Tropical cyclones and permanent El Niño in the early Pliocene epoch. *Nature* **463**, 1066–1070 (2010).
  50. Menkes, C. E. *et al.* Global impact of tropical cyclones on primary production. *Global Biogeochemical Cycles* **30**, 767–786 (2016).
  51. Chai, F. *et al.* A limited effect of sub-tropical typhoons on phytoplankton dynamics. *Biogeosciences* **18**, 849–859 (2021).
  52. Vincent, E. M. *et al.* Processes setting the characteristics of sea surface cooling induced by tropical cyclones. *J. Geophys. Res.* **117**, (2012).
  53. Lin, I. *et al.* New evidence for enhanced ocean primary production triggered by tropical cyclone. *Geophys. Res. Lett.* **30**, (2003).
  54. Lin, I.-I. *et al.* A Tale of Two Rapidly Intensifying Supertyphoons: Hagibis (2019) and Haiyan (2013). *Bulletin of the American Meteorological Society* **102**, E1645–E1664 (2021).
  55. Lin, I. I. Typhoon-induced phytoplankton blooms and primary productivity increase in the western North Pacific subtropical ocean. *Journal of Geophysical Research: Oceans* **117**, (2012).
  56. Emanuel, K. Tropical Cyclones. *Annu. Rev. Earth Planet. Sci.* **31**, 75–104 (2003).
  57. Lorenz, E. N. Deterministic Nonperiodic Flow. *J. Atmos. Sci.* **20**, 130–141 (1963).
  58. Jiang, G., Xu, J. & Wei, J. A Deep Learning Algorithm of Neural Network for the Parameterization of Typhoon-Ocean Feedback in Typhoon Forecast Models. *Geophys. Res. Lett.* **45**, 3706–3716 (2018).
  59. Chiswell, S. M., Calil, P. H. R. & Boyd, P. W. Spring blooms and annual cycles of phytoplankton: a unified perspective. *Journal of Plankton Research* **37**, 500–508 (2015).
  60. Chen, Y., Straub, D. & Nadeau, L.-P. Interaction of Nonlinear Ekman Pumping, Near-Inertial Oscillations, and Geostrophic Turbulence in an Idealized Coupled Model. *Journal of Physical Oceanography* **51**, 975–987 (2021).
  61. Zhang, H. *et al.* Upper ocean response to typhoon Kalmaegi (2014). *Journal of Geophysical Research: Oceans* **121**, 6762–6778 (2016).
  62. Firing, E., Lien, R.-C. & Muller, P. Observations of strong inertial oscillations after the passage of tropical cyclone Ofa. *Journal of Geophysical Research: Oceans* **102**, 3317–3322 (1997).
  63. Geisler, J. E. Linear theory of the response of a two layer ocean to a moving hurricane.

- Geophysical and Astrophysical Fluid Dynamics* **1**, 249–272 (1970).
- 64. Palter, J. Storms bring ocean nutrients to light. *Nature News and Views* 1–2 (2015).
  - 65. Christensen, N., de la Paz, R. V. & Gutiérrez, G. V. A study of sub-inertial waves off the west coast of Mexico. *Deep Sea Research Part A. Oceanographic Research Papers* **30**, 835–850 (1983).
  - 66. Bianucci, L., Balaguru, K., Smith, R. W., Leung, L. R. & Moriarty, J. M. Contribution of hurricane-induced sediment resuspension to coastal oxygen dynamics. *Sci Rep* **8**, 15740 (2018).
  - 67. Krall, K. E. & Jähne, B. First laboratory study of air–sea gas exchange at hurricane wind speeds. *Ocean Sci.* **10**, 257–265 (2014).
  - 68. Iwano, K., Takagaki, N., Kurose, R. & Komori, S. Mass transfer velocity across the breaking air–water interface at extremely high wind speeds. *Tellus B: Chemical and Physical Meteorology* **65**, 21341 (2013).
  - 69. Bates, N. R., Knap, A. H. & Michaels, A. F. Contribution of hurricanes to local and global estimates of air-sea exchange of CO<sub>2</sub>. *Nature* **395**, 58–61 (1998).
  - 70. Takahashi, T. *et al.* Climatological mean and decadal change in surface ocean pCO<sub>2</sub>, and net sea–air CO<sub>2</sub> flux over the global oceans. *Deep Sea Research Part II: Topical Studies in Oceanography* **56**, 554–577 (2009).
  - 71. Wanninkhof, R. Relationship between wind speed and gas exchange over the ocean revisited: Gas exchange and wind speed over the ocean. *Limnol. Oceanogr. Methods* **12**, 351–362 (2014).

# Chapter One: Tropical cyclones drive simultaneous oxygen minimum zone shoaling and enhanced organic matter supply

Manuscript in preparation

Genco, B.M.<sup>1</sup>, M.E. White<sup>2,3</sup>, I. Koester<sup>2</sup>, S.M. Vargas<sup>1</sup>, J.K. Saunders<sup>4,5</sup>, M.A. Saito<sup>4</sup>, J.Q. Garcia Maldonado<sup>6</sup>, L.I. Aluwihare<sup>2</sup>, J.M. Beman<sup>1</sup>

<sup>1</sup>Life and Environmental Science and Sierra Nevada Research Institute, University of California Merced, California, United States of America

<sup>2</sup>Geosciences Research Division, Scripps Institution of Oceanography, University of California San Diego, California, United States of America

<sup>3</sup>Department of Earth Sciences, ETH Zürich, Switzerland

<sup>4</sup>Marine Chemistry and Geochemistry Department, Woods Hole Oceanographic Institution, Massachusetts, United States of America

<sup>5</sup>Department of Marine Sciences, University of Georgia, Georgia, United States of America

<sup>6</sup>Interfaculty Institute of Microbiology and Medicine, University of Tuebingen, Tuebingen, Germany

<sup>7</sup>Department of Biochemistry, University of California Riverside, California, United States of America

<sup>8</sup>Skaggs School of Pharmacy and Pharmaceutical Sciences, University of California San Diego, California, United States of America

<sup>9</sup>Departamento de Recursos del Mar, Centro de Investigación y de Estudios Avanzados del Instituto Politécnico Nacional, Unidad Mérida, Yucatán, Mexico

<sup>10</sup>Collaborative Mass Spectrometry Innovation Center, Skaggs School of Pharmacy and Pharmaceutical Sciences, University of California San Diego, California, United States of America

**Corresponding author:** Prof. J. Michael Beman, Life and Environmental Sciences, University of California, Merced, 5200 North Lake Road, Merced, CA 95343, USA

**Author Contributions:** J.M.B. designed the study; B.M.G., M.E.W., I.K., S.M.V., J.K.S., J.Q.G.M., and J.M.B performed the research; all authors contributed new analytical tools; and B.M.G., M.E.W., and J.M.B. wrote the paper.

## Abstract

Tropical cyclones regularly form above the ocean's largest subsurface oxygen minimum zone (OMZ) in the eastern tropical North Pacific Ocean (ETNP), yet how these powerful storms affect this biogeochemically-important region remains unknown. Here we report multiple effects of a Category 4 hurricane (Bud) that occurred during a research cruise in the ETNP OMZ. Profiles and samples collected beneath Bud's wake captured storm-driven alteration of the upper water column, including elevated particulate organic carbon and chlorophyll concentrations indicative of an active phytoplankton bloom. Comparison of dissolved oxygen profiles between repeat cruises and additional data demonstrate that the OMZ shoaled by 29–50 m, reaching depths as shallow as 41 m. Coincident with the bloom and OMZ shoaling, molecular-level characterization of organic matter showed accumulation of phytoplankton-derived organic compounds, while 16S rRNA transcripts from active microbes were dominated by known degraders of phytoplankton-derived organic matter near the surface and by anoxic bacteria (including sulfate reducers) in the OMZ—indicating rapid hurricane-driven biogeochemical changes. Collectively our data demonstrate that tropical cyclones drive OMZ shoaling, increase the supply of fresh organic material to these oxygen-depleted waters, and alter the subsurface biogeochemistry of the ETNP.

## Introduction

Tropical cyclones form over the low latitudes of the ocean where sea surface temperatures (SSTs) are elevated. However, the eastern tropical North Pacific (ETNP) is unique in that major tropical cyclones (hurricanes) consistently form above the ocean's largest subsurface oxygen minimum zone (OMZ). OMZs occur where elevated surface production and sluggish circulation combine to drive rapid rates of oxygen consumption and slow resupply<sup>1</sup>, depleting dissolved oxygen (DO) concentrations below 20 µM<sup>2</sup> and eventually to undetectable levels<sup>3</sup>. These low DO concentrations allow for anaerobic nitrogen cycling and the loss of bioavailable nitrogen to occur<sup>4</sup>, while also leading to enhanced carbon export<sup>5</sup>, making OMZs globally important regions of biogeochemical cycling. The major tropical OMZs are found in the ETNP, the Arabian Sea, and the eastern tropical South Pacific (ETSP). Large hurricanes are a common occurrence in the ETNP, as historical tracks of category 4 and 5 storms<sup>6</sup> coincide with the boundaries of the OMZ<sup>2</sup>. In contrast, tropical cyclones are less common in the Arabian Sea<sup>7</sup> and powerful category 4 and 5 equivalent storms are rare<sup>8</sup> (although both cyclone frequency and intensity are increasing in the Arabian Sea due to climate change<sup>9,10</sup>), while tropical cyclones do not form in the ETSP due to prevailing oceanographic and atmospheric conditions. Given that changes in the breadth, depth, and intensity of OMZ regions can have global biogeochemical ramifications<sup>11,12</sup>, and that cyclone intensity is increasing globally with climate change<sup>13</sup>, understanding the potential effects of tropical cyclones within the ETNP OMZ is crucial.

Cyclones are known to fuel phytoplankton blooms through mixing, entrainment, and upwelling of nutrients into the upper water column<sup>14–16</sup>, resulting in an overall increase in primary productivity throughout the ocean<sup>14,17</sup>. However, differences exist at

the scale of individual storms and between ocean basins<sup>14</sup>, and multiple interacting factors—including sustained wind speeds, storm size, storm translational speed, and the depth of the nutricline—must align in order to result in increased productivity<sup>14,16,18</sup>. In the ETNP, modeling and remote sensing analyses indicate that tropical cyclones support ca. 15% of net primary production (NPP)<sup>14</sup> and have driven a long-term increase in chlorophyll concentrations<sup>19</sup>. This suggests an important biogeochemical role for tropical cyclones in the ETNP. However, the full range of potential biogeochemical effects—including any associated changes in organic matter production, carbon cycling, and microbial activity—have not been examined in detail.

Globally and in the ETNP, most available information regarding the biogeochemical effects of cyclones necessarily comes from satellites rather than *in situ* measurements, which further limits our understanding due to the inherent temporal and spatial constraints of sensing the ocean from space (e.g., cloud cover, depth resolution). For example, recent ship-based research shows export of labile organic material from the surface to depth following tropical cyclone-driven mixing in the North Atlantic<sup>20</sup>—an effect that cannot be observed remotely. In OMZs, export production is important in driving oxygen depletion, such that increased export could lead to additional dissolved oxygen (DO) consumption at depth<sup>4</sup>. More simply, tropical cyclones could alter DO distributions in the ETNP by disrupting the structure of the water column through cyclone induced<sup>16</sup> mixing and upwelling. This could lead to shoaling of the OMZ and influence associated biogeochemical processes<sup>4</sup>. However, whether tropical cyclones alter the subsurface biogeochemistry of the ETNP is completely unknown.

The year 2018 was the most active storm season on record in the ETNP, with an accumulated cyclone energy index value of 317 (ref. <sup>21</sup>). Hurricane Aletta formed immediately prior to our cruise (Supplementary Note 1), and was followed by Bud, which was active while we were at sea in mid-June. Hurricane Bud passed between and over several stations that we sampled the previous year (2017), and we sampled an additional location (Station 3.5) that was directly in the storm’s wake—presenting an ideal opportunity to directly assess the effects of tropical cyclones on this important region of the ocean (Figures 1 and 2). Station 4 also fell beneath Bud’s previous track, while Bud passed to the northeast of Station 2 (Figure 1). We examined the surface effects of Bud based on satellite imagery and ship-based flow-through data, and the subsurface effects based on depth profiles of oxygen, temperature, chlorophyll, nutrients and organic matter concentrations. Dissolved organic matter was further characterized using high resolution liquid chromatography tandem mass spectrometry (LC-MS/MS), and 16S rRNA transcripts were sequenced from the near surface and OMZ at Station 3.5. All of these data demonstrate that tropical cyclones fundamentally alter the biogeochemistry of the ETNP in multiple ways.

## Methods

### Cruise measurements

Samples and data were collected in April 2017 and June 2018 aboard the *R/V Oceanus*, with samples and data collected in Mexican territorial waters under Instituto Nacional de Estadística y Geografía permits EG0062017 and EG0032018, and Permiso de Pesca de Fomento permits PPFE/DGOPA-016/17 and PPFE/DGOPA- 027/18. The 2017 cruise sampled stations in reverse order while the 2018 cruise proceeded in numerical order. In 2018, Hurricane Bud disrupted sampling after station 1, at which point the ship was relocated to the east (see Figure 1). At each station, water column profiles were collected using a SeaBird SBE 9+ CTD equipped with a SBE-43 DO sensor and WetLabs ECO-FLR fluorometer. Surface flow-through SST and chlorophyll fluorescence were continuously measured by a Sea-Bird SBE-38 and a WET Labs WETStar. CTD profiles and flow-through data are available via the Rolling Deck to Repository for both cruises<sup>24,25</sup>. Profiles plotted correspond to those where nutrient and organic matter samples were collected.

### Remote sensing data, additional cruise and float data, and hurricane data

Remotely sensed chlorophyll a concentrations [Chl a] were used to examine the spatial and temporal extent of the phytoplankton bloom induced by Bud, following previous work on other storms<sup>26</sup>. Four km resolution [Chl a] data are daily average composites from Level 3 MODIS Aqua<sup>27</sup>, Terra<sup>28</sup>, or VIIRS SNPP<sup>29</sup> based on available coverage. Current Level 3 products use algorithm switching to account for the range of possible [Chl a] values<sup>30,31</sup> and mean values were taken when chlorophyll values were available from more than one sensor/satellite for a given grid cell. In order to visualize the hurricane itself, [Chl a] data were overlaid on top of RGB images (1 km resolution) originally derived from VIIRS imagery, downloaded and available on the NASA Worldview interactive website<sup>32</sup>.

For comparison to Station 3.5 data collected aboard the *R/V Oceanus* in 2018, CTD data were obtained from cruises and Argo floats that sampled at similar coordinates. Two cruises collected CTD profiles at 18.9°N and 108.8°W in 2013 and 2014 (NH1315: 2013-06-22 and NH1410: 2014-05-26), while two Argo floats collected autonomous profiles in January 2021 (float 6903093, 18.48°N 108.12°W; float 6903094, 18.65°N 108.3°W). Data from cruises NH1315<sup>33</sup> and NH1410<sup>34</sup> were obtained from the Biological & Chemical Oceanography Data Management Office (BCO-DMO) database<sup>35</sup> and data from Argo floats<sup>36</sup> 6903093 and 6903094 were acquired via the Euro-Argo web portal<sup>37</sup>. We also compared Station 3.5 data to the depth of the ODZ in the ODZ Atlas<sup>38</sup>, where the ODZ is defined as “the depth layer where the vertical oxygen gradient was near zero and [DO] was less than 5  $\mu\text{mol kg}^{-1}$ ”<sup>38</sup>. Reference data for the bottom of the OMZ within our study area are from ENTP time series cruises<sup>38</sup>.

Hurricane track, position, eye pressure, and wind speed data are from the NE/NC Pacific HURDAT2 dataset, published by NOAA<sup>22</sup>. Temporal resolution is every six hours. Translational speed was calculated based on change in storm eye position between each six hour location.

## Nutrient and bulk organic matter analyses

Samples for further analyses were collected using Niskin bottles mounted on the CTD-rosette. Nutrient samples were analyzed for  $\text{NH}_4^+$  and  $\text{NO}_2^-$  aboard the ship, with additional shore-based analyses of combined  $\text{NO}_3^- + \text{NO}_2^-$  and  $\text{PO}_4^{3-}$  at the University of California Santa Barbara Marine Science Institute Analytical Lab and SOEST Laboratory for Analytical Biogeochemistry at the University of Hawaii at Manoa<sup>39</sup>.

Seawater for [DOC] analysis was filtered through pre-combusted GF/F filters (0.7 mm pore size; Whatman, GE Life Sciences, Marlborough, MA, USA) and collected directly into combusted 40-mL borosilicate vials. Samples were immediately acidified to pH 2 using trace metal grade 12N HCl (Fisher Scientific), sealed using acid-washed vial caps with septa, and stored at room temperature in the dark until analyzed via high-temperature combustion on a Shimadzu 500 V-CSN/TNM-1 (Shimadzu Corp, Kyoto, Japan). The Shimadzu was modified from the manufacturer's design, and the combustion oven contained a quartz column filled with platinum (Pt) catalyst beads. Combustion columns were pre-conditioned on 40 - 100 injections of filtered (0.2  $\mu\text{m}$ ) seawater until the baseline of measured carbon was stable. A magnesium perchlorate water-trap was placed prior to the halogen trap and changed daily. CO<sub>2</sub>-free carrier gas was used to precondition the column, and ultra-high purity grade O<sub>2</sub> gas was delivered to the instrument as the carrier gas during sample analysis.

Each acidified sample was sparged for two minutes and measured following high-temperature combustion at 680°C. During analysis, five 100  $\mu\text{L}$  injections were made from a single sample reservoir, and samples were reanalyzed when the %CV of the best 3 injections was >5%. Measurements were calibrated using an 8-point calibration curve between 10 and 100  $\mu\text{M}$  C of potassium phthalate in Milli-Q water. Milli-Q water and a reference water sample were analyzed every 10 samples. Reference standards were obtained from NSF-supported deep Florida Strait (Batch 6FS – 2006; Dennis Hansell, RSMAS, University of Miami). The expected concentration range for Batch reference materials is provided online<sup>40</sup>.

For POC analysis, inorganic carbon was removed by acidifying the filters with HCl vapor, followed by oven drying, overnight. One half of the filter was transferred to a pre-weighed tin cup for analysis. Blank filters were prepared in the same way to constrain any process contamination. Filter material was analyzed for carbon and nitrogen mass on an elemental analyzer (Costech, model ECS 2010) at Scripps Institution of Oceanography's unified laboratory facility.

## Estimated export flux

Export flux was calculated as a proportion<sup>41</sup> of net primary production derived from the vertical generalized production model<sup>42</sup> (VGPM), which was adjusted

regionally<sup>43</sup>. Although there are limitations to this approach (see Methods), it provides an estimate that compares well with in situ measured fluxes—including previous work on episodic events in other regions of the eastern Pacific<sup>44,45</sup>. Eight-day modeled NPP based on the standard vertical generalized production model<sup>42</sup> (VGPM) was acquired from Oregon State's Ocean Productivity website<sup>46</sup> and was regionally adjusted following a logarithmic relationship<sup>43</sup> (VGPM-CAL). Export flux is a proportion of this adjusted value following a regression equation<sup>41</sup>. Mathematically:

$EF = (0.284 \times NPP_{(VGPM-CAL)} + 9.75)$ , where  $NPP_{(VGPM-CAL)} = 10^{(\log_{10}(VGPM) - .1924)}$

We calculated export flux within a region set by the union of gridded NPP and a circle of 100 km radius (see below) around Station 3.5, which returns a window area of 39440 km<sup>2</sup>. We examined whether tropical cyclones significantly increased export flux in this area around Station 3.5 by testing for a significant positive slope in EF values for the 24 day period that includes the passage of a storm within this window.

We used the standard VGPM model given its global ubiquity, ecological basis, and its potential usefulness in capturing carbon export associated with phytoplankton blooms in the context of tropical cyclone-induced cold wakes<sup>14</sup>. VGPM uses 8-day composites of satellite-derived [Chl a], SST, and solar irradiance as input observations, as well as derived model parameters (e.g., PAR). In particular, the VGPM model parameter  $P^B_{opt}$  (maximum carbon fixation rate) is a temperature-dependent complex polynomial that increases from 0 to 20°C, but decreases from 20 to 28°C. The model's authors note that this relationship between the derived variable  $P^B_{opt}$  and SSTs is a result of spatial and regional confounding factors related to SST in warm oligotrophic waters<sup>42</sup>; specifically, low carbon fixation rates in regions with higher SSTs are associated with vertical stratification and nutrient limitation, not temperature directly. As a result, both SST decreases and [Chl a] increases corresponding with tropical cyclone overpasses in the ETNP were correlated with increases in export flux, as both of these observational variables drive increases in the VGPM model and therefore subsequent estimated export flux (Supplementary Figure S5c). However, high [Chl a] values are the first order driver of export flux (Supplementary Figure S5b), and changes in the order of magnitude of [Chl a] are most important to expected increases in export flux.

## Dissolved organic matter characterization

(not yet complete coauthor edits needed)

For analysis of organic matter at Station 3.5, 1L seawater samples were collected directly from Niskin bottles into HDPE plastic bottles and acidified to pH 2 using trace metal grade 12N HCl (Fisher Scientific). DOM was extracted from acidified water samples by using teflon tubing connected to vacuum stations for solid phase extraction (SPE) using Bond Elut PPL resin (200 mg bed mass cartridges, Agilent 2105005, USA) following previous work<sup>47,48</sup>. After desalination of the SPE columns with LCMS grade water (Fisher Chemical, Belgium), cartridges were dried using ultra-high purity compressed N<sub>2</sub> gas. DOM was eluted into glass vials using 2 mL of methanol (LC-MS grade, Fisher Chemical, Belgium) and kept frozen at -80°C. DOM extracts were subsequently dried in a vacuum centrifuge and re-dissolved in 100 µL 80% methanol with 1% formic acid before analysis. All glassware was pre-combusted for 4 h at 450 °C,

while all other material was cleaned with acidified Milli-Q water and rinsed with samples before use.

The method used for characterization of DOM using LC-MS/MS is described in detail in Petras et al 2017. In short, 10 µL DOM extracts were injected into a Vanquish Ultra-High-Performance Liquid Chromatography (UHPLC) system coupled to a Q-Exactive orbitrap mass spectrometer (Thermo Fisher Scientific, Bremen, Germany). DOM extracts were separated via UHPLC using a reversed-phase C18 porous core column (Kinetex C18, 150 x 2 mm, 1.8 µm particle size, 100 Å pore size, Phenomenex, Torrance, USA), ionized via positive electrospray ionization (ESI+), and analyzed in data-dependent acquisition (DDA) mode with mass range 150 - 1500 m/z. Thermo .raw data files were converted to .mzML in centroid mode using MSConvert (Chambers et al., 2012) and feature finding was performed in MZmine 3 (Schmid et al., 2023), with all parameters listed in Table S3. In total, 554 samples (including samples not presented here from other experiments and environmental sampling) were processed together and resulted in identification of 8542 molecular features in DOM. To remove potential contaminants, we subtracted features with intensities >30% in procedure blanks (5 samples using LC MS grade water and treated the same as the samples) compared to the mean intensities of all samples. For our detailed analysis of DOM at Station 3.5, only features abundant in the 13 samples from station 3.5 (sum intensities > 1E5 in at least 2 samples) were considered, resulting in 1666 features. Feature intensities were log 10 transformed and z-score was calculated for the two way hierarchical cluster analysis (using software JMP).

We used the Feature-Based Molecular Networks (FBMN)<sup>49</sup> workflow in GNPS<sup>50</sup> to build molecular networks and search public and commercial spectral libraries for matches. To connect features within networks and consider a positive library match, we required a cosine score above 4 and at least 6 matched peaks. For molecular formula assignment and annotating spectra in compound class level we used the SIRIUS 5 workflow<sup>51</sup>, including ZODIAC for molecular formula refinement<sup>52</sup> and CANOPUS for prediction of compound classes<sup>52</sup>. Parameters are listed in Supplementary Table S3. Molecular formulas were only considered if the ZODIAC score exceeded 0.98 and following rules were true: O ≤ C, 0.3C ≤ H ≤ 2C+2, O > 2P+S, N/C < 0.25, O/C < 2, and H/C < 2.5.

## Microbial community characterization

(not yet complete coauthor edits needed)

Water samples were collected at Station 3.5 for RNA extraction and 16S rRNA transcript sequencing using sampling bottles deployed on the CTD rosette. 2L water samples were filtered through 0.22 µm filters (Millipore, Darmstadt, Germany) within 15 minutes of collection, submerged in RNAlater® (Ambion™, AM7021) in pre-prepped Lysing Matrix E tubes (MP Bio, Eschwege, Germany), and frozen at -80°C until extraction. RNA was extracted using the Qiagen RNeasy PowerBiofilm kit (Qiagen, Inc., Valencia, CA, USA) following the manufacturer's protocol. cDNA was generated from extracted RNA using the Invitrogen SuperScript III Reverse Transcriptase kit (Life Technologies Corporation, Carlsbad, CA, USA) and remaining RNA was removed through incubation with RNase H (Invitrogen) at 37 °C for 20 min. cDNA samples were diluted to a common concentration (2 ng/µL); amplified using the universal 16S primers 515F-Y

(5'-GTGYCAGCMGCCGCGTAA) and 926R (5'-CCGYCAATTYMTTTRAGTTT), which are effective for analysis of marine microbial communities<sup>54</sup>; and sequenced at CINVESTAV Mérida on an Illumina MiSeq (Illumina, San Diego, CA, USA).

ASVs were generated from 16S rRNA sequence data using the Divisive Amplicon Denoising Algorithm (DADA2)<sup>55</sup> as implemented in QIIME 2<sup>Boylen REF</sup>, and then used for subsequent analyses. After import and demultiplexing, read quality was visualized using the ‘qiime tools view’ command. Reads were then processed using the ‘qiime dada2 denoise-paired’ command, with 13 bp trimmed from both the forward and reverse reads, truncation of reverse reads to 183 bp (due to the well-known decline in sequence quality observed for MiSeq reverse reads), and training of the denoising algorithm on 1 million reads. ASVs were classified using the SILVA 138 database in QIIME 2.

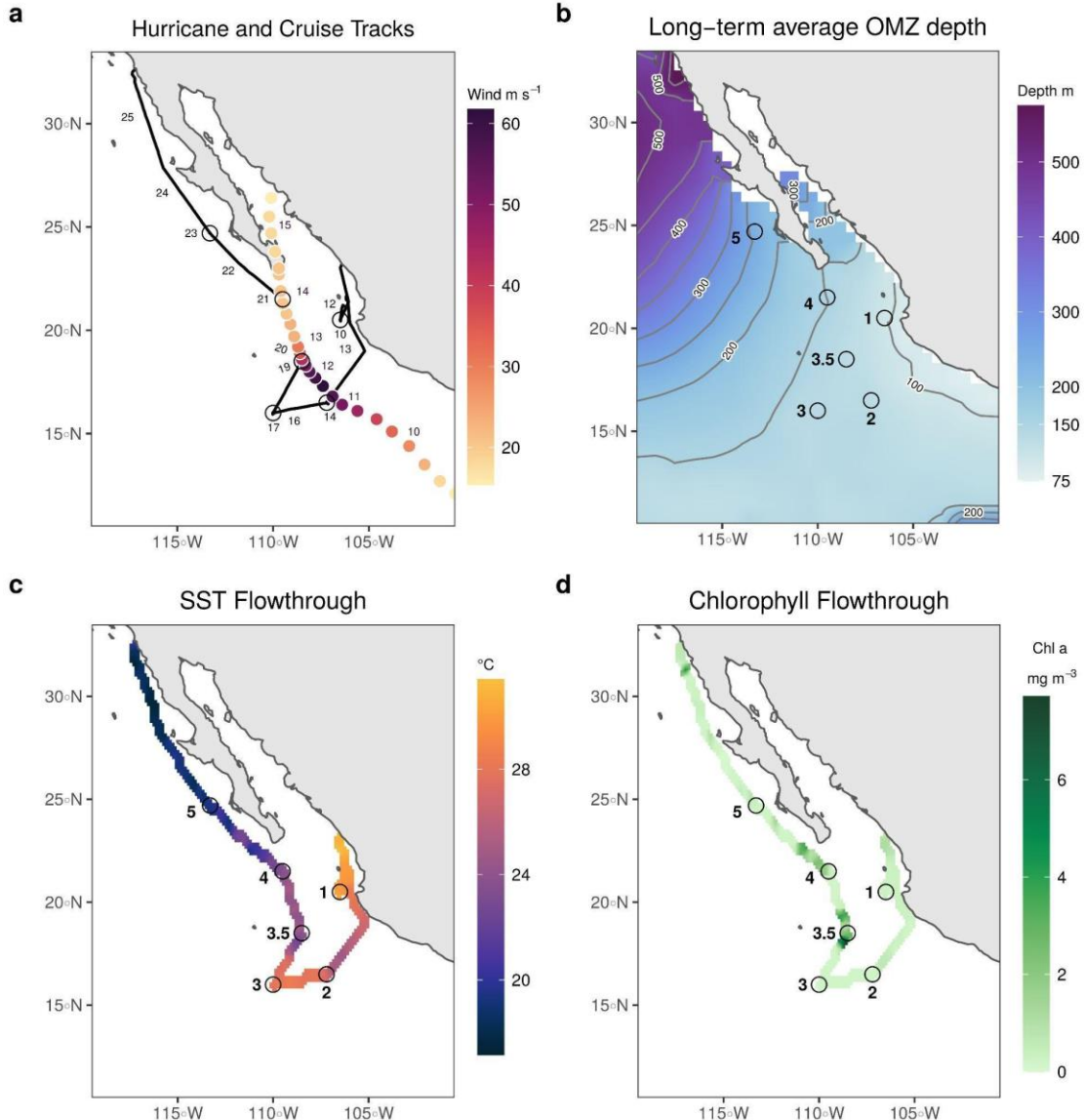
## Results

### Surface effects of Category 4 Hurricane Bud

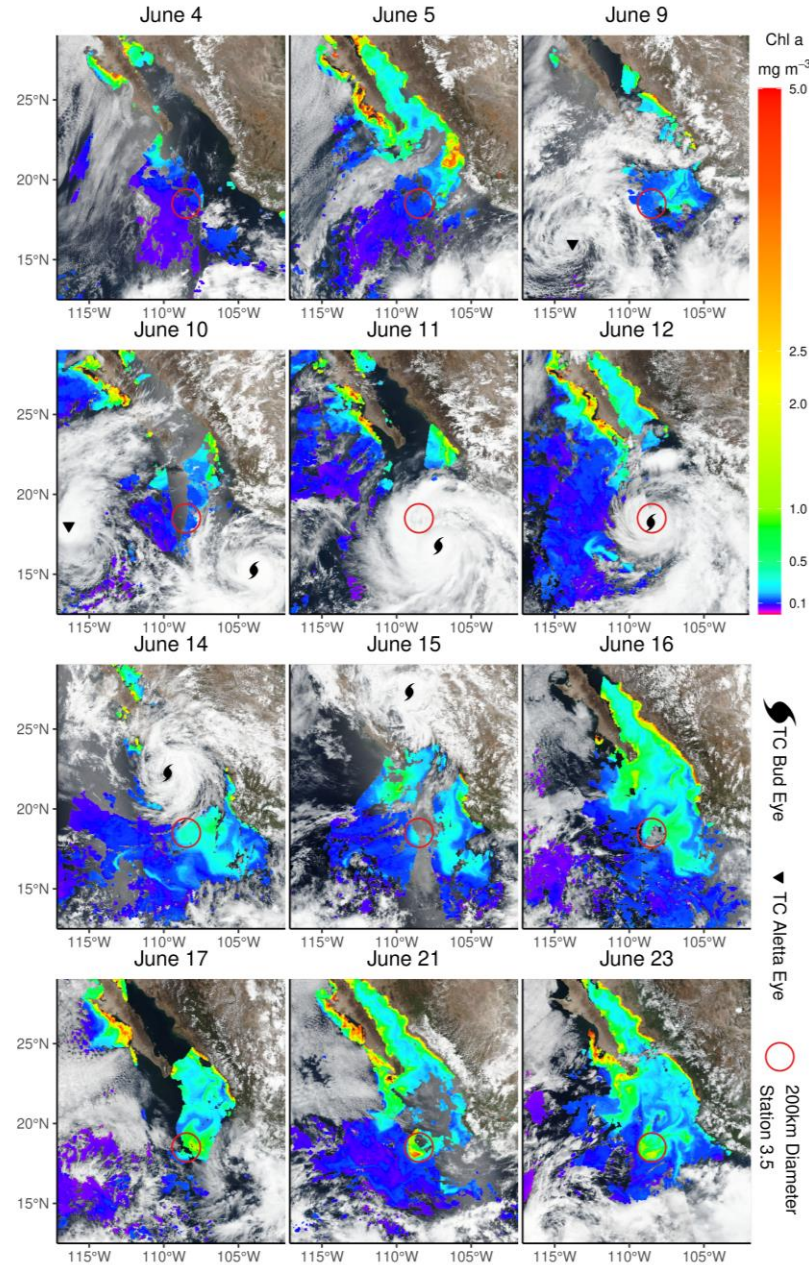
Hurricane Bud formed on June 9th 2018 at 12.1°N and 100.5°W in the ETNP. Moving in a northwesterly direction, Bud reached hurricane strength on June 10th (Figure 1 and Supplementary Table S1). Bud subsequently rapidly intensified to a Category 4 hurricane, with peak wind speeds of 120 knots (62 m s<sup>-1</sup>) occurring early on June 12th at 17.3°N and 107.4°W. These coordinates are located to the northwest of Station 2 (16.5°N 107.2°W), which we sampled on June 14th-15th (having crossed over the hurricane’s previous path; Fig. 1). Bud’s forward speed slowed, and it passed over Station 3.5 (18.5°N 108.5°W) as a major hurricane late on June 12th (Supplementary Tables S1 and S2). Bud then passed near to Station 4 as a tropical storm on June 14th (moving in a more northerly direction). We sampled Station 3.5 on June 19th-20th, and Station 4 on June 21st. Our cruise track from June 19th-21st therefore closely followed Bud’s previous path from a week earlier (Fig. 1).

Flow-through data were collected along this cruise track via sensors aboard the *R/V Oceanus*. Chlorophyll concentrations were slightly elevated (0.8 mg m<sup>-3</sup>) to the northeast of Station 2 and sea surface temperatures (SSTs) were reduced by 1°C, corresponding with the previous path of Bud (Fig. 1c and d and Supplementary Figure S1). Further along the cruise track, surface chlorophyll reached much higher values of 3 - 8.9 mg m<sup>-3</sup> at and near Station 3.5—again corresponding with the wake of the hurricane. These are notably high values for open ocean surface waters, and present a sharp contrast with the extensive low-chlorophyll surface waters encountered from Stations 2 to 3 and north to Station 3.5 (Figs. 1d and S1). (Chlorophyll concentrations were also elevated to the north of Station 4, likely due to coastal upwelling along the Baja California peninsula.) SST showed local minima along the cruise track that corresponded with increased chlorophyll, demonstrating that the chlorophyll signal was associated with 2-4°C cooler SSTs (Supplementary Figure S1). These results are consistent with cyclone-

induced vertical mixing reducing SST<sup>56</sup> and supplying limiting nutrients to phytoplankton (see below), leading to increased chlorophyll concentrations<sup>13</sup>.



**Ch 1 - Figure 1:** Maps of (a) hurricane and cruise tracks, (b) long-term average OMZ depth, and shipboard flowthrough (c) SST and (d) chlorophyll in the ETNP. In panel (a), color-shaded dots show maximum sustained wind speeds<sup>22</sup> every six hours along Hurricane Bud's track, with the daily hurricane eye position during June 2018 labeled by purple numbers. The black line with dates in June 2018 (black numbers ranging from June 10-25) shows the cruise track. Panel (b) displays the long-term average depth of the OMZ (defined by 20 µM DO) based on the World Ocean Atlas climatology<sup>23</sup>. OMZ depth is indicated by 50 m contours and shading. Ship-board flowthrough (c) SST and (d) chlorophyll-a concentrations are shown by color shading. In panels b, c, and d, black circles with numbers indicate sampling stations.



**Ch 1 - Figure 2:** Remotely sensed [Chl a] images ( $\text{mg m}^{-3}$ ) prior to (June 4<sup>th</sup>-10<sup>th</sup> 2018), during (June 11<sup>th</sup>-15<sup>th</sup>), and following (June 16<sup>th</sup>-23<sup>rd</sup>) Hurricane Bud demonstrate the presence and influence of the tropical cyclone. [Chl a] values are shown on the color scale, with values above  $5 \text{ mg m}^{-3}$  shown in red. Overlayed true-color imagery shows cloud cover, land cover, and areas with no available [Chl a] values. Eye position is shown for tropical cyclones Bud (storm symbol) and Aletta (triangle), and the red circle (200 km diameter) is centered on station 3.5. See text for dates and specific storm strength designation. Images are ca. local solar noon.

We examined whether a widespread increase in chlorophyll concentrations was also evident in satellite imagery, and found elevated remotely sensed chlorophyll concentrations [Chl a] that align with our flowthrough data (Figure 2). For example,

when Bud was still located to the south of the sampling region on June 10th, remotely sensed [Chl a] concentrations were low ( $0.1\text{-}0.35 \text{ mg m}^{-3}$ ) at Station 3.5 and Station 4. As Bud progressed northward, [Chl a] increased in the storm's wake. Immediately after passage over Stations 3.5 and 4, remotely sensed [Chl a] values were  $0.2\text{-}0.3 \text{ mg m}^{-3}$  at both stations on June 15th, and then increased to  $1.5 \text{ mg m}^{-3}$  on June 17th at Station 4. Meanwhile, a persistent and intense [Chl a] signal was present near station 3.5 (Fig. 2). This feature extended from  $17.7^\circ$  to  $20.1^\circ \text{ N}$  and  $107.2^\circ$  to  $109.2^\circ \text{ W}$ , encompassing an area of  $>30,000 \text{ km}^2$ . In portions of this evident bloom, remotely sensed [Chl a] reached values as high as  $2\text{-}4 \text{ mg m}^{-3}$  through June 25th. [Chl a] remained elevated ( $>0.4 \text{ mg m}^{-3}$ ) compared with pre-hurricane concentrations until at least June 30th, after which Hurricane Fabio and tropical storm Emilia passed within relatively close proximity (Supplementary Figure S2).

We also calculated Bud's translational speed—an indicator of time over a patch of ocean—as slower translational speeds correlate with bloom incidence and intensity<sup>7,16</sup>. Hurricane Bud translational speeds were comparatively slow<sup>7,16</sup>, with a mean of  $2.4 \text{ m s}^{-1}$  from June 9th-15th (Supplementary Table S1). The slowest translational speeds ( $0.7\text{-}1.2 \text{ m s}^{-1}$ ) corresponded with the overpass of stations 2, 3.5 and 4 on June 11th-13th, with the very lowest translational speeds occurring south of and over Station 3.5. Slower translational speeds and stronger winds can act together to increase localized mixing<sup>7,16,57</sup>. As a result, the ratio of wind speed cubed over translational speed provides a simplified metric of storm energy imparted to a section of ocean per unit time. All of these ratios were highest over Station 3.5 (Supplementary Table S1), coinciding with the ship- and satellite-based chlorophyll signals.

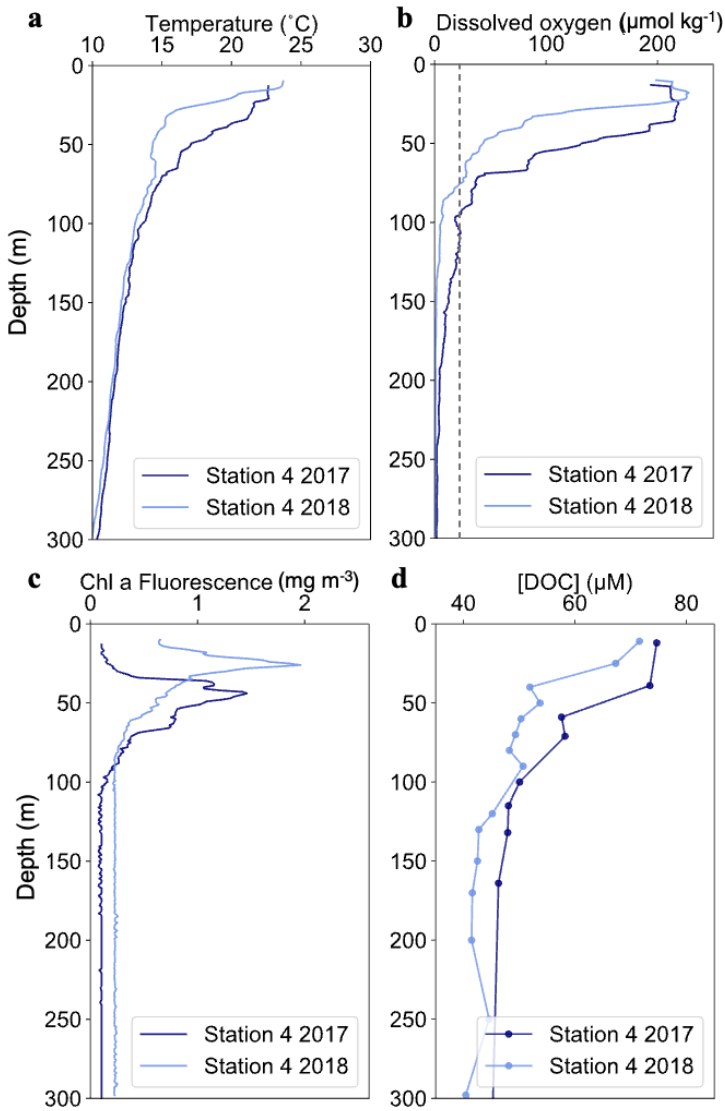
## Subsurface alteration of OMZ biogeochemistry

Flow-through and remote sensing data are indicative of a phytoplankton bloom associated with storm-driven mixing of the upper water column, and we examined potential subsurface effects using additional sampling and analysis provided by the unique opportunity of being on a research vessel at sea following the storm. Bud passed  $\sim 100 \text{ km NE}$  of Station 2—placing the weaker side of the storm closer to Station 2—while passing nearly directly over Stations 3.5 and 4 (Fig. 1). We sampled stations 2 and 4 in the previous year (2017), while Station 3.5 was sampled opportunistically in 2018. Bud was also near maximum strength at Station 3.5. Consistent with Bud's position and strength relative to our sampling stations, we observed decreased upper ocean temperatures at Stations 2 and 4 (Figure 3a) compared with those measured during our previous cruise in April 2017.

At Station 4, we also observed shoaling of the oxycline (Fig. 3b) and chlorophyll maximum (Fig. 3c) following Hurricane Bud. For example, the depth of  $20 \mu\text{M DO}$  (typically used to define OMZs) was 100 m in 2017, but 71 m in 2018. To provide additional context, data from multiple cruises along the  $110^\circ \text{ West}$  meridian indicate that the long-term depth of the OMZ near Station 4 is 100-150 m and so substantially deeper (Supplementary Figure 3). Comparison of reference cruise profiles to our 2018 data at Station 4 also showed a stable lower boundary of the OMZ at ca. 800m, with the depth and shape of the curve similar for all profiles over time<sup>24,58</sup>. This indicates that Bud's

influence on DO is limited to the upper margin of the OMZ and does not extend to the bottom margin at 800 m depth.

DOC concentrations in the upper 100 m at Station 4 were also lower in 2018 following the hurricane than in April 2017 (Fig. 3d). DOC generally displays an expected trend of decreasing concentrations with depth and a tight relationship with density. Surface ocean production can provide additional DOC, such that depths with higher chlorophyll concentrations typically also have higher DOC concentrations (e.g., Stations 1, 2 and 3), but DOC production lags the initiation of phytoplankton blooms by multiple days<sup>59</sup>. Stations 3.5 and 4 showed the lowest near-surface DOC concentrations in 2018 despite high chlorophyll (Fig. 3c and d, Fig. 4 c and e); DOC concentrations were 46-56  $\mu\text{M}$  near 50 m at both sites. This indicates that low DOC water was delivered towards the surface, lowering overall concentrations. This is also evident from (i) the steep gradient in DOC profiles in the upper 50 m at Stations 3.5 and 4, (ii) the shift in DOC profiles from 2017 to 2018 at station 4, and (iii) the low absolute values in DOC observed at Station 3.5.

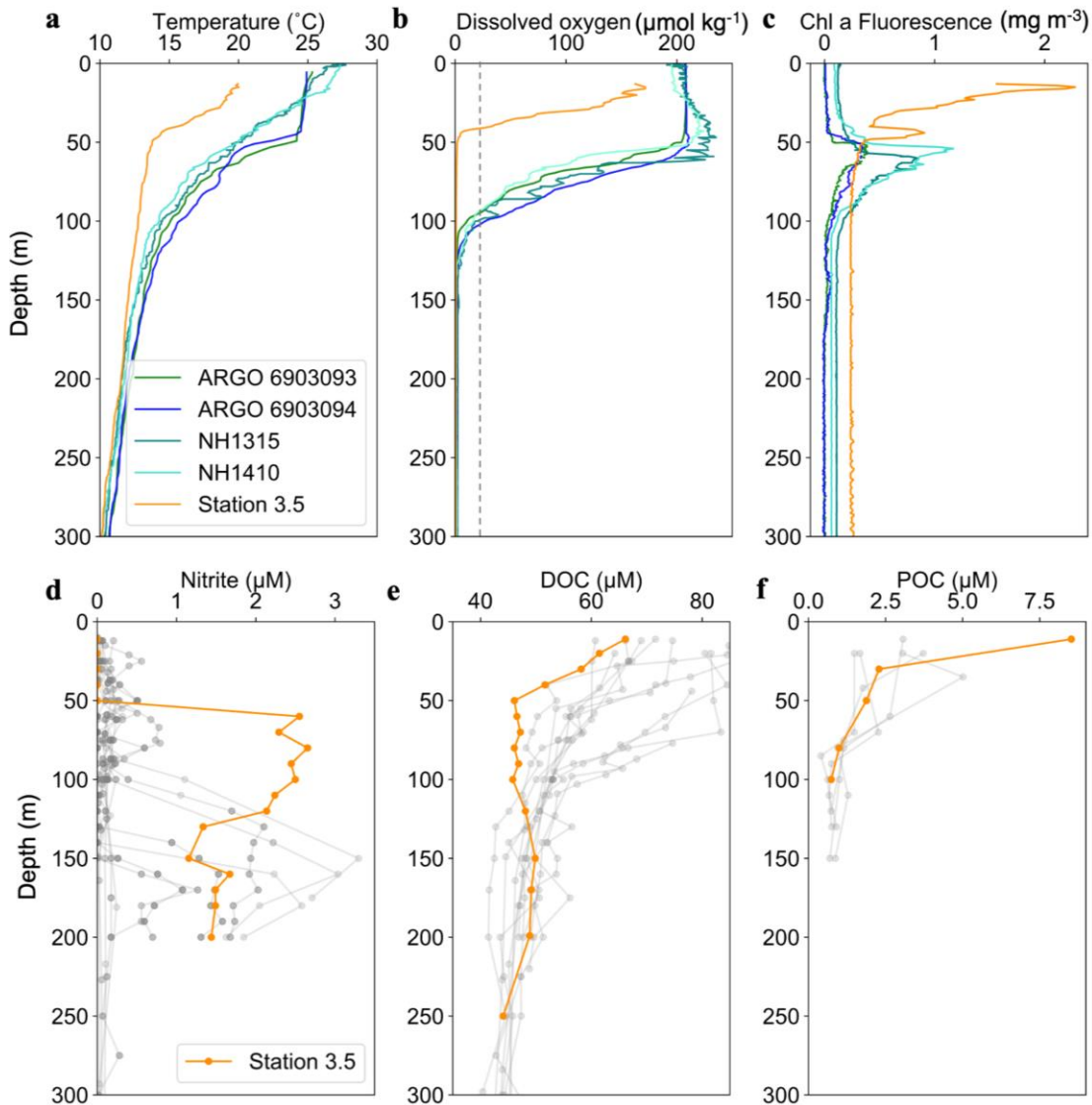


**Ch 1 - Figure 3:** Water column profiles at Station 4 demonstrate hurricane-driven shifts in (a) temperature, (b) dissolved oxygen, (c) chlorophyll, and (d) dissolved organic carbon (DOC) concentrations between 2017 (dark blue profiles) and 2018 (light blue profiles). The dashed line in panel b indicates 20  $\mu\text{M}$  DO.

Station 3.5 displayed multiple patterns indicative of disturbance (Figure 4). In CTD data, temperatures were lower, the oxycline was shallower, and chlorophyll concentrations were elevated in contrast with previous cruise profiles and Argo float profiles (Fig. 4 a-c). The upward displacement of the OMZ and its potential biogeochemical implications are particularly notable. Station 3.5 was added as an additional sampling station due to the hurricane, and so we lack a direct comparison with the 2017 cruise. However, previous research cruises sampled a nearby station in 2013 and 2014, and two Argo floats sampled very near to station 3.5 in 2021. Along with World Ocean Atlas data (Fig. 1), all of these data indicate a typical OMZ (DO concentration of

20  $\mu\text{M}$ ) depth of at least 100 m near Station 3.5. In contrast, our 2018 cruise data show that the depth of the OMZ was as shallow as 41 m following Hurricane Bud (Fig. 4 b). Changes in the depth of the anoxic oxygen deficient zone (ODZ) were even more severe, with an expected depth of 140 m in the ODZ atlas<sup>29</sup> reduced to 50 m following Hurricane Bud (Fig. 4b).

OMZ and ODZ shoaling are further consistent with a shallow (50-60 m depth) and broad secondary nitrite maximum at Station 3.5 (Fig. 4d), which is diagnostic of anaerobic nitrogen cycling<sup>3</sup>. Dissolved nitrate and phosphate were also present at 11 m depth at Station 3.5 (Supplementary Figure S3). Consistent with increased nutrient availability, chlorophyll concentrations were elevated in CTD profiles, flow-through data, and satellite imagery from Station 3.5. Finally, POC concentrations were unusually high at Station 3.5, reaching 8.5  $\mu\text{M}$  compared with values <4  $\mu\text{M}$  measured at other stations sampled on the same cruise (Fig. 4f). Elevated POC is further consistent with a newly initiated phytoplankton bloom, and particulate C:N ratios were approximately equal to the expected Redfield value of 6.6 for phytoplankton biomass (Supplementary Figure S5).

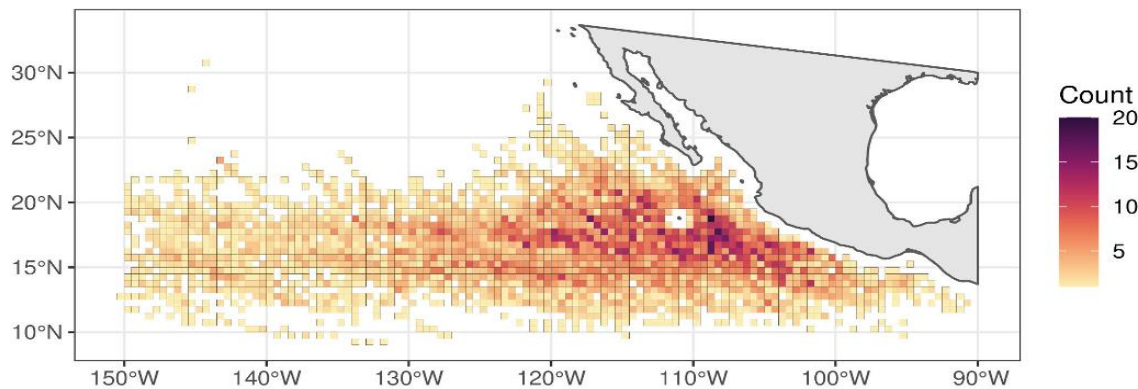


**Ch 1 - Figure 4:** Post-hurricane profiles from Station 3.5 show substantial differences with data from other cruises, floats, and stations in (a) temperature, (b) dissolved oxygen concentrations, (c) chlorophyll, (d) nitrite concentrations, (e) DOC, and (f) particulate organic carbon (POC) concentrations. In panels a-c, Station 3.5 data (orange) are shown in comparison to earlier cruises and recent float data (blue and green profiles) collected nearby (see text). In panels d-f, Station 3.5 data (orange) show distinct patterns in comparison to all other data collected on our cruises (gray). The dashed line in panel c indicates  $20 \mu\text{M}$  DO.

## Tropical cyclone-driven changes in organic matter production and microbial communities

We examined Station 3.5 in greater detail as it fell directly in the path of Hurricane Bud at near maximum strength. Through analysis of all historical tropical

cyclone tracks in the ETNP, we also found that Station 3.5 and surrounding waters experience the highest overall number of tropical cyclones in the basin (Supplementary Note 2 and Figure 5). To constrain the effect of these tropical cyclones on organic matter production and subsurface biogeochemistry in the ETNP, we examined remote sensing estimated Chl a and export flux following tropical cyclones over the last 20 years. We found that increases in both were closely associated in time with tropical cyclones near Station 3.5 (Supplementary Figure S6; export flux is expected to lag new production<sup>30</sup>). From 2002 through the 2021 hurricane season, there were 47 tropical cyclones whose eyes passed within 100 km of Station 3.5, 14 of which were hurricane-strength. 13 of these 14 hurricanes generated a phytoplankton bloom and an increase in estimated export flux (Supplementary Figure S5 a), as did 48% of the remaining, sub-hurricane strength tropical cyclones. For example, the active 2015 hurricane season saw two hurricanes pass within 100 km of Station 3.5, and both generated distinct peaks in Chl a and export flux. (Additional peaks at Station 3.5 were associated with additional tropical cyclones whose eyes passed beyond 100 km but within 200 km of Station 3.5.) Based on the full remote sensing record, we calculated the proportion of export flux at Station 3.5 occurring 16-32 days after passage of a tropical cyclone. We found that this ranged from 7-15%—similar to the effects of tropical cyclones on NPP in the ETNP<sup>14</sup> and to the effects of episodic events in other regions of the Pacific<sup>31,32</sup>. Comparing the long-term trends in export flux, whether net or decomposed into a TC-noise and background signal component, indicated that our time series matched the Pacific Decadal Oscillation (Supplementary Note 3).

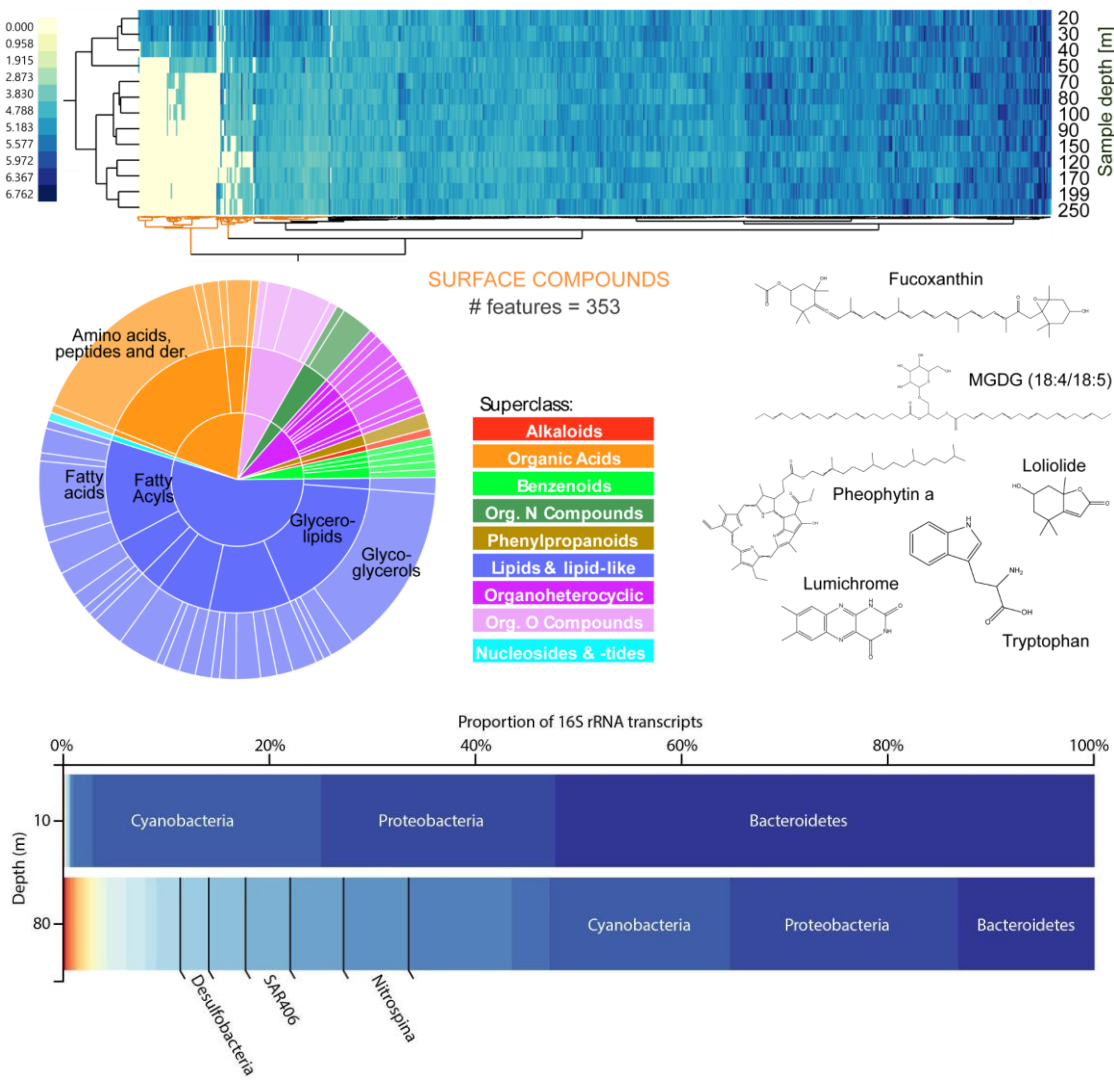


**Ch 1 - Figure 5:** Hurricane occurrence in the ENTP. Color scale shows hurricane eye observations per  $0.5^\circ \times 0.5^\circ$  cell from 1942 to 2021 in the NOAA HURDAT database. Hurricanes outside of the ETNP (~5-33°N, and 150-90°W) and within 200 km distance from land (including islands located off the Pacific coast of Mexico) were excluded.

These remote sensing analyses and our direct measurements (Figures 3 and 4) indicate that tropical cyclones can produce significant amounts of organic matter in the ETNP. As a result, we further characterized dissolved organic matter (DOM) at Station 3.5 using LC-MS/MS, identifying 1666 molecular features in the water column (Figure 6). Two-way hierarchical clustering of molecular features and samples showed several distinct patterns driven by the hurricane. We found that DOM composition mapped to

depth in the water column and exhibited a sharp change in composition from above to below the shallow AMZ (<50 m; Figure 6). This closely tracked shifts in the biogeochemical profiles with depth (Figure 4), and was driven by variations in specific molecular features superimposed on background DOM. Clustering showed 353 molecular features were unique to or enriched in the upper 50 m (Figure 6a), while the remaining features were found throughout the water column in slightly varying intensities (likely representing part of the refractory DOM pool present at all water depths).

Molecular features unique to or enriched in the surface were compositionally diverse and distinct from the background features that were ubiquitous in the water column (Supplementary Figure S7 comparing both sunbursts). Although lipid/lipid-like compounds dominated both surface and ubiquitous features, the composition within this superclass differed, with the ubiquitous background lipid/lipid-like compounds consisting almost entirely of terpene lactones characteristic of refractory DOM<sup>60–62</sup>. In contrast, surface-enriched and -unique features were more diverse in their lipid/lipid-like composition, with more glycoglycerols and fatty acids and conjugates. Outside of lipid/lipid-like compounds, surface-enriched and -unique features also included more alkaloids and organonitrogen compounds. In addition, our analysis revealed the presence of several compounds in notably high abundance at the surface only—including fucoxanthin, pheophytin *a*, monogalactosyldiacylglycerol (MGDG (18:4/18:5)), loliolide, tryptophan, and lumichrome. Many of these are directly derived from phytoplankton, reinforcing the evidence of an ongoing bloom at Station 3.5: fucoxanthin is a prominent carotenoid pigment found in eukaryotic microalgae, pheophytin *a* is a breakdown product of chlorophyll, MGDG is a lipid commonly associated with photosynthetic, and loliolide is diatom biomarker<sup>63</sup>. Tryptophan can also be produced by diatoms as signaling molecule<sup>64</sup>, while lumichrome is a photodegradation product of Vitamin B2<sup>65</sup>.



**Ch 1 - Figure 6:** Organic matter and microbial communities show unique compositions and variations at Station 3.5. The heatmap displays the relative abundance (color scale at left) of molecular features at different sampling depths (right axis). Two way hierarchical clustering of abundant molecular features is shown at the bottom of the heatmap, with clusters of features unique to or enriched in surface samples highlighted in orange ( $n=353$ ). ‘Sunburst’ plot at left displays the chemical composition of the surface-enriched or -unique features at the Superclass, Class, and Subclass (progressing from innermost to outermost circle). Chemical structures of key surface-enriched or -unique features are shown at right. 16S rRNA data show active microbial groups at 10 m and 80 m depth at Station 3.5, with key microbial phyla indicated.

We also statistically compared the oxidation state, elemental composition, and aromaticity of features found exclusively or enriched at the surface to those distributed ubiquitously throughout the water column (Table S4). We focused on high-quality molecular formula predictions to ensure the reliability of our findings (265 surface features, 1203 ubiquitous features). Surface compounds displayed lower oxidation states,

fewer oxygen (O) atoms, and reduced O/C ratios (Supplementary Figure S8)—all of which align with the expectation of a more reduced character in freshly produced organic matter. Additionally, higher concentrations of hydrogen (H) and phosphorus (P) atoms, as well as elevated H/C ratios (Supplementary Figure S6), indicate the presence of lipids (particularly phospholipids), which constitute a crucial component of cellular membranes. Compounds at the surface also exhibited longer retention times, suggesting reduced solubility, potentially due to associations with lipid-like compounds. DOM at the surface was also more saturated as indicated by lower values of Double Bond Equivalent (DBE) and Aromaticity Index (DBE, DBE/C, DBE/AI\_mod, and AI-mod). Collectively these properties suggest that the features unique to or enriched at the surface represent recently produced organic matter originating from the ongoing phytoplankton growth.

Finally, we examined the microbial community response at Station 3.5 by sequencing 16S rRNA transcripts—which capture the portion of the overall community that is actively synthesizing ribosomes—near the surface (10 m) and within the shoaled ODZ at 80 m depth (Figure 6). 16S rRNA transcript data showed that the active surface community was dominated (52% of 16S rRNA transcripts) by Bacteroidetes, and specifically by multiple groups of marine Flavobacteria known to associate with phytoplankton blooms and specialize in breakdown of phytoplankton-derived organic matter<sup>66,67</sup>. Two other major phyla active at 10 m were the Cyanobacteria (23%; primarily Prochlorococcus) and the Proteobacteria (22%)—such that these three phyla collectively comprised >97% of all 16S rRNA transcripts. Proteobacteria active at 10 m included comparatively low abundances of SAR11 (<1.6%) and a mix of gammaproteobacteria, especially Alteromonas (8.9%) and Oceanospirilla (2.4%). At 80 m in the shoaled ODZ, Flavobacteria, Cyanobacteria, and Proteobacteria were active at lower overall abundances (13%-22%) alongside known OMZ-inhabiting groups such as Nitrospina (6.3%), Marinimicrobia (aka SAR406; 4.3%), and Planctomyces (2.3%). The ODZ also contained 16S rRNA transcripts from sulfate-reducing bacteria (2.8%)—indicating the potential for sulfur cycling at 80 m depth in the ETNP following a major tropical cyclone.

## Discussion

Our analysis of flow-through measurements, satellite imagery, CTD profiles, organic matter, and microbial communities indicates that tropical cyclones can drive rapid production of organic matter and OMZ shoaling in the ETNP. To our knowledge, these are the first ship-based observations of the effects of tropical cyclones reported from the ETNP—a region that is globally important for marine biogeochemistry. Together these data provide direct *in situ* evidence for cyclone-driven mixing, upwelling, and subsequent biogeochemical effects. For example, high chlorophyll concentrations, a shallow OMZ, and high concentrations of POC (Figures 3 and 4) all support the idea of increased water column productivity at Stations 3.5 and 4. This coincides with previous studies suggesting that large storms drive significant chlorophyll increases<sup>68</sup>, and can subsequently affect biogeochemical processes<sup>20</sup>. For the first time, we also show that tropical cyclones can drive the rapid vertical expansion of an oceanic OMZ (Figures 3 and 4), as well as associated changes in organic matter and microbial communities. Our

results suggest multiple implications for this important region and the oceans' other major OMZs.

First, our results show that tropical cyclones generate intense, spatially and temporally constrained, pulses of productivity in the ETNP (Figs. 1-4). This would generate a mosaic of altered biogeochemical and/or ecological conditions over the course of hurricane season in the ETNP, yet these effects are not typically included in conceptual models nor resolved in numerical biogeochemical models of OMZs<sup>11,69</sup>. Recent trend analysis (20-35 years) indicates a global increase in [Chl a] in response to tropical cyclones, with the Northeast Pacific basin showing the largest increase of all the basins studied<sup>19</sup>. This [Chl a] increase is thought to be linked to the increasing intensity of tropical cyclones<sup>19</sup>, but direct measurements of high-intensity tropical cyclones are needed to verify this. Our data fill this gap by documenting an intense and long-lasting phytoplankton bloom in the wake of a Category 4 hurricane. Our ship-based chlorophyll measurements reached highly elevated values of up to 8.9 mg m<sup>-3</sup> (Fig. 1)—higher than remotely sensed values (Fig. 2)—and were associated with elevated POC and the presence of organic compounds unique to the surface (Figs. 5 and 6). These surface-enriched and -exclusive organic compounds included known phytoplankton biomarkers, as well as more reduced, saturated, and hydrogen-enriched material overall (Figure 6). In addition, satellite imagery indicates that the hurricane-driven bloom lasted approximately one month (Fig. 2 and Supplementary Figure S2). Although the temporal and spatial scales of tropical cyclone-induced plankton blooms are variable (not only by storm, but also by the method used to quantify chlorophyll), blooms typically last from two to three weeks, generally exhibiting a wide peak centered at 3 days after an overpass and slowly diminishing after 10 days<sup>14,17</sup>. Our data demonstrate that Category 4 storms in the ETNP could increase overall chlorophyll in the basin by the intensity of the generated bloom, its duration, or both. Notably, our study location covers a section of ocean that experiences a high number of tropical cyclone overpasses—making it a representative sample region for OMZs impacted by tropical cyclones (Figure 5).

Where and how phytoplankton production is subsequently utilized—or exported—is also important. Cyclone-induced mixing and resultant biological productivity has the potential to export comparatively labile organic matter to depth<sup>20</sup>. From a carbon cycle standpoint, this may be a significant (but transient) flux of carbon to the deep ocean<sup>70</sup> if this organic material escapes consumption and respiration. We estimate that 7-15% of export flux in the ETNP is associated with tropical cyclones—in line with their effect on NPP and with episodic events in other locations<sup>45</sup>. However, a portion of tropical cyclone-derived, newly produced organic matter is likely consumed, respired, and remineralized within the water column, and so may affect microbial communities and/or the distribution and behavior of other organisms. For example, additional nitrogen cycling at the base of the euphotic zone may have implications for the production of the greenhouse gas nitrous oxide<sup>71-73</sup>. Alternatively, if labile carbon is respired by ‘optimized’ microbial communities<sup>74,75</sup> found in OMZs, this could further reduce oxygen concentrations in an area of the ocean that is already oxygen-depleted. DOM data provide evidence for hurricane-drive effects throughout the water column, as we found surface-enriched compounds that extended into OMZ waters (Figure 6). In

parallel, 16S rRNA data indicate that active remineralizers were present near the surface, with a shift to active anoxic microbial groups at 80 m depth in the OMZ/ODZ (Figure 6).

Related to this, CTD profiles show shoaling of the ETNP OMZ in the wake of the hurricane. To our knowledge, our study is the first clearly documented instance of rapid vertical expansion of an oceanic OMZ driven by a tropical cyclone. In the days prior to our ship-based observations, modeling, experiments, and first principles suggest that atmospheric pressure changes<sup>76</sup> and ventilation at high wind windspeeds<sup>77-79</sup> could also act to decrease or increase dissolved gas concentrations (including oxygen). Following the storm, Argo profiles show that the OMZ eventually returned to typical depth (Fig. 4b). Although the effects of tropical cyclones on DO concentrations may therefore be complex and variable through time, our data demonstrate that they include rapid and severe OMZ shoaling. Storm-driven upwelling is likely the major direct and indirect driver of vertical OMZ expansion, as temperature, nutrient, and DOC profiles shoaled in parallel with the DO profiles (Figures 3 and 4). However, OMZ shoaling also coincided in space and time with large amounts of labile organic matter produced by a phytoplankton bloom, and our timing on Stations 3.5 and 4 coincided with expected peak export flux out of the base of the euphotic zone<sup>41</sup>. In coastal waters of the Gulf of Mexico, tropical cyclones have been shown to resuspend sediment, resulting in reduced oxygen concentrations through microbial respiration of sediment-derived carbon<sup>80</sup>. While this phenomenon is limited to locations where mixing generated by tropical cyclones directly interacts with the seafloor (<50 m water depth<sup>80</sup>), tropical cyclone-driven phytoplankton bloom biomass may have analogous effects within the larger oceanic OMZs. Additional work is needed to determine the relative contributions of different physical and biogeochemical processes to the sharp changes in oxygen concentrations that we observed, and the degree to which they occur following other storms in the ETNP or in other locations.

Finally, an oceanic OMZ located near the surface means that the region of anaerobic nitrogen cycling is also near the surface. The ETNP is the largest region of fixed nitrogen loss in the ocean, and in our data, the secondary nitrite maximum—which is diagnostic of anaerobic nitrogen cycling<sup>3</sup>—was found at just 50-60 m depth at station 3.5. This shoaling of the OMZ, combined with additional organic matter supply from the surface bloom, may act together to drive enhanced anaerobic activity in the OMZ—including production and fluxes of nitrogen gases<sup>72</sup>. 16S rRNA data also indicates the possibility of active sulfate reduction within the shoaled OMZ. In other words, we show that tropical cyclones generate high concentrations of labile organic matter (Figs. 3-6) directly above a shallow OMZ (Figs. 3 and 4)—a combination with implications for carbon<sup>5</sup>, nitrogen<sup>72,73</sup>, oxygen<sup>11</sup> and sulfur cycling in the ETNP. Collectively our data indicate that tropical cyclones severely disrupt the biogeochemistry of this globally significant region of the ocean. Understanding the potential biogeochemical interactions and feedbacks, and how these may be affected by increased cyclone intensity in a warming ocean, will be critical.

## Acknowledgments

This work was supported by United States National Science Foundation grants OCE-1555375 (to J.M.B.) and OCE-1736656 (to L.I.A.), a UC MEXUS-CONACyT Collaborative Grant (to J.M.B. and J.Q.G.M.), and the UC San Diego Academic Senate. We thank the officers and crew of the *R/V Oceanus* for their help at sea (particularly during the hurricane); thank Jesse Wilson, Sarah Abboud, Jennifer Karolewski, and Kevin Testo for their assistance in the field; thank Fidel Machado-Perez and Abril Gamboa for their help in the lab; and thank Bruce Deck at SIO.

## References

1. Wyrtki, K. The oxygen minima in relation to ocean circulation. in *Deep Sea Research and Oceanographic Abstracts* vol. 9 11–23 (Elsevier, 1962).
2. Paulmier, A. & Ruiz-Pino, D. Oxygen minimum zones (OMZs) in the modern ocean. *Prog. Oceanogr.* **80**, 113–128 (2009).
3. Thamdrup, B., Dalsgaard, T. & Revsbech, N. P. Widespread functional anoxia in the oxygen minimum zone of the Eastern South Pacific. *Deep Sea Res. Part Oceanogr. Res. Pap.* **65**, 36–45 (2012).
4. Gilly, W. F., Michael Beman, J., Litvin, S. Y. & Robison, B. H. Oceanographic and biological effects of shoaling of the oxygen minimum zone. *Annu. Rev. Mar. Sci.* **5**, 393–420 (2013).
5. Pavia, F. J. *et al.* Shallow particulate organic carbon regeneration in the South Pacific Ocean. *Proc. Natl. Acad. Sci.* **116**, 9753–9758 (2019).
6. Murakami, H. *et al.* Simulation and prediction of category 4 and 5 hurricanes in the high-resolution GFDL HiFLOR coupled climate model. *J. Clim.* **28**, 9058–9079 (2015).
7. Kuttippurath, J., Sunanda, N., Martin, M. V. & Chakraborty, K. Tropical storms trigger phytoplankton blooms in the deserts of north Indian Ocean. *Npj Clim. Atmospheric Sci.* **4**, 1–12 (2021).
8. Evan, A. T. & Camargo, S. J. A Climatology of Arabian Sea Cyclonic Storms. *J. Clim.* **24**, 140–158 (2011).
9. Murakami, H., Vecchi, G. A. & Underwood, S. Increasing frequency of extremely severe cyclonic storms over the Arabian Sea. *Nat. Clim. Change* **7**, 885–889 (2017).
10. Deshpande, M. *et al.* Changing status of tropical cyclones over the north Indian Ocean. *Clim. Dyn.* **57**, 3545–3567 (2021).
11. Deutsch, C., Brix, H., Ito, T., Frenzel, H. & Thompson, L. Climate-Forced Variability of Ocean Hypoxia. *Science* **333**, 336–339 (2011).
12. Long, M. C., Deutsch, C. & Ito, T. Finding forced trends in oceanic oxygen. *Glob. Biogeochem. Cycles* **30**, 381–397 (2016).
13. Bhatia, K. T. *et al.* Recent increases in tropical cyclone intensification rates. *Nat. Commun.* **10**, 1–9 (2019).
14. Menkes, C. E. *et al.* Global impact of tropical cyclones on primary production. *Glob. Biogeochem. Cycles* **30**, 767–786 (2016).
15. Price, J. F. Upper ocean response to a hurricane. *J. Phys. Oceanogr.* **11**, 153–175 (1981).
16. Zhang, H., He, H., Zhang, W. Z. & Tian, D. Upper ocean response to tropical cyclones: a review. *Geosci. Lett.* **8**, 1–12 (2021).
17. Foltz, G. R., Balaguru, K. & Leung, L. R. A reassessment of the integrated impact of tropical cyclones on surface chlorophyll in the western subtropical North Atlantic. *Geophys. Res. Lett.* **42**, 1158–1164 (2015).

18. Hu, C., Lee, Z. & Franz, B. Chlorophyll a algorithms for oligotrophic oceans: A novel approach based on three-band reflectance difference. *J. Geophys. Res. Oceans* **117**, (2012).
19. Da, N. D., Foltz, G. R. & Balaguru, K. Observed Global Increases in Tropical Cyclone-Induced Ocean Cooling and Primary Production. *Geophys. Res. Lett.* **48**, (2021).
20. Pedrosa-Pàmies, R., Conte, M. H., Weber, J. C. & Johnson, R. Hurricanes Enhance Labile Carbon Export to the Deep Ocean. *Geophys. Res. Lett.* **46**, 10484–10494 (2019).
21. NOAA National Centers for Environmental Information. *State of the Climate: Tropical Cyclones for Annual 2018, Published Online January 2019, Retrieved on May 18, 2021 from Https://Www.Ncdc.Noaa.Gov/Sotc/Tropical-Cyclones/201813.* (2019).
22. NOAA. NHC Data Archive. <https://www.nhc.noaa.gov/data/#hurdat>.
23. Boyer, T. P. *et al.* World Ocean Atlas 2018. [Dissolved O2 Climatological mean, all years]. *NOAA National Centers for Environmental Information. Dataset*.
24. R2R. Cruise ID OC1806A. *Rolling Deck To Repository* <https://www.rvdata.us/search/cruise/OC1806A> doi:10.7284/907990.
25. R2R. Cruise ID OC1704A. *Rolling Deck To Repository* <https://www.rvdata.us/search/cruise/OC1704A> doi:10.7284/907821.
26. Chang, Y. *et al.* Multisatellite observation on upwelling after the passage of Typhoon Hai-Tang in the southern East China Sea. *Geophys. Res. Lett.* **35**, 1–5 (2008).
27. NASA Goddard Space Flight Center, Ocean Ecology Laboratory, Ocean Biology Processing Group. Moderate-resolution Imaging Spectroradiometer (MODIS) Aqua Chlorophyll Data; 2018 Reprocessing. NASA OB DAAC, Greenbelt, MD, USA <https://doi.org/10.5067/AQUA/MODIS/L3M/CHL/2018> (2018).
28. NASA Goddard Space Flight Center, Ocean Ecology Laboratory, Ocean Biology Processing Group. Moderate-resolution Imaging Spectroradiometer (MODIS) Terra Chlorophyll Data; 2018 Reprocessing. NASA OB DAAC, Greenbelt, MD, USA <https://doi.org/10.5067/TERRA/MODIS/L3B/CHL/2018> (2018).
29. NASA Goddard Space Flight Center Ocean Ecology Laboratory Ocean Biology Processing Group. Visible and Infrared Imager/Radiometer Suite (VIIRS) Chlorophyll Data; 2018 Reprocessing. doi:[data/10.5067/NPP/VIIRS/L3B/CHL/2018](https://doi.org/10.5067/NPP/VIIRS/L3B/CHL/2018).
30. Hu, C. *et al.* Improving Satellite Global Chlorophyll *a* Data Products Through Algorithm Refinement and Data Recovery. *J. Geophys. Res. Oceans* **124**, 1524–1543 (2019).
31. O'Reilly, J. E. & Werdell, P. J. Chlorophyll algorithms for ocean color sensors - OC4, OC5 & OC6. *Remote Sens. Environ.* **229**, 32–47 (2019).
32. NASA Earth Observing System Data and Information System (EOSDIS. EOSDIS Worldview. <https://worldview.earthdata.nasa.gov/>.
33. Rolling Deck To Repository. Cruise NH1315 on RV New Horizon. (2015) doi:10.7284/903869.
34. Rolling Deck To Repository. Cruise NH1410 on RV New Horizon. (2015) doi:10.7284/904782.
35. BCO-DMO. Biological and Chemical Oceanography Data Collection. *BCO-DMO MapServer Geospatial Interface* <http://mapservice.bco-dmo.org/mapserver/maps-ol/index.php>.
36. Argo. Argo float data and metadata from Global Data Assembly Centre (Argo GDAC). SEANOE <https://doi.org/10.17882/42182> (2021).
37. Argo. Argo Fleet Monitoring - Euro-Argo. <https://fleetmonitoring.euro-argo.eu>.
38. Kwiecinski, J. V. & Babbin, A. R. A High-Resolution Atlas of the Eastern Tropical Pacific Oxygen Deficient Zones. *Glob. Biogeochem. Cycles* **35**, (2021).
39. Beman, J. M. *et al.* Biogeochemistry and hydrography shape microbial community assembly and activity in the eastern tropical North Pacific Ocean oxygen minimum zone. *Environ. Microbiol.* **00**, (2020).
40. Hansell, D. A. *et al.* Compilation of dissolved organic matter (DOM) data obtained from global ocean observations from 1994 to 2020 (NCEI Accession 0227166) Dissolved organic carbon

- concentrations. NOAA National Centers for Environmental Information <https://doi.org/10.25921/S4F4-YE35> (2021).
41. Kahru, M., Goericke, R., Kelly, T. B. & Stukel, M. R. Satellite estimation of carbon export by sinking particles in the California Current calibrated with sediment trap data. *Deep Sea Res. Part II Top. Stud. Oceanogr.* **173**, 104639 (2020).
  42. Behrenfeld, M. J. & Falkowski, P. G. Photosynthetic rates derived from satellite-based chlorophyll concentration. *Limnol. Oceanogr.* **42**, 1–20 (1997).
  43. Kahru, M., Kudela, R., Manzano-Sarabia, M. & Mitchell, B. G. Trends in primary production in the California Current detected with satellite data. *J. Geophys. Res.* **114**, C02004 (2009).
  44. Smith, K. L., Ruhl, H. A., Kahru, M., Huffard, C. L. & Sherman, A. D. Deep ocean communities impacted by changing climate over 24 y in the abyssal northeast Pacific Ocean. *Proc. Natl. Acad. Sci.* **110**, 19838–19841 (2013).
  45. Smith, K. L., Ruhl, H. A., Huffard, C. L., Messié, M. & Kahru, M. Episodic organic carbon fluxes from surface ocean to abyssal depths during long-term monitoring in NE Pacific. *Proc. Natl. Acad. Sci.* **115**, 12235–12240 (2018).
  46. O’Malley, R. Ocean Productivity. <http://sites.science.oregonstate.edu/ocean.productivity/index.php>.
  47. Dittmar, T., Koch, B., Hertkorn, N. & Kattner, G. A simple and efficient method for the solid-phase extraction of dissolved organic matter (SPE-DOM) from seawater: SPE-DOM from seawater. *Limnol. Oceanogr. Methods* **6**, 230–235 (2008).
  48. Petras, D. *et al.* High-Resolution Liquid Chromatography Tandem Mass Spectrometry Enables Large Scale Molecular Characterization of Dissolved Organic Matter. *Front. Mar. Sci.* **4**, 405 (2017).
  49. Nothias, L.-F. *et al.* Feature-based molecular networking in the GNPS analysis environment. *Nat. Methods* **17**, 905–908 (2020).
  50. Wang, M. *et al.* Sharing and community curation of mass spectrometry data with Global Natural Products Social Molecular Networking. *Nat. Biotechnol.* **34**, 828–837 (2016).
  51. Dührkop, K. *et al.* SIRIUS 4: a rapid tool for turning tandem mass spectra into metabolite structure information. *Nat. Methods* **16**, 299–302 (2019).
  52. Ludwig, M. *et al.* Database-independent molecular formula annotation using Gibbs sampling through ZODIAC. *Nat. Mach. Intell.* **2**, 629–641 (2020).
  53. Dührkop, K. *et al.* Systematic classification of unknown metabolites using high-resolution fragmentation mass spectra. *Nat. Biotechnol.* **39**, 462–471 (2021).
  54. Parada, A. E., Needham, D. M. & Fuhrman, J. A. Every base matters: assessing small subunit rRNA primers for marine microbiomes with mock communities, time series and global field samples. *Environ. Microbiol.* **18**, 1403–1414 (2016).
  55. Callahan, B. J. *et al.* DADA2: High-resolution sample inference from Illumina amplicon data. *Nat. Methods* **13**, 581–583 (2016).
  56. Dickey, T. Seasonal variability of bio-optical and physical properties in the Sargasso Sea. *J. Geophys. Res.* **98**, 865–898 (1993).
  57. Lin, I. *et al.* New evidence for enhanced ocean primary production triggered by tropical cyclone: ENHANCE PRIMARY PRODUCTION BY TYPHOON. *Geophys. Res. Lett.* **30**, (2003).
  58. Evans, Natalya, Tichota, Juliana, Ruef, Wendi, Moffett, James W. & Devol, Allan H. ETNP\_ODZ\_time\_series. Zenodo <https://doi.org/10.5281/ZENODO.6519188> (2022).
  59. Stephens, B. M. *et al.* Nonsinking Organic Matter Production in the California Current. *Glob. Biogeochem. Cycles* **32**, 1386–1405 (2018).
  60. Hertkorn, N. *et al.* Characterization of a major refractory component of marine dissolved organic matter. *Geochim. Cosmochim. Acta* **70**, 2990–3010 (2006).

61. Lam, B. *et al.* Major Structural Components in Freshwater Dissolved Organic Matter. *Environ. Sci. Technol.* **41**, 8240–8247 (2007).
62. Arakawa, N. *et al.* Carotenoids are the likely precursor of a significant fraction of marine dissolved organic matter. *Sci. Adv.* **3**, e1602976 (2017).
63. Repeta, D. J. Carotenoid diagenesis in recent marine sediments: II. Degradation of fucoxanthin to loliolide. *Geochim. Cosmochim. Acta* **53**, 699–707 (1989).
64. Koester, I. *et al.* Illuminating the dark metabolome of *Pseudo-nitzschia* –microbiome associations. *Environ. Microbiol.* **24**, 5408–5424 (2022).
65. Huang, R., Kim, H. J. & Min, D. B. Photosensitizing Effect of Riboflavin, Lumiflavin, and Lumichrome on the Generation of Volatiles in Soy Milk. *J. Agric. Food Chem.* **54**, 2359–2364 (2006).
66. Teeling, H. *et al.* Substrate-Controlled Succession of Marine Bacterioplankton Populations Induced by a Phytoplankton Bloom. *Science* **336**, 608–611 (2012).
67. Buchan, A., LeCleir, G. R., Gulvik, C. A. & González, J. M. Master recyclers: features and functions of bacteria associated with phytoplankton blooms. *Nat. Rev. Microbiol.* **12**, 686–698 (2014).
68. Lin, I. I. Typhoon-induced phytoplankton blooms and primary productivity increase in the western North Pacific subtropical ocean. *J. Geophys. Res. Oceans* **117**, (2012).
69. Engel, A., Kiko, R. & Dengler, M. Organic Matter Supply and Utilization in Oxygen Minimum Zones. *Annu. Rev. Mar. Sci.* **14**, 355–378 (2022).
70. Hung, C.-C. & Gong, G.-C. Biogeochemical responses in the southern East China Sea after typhoons. *Oceanography* **24**, 42–51 (2011).
71. Fuhrman, J. A. & Capone, D. G. Possible biogeochemical consequences of ocean fertilization. *Limnol. Oceanogr.* **36**, 1951–1959 (1991).
72. Naik, H., Naqvi, S., Suresh, T. & Narvekar, P. Impact of a tropical cyclone on biogeochemistry of the central Arabian Sea. *Glob. Biogeochem. Cycles* **22**, (2008).
73. Beman, J. M., Popp, B. N. & Alforda, S. E. Quantification of ammonia oxidation rates and ammonia-oxidizing archaea and bacteria at high resolution in the Gulf of California and eastern tropical North Pacific Ocean. *Limnol. Ocean.* **57**, 711–726 (2012).
74. Kalvelage, T. *et al.* Aerobic Microbial Respiration In Oceanic Oxygen Minimum Zones. *PLOS ONE* **10**, e0133526 (2015).
75. Bertagnolli, A. D. & Stewart, F. J. Microbial niches in marine oxygen minimum zones. *Nat. Rev. Microbiol.* **16**, 723–729 (2018).
76. Nicholson, S.-A. *et al.* Storms drive outgassing of CO<sub>2</sub> in the subpolar Southern Ocean. *Nat. Commun.* **13**, 158 (2022).
77. Krall, K. E. & Jähne, B. First laboratory study of air–sea gas exchange at hurricane wind speeds. *Ocean Sci.* **10**, 257–265 (2014).
78. Iwano, K., Takagaki, N., Kurose, R. & Komori, S. Mass transfer velocity across the breaking air–water interface at extremely high wind speeds. *Tellus B Chem. Phys. Meteorol.* **65**, 21341 (2013).
79. McNeil, C. & D’Asaro, E. Parameterization of air–sea gas fluxes at extreme wind speeds. *J. Mar. Syst.* **66**, 110–121 (2007).
80. Bianucci, L., Balaguru, K., Smith, R. W., Leung, L. R. & Moriarty, J. M. Contribution of hurricane-induced sediment resuspension to coastal oxygen dynamics. *Sci. Rep.* **8**, 15740 (2018).

# Chapter One Supplement

## Supplementary Note 1: Hurricane Aletta

Hurricane Aletta preceded Bud by four days, and was a weaker and faster moving storm (median eye pressure 1004 versus 996 mbar). Aletta did not fall within our 400km diameter selection window. Aletta was classified as a hurricane from June 6th - 9th, then weakened to a tropical storm on the morning of the 10th, further weakening to a low pressure system the evening of the 11th. Aletta's median translational speed was faster than Bud's ( $2.59 \text{ m s}^{-1}$ ,  $1.65 \text{ m s}^{-1}$ ) and median wind speed was lower than Bud's ( $18 \text{ m s}^{-1}$ ,  $25.7 \text{ m s}^{-1}$ ). Aletta passed tangentially to our immediate study area, as its track was west to west northwest, whereas Bud's track was northwest to northerly through our study area. Aletta's eye passed 256 km and 384 km south of Stations 2 and 3.5, respectively. Aletta also passed 67 km south of Station 3 on 2018-06-08, 10 days prior to our sampling at that station. At that distance Station 3 was within the 50 knot ( $25.7 \text{ m s}^{-1}$ ) wind swath, on the weaker side of the storm. The 50 knot wind swath outer boundary was 308 km south of Station 3.5. The closest eye time point to Station 3 was also the closest point to Station 3.5. The mean translational speed for Aletta in the vicinity of Station 3 was  $2.7 \text{ m s}^{-1}$ , and had a mean max sustained wind speed of  $41.9 \text{ m s}^{-1}$ .

The close timing of Aletta prior to Bud makes interpretation of RS imagery difficult for the potential blooms caused by Aletta. A small filament can be seen in Figure 2 on June 12th and 14th, in Aletta's wake. This filament is separated from the filament over Station 3.5 by a large region of low chlorophyll. In Supplementary Figure 6, we don't see evidence of increased chlorophyll under Aletta (e.g., June 13th). The weakness, distance, and lack of chlorophyll suggest Aletta may not have had an impact on the OMZ shoaling over Station 3.5. Without subsurface measurements we only have weak confidence in this conclusion.

## Supplementary Note 2: Repeat TCs over Station 3.5

Our sampling of Bud, which was preceded and followed by other tropical cyclones, is a normal occurrence in the vicinity of Station 3.5 (Supplementary Figure 8). This is indicated in the following summary statistics for the 400km window around Station 3.5. Within that window, the average time of year for the first TC overpass is July 7th. The yearly mean length of the TC season was 100 days. The median overpass per season was September 1st, with slightly less than five storms occurring per year on average (two to 9 storms per season). TCs were present as early as May 23rd, and as late as November 28th. Time between two consecutive storms within a year ranged from as low as 30 hours to 134 days. The distribution was skewed to shorter intervals (median = 17.6, mean = 24.8 days). When inspecting the full date range of TCs in the HURDAT2 dataset<sup>1</sup> (beginning on 1949-06-11, to 2021-11) there were 331 TCs, of those 132 reached hurricane strength, within the 400 km window. Prior to the use of satellite remote sensing TC count was not systematic and therefore incomplete, with likely spatial and strength biases in reporting. However, when comparing spatial density of TCs within the whole

date range, and starting in 2002, patterns are similar. The 400km window falls within a region of high TC density relative to other areas in the Eastern Pacific cyclone zone<sup>1</sup>. A recent review suggests more studies on the upper ocean response to consecutive TCs are needed<sup>2</sup>.

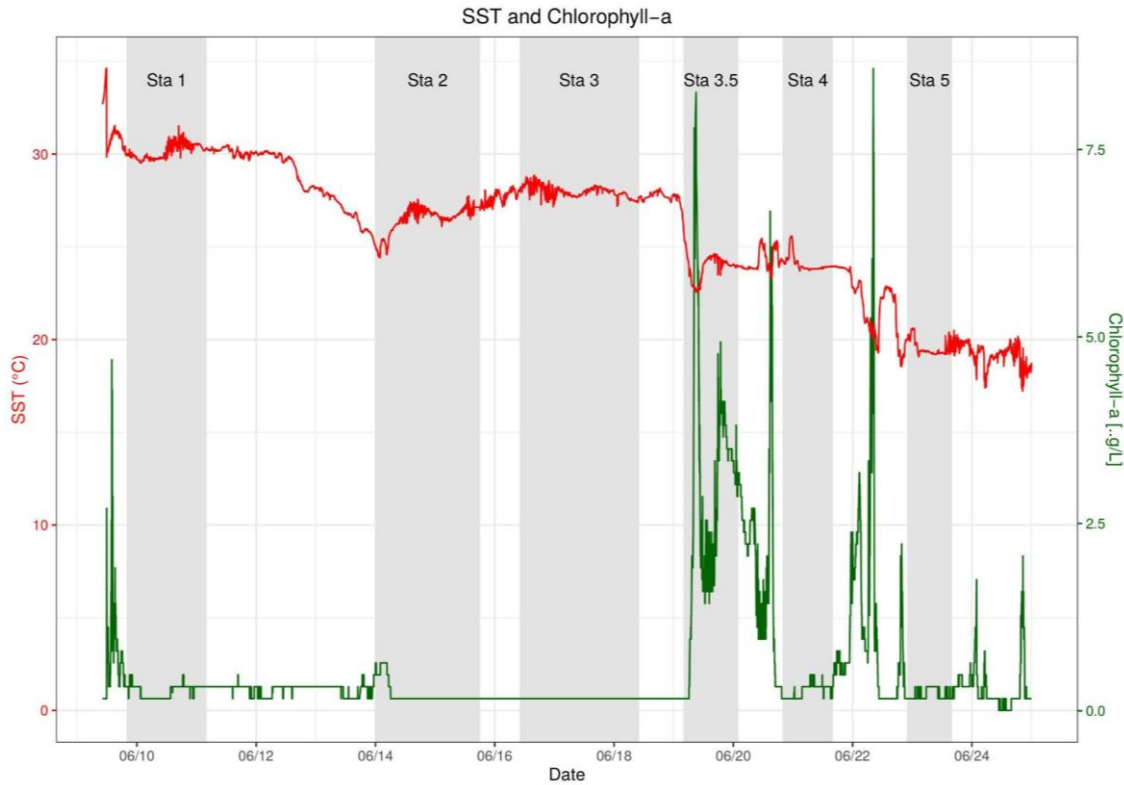
### Supplementary Note 3: Trends in export flux

We investigated trends in modeled export flux and the related observational variables, SST, Chl-a, and export flux (EF). Variables were separated into a background component, the signal, and the TC noise component. The background signal is the net combination of all non TC induced productivity. Primarily assumed to be driven by coastal upwelling but other mechanisms play a role (e.g., mesoscale eddy instructions<sup>3</sup>).

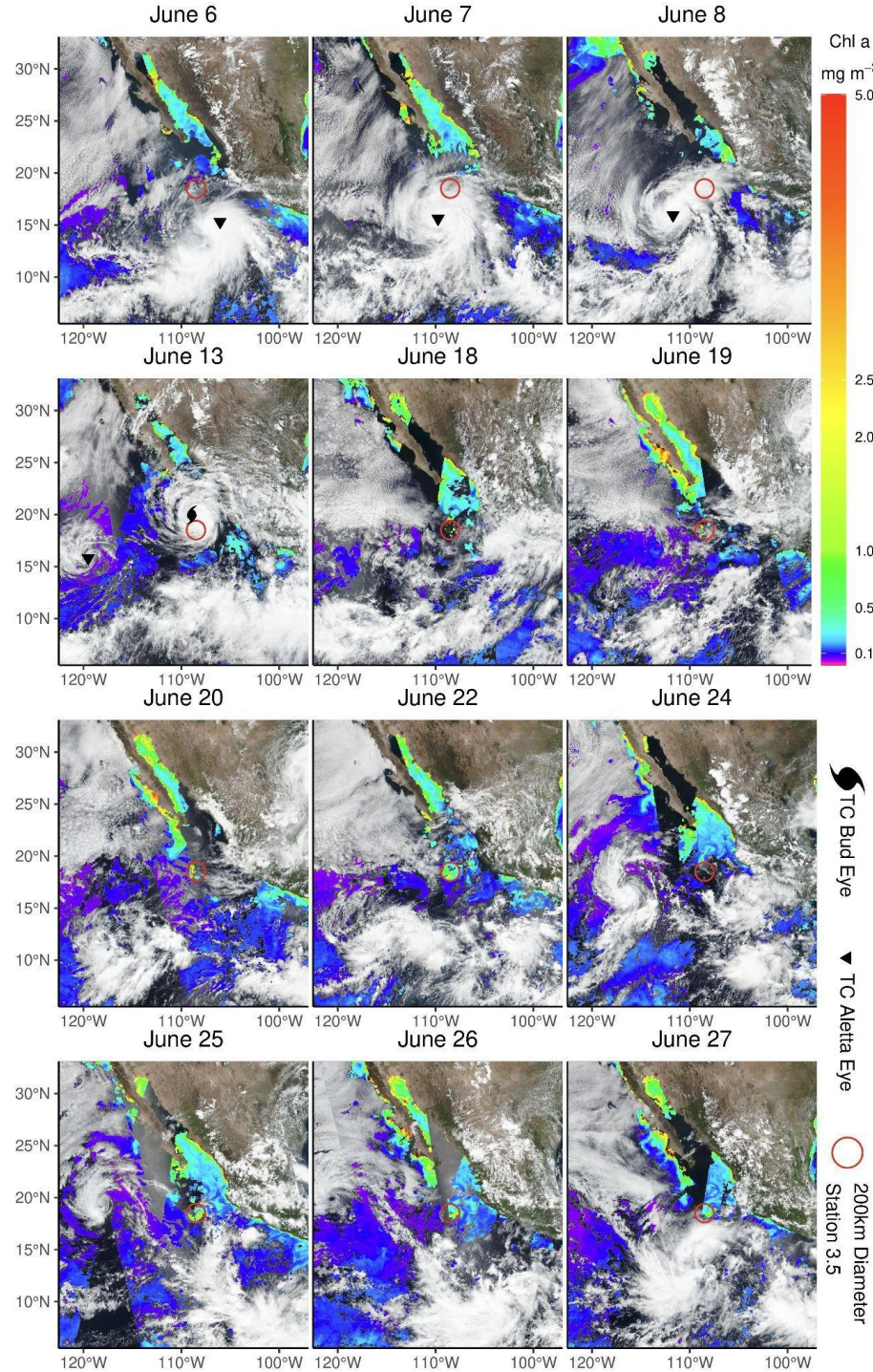
When splitting the export flux into noise and signal, the noise component covers a significant number of observations with ratio of noise to signal close to  $\frac{1}{2}$  (296/601). A shorter TC lag window would of course affect this; however, the high chlorophyll and EF values were dominated by TC overpasses. The median number of days between consecutive TCs is 18 days between storms, which is less than the duration of the observed Chl-a feature following Bud (Fig. 1, and Sup. Fig. 2). But would be adequately captured using three 8 day periods.

The upper values of Chl-a were the same for noise and signal components, with the lower range appearing to be pulled down by two values in the noise. EF values were on average higher for the noise as compared to the signal. Low SST temperatures were dominated by noise, but it would be best to view them as superimposed on top of seasonal variation. The trend lines of Chl-a, EF and SST match the PDO index well. Partitioning the time series altered the trends for the subcomponents' amplitudes but not necessarily the periodicity/frequency. Chl-a, and EF noise did show a greater positive slope in the trend line near the end of the time series. The start of the time series is based on available data, and trimming or adjusting may alter the trend in the noise observed.

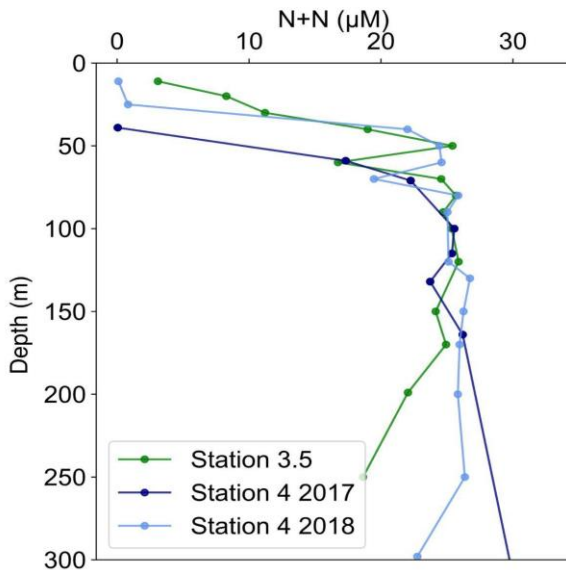
The VGPM is an older model, but it checks out, in that it captures the cold wake and Chlorophyll-a changes post TC, which the global satellite literature has well documented. Its dependency on PAR/seasonal light levels and their importance for the second chlorophyll maxima adds to its usefulness here. Rerunning with different observation inputs, especially SST, would improve the accuracy of the VGPM. Using an ensemble set of models can also be used to supplement, or in addition to improvements in the VGPM. Given the findings on POC in this study, and cloud interference, emphasis on particle driven models and active based sensors (LiDAR/clouds) may be a useful direction.



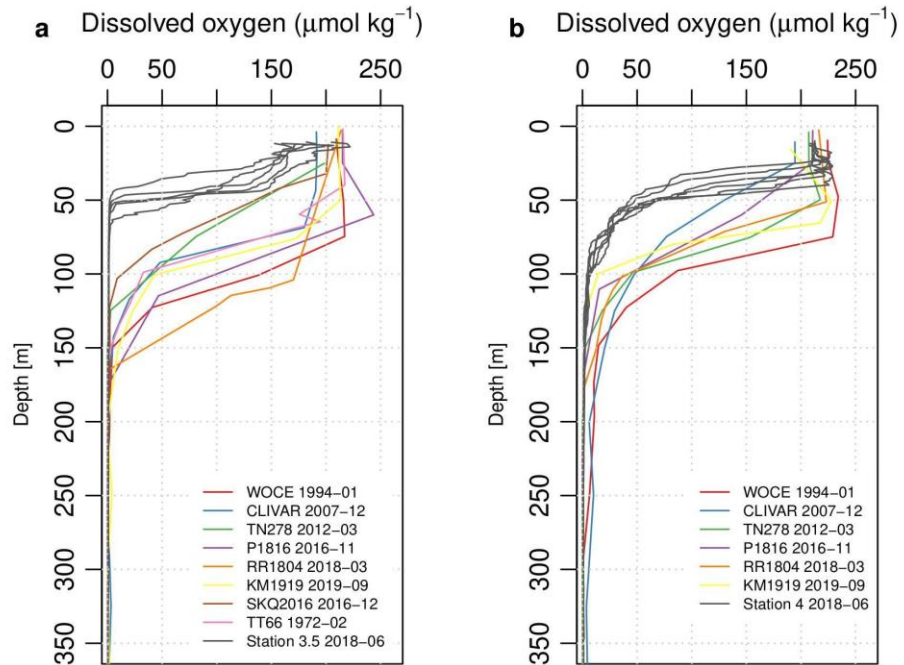
**Ch 1 - Supplementary Figure 1:** Continuous flowthrough data of Sea Surface Temperature (SST; red line) and chlorophyll-*a* concentration (in  $\mu\text{g/L}$ ; green line) from the 2018 *R/V Oceanus* cruise. Chlorophyll increases coincide with decreases in SST near stations 2, 3.5, and 4 in wake of Hurricane Bud. Gray bars denote periods on station when water profile measurements and biogeochemical casts were collected (see Figures 1 & 3). Date/times are local (MDT/UTC-6). Data are available on the R2R repository<sup>4</sup>.



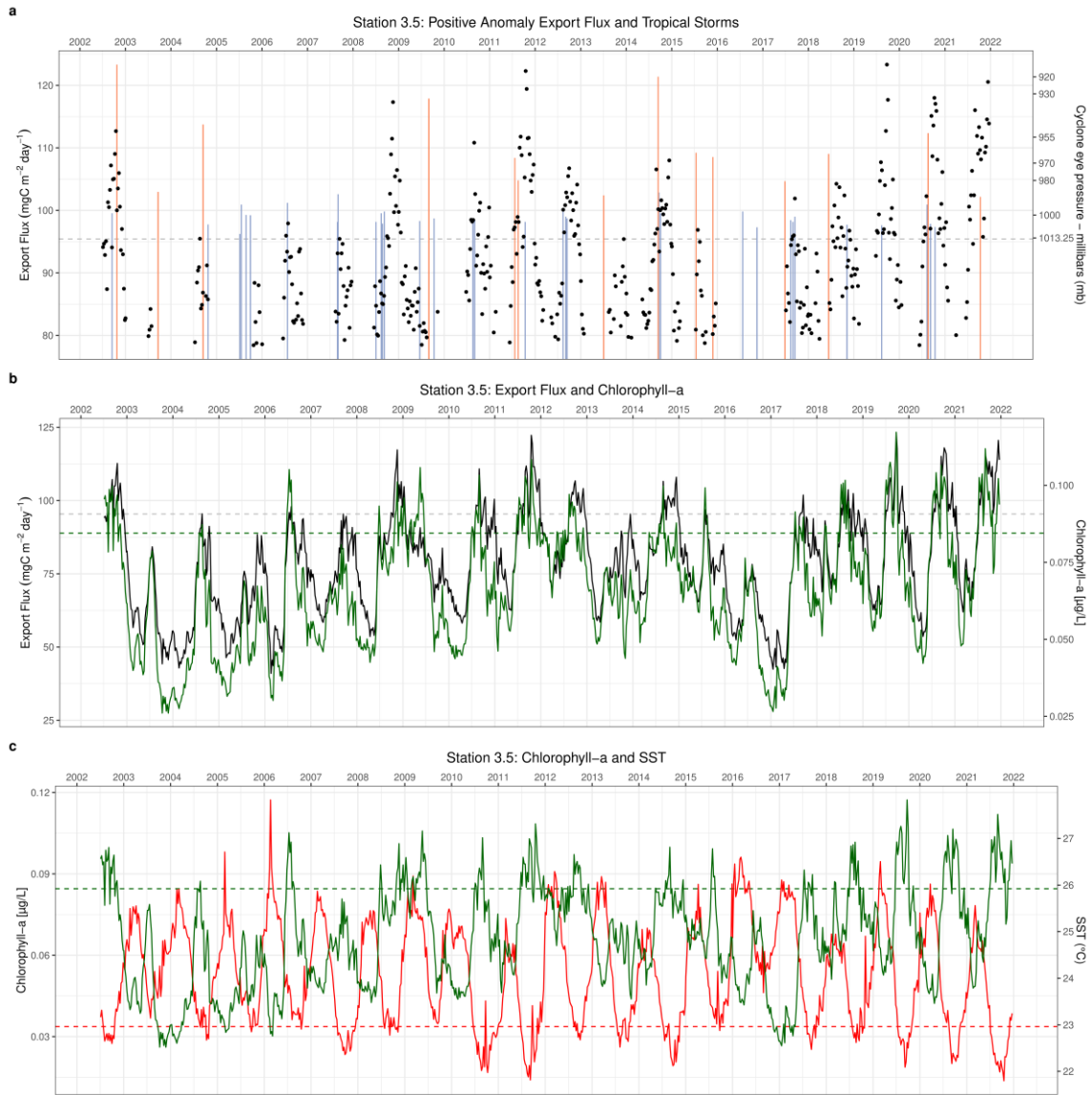
**Ch 1 - Supplementary Figure 2:** Select daily remotely sensed [Chl a] composites ( $\text{mg m}^{-3}$ ) from June 6-27th 2018, with true-color cloud imagery overlayed, demonstrate the presence and influence of Hurricane Bud. [Chl a] values above  $5 \text{ mg m}^{-3}$  are shown as red, while RGB imagery is shown for areas with no available [Chl a] values. The red circle (100 km radius) in all images is centered on Station 3.5. Eye position is shown for tropical cyclones Bud, and Aletta. See text for dates and specific storm strength designation. Images are ca. local solar noon. Larger area, and alternate days from Figure 2 main text.



**Ch 1 - Supplementary Figure 3:** Water column profiles of combined nitrate + nitrite concentrations at Station 3.5 (green; 2018 only) and Station 4 (blue; 2017 and 2018). For Station 4, 2017 data are shown in dark blue, and 2018 data collected following the hurricane are shown in light blue.



**Ch 1 - Supplementary Figure 4:** Dissolved oxygen profiles, CTDs from 2018 cruise with reference cruise measurements closest to (a) Station 3.5, and (b) Station 4. Reference cruises have coarse depth resolution. Colored lines indicate each cruise. Multiple profiles are shown for the 2018 cruise in gray. Dates listed for reference cruises indicate the start month of the cruise.



**Ch 1 - Supplementary Figure 5:** 8-day resolution: Non-lagged export flux (proportion of modeled VGPM). Derived from 8-day remotely sensed Chl-a & SST input variables. Values are mean computed for the 200km box around Station 3.5 ( $\text{m}^{-2} \text{ day}^{-1}$ ) for each variable (a) Export flux left axis (mg C). Positive anomalies only (above or equal to mean). Colored vertical lines are individual tropical disturbances that pass within the export 200 km flux box around Station 3.5. Orange = Hurricane strength, Blue = less than ". Height of each line is the median eye pressure per individual storm, which corresponds to the inverted right axis. Gray dashed horizontal line is 1 SD ( $\sigma$ ) above mean export flux for time series, and corresponds to 1013.25 mb, standard atmospheric pressure at sea level for reference. (b) MODIS derived Chl-a [ $\mu\text{g/L}$ ] in green/right axis, and export flux in black/left axis. Dashed horizontal lines are 1 SD ( $\sigma$ ) above mean for time series (EF = gray, Chl-a = green). (c) MODIS derived Chl-a [ $\mu\text{g/L}$ ] in green/left axis, and sea surface temperature ( $^{\circ}\text{C}$ ) in red/right axis. Dashed lines are 1 SD ( $\sigma$ ) above/below mean for time series (Chl-a = green, SST = red).

**Ch 1 - Supplementary Figure 6:** To be supplied by collaborators. Listed for congruence with the main text of manuscript in preparation.

**Ch 1 - Supplementary Table 1:** Storm position (eye), translational speed, and wind speeds for Hurricane Bud every 6 hours. Times are UTC-0 and coordinates are given for the position of the storm center/eye. Translational speed is calculated for distance traveled from the previous six hour position. Wind speed is maximum sustained for that position. The ratio (WS/TS) is wind speed (WS) over translational speed (TS). It is also given for the cubed wind speed ( $WS^3/TS$ ). Higher numbers indicate more wind energy imparted to a section of ocean per unit time. The simple ratio is reported for congruence with other studies<sup>5</sup>, the cubed wind speed ratio provides an accurate indication of kinetic energy transferred from wind to the ocean<sup>6,7</sup>. Bolded rows correspond to Supplementary Table 2. The last time point is prior to landfall near San Jose del Cabo, Mexico. Position and wind speed data are from NOAA<sup>1</sup>

Month/Day - Hour	Longitude W	Latitude N	Translational Speed (m/s)	Wind Speed (m/s)	WS/TS	$WS^3/TS$
6/10 - 00	101.3	12.7	4.18	18.01	4.31	$1.4 * 10^3$
6/10 - 06	102.1	13.5	4.22	23.15	5.49	$2.9 * 10^3$
6/10 - 12	102.9	14.4	4.26	28.29	6.65	$5.2 * 10^3$
<b>6/10 - 18</b>	<b>103.8</b>	<b>15.1</b>	<b>4.73</b>	<b>33.44</b>	<b>7.08</b>	<b><math>7.9 * 10^3</math></b>
6/11 - 00	104.6	15.7	4.2	38.58	9.18	$1.4 * 10^4$
6/11 - 06	105.6	16.1	5.2	46.3	8.91	$1.9 * 10^4$
6/11 - 12	106.4	16.4	4.16	51.44	12.38	$3.3 * 10^4$
<b>6/11 - 18</b>	<b>106.9</b>	<b>16.8</b>	<b>2.65</b>	<b>56.59</b>	<b>21.35</b>	<b><math>6.8 * 10^4</math></b>
6/12 - 00	107.4	17.3	2.69	61.73	22.92	$8.7 * 10^4$
6/12 - 06	107.8	17.7	2.16	59.16	27.4	$9.6 * 10^4$
<b>6/12 - 12</b>	<b>108.1</b>	<b>18</b>	<b>1.62</b>	<b>56.59</b>	<b>34.89</b>	<b><math>1.1 * 10^5</math></b>
6/12 - 18	108.3	18.3	1.14	51.44	45.08	$1.2 * 10^5$
<b>6/13 - 00</b>	<b>108.5</b>	<b>18.6</b>	<b>1.14</b>	<b>43.73</b>	<b>38.25</b>	<b><math>7.3 * 10^4</math></b>
6/13 - 06	108.6	18.9	0.71	36.01	50.41	$6.5 * 10^4$
6/13 - 12	108.7	19.2	0.72	30.87	43.11	$4.1 * 10^4$
6/13 - 18	108.9	19.7	1.33	23.15	17.44	$9.4 * 10^3$
6/14 - 00	109.1	20.3	1.44	23.15	16.03	$8.6 * 10^3$
6/14 - 06	109.3	20.8	1.34	20.58	15.38	$6.5 * 10^3$
<b>6/14 - 12</b>	<b>109.5</b>	<b>21.3</b>	<b>1.34</b>	<b>20.58</b>	<b>15.32</b>	<b><math>6.5 * 10^3</math></b>
6/14 - 18	109.6	21.9	1.16	20.58	17.75	$7.5 * 10^3$
<b>6/15 - 00</b>	<b>109.7</b>	<b>22.7</b>	<b>1.48</b>	<b>20.58</b>	<b>13.87</b>	<b><math>5.9 * 10^3</math></b>

**Ch 1 - Supplementary Table 2:** Storm position (eye), time, translational speed, and wind speeds for Hurricane Bud corresponding to closest spatial pass to each station. Times are UTC-0. Distance is eye position distance to cruise station. Hours after indicates time after an overpass when cruise subsurface sampling (multiple casts) was at the mean point in time at the specific station. Data and methods are the same as Supplementary Table 1.

Month/Day - Hour	Longitude W	Latitude N	Translational Speed (m/s)	Wind Speed (m/s)	Closest Station Overpass	Distance km	Hours After
6/10 - 18	103.8	15.1	4.73	33.44	1	664	2
6/11 - 18	106.9	16.8	2.65	56.59	2	46	80
6/12 - 12	108.1	18	1.62	56.59	3	300	132
6/13 - 00	108.5	18.6	1.14	43.73	3.5	11	169
6/14 - 12	109.5	21.3	1.34	20.58	4	22	175
6/15 - 00	109.7	22.7	1.48	20.58	5	428	212

**Ch 1 - Supplementary Table 3:** To be supplied by collaborators. Listed for congruence with the main text of manuscript in preparation.

**Ch 1 - Supplementary Table 4:** To be supplied by collaborators. Listed for congruence with the main text of manuscript in preparation.

## Supplementary methods:

See main text for methods related to Supplementary Figures 1 and 2, and Supplementary Tables 1 and 2.

### 8- remotely sensed [Chl a] and SST

For use in Supplementary Figure 5, Modis derived SST and Chl-a was acquired from Oregon State's Ocean Productivity website<sup>8</sup>. See Methods section in main text. These reanalysis products are the input variables used for the VGPM export products acquired from the same resource. For the signal and noise separation, selection of the TC noise component was based on a temporal correlation of TC overpass. The time window used was 10 days prior to the overpass and 24 post storms. This gives a two day buffer prior to the storm and a net post storm window of 32 days, because 8-day composites begin with the first date of integration. All 8-day time series variables from the main time series were separated into noise (TC-overpass) and signal (outside overpass). For the statistical analysis of export flux and TC overpass in CH 1, we conservatively limited reporting the export flux within the 200km box to only storms that pass within this box. The majority of positive anomalies are indeed associated with these TCs (Sup. Fig. 5). By including the TCs that pass within a 100 km buffer around the 200km box (i.e., a 400km box), some anomalies can be explained by these more distant storms (Sup. Fig. 5: e.g., 3rd quarter 2018, and midyear/fall 2019). For the noise separation here, the 400 km spatial association was used.

The resulting data were transformed into the time series objects using the R package “exts”<sup>9</sup> for trend analysis, after missing data from the datasets were removed. Trend similarity was determined by comparing loews smother, with the PDO climatic index, for all variables. The PDO climatic index downloaded from NOAA repositories using the R package “rsoi”<sup>10</sup>. Ended time series at 2020-08-05 because of missing export flux values and SST values both during different TCS. Given how missing values are treated, trends were not calculated past this date. The R package “feasts” was used to confirm/calculate the primary period/first harmonic of the data set matched the PDO.

## Oxygen Deficient Zones reference cruises

To supplement interpolated OMZ depth reference data (WOA<sup>11</sup> & ODZ Atlas<sup>12</sup>) we looked at data from the ENTP ODZ time series cruises<sup>13</sup> (Supplementary Figure 5). These cruise data are publicly available on the zenodo.org repository<sup>14</sup>, and are from the GLODAP program. For comparison to Station 4 (109.5 W, 21.5 N), we chose reference Stations at or within 0.1 degree north or south of those coordinates and on the 110 west line. For Station 3.5 (108.5 W, 18.5) cruise samples were located from 18.4 - 19 N, with all but one station on the 110 W line (Station 2, for cruise SKQ2016 was at 108.01 W). Depth resolution and methods for O<sub>2</sub> measurements increase and evolve over the time series. CTD profiles from our cruise have better depth resolution.

## Supplementary references

1. NOAA. NHC Data Archive. <https://www.nhc.noaa.gov/data/#hurdat>.
2. Zhang, H., He, H., Zhang, W. Z. & Tian, D. Upper ocean response to tropical cyclones: a review. *Geoscience Letters* **8**, 1–12 (2021).
3. Stramma, L., Bange, H. W., Czeschel, R., Lorenzo, A. & Frank, M. On the role of mesoscale eddies for the biological productivity and biogeochemistry in the eastern tropical Pacific Ocean off Peru. *Biogeosciences* **10**, 7293–7306 (2013).
4. R2R. Cruise ID OC1806A. *Rolling Deck To Repository* <https://www.rvdata.us/search/cruise/OC1806A> doi:10.7284/907990.
5. Kuttippurath, J., Sunanda, N., Martin, M. V. & Chakraborty, K. Tropical storms trigger phytoplankton blooms in the deserts of north Indian Ocean. *npj Climate and Atmospheric Science* **4**, 1–12 (2021).
6. Price, J. F. Upper ocean response to a hurricane. *Journal of Physical Oceanography* **11**, 153–175 (1981).
7. Kuttippurath, J., Sunanda, N., Martin, M. V. & Chakraborty, K. Tropical storms trigger phytoplankton blooms in the deserts of north Indian Ocean. *Npj Clim. Atmospheric Sci.* **4**, 1–12 (2021).
8. O’Malley, R. Ocean Productivity. <http://sites.science.oregonstate.edu/ocean.productivity/index.php>.
9. Jeffrey A. Ryan and Joshua M. Ulrich. xts: eXtensible Time Series R package version 0.13.1. (2023).
10. Sam Albers. rsoi: Import Various Northern and Southern Hemisphere Climate Indices R package version 0.5.5. (2022).
11. Boyer, T. P. *et al.* World Ocean Atlas 2018. [Dissolved O<sub>2</sub> Climatological mean, all years]. *NOAA National Centers for Environmental Information. Dataset*
12. Kwiecinski, J. V. & Babbin, A. R. A High-Resolution Atlas of the Eastern Tropical Pacific

- Oxygen Deficient Zones. *Global Biogeochemical Cycles* **35**, (2021).
13. Evans, N., Tichota, J., Ruef, W., Moffett, J. & Devol, A. *Rapid expansion of fixed nitrogen deficit in the eastern Pacific Ocean revealed by 50 year time series.* <http://www.essoar.org/doi/10.1002/essoar.10512279.1> (2022)  
doi:10.1002/essoar.10512279.1.
14. Evans, Natalya, Tichota, Juliana, Ruef, Wendi, Moffett, James W. & Devol, Allan H. ETNP\_ODZ\_time\_series. (2022) doi:10.5281/ZENODO.6519188.

# Chapter Two: Fine scale temporal subsurface oceanographic dynamics and a resultant ecological model from the 2018 process cruise and Hurricane Bud

## Abstract

Tropical cyclones are known to mix the subsurface ocean through several well understood physical oceanographic mechanisms. However, little is known about the connection between these mechanisms and the biological response to TC disturbances. To address this knowledge gap and investigate ecological dynamics in the wake of Hurricane Bud in the eastern tropical North Pacific (ETNP) oxygen minimum zone (OMZ), multiple profiles at three separate sampling stations were analyzed using Conductivity Temperature Depth instruments with optical sensors (CTDs) and continuous subsurface current velocities were measured with an Acoustic Doppler Current Profiler array (ADCP). CTD profiles yielded information on subsurface water properties, while shipboard ADCP data captured storm-induced subsurface current mixing. Conducting inter-station and intra-station comparisons produced a comprehensive landscape level perspective under a single storm. Comparing profiles to subsurface current patterns suggests oscillations of the isopycnal at the base of the mixed layer have ecological ramifications for deep microbial communities. In particular, a concentration of active microbial communities and biomass is actively transported through varying nutrient and light regimes of the mixed layer. These findings may apply to TC disturbances, not only for microbial communities in the ETNP OMZ, but also in all oligotrophic ocean regions under tropical cyclones, with implications for carbon export, and the eco-evolutionary dynamics of subsurface microbial communities.

## Introduction

Tropical cyclones (TCs) act as pervasive subsurface disturbance events throughout large regions of the tropical oceans. However, the physical oceanographic science literature documenting subsurface phenomena under TCs is far more mature than current biological work<sup>1-8</sup>. In particular, satellite surface studies indicate the importance of plankton blooms under TC wakes<sup>2</sup>, but lack the dimensionality needed to fully capture subsurface physical mixing. Additionally, the few biological oceanographic ship-based investigations that have conducted subsurface sampling after TC wakes lack analyses between profiles per single location<sup>2</sup>. This limitation potentially neglects the spatial-temporal biological dynamics that ensue after severe disturbances. This study addresses unanswered questions related to TC-induced physical mixing mechanisms and the coupled biological response to these disturbances.

The subsurface physical mixing induced by TCs, while complex<sup>1</sup>, may be simplified as the net effect of two categories of mixing: (1) vertical entrainment and (2) geostrophic mixing. Entrainment involves the localized overturning and mixing of the ocean's surface layer due to turbulence caused by wind, waves, and surface currents. This process results in a colder, thicker surface mixed layer. In contrast, geostrophic mixing, upwelling (Ekman suction), and downwelling (Ekman pumping) are due to the TC interacting with the ocean and resultant geostrophic advective currents.

Near-inertial waves are a second type of non-independent geostrophic mixing that interacts with Ekman transport<sup>3,4</sup>. They are associated with upwelling and horizontal mixing post-TC<sup>5,6</sup>; but do not always form for every storm. Near-Inertial waves (NIWs) are non intuitive in structure, and are more difficult to measure than wind induced entrainment. Wind induced forcing initiates the formation of near-inertial waves, while the apparent Coriolis force acts as the restoring force<sup>1</sup>. They can be recognized by their main wavelength, the first harmonic. Studies using Acoustic Doppler Current Profilers (ADCPs) on moored<sup>5,7</sup> or lagrangian platforms<sup>8</sup> commonly detect subsurface NIWs following TCs. Additionally current velocity profiles from shipboard ADCP sensors may be used to measure near-inertial waves generated by hurricanes<sup>6</sup>. These measurements show that NIWs form in the wake of storms and are a common and persistent subsurface phenomenon of TCs. These features could affect subsurface biological activity, if they alter the abiotic structure that is the scaffolding for microbial ecosystems. However, this has not been examined in the biogeochemically important eastern tropical North Pacific (ETNP) oxygen minimum zone (OMZ).

Exploring the connections between different oceanographic measurements provides a needed integration of the coupled ecological and physics based phenomena unique to TCs. Importantly, both the effects of entrainment and geostrophic mixing mechanisms must be included in order to understand the biological response to physical phenomenon. This study addresses this knowledge gap by comparing physical and biological oceanographic measurements taken along a cruise track and at specific sampling stations following Hurricane Bud (2018) in the ETNP OMZ. Taken together, results of the subsurface cruise measurements indicate that differences in stations may be due to varying combinations of destructive mixing and nondestructive geostrophic mixing mechanisms related to distance from the storm. The physical mixing findings are congruent with the physical oceanographic literature for subsurface TC effects, including the confirmation of NIWs. Results also indicate a unique boundary effect at the permanent pycnocline correlated with net biological particles and fluorescence associated with the deep chlorophyll maximum (DCM) at Station 3.5. This may be the first direct evidence of this unique ecological-oceanographic relationship under a TC, with implications for the low light adapted deep microbial communities and their transport through depth defined biological and physical niche space<sup>9</sup>.

## Methods

### Physical mixing

The research vessel *R/V Oceanus* was equipped with an ADCP sensor package. In the package there are two separate sensors. An Ocean Surveyor (Phased array), 75 kHz, used to plot vertical and horizontal components at a lower resolution but higher range - that is to greater depth. A Workhorse Mariner (Non-phased array), 300 kHz - broad band was used for surface vectors. The OS 75 operates in both the narrowband and the broadband, because the narrowband is less susceptible to noise it was chosen for all analysis.

ADCP data were analyzed using processing software and procedures from the CODAS+UHDAS open source software pipeline<sup>10</sup>. Data was downloaded from the R2R repository<sup>11</sup>. Standard protocols were implemented following guidance by the extensive CODAS+UHDAS Documentation website<sup>10</sup>. Steps include: (1) Removal of data with ship velocities above 3 m s<sup>-1</sup>. (2) Manual removal of rapid changes in heading, and ship acceleration (which bias towards upwelling in vertical velocity). (3) A final heading correction was the last step. The Ocean Surveyor 75 was processed as above, while the Workhorse Mariner 300 was processed, both as above, and without removal of data. For the basic calculations of harmonic oscillation, selection of ADCP data was limited to profiles away from the shelf break, because of associated confounding factors introduced through internal currents<sup>12</sup>, and TC<sup>13</sup> mixing interacting with the shelf. Shipboard velocity induced noise has a greater impact on the deep current profiles as compared to shallow velocities profiles. The textbook formulas for harmonic oscillations are:

$$u = V \sin ft \quad v = V \cos ft \quad V^2 = u^2 + v^2$$

Where  $u$  and  $v$  are the horizontal vectors of current flow in the east, and northerly directions,  $f$  is the coriolis parameter that varies by latitude,  $t$  is the period of oscillation, and  $V$  is the product of the horizontal components.

Using the above listed software, distinct transitions were used to calculate  $t$ . Independently surface velocity oscillations were calculated in the software, for both components of the horizontal flow. Multiple variables and multiple equations were solved and combined as above. This provided a simple back of the envelope calculation using both sensors, over the cruise track. See (ref<sup>6</sup>) for detailed work using ADCP on ships to measure TC NIWs.

Processing and editing ADCP, via visual interpretation of data by skilled workers is commonly done manually. This is done to address a number of possible noise issues ranging from shipboard movement errors, to the presence of a deep scattering layer. Here only shipboard measurements were removed as they were the most obvious to detect and validate. Figures 22 & 23 include some of the many diagnostic tools built into the software. Processing of the ADCP data other than for visual, and qualitative means beyond calculating the first harmonic was beyond the current abilities of this author. A more experienced specialist could certainly investigate this dataset for a more comprehensive analysis. (e.g., determining base of the mixed layer, and location of the

pycnocline from the Workhorse Mariner array.) As such, minimally processed ADCP data is presented.

## CTD profiles

The CTD profiler was a SeaBird SBE 9+ system, equipped with a SBE-43 DO sensor, WetLabs ECO-FLR fluorometer and a C-Star Transmissometer, which gives local beam attenuation. CTD profiles are available via the Rolling Deck to Repository<sup>11</sup>. The R package “oce: Analysis of Oceanographic Data”<sup>14</sup> was used for profile analysis including default QA/QC functions.

Units for salinity are practical salinity using international standards of the Joint Panel on Oceanographic Tables and Standards (PSS-78). Software defaults were used for different density measurements, which were most appropriate to the particular graph. The three different Sigmas utilized are: Sigma-t (calculated with *in situ* salinity and temperature, but pressure equal to zero); Sigma-theta (density calculated with *in situ* salinity, potential temperature, and pressure equal to 0, minus 1000 kg/m<sup>3</sup>); Sigma-0 (density calculated with absolute salinity, conservative temperature, with respect to the reference pressure 0, so minus 1000 kg/m<sup>3</sup>). The software was used to calculate additional derived oceanographic parameters including Spice and Rrho [Rp]. Rrho is a density ratio of the smoothed splines of absolute salinity and conservative temperature, which is then passed to the GSW implementation of the equation of state. Either as  $(\beta * dS/dz) / (\alpha * d(\theta)/dz)$  for the diffusivity implementation, or the reciprocal for salt finger implementation. Implementations were used based on relative estimation of importance per individual profile according to their temperature and salinity plots.

Salt fingers are sinking high salinity warm, water masses that lose heat faster than decrease in salt concentration, which can be replaced by upward cold and fresh fingers as they sink creating a structured mixing that cannot be described by diffusion alone. Spice is a related ratio, used to compare the relative contribution of temperature and salinity makeup of water masses of equal density. Higher numbers indicate warmer and saltier “spicy”, lower values indicate colder and fresher “minty”.

The number given for photosynthetically available radiation (400-700nm) is the percentage as measured from the difference in the vessel’s radiometer and the *in situ* LI-COR Biospherical Sensor on the CTD profiler. CTD profiles include metadata parameters. Metadata errors such as station indicators, were validated and corrected using paper data sheets collected while at sea. Metadata values of bottom depth could be erroneous, not conforming to known values at GPS coordinates. Data sheets were collected at sea (see author list Chapter One). Care should be taken by future users of this data if using any metadata fields. Sampling resolution of individual points in CTD profiles can range from ca. ½ meter to 2 meters in the upper 200m, with the surface profiles usually exhibiting highest variance between samples. All profiles shown are on the downcast, following standard practice. A common feature in CTD profiles near the surface is spikes, due to sensor noise upon entering the ocean and ship movement.

## Results

### Physical mixing and time progression

ADCP data from the 2018 cruise were indicative of the presence of inertia waves (Figs. 1, 2:4, 12, 16 & 17). For the cruise track relevant to post TC overpass; (Stations 2-4), peak meridional and zonal current velocities in the upper 200m were observed to be approximately  $0.6 \text{ m s}^{-1}$ , and associated oscillation periods of ca. 36 hrs integrated along the whole cruise track (Fig. 2). It should be noted that time, latitude, and distance of measurements produces a range of periods and associated current velocities. For example, at Station 3 peak velocities were closer to  $0.3 \text{ m s}^{-1}$  with a 24 hour period (Figures 16 & 17). The range of periods, for the range of conditions, fit the expected inertial wave harmonic oscillation well. Observations fit the known weakly dispersive nature of NIWs.

The vessel was on these stations for enough time (e.g., 2 days) to satisfy basic Nyquist frequency requirements (i.e., Station 3, Fig. 17 & Table 3). Changes in ship heading, speed, and the resultant introduced noise prohibited the ability to use all of the ADCP data (methods). Vertical velocity transitions from upwelling to downwelling versus downwelling to upwelling phases (slow and moderate, versus quick and intense, (Figs: 2c, 4, 12, and 17) are associated with inertial wave and TC induced mixing<sup>1</sup>. Additionally, near surface phase velocity and group velocity patterns, as well as alternating temperatures (Fig. 1), were indicative of inertial waves when transiting between stations<sup>1</sup>. In general, tropical cyclone-induced mixing intensity increases with the cube of the wind speed and varies inversely with translational speed<sup>15</sup>. The radius of maximum SST cooling (an indicator of spatial extent of mixing) increases linearly for low to mean values of translational speeds ( $0.5 - 6 \text{ m s}^{-1}$ )<sup>15</sup>. Winds were high and the storm was slow moving (CH 1 Sup. Table 1) near Station 2 and over stations 3.5 and 4. The input force was high over the spatial domain covered by the ship track. These observations and basic calculations; the slow, powerful storm; and persistent Chl-a phenomena are all congruent with storm driven upwelling. Upwelling is a key component of cyclone induced mixing, which contributes to bloom formation.

These results indicate that storm driven mixing dominates the hydrography at Station 3.5, and likely has some impact on Station 4, whereas Station 3 was too far away to be adequately mixed via entrainment (CH 1 Sup. Table 1 & 2). The potential energy available for subsurface mixing due to cyclone winds decays as a power function of increasing distance<sup>15</sup>. The distance of Station 3.5 from the coast and the abyssal shelf margin (c.a. 350 km and 280 km) is far, *a priori* insulating it from along shore winds and associated the coastal upwelling that fuels productivity—which can be a dominant feature in this region of the ETNP<sup>16-18</sup>.

Entertainment and upwelling will occur at different spatial and temporal scales following a TC. In general, entrainment may be more localized in time (winds of the TC) and cover a larger spatial domain, with upwelling lasting longer yet, more localized around a storm's center<sup>8,15</sup>. Inertial waves propagated outward for a longer (outward propagation increases with increasing depth<sup>5,7</sup>) period after storm overpass<sup>15</sup>. These

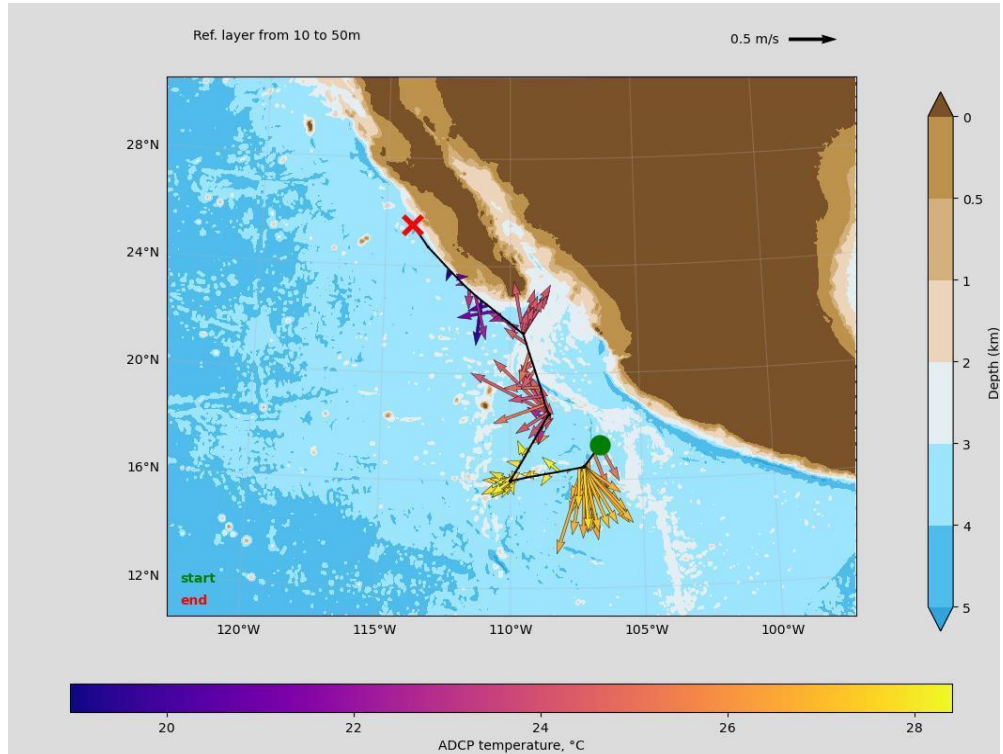
patterns can be well explained by a simple model where wind vectors shift from radial to tangential with increasing distance from the storm eye<sup>5</sup>.

Upwelling may be more important for maintaining a sustained response, especially for persistence of blooms, as inertial waves may persist for weeks after a storm as they are weakly dispersive lasting much longer than 10 days and propagating outward for hundreds of kilometers<sup>5–7</sup>. All stations showed evidence of NIWs in their ADCP plots, with differences explained in subsections below. Station 4, the latest shown (Fig. 1), was measured 8 days after the storm overpass.

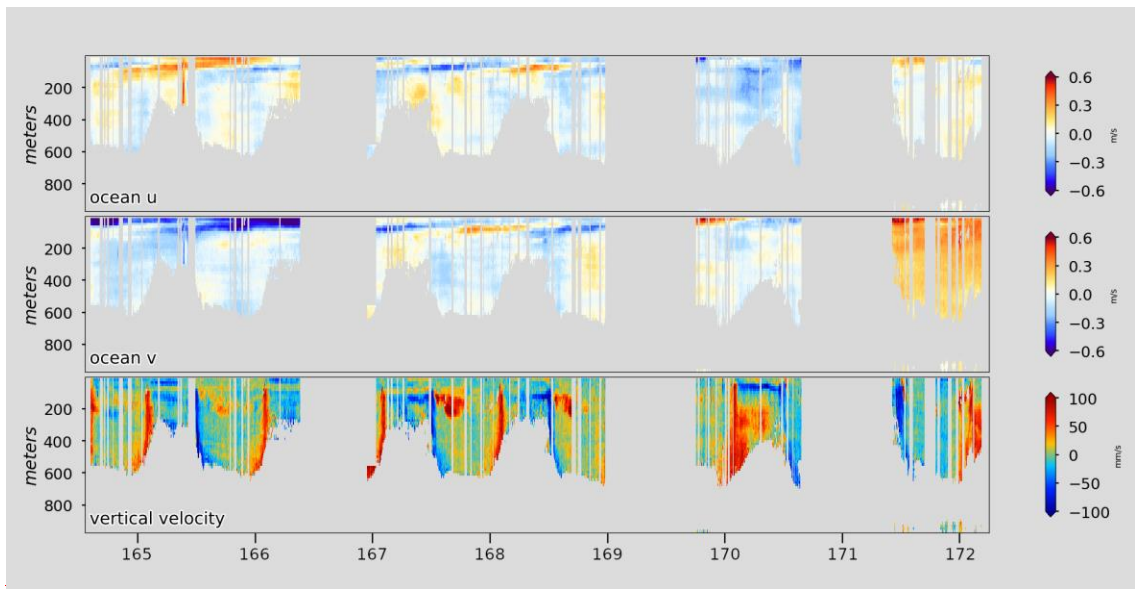
## Individual stations and multiple CTD casts

Multiple profiles were available for each station, however for Chapter One water samples were not taken for all CTD casts. CTDs are equipped with optical based sensors that complement actual water measurements of organic matter and flowthrough sampling of RNA; what they lack in detail, they gain in greater sampling frequency per profile.

Oxygen and physical water parameters can be compared to optical methods which give estimates of particulate matter in the water, a proxy for net biomass. Specifically, beam attenuation was the optical sensor/parameter chosen, as it gives a 1<sup>st</sup> order measure of total suspended matter<sup>19</sup>. Produced variables such as POC are often based on a derivation of this measurement, but derivation algorithms are based on statistical relationship to empirical studies, which are in turn based on mean patterns in a stratified and undisturbed oligotrophic ocean. Post TC overpass would fall outside these mean assumptions. A few water samples under a plankton bloom in the OMZ may be used to constrain empirically derived existing models but may not be sufficient for constructing novel empirical relationships. Likewise raw fluorescence is displayed given complexities in using it to measure secondary variables (e.g., biomass) for cyanobacteria<sup>20</sup>. Also, microbes common in the secondary chlorophyll maximas of OMZ's often rely on pigments other than Chl-a<sup>21</sup>. Intra-station CTD comparison allows for a high resolution understanding of temporal variance at the scale of multiple hours, greater than satellites or other subsurface arrays<sup>22</sup>. Inter-station comparison allows for understanding ecological processes at the landscape scale and the associated spatial diversity.



**Ch 2 - Figure 1:** Ocean current profiles from shipboard ADCP sensors. 2-hour averaged, depth integrated (10-50m) horizontal vector (m/s) components with colors indicating temperature using Wh300 hz bb surface ADCP. Track on map corresponds to the three panels in Figure 2.



**Ch 2 - Figure 2:** Ocean current profiles from shipboard ADCP sensor. Corresponds to the cruise track in Figure 1. Top panel is zonal velocity,  $u$ , ( $\text{m s}^{-1}$ ). Middle panel is meridional,  $v$ , “ ”. Bottom panel vertical velocity,  $w$ , ( $\text{mm s}^{-1}$ ). Gray indicates no data, or data removed due to ship movement induced noise. Red is positive (East, North, Up). Blue is negative (West, South, Down). Left axis is depth to 1000m. Times in decimal yr-day UTC-0. Panels are velocity components from the 75 kHz near-band sensor.

### Station 3.5

For Station 3.5, profiles of important biogeochemical variables varied by depth for casts and over time (Fig. 5); however, a consistent pattern exists for all variables through multiple casts and through time when examining their relationship to the base of the pycnocline. Cast two (Table 1, Fig. 5) showed an even more pronounced shoaling of both biological and physical variables, which for the remaining casts seemed to slowly deepen and then stabilize over time (Figs. 5 & 9).

The deep chlorophyll maxima (as indicated by fluorescence), otherwise known as the deep chlorophyll maxim (DCM<sup>23</sup>) is at the base of pycnocline for all casts (Figs. 5, 6, & 9), which corresponds to the second net particle maxima measured by the beam attenuation. Typically, a second chlorophyll maxima (SCM) is expected in OMZs.

When plotting density versus depth for beam attenuation and fluorescence, both show a tighter fit to density than depth (Figs. 6 & 9 vs. 7 & 10). Comparing peak beam attenuation and fluorescence by depth puts the DCM at ca. 45 m, with PAR at 10% percent of surface values. PAR will be all available light as a function of light attenuation through the entire column above, whereas beam attenuation is a discrete depth measurement.

Oxygen profiles in the upper water column (< 50 m depth) showed high variability between casts (Fig. 9) and casts were not sufficient to cover the full diurnal cycle (Table 1), which is known to affect profiles of Oxygen<sup>24-27</sup>. However, the upper bounds of the OMZ tracks the base of the pycnocline, along with the DCM, and the spike in beam attenuation (Figs. 5:7, 9, & 10).

The fluorescence profiles via the same mechanisms as oxygen (biological activity) will be expected to show changes due to diurnal activity between casts. Indeed, in the upper ocean mixed layer profiles showed shifts within a period of four hours for three casts, (Table 1) transitioning from narrow peak to a wide peak and back to narrow (Figure 9 - l:n). The morning profile (Fig. 9o) had the weakest defined DCM of all profiles.

The oceanographic plots for cast two (Fig. 8) indicate a very sharp stable pycnocline and a stratified upper ocean. This figure is indicative of patterns for all casts, which vary not in structure but depth of pycnocline (all casts not shown). A singular buoyancy feature (Fig. 8a) around the sharp density profile indicates a very stable isopycnal surface. Salinity and temperature are both important to density, and besides a surface salinity anomaly (see methods) shows relatively stable changes with depth. Salinity values are near the ocean average of 34.7 PSU (Fig. 8 b) Spice and diffusive Rrho values indicate a thoroughly mixed upper ocean with both ratios approaching zero, or becoming more stable below the pycnocline. These values were low for all casts, not shown, but like cast two (Fig. 8c,d). QA/QC of CTD profiles 1-3 did not indicate the anomalous shoaling was due to deployment or instrument error. The correlation of multiple variables, derived from different sensors across casts, also gives greater confidence in this conclusion.

Beam attenuation at the DCM depth showed the least variability in magnitude or shape for all casts and was also strongly associated with the base of the pycnocline (Figs. 9f:j, & 10k:o). The slight drop in beam attenuation below the pycnocline for cast two (Figs. 6 & 7, Table 1) and all casts (Figs. 9 & 10) indicates matter is not exported out of

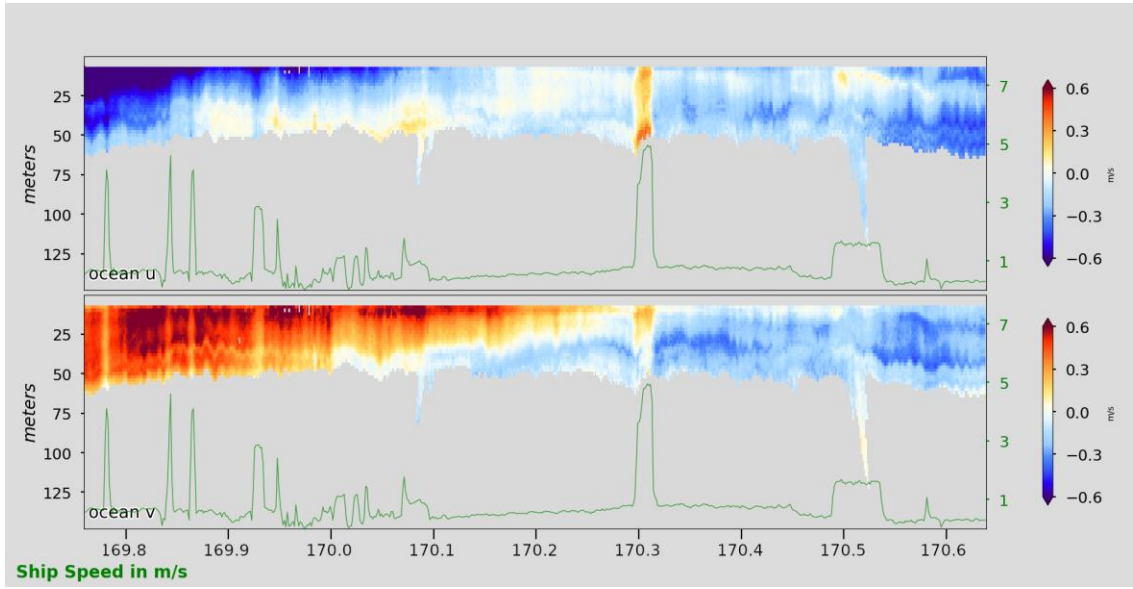
this highly active biological area, but rather consumed at, or just below the base of the pycnocline. The 26 [kg/m<sup>3</sup>] isopycnal surface appears to be at the base of the pycnocline (Fig. 8 a, Fig 6), so below that density would be considered the underlying deep water mass. This particular density surface is generally a useful value/location for biogeochemical cycling in the ETNP OMZ<sup>28</sup>.

Figures 3 & 4 show the subsurface currents collected continuously under the discrete casts at Station 3.5. Cast two occurred immediately following a period of high horizontal velocity in the North and Westerly direction (Fig. 3, Table 1), with vertical velocity in the beginning of an upwelling phase, following a period of slack flow (Fig. 4). The fourth cast coincides within a few hours prior to peak upwelling in the velocity field below the pycnocline (Fig. 4), and also during a period of relaxation in both the horizontal upper ocean horizontal vectors (Fig. 3). By the time of the last cast, the meridional velocity has switched direction to the south (Fig. 3) and dowelling has begun in the deeper water mass (Fig. 4, Table 1). The time between the 4th and 5th casts and the changing current flows may be related. However, sampling frequency of CTDs is not high enough to draw meaningful conclusions on the fine scale association of the movement of the pycnocline and the near-inertial wave currents. Any lagged elasticity in a rebounding density layer (Fig. 8a) would make these simple temporal correlations more obscure.

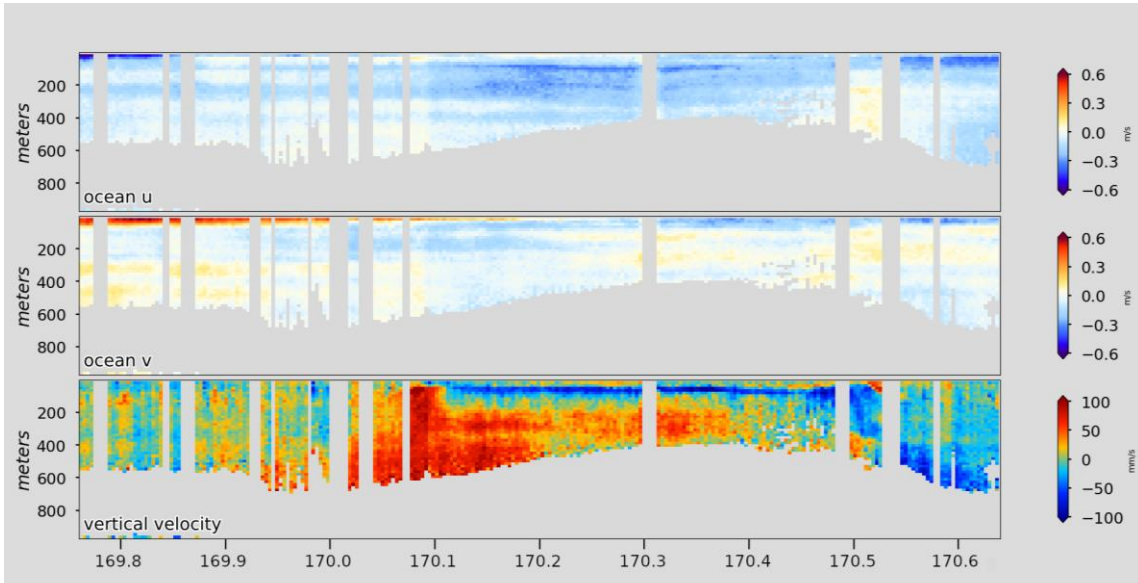
The ADCP data are continuous. Secondary patterns in subsurface currents do indicate (Figs. 22b & 23) an additional upwelling, at a different scale than the main NIW. These patterns do not appear to be noise based errors (same figures, bottom panels).

**Ch 2 - Table 1:** Station 3.5 CTD individual cast times. UTC-0, and with local time for diurnal context.

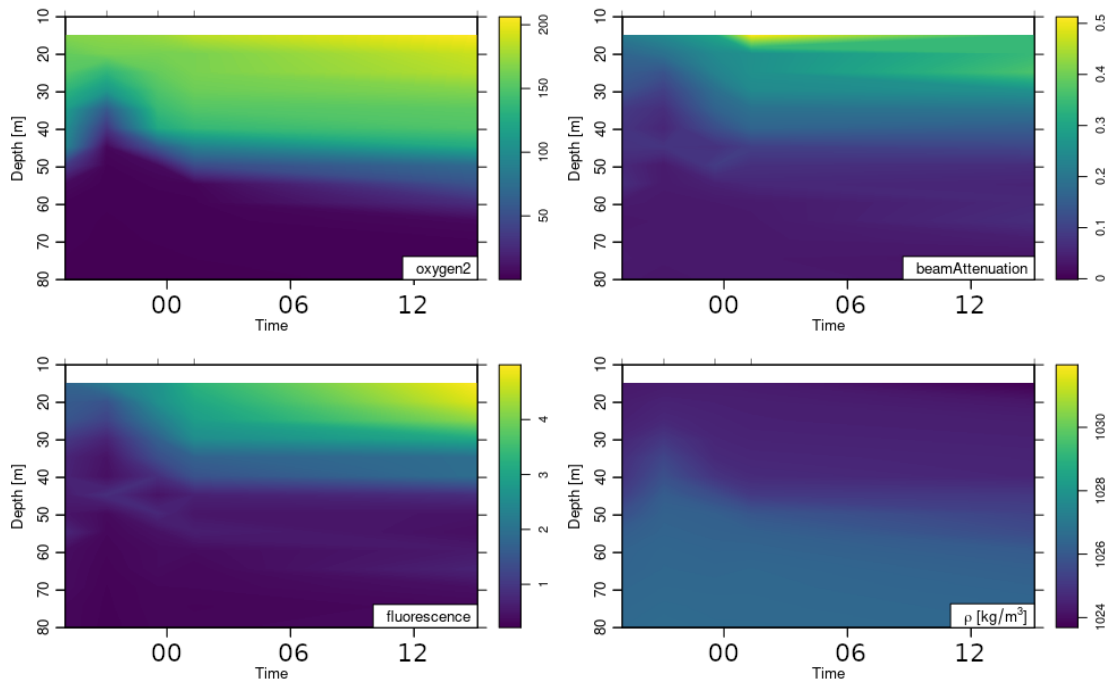
Cast #	UTC-0	Local Time UTC - 6
1	19 - 19:04	19 - 13:04
2	19 - 21:04	19 - 15:04
3	19 - 23:33	19 - 17:33
4	20 - 01:19	19 - 19:19
5	20 - 15:05	20 - 09:05



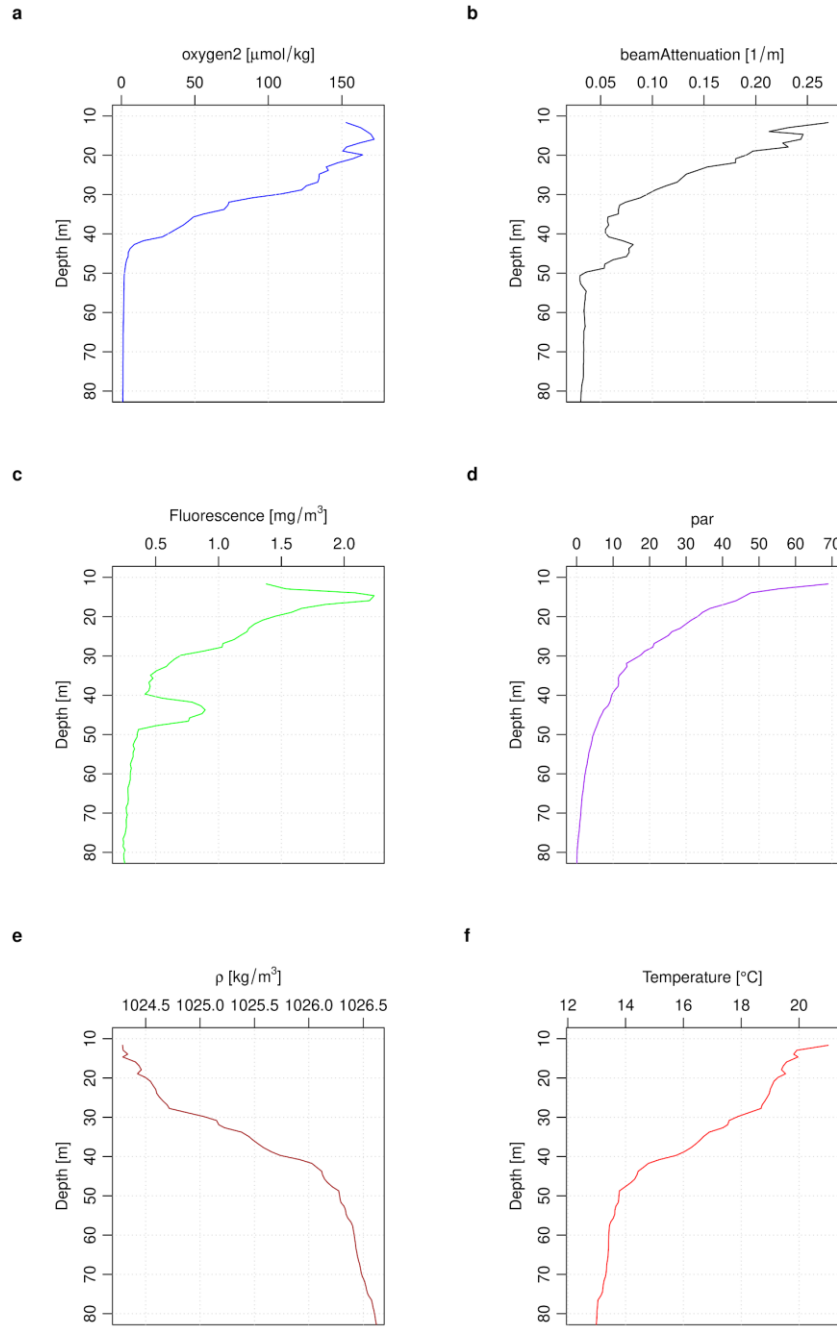
**Ch 2 - Figure 3:** Station 3.5 surface ADCP. Ocean current profiles from shipboard ADCP surface sensor over station 3.5. Time window corresponds to vessel sampling at Station 3.5. Top panel is zonal velocity,  $u$ , ( $\text{m s}^{-1}$ ). Bottom panel is meridional,  $v$ , “ ”. Red is positive (East, North). Blue is negative (West, South). Times in decimal yr-day (169.80 ~ 2018-06-19 19:13 UTC-0). Green overlay/right axis is ship velocity ( $\text{m s}^{-1}$ ). Left axis is depth to 150m. Panels are velocity components from the 300 kHz sensor.



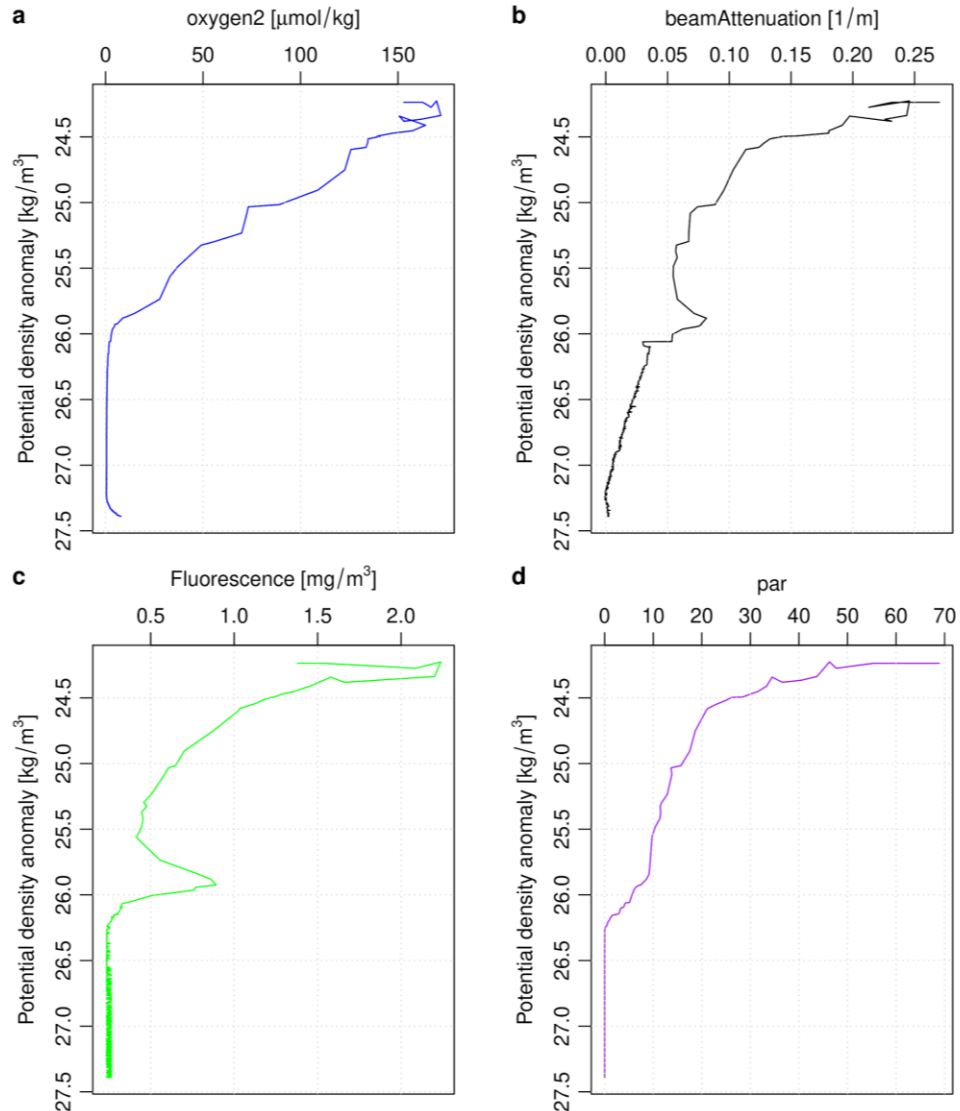
**Ch 2 - Figure 4:** Station 3.5 deep. Ocean current profiles from shipboard ADCP sensor over station 3.5. Time window corresponds to vessel sampling at Station 3.5. Top panel is zonal velocity,  $u$ , ( $\text{m s}^{-1}$ ). Middle panel is meridional,  $v$ , “ ”. Bottom panel is vertical velocity,  $w$ , ( $\text{mm s}^{-1}$ ). Gray indicates no data, or data removed due to ship movement induced noise. Red is positive (East, North, Up). Blue is negative (West, South, Down). Times in decimal yr-day (169.80 ~ 2018-06-19 19:13 UTC-0). Left axis is depth to 1000m. Panels are velocity components from the 75 kHz near-band sensor.



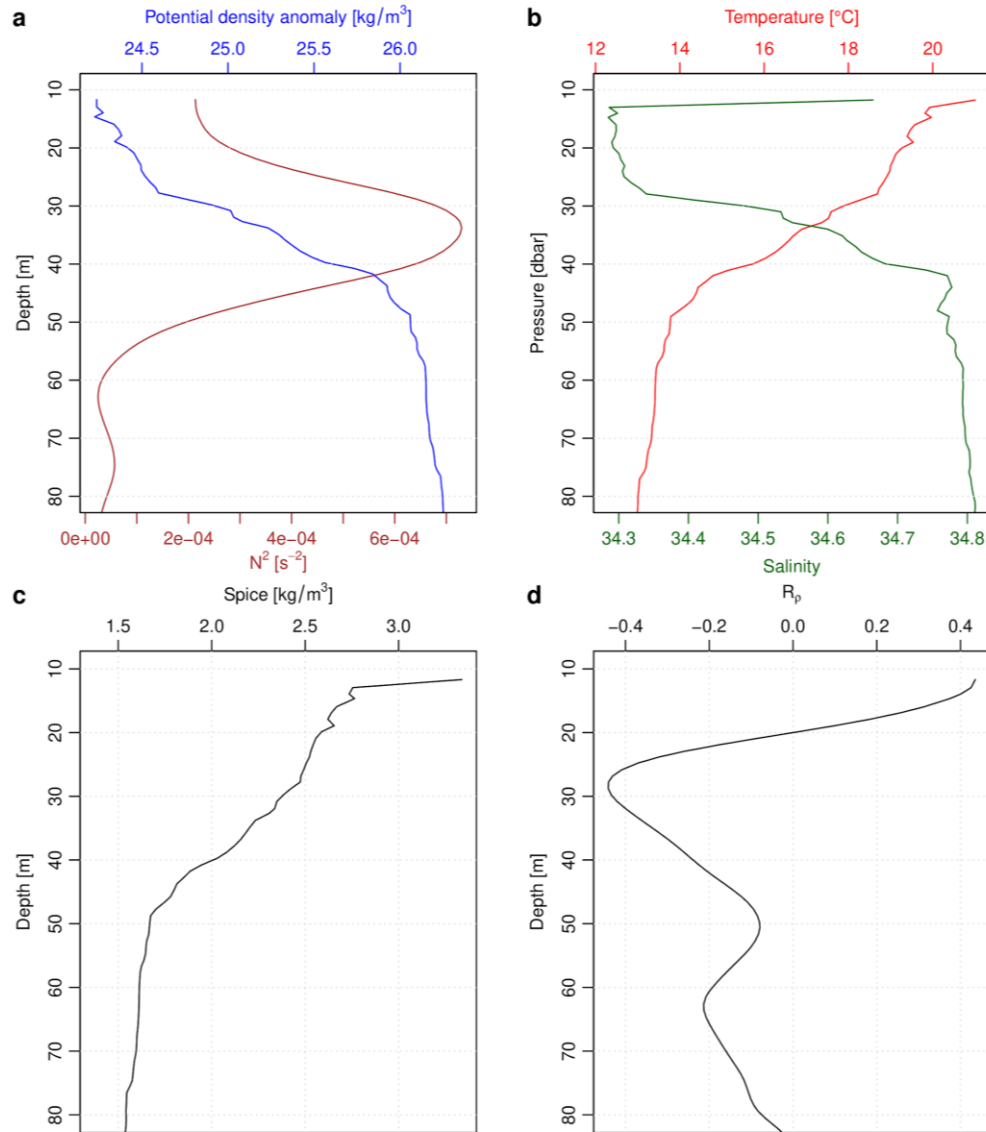
**Ch 2 - Figure 5:** Station 3.5 CTD sections. Time is listed as hrs in UTC-0 in panels on x-axis, for 06-20. Sections are interpolated between CTD casts as indicated by dashed lines at top of each panel. Four panels clockwise from top left are, oxygen [ $\mu\text{mol/kg}$ ], beam attenuation [ $1/\text{m}$ ], fluorescence [ $\text{mg/m}^3$ ], and density as Sigma-t [ $\text{kg/m}^3$ ]. Variables on right y-axis, depth to 80m on left y-axis.



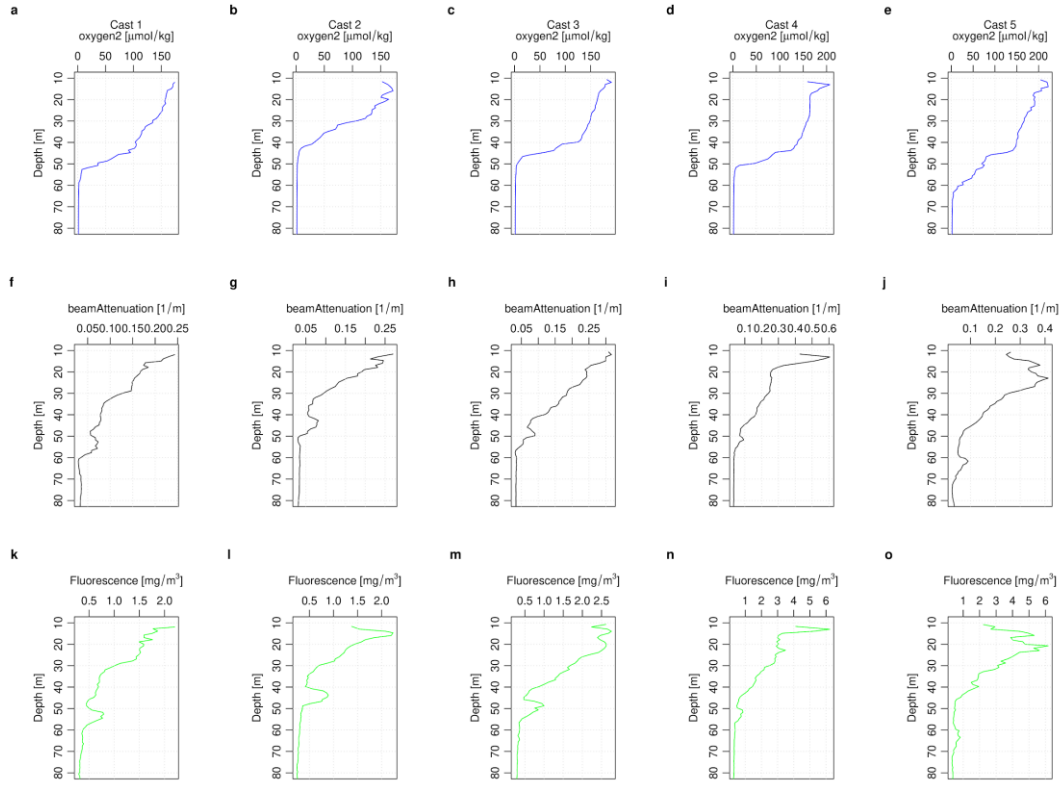
**Ch 2 - Figure 6:** Station 3.5 CTD profiles for the second cast, 19 - 21:04 UTC-0. (a) oxygen [ $\mu\text{mol/kg}$ ], (b) beam attenuation [1/m], (c) fluorescence [ $\text{mg/m}^3$ ], (d) percentage of photosynthetically active radiation [%] (e) density as Sigma-theta [ $\text{kg/m}^3$ ], and (f) temperature in Celsius. The y-axis is increasing depth in meters.



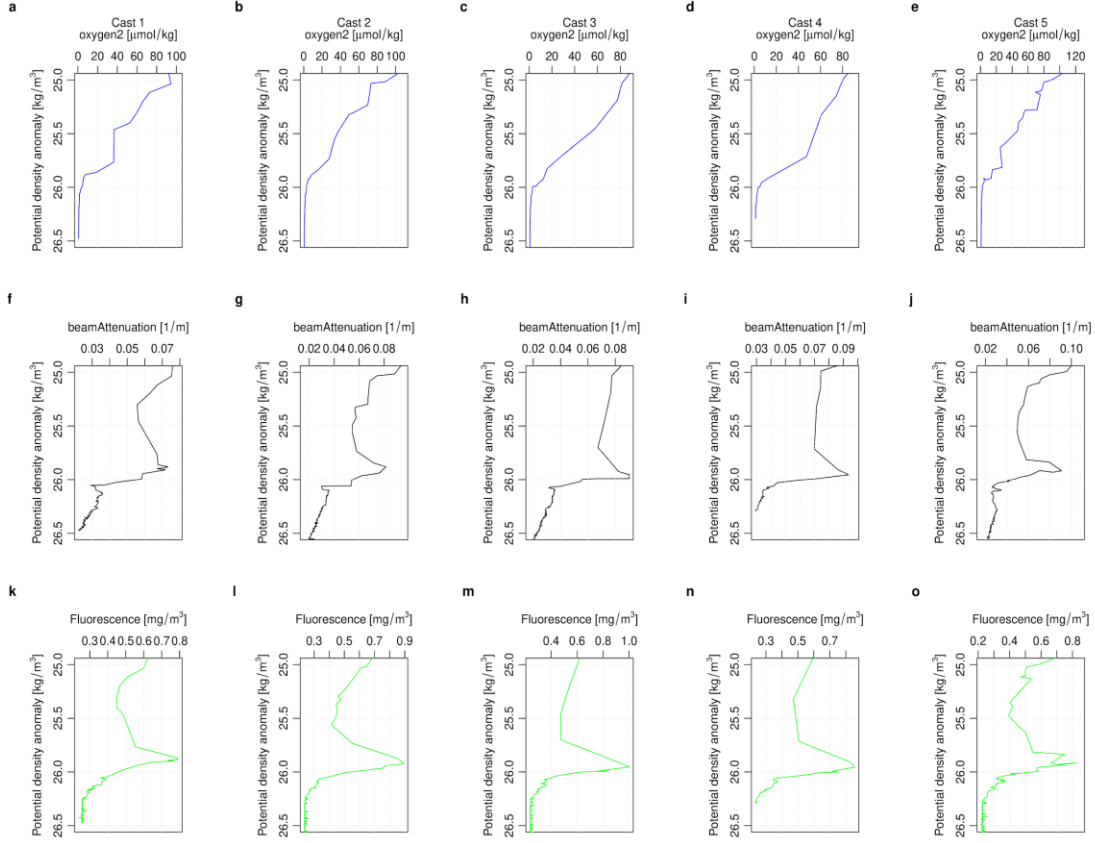
**Ch 2 - Figure 7:** Station 3.5 CTD profiles for the second cast, 19 - 21:04 UTC-0, by isopycnal surfaces. (a) oxygen [ $\mu\text{mol/kg}$ ], (b) beam attenuation [1/m], (c) fluorescence [ $\text{mg/m}^3$ ], and (d) percentage of available photosynthetically active radiation in purple [ % ]. y-axis being Sigma-0 , potential density anomaly [ $\text{kg/m}^3$ ], as opposed to depth.



**Ch 2 - Figure 8:** Station 3.5 descriptive oceanographic CTD profiles for the second cast, 19 - 21:04 UTC-0. (a) potential density anomaly Sigma-0 [ $\text{kg}/\text{m}^3$ ] top x-axis in blue, with the square of the buoyancy frequency in brown [ $\text{N}^2[\text{s}^{-2}]$ ], bottom x-axis. (b) Temperature in Celsius in red top x-axis, Salinity in PSUs in green bottom x-axis. (c) Spice, ratio of (warm + salty)/(cold+fresh) of water mass [ $\text{kg}/\text{m}^3$ ]. (d)  $R_\rho$  = change in  $f'$  of salinity/temperature over depth as described in methods. Diffusivity implementation.



**Ch 2 - Figure 9:** Station 3.5 CTD profiles by depth. Each column is an individual cast plotted in sequential order corresponding to Table 1 (e.g., cast 1 {a,f,k}). (a-e) oxygen [ $\mu\text{mol/kg}$ ], (f-j) beam attenuation [1/m], (k-o) fluorescence [ $\text{mg/m}^3$ ]. The y-axis is increasing depth in meters.



**Ch 2 - Figure 10:** Station 3.5 CTD profiles by isopycnal surfaces. Each column is a unique cast plotted in sequential order corresponding to Table 1 (e.g., cast 1 {a,f,k}). (a-e) oxygen [ $\mu\text{mol}/\text{kg}$ ], (f-j) beam attenuation [ $1/\text{m}$ ], (k-o) fluorescence [ $\text{mg}/\text{m}^3$ ]. y-axis being  $\Sigma_0$ , potential density anomaly [ $\text{kg}/\text{m}^3$ ], as opposed to depth.

#### Station 4

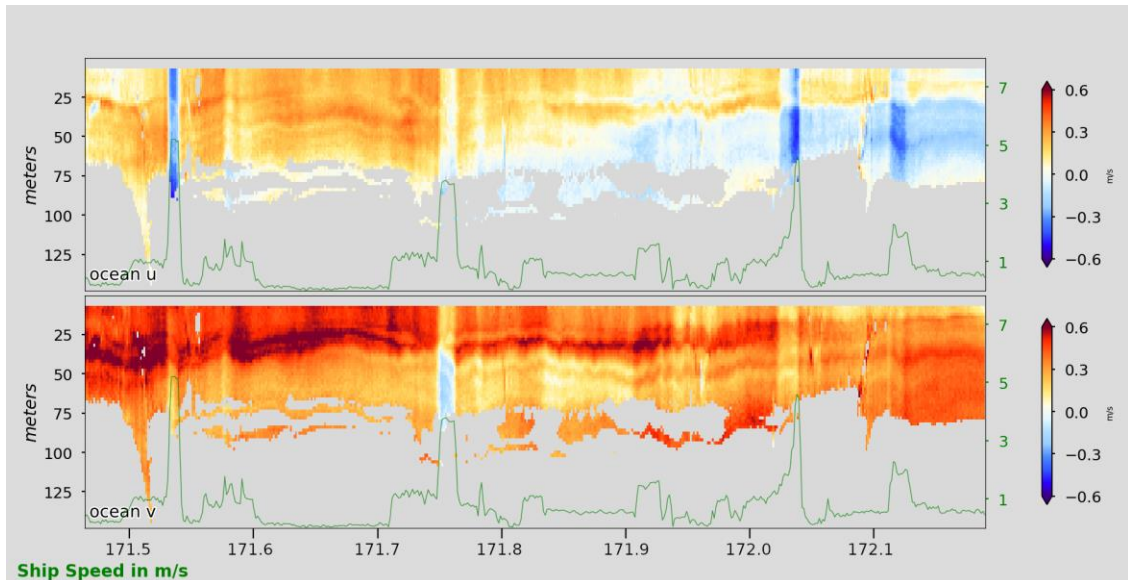
Like station 3.5, Station 4's deep ADCP profiles indicate the primary upwelling to downwelling harmonic of the NIW (Fig. 12). Surface horizontal vectors show an oscillation in the meridional direction, starting in the easterly direction for casts 1-3, a switch at cast four and becoming westerly for casts five and six (Fig. 11, Table 2). However, the zonal component maintains a North flow for all casts, in both the surface and the deep ADCP data (Figs. 11 & 12). In the surface flow, peak velocities seem to be concentrated at a depth between 25-50m, at or around 30m. This corresponds to a dynamic but not ephemeral mixing in the upper water column (Fig. 15).

Several interesting features include multiple buoyancy and density layers, with oscillating salt and temperature patterns (Fig. 15 sub plots 3 & 4 in panel a & b) likely contributing to a surface layer that is not homogeneously mixed but rather more chaotic than the upper ocean above station 3.5. Indeed, the pycnocline is much more defined in Station 3.5 versus Station 4. Additionally, while both Station 3.5 and 4 show similar Spice profiles, Station 4 is comparatively spicier (warmer & salty).

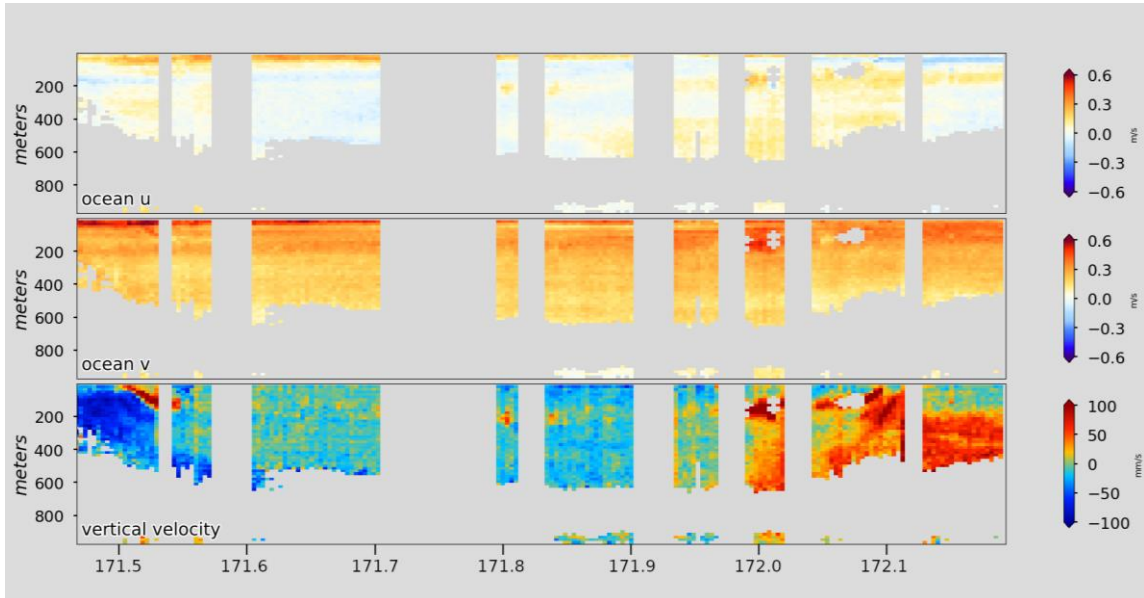
The primary difference between station 3.5 and 4 is a lack of a DCM feature in Station 4, despite a shoaled OMZ and large net integrated fluorescence in the upper ocean. Despite strong oscillations in depth between casts, the OMZ, beam attenuation and fluorescence track each other well; in tandem with fluctuations in upper ocean mixing (Figs. 13, 14 & 15). As indicated in Chapter One, Station's 4 OMZ and chlorophyll feature is shoaled as compared to reference data (CH 1 Sup. Fig. 4).

**Ch 2 - Table 2:** Station 4 CTD individual cast times. UTC-0, and with local time for diurnal context.

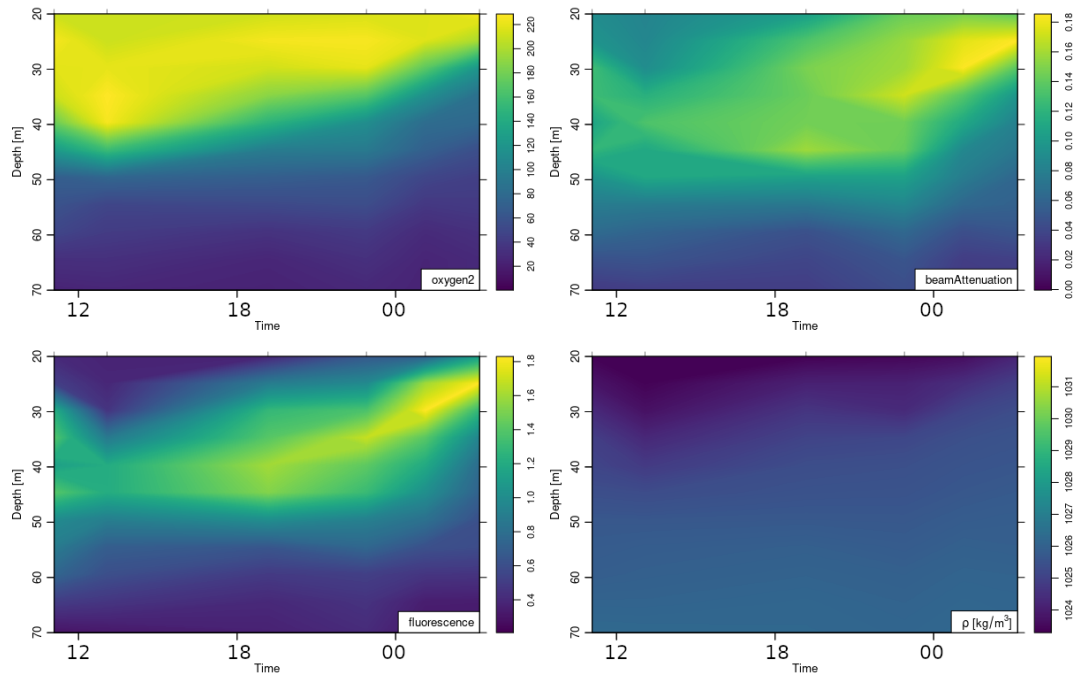
Cast #	UTC-0	Local Time UTC - 6
1	21 - 11:06	21 - 05:06
2	21 - 13:06	12 - 07:06
3	21 - 19:11	21 - 13:11
4	21 - 22:54	21 - 16:54
5	22 - 01:06	21 - 07:06
6	22 - 03:12	21 - 21:12



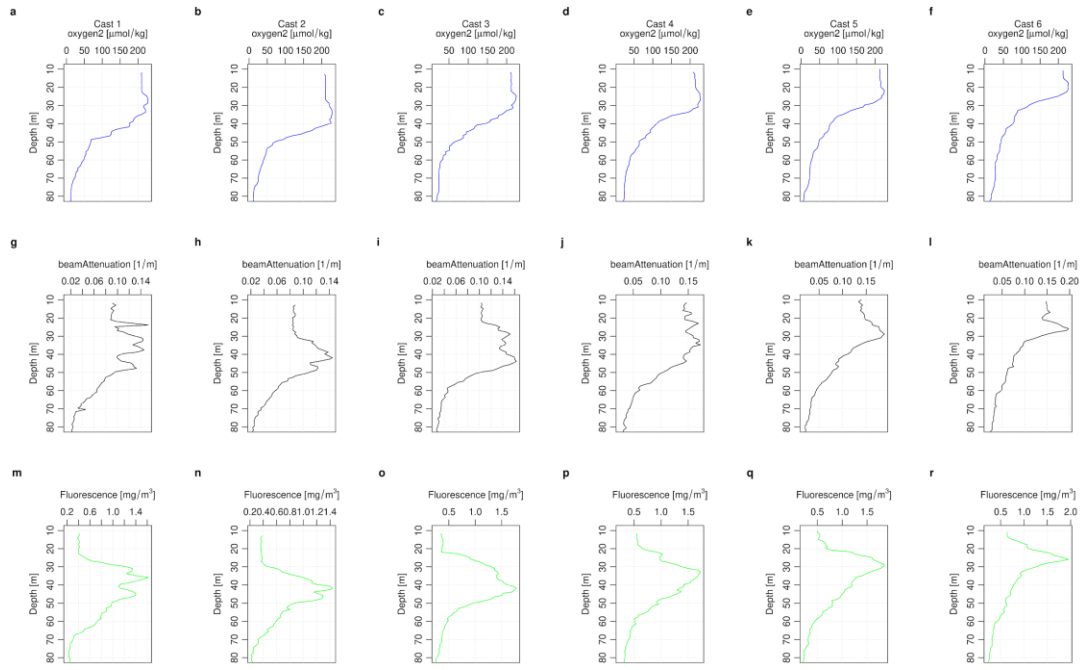
**Ch 2 - Figure 11:** Station 4 surface ADCP. Ocean current profiles from shipboard ADCP surface sensor over station 4. Time window corresponds to vessel sampling at Station 4. Top panel is zonal velocity,  $u$ , ( $m s^{-1}$ ). Bottom panel is meridional,  $v$ , “ ”. Red is positive (East, North). Blue is negative (West, South). Times in decimal yr-day (171.5 ~ 2018-06-21 11:59 UTC-0). Green overlay/right axis is ship velocity ( $m s^{-1}$ ). Left axis is depth to 150m. Panels are velocity components from the 300 kHz sensor.



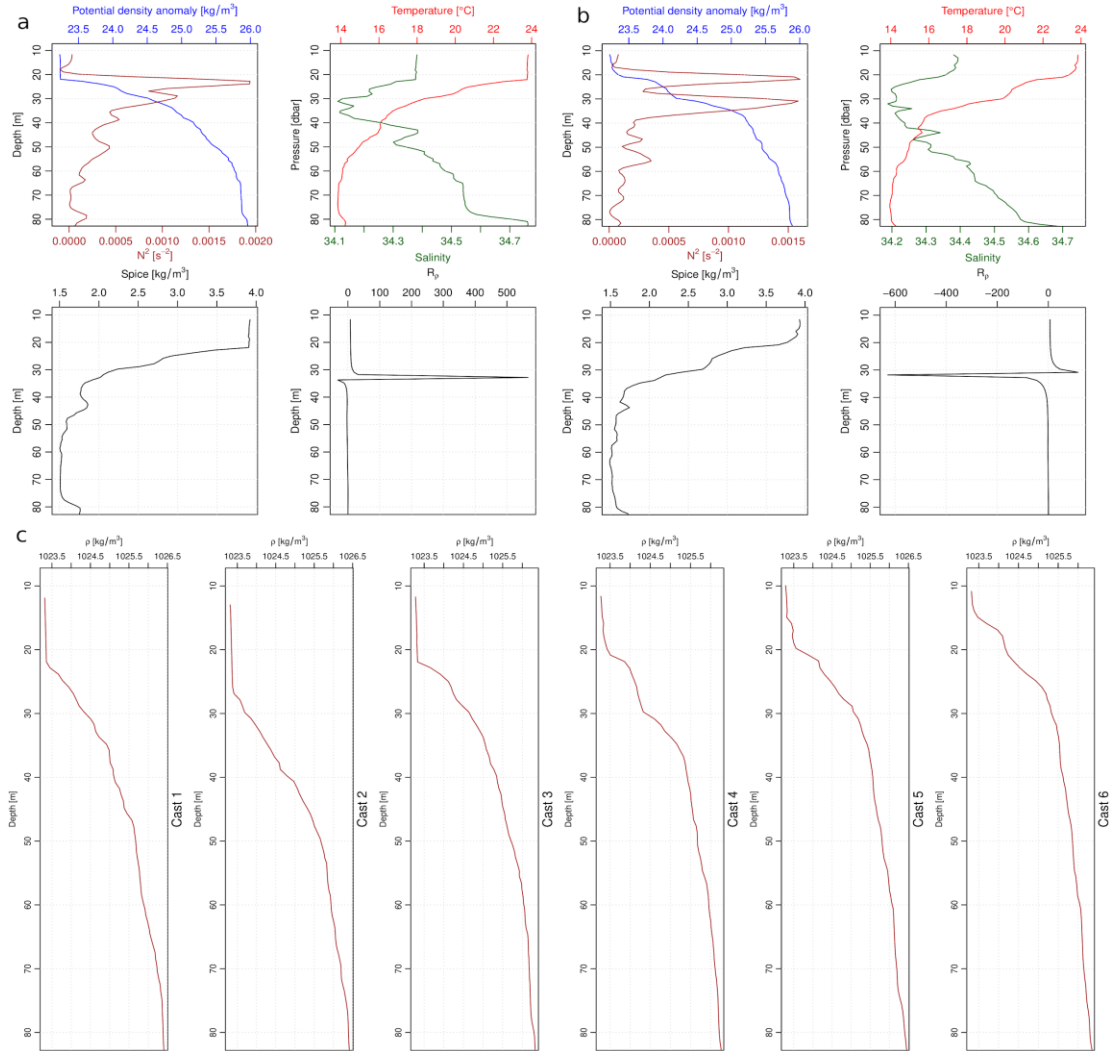
**Ch 2 - Figure 12:** Station 4 deep. Ocean current profiles from shipboard ADCP sensor over Station 4. Time window corresponds to vessel sampling at Station 4. Top panel zonal velocity, *u*, (m s<sup>-1</sup>). Middle panel is meridional, *v*, “ ”. Bottom panel is vertical velocity, *w*, (mm s<sup>-1</sup>). Gray indicates no data, or data removed due to ship movement induced noise. Red is positive (East, North, Up). Blue is negative (West, South, Down). Times in decimal yr-day (171.5 ~ 2018-06-21 11:59 UTC-0). Left axis is depth to 1000m. Panels are velocity components from the 75 kHz near-band sensor.



**Ch 2 - Figure 13:** Station 4 CTD sections. Time is listed as hrs in UTC-0 in panels, for 06-21/22. Sections are interpolated between CTD casts as indicated by dashed lines at top of each panel. Four panels clockwise from top left are, oxygen [ $\mu\text{mol/kg}$ ], beam attenuation [1/m], fluorescence [ $\text{mg/m}^3$ ], and density as Sigma-t [ $\text{kg/m}^3$ ]. Variables on right y-axis, depth to 70m on left y-axis.



**Ch 2 - Figure 14:** Station 4 CTD profiles by depth. Each column is an individual cast plotted in sequential order corresponding to Table 2 (e.g., cast 1 {a,g,m}). (a-f) oxygen [ $\mu\text{mol/kg}$ ], (g-l) beam attenuation [ $1/\text{m}$ ], (m-r) fluorescence [ $\text{mg}/\text{m}^3$ ]. The y-axis is increasing depth in meters.



**Ch 2 - Figure 15:** Station 4 oceanographic plots, (a) four subplots for cast 3, clockwise from top left: {1} potential density anomaly Sigma-0 [ $\text{kg}/\text{m}^3$ ] top x-axis in blue, with the square of the buoyancy frequency in brown [ $\text{N}^2[\text{s}^{-2}]$ ], bottom x-axis. {2} Temperature in Celsius in red top x-axis, Salinity in PSUs in green bottom x-axis. {3} Spice, ratio of (warm + salty)/(cold+fresh) of water mass [ $\text{kg}/\text{m}^3$ ]. {4} Rrho = change in  $f^\circ$  of salinity/temperature over depth as described in methods. Salt finger implementation. (b) same sub plots for cast 4. (c) is casts: 1-6 of density as Sigma-theta [ $\text{kg}/\text{m}^3$ ].

### Station 3

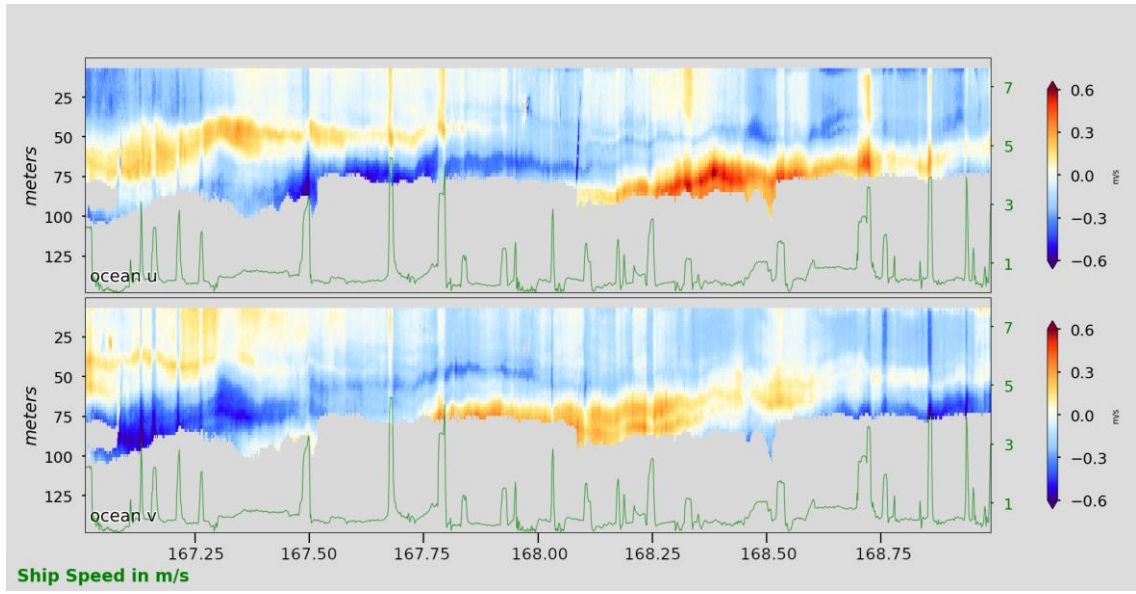
Station 3 was over 300 km from the overpass of the storm, on the left and weaker side of the storm. It was sampled prior to station 3.5 and 4. ADCP plots are again indicative of NIWs, but surface horizontal velocities are weaker and thinner (Figs. 16 & 17). Net weaker vertical velocities ( $0.3 \text{ ms}^{-1}$ ) at this latitude correspond with an observed period of 24 hrs. Station 3 had double the total casts as either station 3.5, or 4, yet casts were not equally spaced in time (Table 3). Figure 18 indicates a stable dual fluorescence feature that shows muted oscillation. Figure 19 indicates a weaker density stratification

with the primary fluorescence feature at ~ 75m, and a SCM at 125, much below the OMZ. The casts shown are 24, and 22 hours apart respectively.

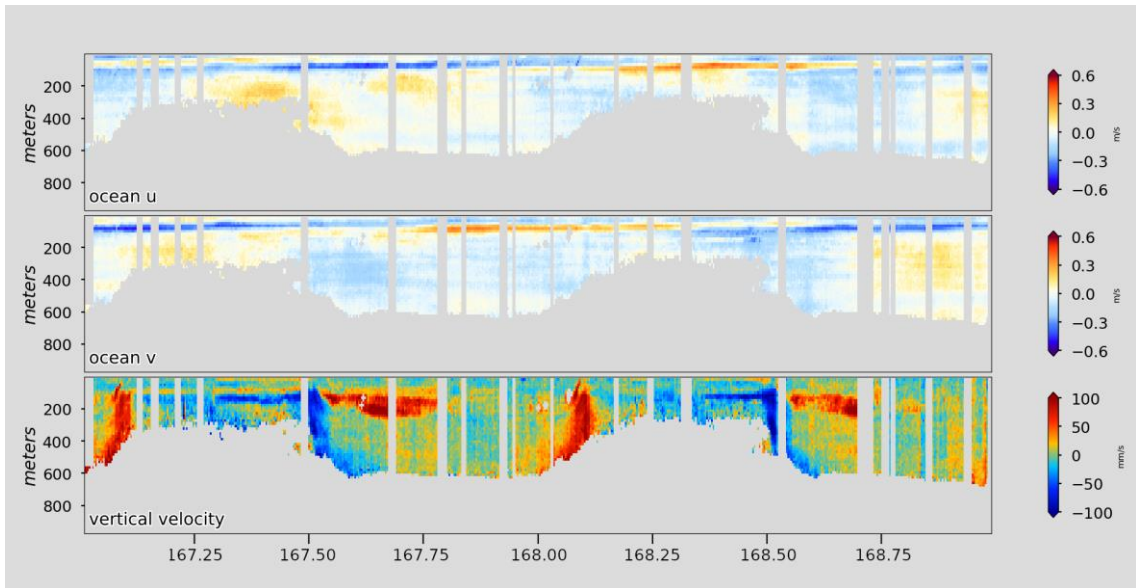
PAR values for the two casts closest to solar noon indicated the top of the SCM were ca. 0.4% of available surface radiation. These values are what would be expected in a non disturbed OMZ<sup>29</sup>. Like station 3.5, The 26 [kg/m<sup>3</sup>] isopycnal surface appears to be at the base of the pycnocline for Station 3 (Fig. 19j:l). When comparing the SCM indicators, beam attenuation and fluorescence to appear to be related to the same isopycnal surface, the SCM appears to be below it, and again below the OMZ boundary, instead of occurring at it (Fig. 20). Very much opposite of Station 3.5. Figure 21 shows the oceanographic descriptive plot for the 6th cast, which has the highest spice values for all three stations. Note the heterogeneous mixed layer, which varied between all casts, but is representative of Station 3 (plots not shown).

**Ch 2 - Table 3:** Station 3.5 CTD individual cast times. UTC-0, and with local time for diurnal context

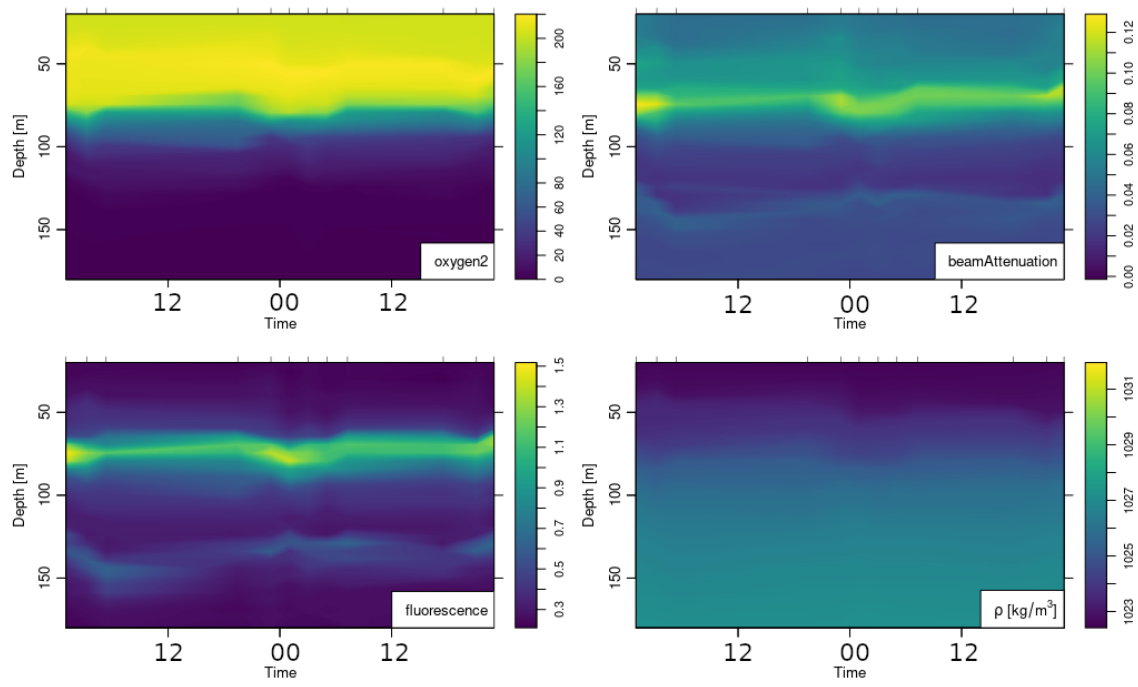
Cast #	UTC-0	Local Time UTC - 6
1	17 - 01:03	16 - 19:03
2	17 - 03:17	16 - 21:17
3	17 - 05:22	16 - 23:22
4	17 - 19:29	17 - 13:29
5	17 - 23:03	17 - 17:03
6	18 - 01:01	17 - 19:01
7	18 - 03:02	17 - 21:03
8	18 - 05:03	17 - 23:04
9	18 - 07:17	18 - 01:17
10	18 - 17:34	18 - 11:34
11	18 - 21:07	18 - 15:07
12	18 - 23:01	18 - 17:01



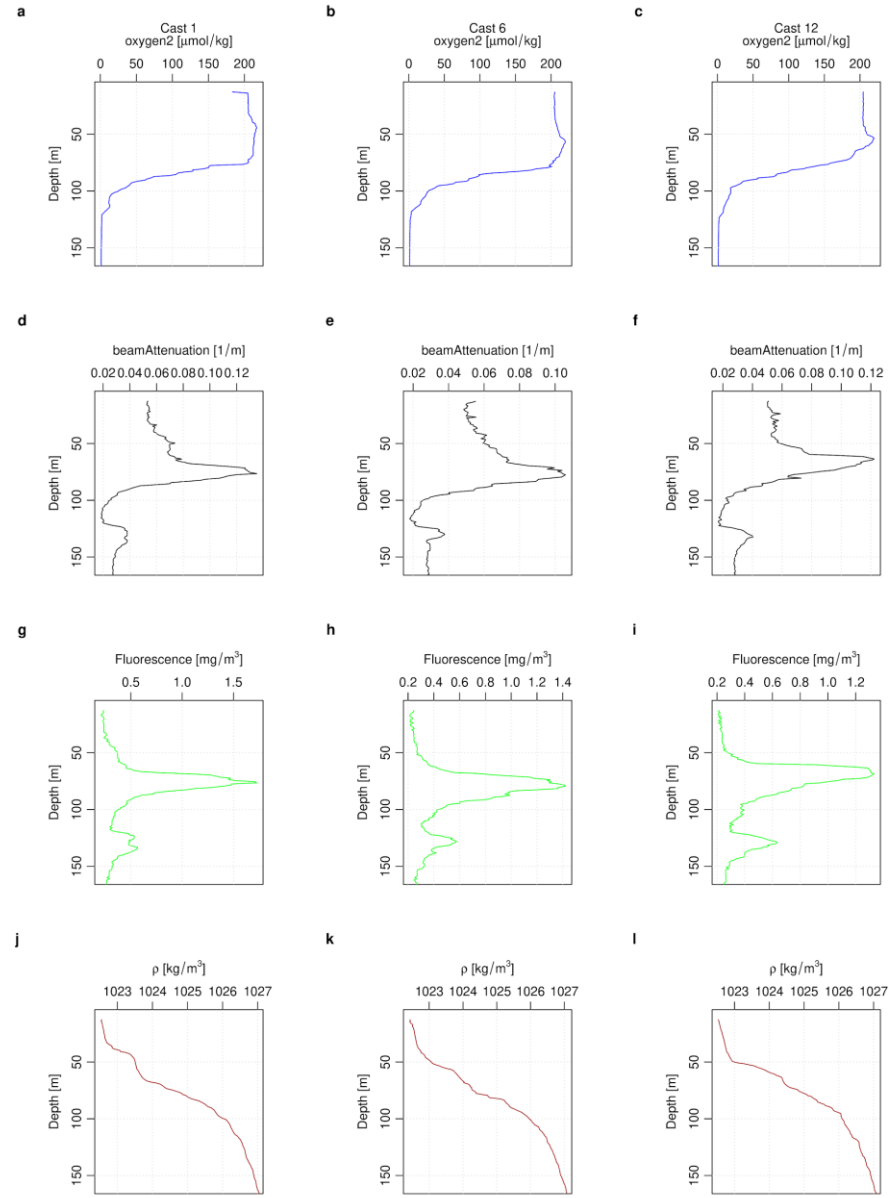
**Ch 2 - Figure 16:** Station 3 surface ADCP. Ocean current profiles from shipboard ADCP surface sensor over station 3. Time window corresponds to vessel sampling at Station 3. Top panel is zonal velocity,  $u$ , ( $\text{m s}^{-1}$ ). Bottom panel is meridional,  $v$ , “ ”. Red is positive (East, North). Blue is negative (West, South). Times in decimal yr-day (167.25 ~ 2018-06-17 06:02 UTC-0). Green overlay/right axis is ship speed ( $\text{m s}^{-1}$ ). Left axis is depth to 150m. Panels are velocity components from the 300 kHz sensor.



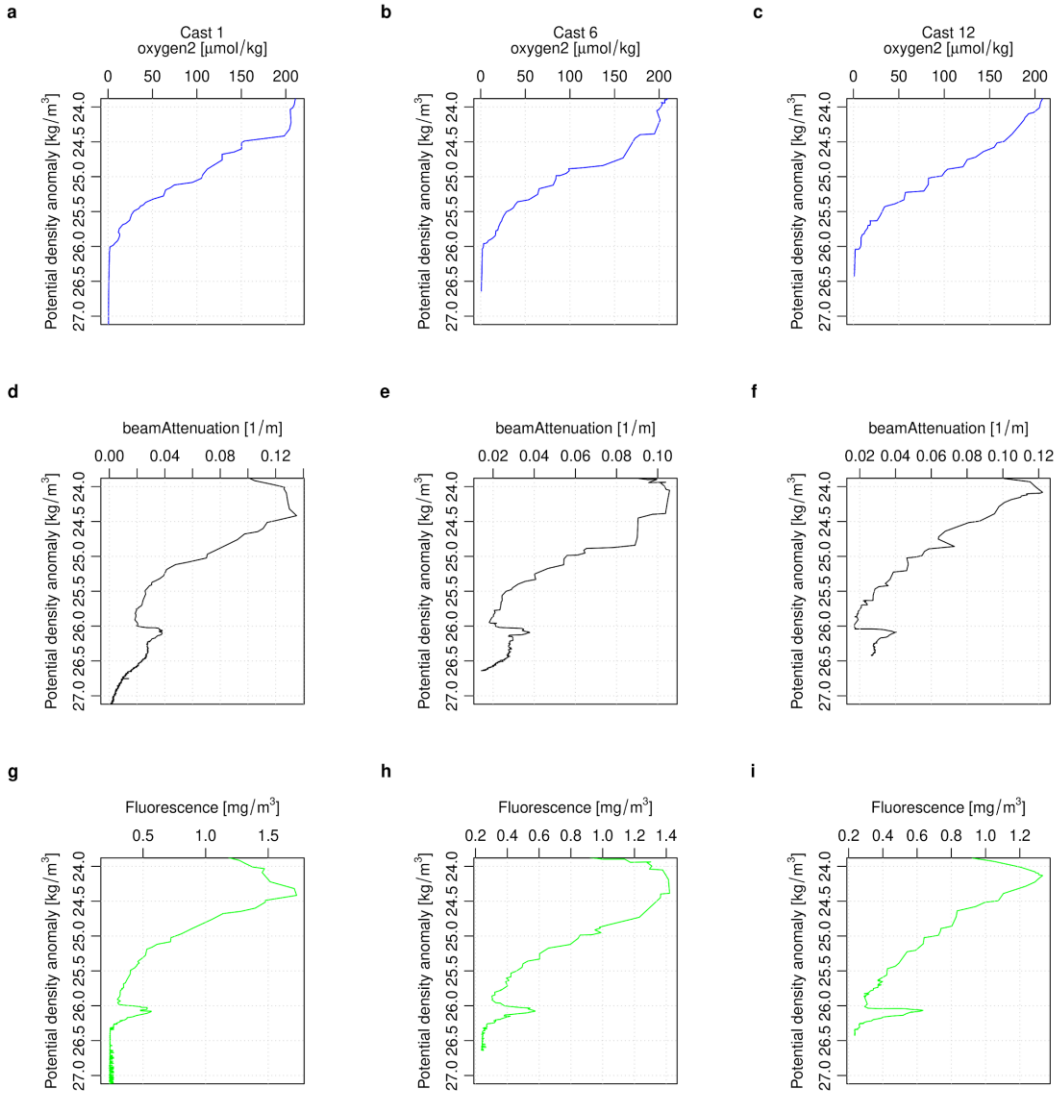
**Ch 2 - Figure 17:** Station 3 deep. Ocean current profiles from shipboard ADCP sensor over Station 3. Time window corresponds to vessel sampling at Station 3. Top panel zonal velocity,  $u$ , ( $\text{m s}^{-1}$ ). Middle panel is meridional,  $v$ , “ ”. Bottom panel is vertical velocity,  $w$ , ( $\text{mm s}^{-1}$ ). Gray indicates no data, or data removed due to ship movement induced noise. Red is positive (East, North, Up). Blue is negative (West, South, Down). Times in decimal yr-day (167.25 ~ 2018-06-17 06:02 UTC). Left axis is depth to 1000m. Panels are velocity components from the 75 kHz near-band sensor.



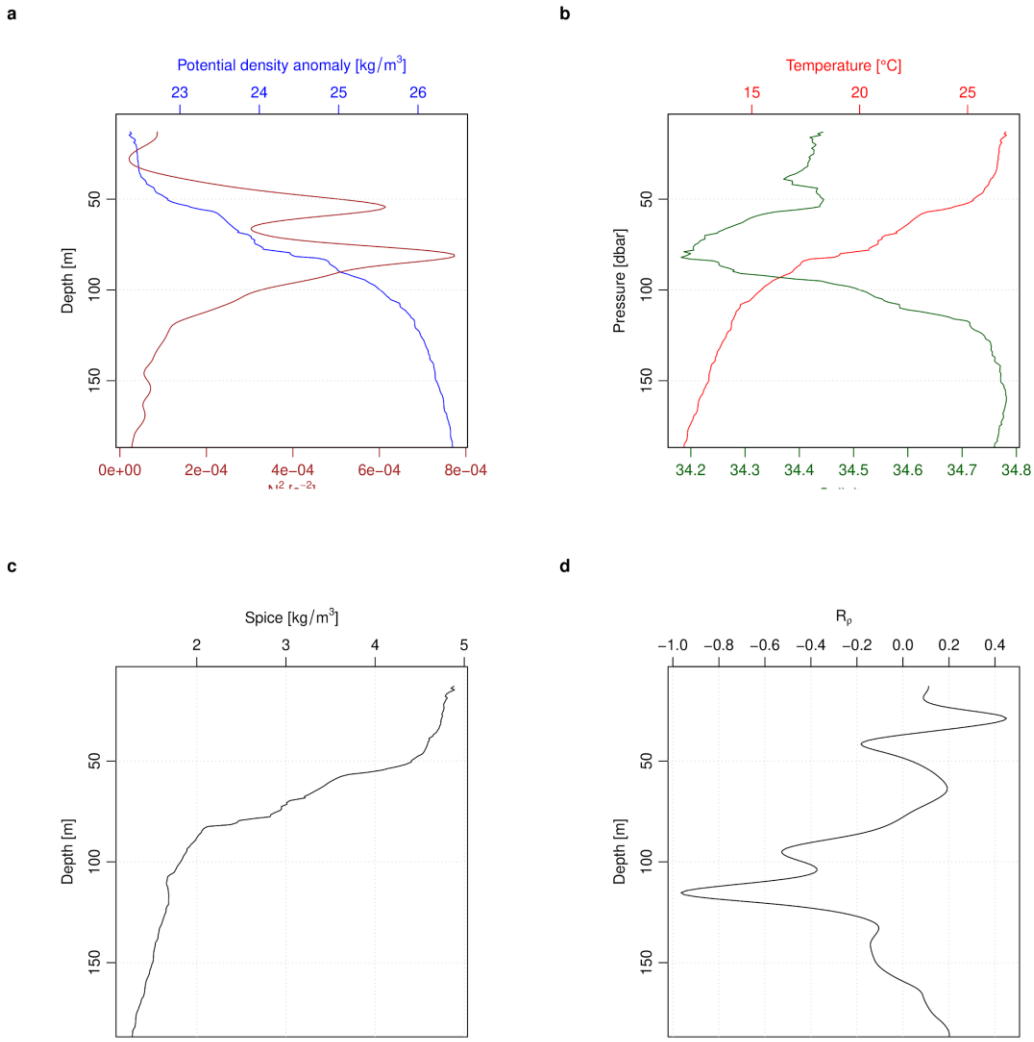
**Ch 2 - Figure 18:** Station 3 CTD sections. Time is listed as hrs in UTC-0 in panels, for 06-17/18. Sections are interpolated between CTD casts as indicated by dashed lines at top of each panel. Four panels clockwise from top left are, oxygen [ $\mu\text{mol}/\text{kg}$ ], beam attenuation [ $1/\text{m}$ ], fluorescence [ $\text{mg}/\text{m}^3$ ], and density as Sigma-t [ $\text{kg}/\text{m}^3$ ]. Variables on right y-axis, depth to 175m on left y-axis.



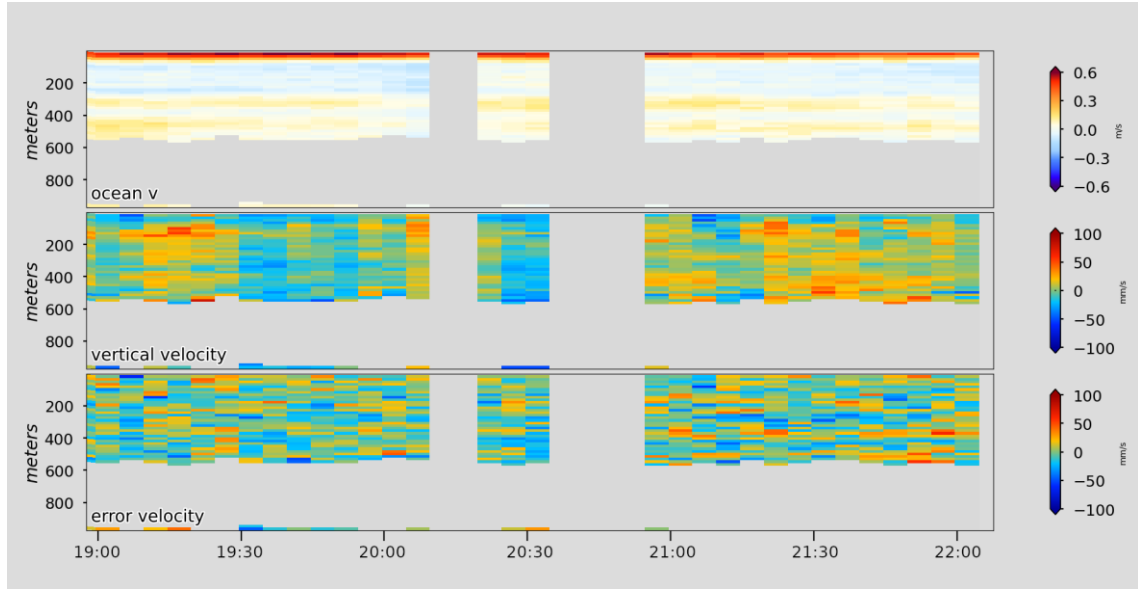
**Ch 2 - Figure 19:** Station 3. CTD profiles by depth. Each column is an individual cast plotted in sequential order corresponding to Table 2, casts were chosen to be  $\sim 24$  hours apart. (e.g., cast 1 {a,d,g,j}). (a-c) oxygen [ $\mu\text{mol}/\text{kg}$ ], (d-f) beam attenuation [1/m], (g-i) fluorescence [ $\text{mg}/\text{m}^3$ ], and (j-l) density as Sigma-theta [ $\text{kg}/\text{m}^3$ ]. The y-axis is increasing depth in meters.



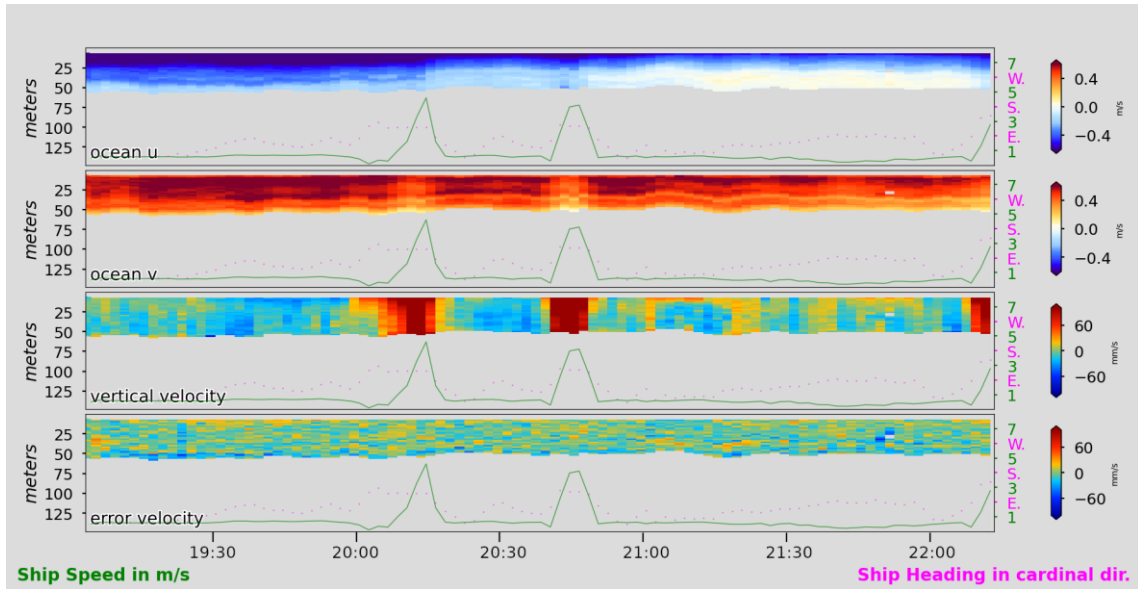
**Ch 2 - Figure 20:** Station 3 CTD profiles by isopycnal surfaces. Each column is a unique cast plotted in sequential order corresponding to Table 2. Casts were chosen to be ~ 24 hours apart. (e.g., cast 1 {a,d,g}). (d-f) beam attenuation [ $1/\text{m}$ ], (g-i) fluorescence [ $\text{mg/m}^3$ ]. y-axis being Sigma-0 , potential density anomaly [ $\text{kg/m}^3$ ], as opposed to depth.



**Ch 2 - Figure 21:** Station 3 descriptive oceanographic CTD profiles for the sixth cast, 18 - 01:01 UTC-0. (a) potential density Sigma-0 [ $\text{kg/m}^3$ ] top x-axis in blue, with the square of the buoyancy frequency in brown [ $\text{N}^2[\text{s}^{-2}]$ ], bottom x-axis. (b) Temperature in Celsius in the red top x-axis, Salinity in PSUs in green bottom x-axis. (c) Spice, ratio of (warm + salty)/ (cold+fresh) of water mass [ $\text{kg/m}^3$ ]. (d) Rrho = change in f' of salinity/temperature over depth as described in methods. Diffusivity implementation.



**Ch 2 - Figure 22:** ADCP station 3.5 deep, casts 1 & 2. Ocean current profiles from shipboard ADCP sensor over station 3.5. Time window corresponds to CTD casts 1 and 2 (Table 1). Top panel is meridional velocity,  $v$ , ( $\text{m s}^{-1}$ ). Middle panel is vertical velocity,  $w$ , ( $\text{mm s}^{-1}$ ). Bottom panel is error velocity in the vertical velocity panel. Gray indicates no data, or data removed due to ship movement induced noise. Red is positive (North, Up). Blue is negative (South, Down). Times in UTC-0 for 06-19. Left axis is depth to 1000m. Panels are velocity components from the 75 kHz near-band sensor.



**Ch 2 - Figure 23:** ADCP station 3.5 shallow, casts 1 & 2. Ocean current profiles from shipboard ADCP surface sensor over station 3.5. Time window corresponds to CTD casts 1 and 2 (Table 1). First panel is zonal velocity,  $u$ , ( $\text{m s}^{-1}$ ). Second panel is meridional,  $v$ , “”. Third panel is vertical velocity,  $w$ , ( $\text{mm s}^{-1}$ ) a depth in meters. Gray indicates no data, or data removed due to ship movement induced noise. Bottom panel is error velocity in the vertical velocity panel. Gray indicates no data, or data removed due to ship movement induced noise. Red is positive (East, North, Up). Blue is negative (West, South, Down). Times in UTC-0 for 06-19. Green overlay/right axis is ship velocity. Pink dots/right axis is ship heading in cardinal direction. Left axis is depth to 1000m. Panels are velocity components from the 300 kHz sensor.

## Discussion

Simultaneous inclusive *in situ* measurements of multiple state variables are required to understand the impacts of tropical cyclone overpasses on subsurface biological processes. This study collected physical and biological subsurface water properties across three stations, and at high temporal frequency at each station, following a strong hurricane. Collectively, the methods used captured the expected range of the spatial-temporal heterogeneity in upper ocean profiles and the persistent signal of TC-induced near-inertial waves, which caused a subsurface undulation of the pycnocline across all stations. Differences between subsurface profiles at Stations 3.5 and Station 4 indicate organic matter may be rapidly consumed at the mixed layer, or material may be exported out of it, at each station, respectively; having important repercussions on how to view TC's effects on the transportation of organic matter to the deep ocean. The results, when taken together, provide context for the biogeochemical anomalies at Station 3.5 — the high concentration of biomass associated with unexpected subsurface chlorophyll features and strongly associated with the vertical moving density interface; suggest a general oceanographic and ecological conceptual model that may be scalable to the subsurface biology response to physical mixing in all TC ocean zones. While unique concerning tropical cyclones, this model is congruent with the community's understanding of how physical oceanographic processes and structure dictate the concentration of biota in the ocean. The rapid biological response to this disturbance event suggests that ETNP OMZ microbial life may be adapted to these extreme conditions. Laboratory experiments and modeling of physical processes would be one possible avenue to explore these concepts.

The heterogeneity in the upper ocean profiles of both Station 3 and 4 may be due to their relation to the storm track and potential wind induced energy. That is, they were not exposed to enough energy to be thoroughly mixed. However, the observed salinity profiles dilute this simple explanation. Hurricanes produce high rainfall directly impacting the salinity (plus wind induced evaporation<sup>30</sup>) of the upper ocean. Temperature, given its 1<sup>st</sup> order dominance in the equation of state, and the net cold wake of tropical cyclones, is often the dominant variable of interest in many studies looking at the connection of TC induced mixing and biological response. This is especially true of the satellite TC literature. We build models based on what we measure. Increasingly the importance of salinity has been incorporated into an understanding of ocean mixing under TCs. Station 4 showed mixing at ca. 50 m, related in part to salinity profiles. This is in step with a study using a standard physical oceanographic model (HYCOM) and Argo profiles, which found mean depth of salinity induced mixing was close to 50 meters. This study was a global and multi-decadal analysis<sup>31</sup>. Salinity changes induced by TC's will impact the densities of surface water mass, and this plus wind mixing must be considered when determining net mixing and stratification.

While the oceanographic casts are congruent with the community's understanding of physical mixing, the anomalous second cast of biogeochemical variables for station 3.5 raises multiple interesting questions. All casts at Station 3.5 were anomalous in comparison to all other available data from this region, yet the second cast is remarkably different even from the other casts in the shallowness of multiple oceanographic features.

Was this a result of endogenous mixing due to the TC? Was it a soliton wave, passing through the density interface interacting constructively, yet generated exogenously beyond the reach of the TC? To introduce bounds to these interpretations, a more detailed review of NIW work is helpful. Both Zhang *et al.*<sup>7</sup> and Sanabia *et al.*<sup>8</sup> measure NIWs under TCs, and comparison of measured and modeled subsurface movements (Figs. 8 & 5 in refs.<sup>7,8</sup> respectively) is helpful. Models show the smoothed first harmonic undulation of the NIW along the pycnocline, while the actual measurements of spikes in the depth of the pycnocline indicate tertiary patterns may be due to endogenous constructive/destructive interference. Whatever the cause, this does appear to be a real observation. A static and stratified oligotrophic section of ocean in summer might exhibit the same profiles, to a greater depth, as a single cast under Station 3.5. However, multiple casts would change only through slight diurnal thermal fluctuations (similar to Station 3) and would not vary by such drastic depths over time scales of hours. That is with TC induced NIWs, and mixing, there is a surface bloom and undulating density interface under a TC, with an instantaneous stratification profile that mimics a non-disturbed ocean.

It is the DCM community ‘pinned’ to the top of this density undulation that is most interesting for the microbial ecology of OMZs. Typically, a low light deeper photoautotrophic community (DCM/SCM) is expected at the top of the OMZ boundary to be dominated by low light adapted *Prochlorococcus* ecotypes<sup>21,29,32–34</sup>, with possible presence of additionally associated groups (e.g., clades of *Synechococcus*<sup>33</sup>). Expected light levels of association are 0.1 to 2% of surface available radiation<sup>21</sup>, whereas here the maximum occurrence of the top DCM was observed at ca. 10% PAR over Station 3.5. This community also moved through a number of other important structuring variables. This community is expected to be below the thermocline and mixed layer at steady state<sup>33</sup>, not above it as observed here. The same goes for the oxycline, the boundary of the OMZ.

*Prochlorococcus* sp. are some of the smallest cellular biota in the ocean<sup>34</sup>. Their minute size gives them a very low Reynolds number indicating viscous forces are more important than inertial forces. They can be thought of as being embedded in water masses and have trouble moving across the extreme density interfaces and are often concentrated on layers of high buoyancy frequencies<sup>35</sup>, moving with the density layer rather than through it, creating what are called thin layers. Thin layers are analogous phenomena for what is observed here, with scales of cms rather than meters, and occurring at more ephemeral time scales in stratified surface waters with a well developed pycnocline. The underlying physical mechanisms are similar though. Thin layers can also form at locations of high vertical current shear. This shear is caused by a positive derivative of current velocities (magnitude or direction) in the vertical. Vertical velocity shear traps small particles from the top as a water mass ‘flattens out’, thereby redistributing the associated plankton<sup>36</sup>. This vertical velocity shear is a descriptive characteristic of NIWs as the vertical currents in the mixed layer are zero at the pycnocline increasing in magnitude as they rise above. They oscillate in magnitude and duration throughout the lifetime of the NIW. That is, when there are TC-induced NIWs, by definition there will be vertical velocity shear and strong density stratification.

Using the dearth of observations in Chapters 1 & 2 and the literature as a guide, the following is a possible oceanographic and ecological model for what did happen at Station 3.5 and could happen under TC's, of sufficient strength, in this region of the ETNP OMZ:

(1) Entrainment breaks stratification. (2) Upwelling transports OMZ organisms and nutrients into the mixed layer, with horizontal transport probably a significant factor at the boundary of the Hurricane alley region (pelagic/coastal transition). (3) Inertial oscillations and relaxation of winds creates a new mixed layer with a strong stratification, with the DCM/SCM and OMZ boundary microbial community now above the density stratification. (4) Stratification traps the community and fresh organic matter from the bottom. (5) Vertical velocity shear then ‘caps’ particles and microbes to this layer, despite fluctuations of the density interface. (6) The microbial community then would fluctuate with the NIW in and out of different depths and biochemical regimes (with a periodicity out of phase, but similar in magnitude to diurnal frequencies) for multiple generations (generation times can be less than a day for these microbes), which could then be impacted by sequential TC's through the season (as the lagged disturbed community response bleeds into the next disturbance, *etc. et seq.*). This undulation would be in addition to and superimposed on top of the net shoaling observed (Chapter One). Importantly, because NIWs propagate outward, understanding TC subsurface biological effects must account for this.

The model above could be refined and improved upon using *in silico* simulations, and with laboratory experiments. Using a superposition of the first harmonic of the NIW (with a secondary time decay function) and the diurnal frequency, one could create a PAR exposure regime for a multi-day growth experiment. Additionally, variation in oxygen (see experiments conducted during this cruise<sup>37</sup>) and temperature would also likely be of import. Temperature changes due to NIWs were in the range 10 degrees here and should be integrated into any Q10 biogeochemical modeled rate of reaction.

Modeling could supplement laboratory work by inclusion of more complexity in variables of interest (including community structure) and more complexity of natural variation—such as secondary noise in NIWs, as observed in the second cast at Station 3.5. There are many ways to investigate this first attempt at a biophysical theory of TC impact in the ETNP OMZ; these paths are not mutually exclusive of future oceanographic expeditions. Indeed, pursuing laboratory studies and modeling may help inform such efforts.

Finally, growth experiments of a community captured following a TC disturbance, while at sea, would be ideal. The theory above has several interesting ecological implications, and by continuity natural selection implications as well, for the “pseudo optimized” prokaryotes<sup>38</sup> that inhabit this OMZ. A permanent OMZ and frequent TC's are likely strong selection pressures. High energy disturbance regimes are well known to significantly impact coastal boundary zones, e.g., the littoral zone. They may also impact this boundary zone (the pycnocline and the biogeographic zone of high TC density) of the ETNP OMZ. It is feasible that microbial life in the ETNP is adapted to hurricane regimes, as has been suggested for terrestrial systems dominated by fires<sup>39</sup>.

## References

1. Zhang, H., He, H., Zhang, W. Z. & Tian, D. Upper ocean response to tropical cyclones: a review. *Geoscience Letters* **8**, 1–12 (2021).
2. Menkes, C. E. *et al.* Global impact of tropical cyclones on primary production. *Global Biogeochemical Cycles* **30**, 767–786 (2016).
3. Chen, Y., Straub, D. & Nadeau, L.-P. Interaction of Nonlinear Ekman Pumping, Near-Inertial Oscillations, and Geostrophic Turbulence in an Idealized Coupled Model. *Journal of Physical Oceanography* **51**, 975–987 (2021).
4. Alford, M. H., MacKinnon, J. A., Simmons, H. L. & Nash, J. D. Near-Inertial Internal Gravity Waves in the Ocean. *Annu. Rev. Mar. Sci.* **8**, 95–123 (2016).
5. Price, J. F. Upper ocean response to a hurricane. *Journal of Physical Oceanography* **11**, 153–175 (1981).
6. Firing, E., Lien, R.-C. & Muller, P. Observations of strong inertial oscillations after the passage of Tropical Cyclone Ofa. *J. Geophys. Res.* **102**, 3317–3322 (1997).
7. Zhang, H. *et al.* Upper ocean response to typhoon Kalmaegi (2014). *Journal of Geophysical Research: Oceans* **121**, 6762–6778 (2016).
8. Sanabia, E. R. & Jayne, S. R. Ocean Observations Under Two Major Hurricanes: Evolution of the Response Across the Storm Wakes. *AGU Advances* **1**, e2019AV000161 (2020).
9. Bertagnolli, A. D. & Stewart, F. J. Microbial niches in marine oxygen minimum zones. *Nat Rev Microbiol* **16**, 723–729 (2018).
10. CODAS+UHDAS Documentation — UHDAS+CODAS 2021.05.01-python3 documentation. [https://currents.soest.hawaii.edu/docs/adcp\\_doc/#](https://currents.soest.hawaii.edu/docs/adcp_doc/#).
11. R2R. Cruise ID OC1806A. *Rolling Deck To Repository* <https://www.rvdata.us/search/cruise/OC1806A> doi:10.7284/907990.
12. Christensen, N., de la Paz, R. V. & Gutiérrez, G. V. A study of sub-inertial waves off the west coast of Mexico. *Deep Sea Research Part A. Oceanographic Research Papers* **30**, 835–850 (1983).
13. Bianucci, L., Balaguru, K., Smith, R. W., Leung, L. R. & Moriarty, J. M. Contribution of hurricane-induced sediment resuspension to coastal oxygen dynamics. *Sci Rep* **8**, 15740 (2018).
14. Kelley, D. & Richards, C. oce: Analysis of Oceanographic Data. (2023).
15. Vincent, E. M. *et al.* Processes setting the characteristics of sea surface cooling induced by tropical cyclones. *J. Geophys. Res.* **117**, (2012).
16. Zeitzschel, B. Primary productivity in the Gulf of California. *Marine Biology* **3**, 201–207 (1969).
17. Santamaría-del-Angel, E., Alvarez-Borrego, S. & Müller-Karger, F. E. Gulf of California biogeographic regions based on coastal zone color scanner imagery. *J. Geophys. Res.* **99**, 7411 (1994).
18. Michael Beman, J., Arrigo, K. R. & Matson, P. A. Agricultural runoff fuels large phytoplankton blooms in vulnerable areas of the ocean. *Nature* **434**, 211–214 (2005).
19. Wang, S., Qiu, Z., Sun, D., Shen, X. & Zhang, H. Light beam attenuation and backscattering properties of particles in the Bohai Sea and Yellow Sea with relation to biogeochemical properties. *JGR Oceans* **121**, 3955–3969 (2016).
20. Bertone, E., Burford, M. A. & Hamilton, D. P. Fluorescence probes for real-time remote cyanobacteria monitoring: A review of challenges and opportunities. *Water research* **141**, 152–162 (2018).
21. Goericke, R., Olson, R. J. & Shalapyonok, A. A novel niche for Prochlorococcus sp. in low light suboxic environments in the Arabian Sea and the Eastern Tropical North Pacific. *Deep*

- Sea Research Part I: Oceanographic Research Papers* **47**, 1183–1205 (2000).
22. Chai, F. *et al.* A limited effect of sub-tropical typhoons on phytoplankton dynamics. *Biogeosciences* **18**, 849–859 (2021).
  23. Cornec, M. *et al.* Deep Chlorophyll Maxima in the Global Ocean: Occurrences, Drivers and Characteristics. *Global Biogeochemical Cycles* **35**, e2020GB006759 (2021).
  24. Barone, B., Nicholson, D., Ferrón, S., Firing, E. & Karl, D. The estimation of gross oxygen production and community respiration from autonomous time-series measurements in the oligotrophic ocean. *Limnology & Ocean Methods* **17**, 650–664 (2019).
  25. Johnson, K. S. & Bif, M. B. Constraint on net primary productivity of the global ocean by Argo oxygen measurements. *Nat. Geosci.* **14**, 769–774 (2021).
  26. Izett, R. W., Fennel, K., Stoer, A. C. & Nicholson, D. P. *Reviews and syntheses: Expanding the global coverage of gross primary production and net community production measurements using BGC-Argo floats.* <https://bg.copernicus.org/preprints/bg-2023-46/> (2023) doi:10.5194/bg-2023-46.
  27. Nicholson, D. P., Wilson, S. T., Doney, S. C. & Karl, D. M. Quantifying subtropical North Pacific gyre mixed layer primary productivity from Seaglider observations of diel oxygen cycles. *Geophysical Research Letters* **42**, 4032–4039 (2015).
  28. Cinay, T. *et al.* Coincident Biogenic Nitrite and pH Maxima Arise in the Upper Anoxic Layer in the Eastern Tropical North Pacific. *Global Biogeochemical Cycles* **36**, e2022GB007470 (2022).
  29. Ulloa, O., Canfield, D. E., DeLong, E. F., Letelier, R. M. & Stewart, F. J. Microbial oceanography of anoxic oxygen minimum zones. *Proc. Natl. Acad. Sci. U.S.A.* **109**, 15996–16003 (2012).
  30. Natural evaporation from open water, bare soil and grass. *Proc. R. Soc. Lond. A* **193**, 120–145 (1948).
  31. Sala, J. *et al.* Estimating Tropical Cyclone-Induced Changes in the Upper Ocean from Argo Profiles. in *103rd AMS Annual Meeting* (AMS, 2023).
  32. Lavin, P., González, B., Santibáñez, J. F., Scanlan, D. J. & Ulloa, O. Novel lineages of *Prochlorococcus* thrive within the oxygen minimum zone of the eastern tropical South Pacific. *Environ Microbiol Rep* **2**, 728–738 (2010).
  33. Cox, I. *et al.* Distinct habitat and biogeochemical properties of low-oxygen-adapted tropical oceanic phytoplankton. *Limnology & Oceanography* **68**, 2022–2039 (2023).
  34. Ulloa, O. *et al.* The cyanobacterium *Prochlorococcus* has divergent light-harvesting antennae and may have evolved in a low-oxygen ocean. *Proc. Natl. Acad. Sci. U.S.A.* **118**, e2025638118 (2021).
  35. McManus, M. a. *et al.* Observations of Thin Layers in Coastal Hawaiian Waters. *Estuaries and Coasts* **35**, 1119–1127 (2012).
  36. McManus, M. A. & Woodson, C. B. Plankton distribution and ocean dispersal. *Journal of Experimental Biology* **215**, 1008–1016 (2012).
  37. Beman, J. M. *et al.* Substantial oxygen consumption by aerobic nitrite oxidation in oceanic oxygen minimum zones. *Nat Commun* **12**, 7043 (2021).
  38. Kalvelage, T. *et al.* Aerobic Microbial Respiration In Oceanic Oxygen Minimum Zones. *PLoS ONE* **10**, e0133526 (2015).
  39. Keeley, J. E., Pausas, J. G., Rundel, P. W., Bond, W. J. & Bradstock, R. A. Fire as an evolutionary pressure shaping plant traits. *Trends in Plant Science* **16**, 406–411 (2011).

# Chapter Three: Capturing tropical cyclone subsurface impacts using the BGC-Argo float array in the eastern North Pacific

## Abstract

Measurements close in space and time before and after tropical cyclones (TC) are required to understand the subsurface impacts of these perturbation events on biological processes. Ship and satellite studies have indicated unique biogeochemical responses under TCs, but neither of these platforms can adequately capture the state change in the subsurface. In this study, the Biogeochemical Argo (BGC-Argo) oceanic float array was used to examine TC-induced subsurface biological response and oxygen minimum zone (OMZ) shoaling within the eastern tropical North Pacific (ETNP) OMZ and the eastern North Pacific. The findings in Chapters One and Two serve as the motivation of this study, namely shoaling of the OMZ and a concentration of active biomass associated with subsurface chlorophyll features. This is further explored here using two sub studies: (1) A single TC-BGC-Argo overpass similar to Bud was examined; Hurricane Olaf (2021-09) exhibited shoaling of the OMZ and creation of the subsurface deep chlorophyll feature. The bifurcation of the deeper chlorophyll feature and OMZ indicates that density stratification is likely important here, yet it is not as strong as Bud, possibly due to the weaker nature of the TCs in this case study. (2) Statistical analyses to explore the potential of the array to provide a more thorough understanding of TCs and OMZ shoaling throughout the TC region in the Eastern Pacific. Results of the statistical analyses indicate the complexity of hurricanes and heteroscedastic ocean data, yet are similar to studies on plankton blooms and inter-storm variability. Findings imply that as the array matures, conducting further investigations along parallel lines can significantly expand our knowledge of TC impacts in OMZs.

## Introduction

The Biogeochemical Argo (BGC-Argo) array<sup>1-4</sup> is an autonomous robotic subsurface remote sensing tool that gathers subsurface profiles of important biogeochemical variables across the global ocean. This observational array is primarily designed to be used as an integration of multiple floats. For example, it has been used over the global ocean to construct three dimensional fields of interior oxygen over time<sup>5</sup>. However, single floats can also be used to document unique transient ocean disturbance events that are otherwise challenging to study and poorly understood, such as tropical cyclones (TCs).

Tropical cyclones regularly form over the eastern Pacific Ocean, and the associated oxygen minimum zone (OMZ). In Chapter One, a shoaling of the OMZ following a TC overpass was found, yet understanding the complexity of TC subsurface impacts in this OMZ requires further study. One objective of the array is monitoring OMZs, making TC and BGC-Argo coupled interactions likely. Despite low but expanding total spatial coverage over the global ocean (see Methods), interest in OMZs means floats have been preferentially placed there. Oxygen sensors were deployed on floats prior to 2016<sup>4,5</sup>, thus making O<sub>2</sub> concentration measurements more common than other BGC-Argo variables over a longer time. Even with imperfect coverage there is a high conditional likelihood of matching floats in the ENTP to OMZ overpass. The spatial correlation between the core of the ENTP and the ‘hurricane alley’ is also high (Ch 1 Fig 5, and refs.<sup>5,6</sup>). The overlap of these two centroids indicates a possible research avenue, despite otherwise low BGC-Argo global domain coverage.

In Chapter One, co-author’s and I found a shoaling of the OMZ, following TC overpass that was in part due to the subsurface stratification but also could be due to biological consumption. We sampled after the storm, and therefore were limited in our ability to capture the full sequence of oxygen change, as the full balance of gas exchange would need to also consider the ventilation of the storms themselves<sup>7,8</sup>. What is known of oxygen and related subsurface biogeochemical changes under TCs comes from a small but diverse set of ship-based, and BGC-Argo studies (including this work). Single Argo floats can potentially provide equivalent insights as cruises, although differences in sampling frequency cannot be ignored. In a BGC-Argo TC match up study<sup>9</sup> in the Bay of Bengal OMZ, the authors looked at five TCs and oxygen changes. They primarily focused on the physical aspects and found that slow moving storms inject DO into the surface water. While plankton blooms were present in some of their profiles, in that work they did not incorporate the biological impact to DO. Calculating the balance (net integration of profiles) of O<sub>2</sub> in the surface mixed layer is a non-trivial endeavor. One study of a cruise<sup>10</sup> under a TC in the western Pacific attributed O<sub>2</sub> patterns to several biological and physical processes, including: storm entrainment, intrusions from subsurface currents, and the plankton bloom’s photosynthesis outpacing consumption. However, the authors might have missed O<sub>2</sub> loss due to consumption by leaving the area after the initial plankton bloom.

The presence of a subsurface chlorophyll maxima (SSCM), and the top of the OMZ can be correlated in space in time through underlying biological mechanisms. In a study<sup>11</sup> in the Bay of Bengal using a BGC-Argo float under a TC, the authors found that the TC produced a strong surface bloom (Chl-a), then as the bloom receded a strong growth in the SSCM. They observed a shoaled SSCM (above the mixed layer depth), slow translational speeds, with associated high Ekman pumping—similar in many regards to what was observed under Bud (Chapters One & Two). A study of a survey cruise that passed over a typhoon impacted region in the western Pacific, documented an intense subsurface bloom (SSCM), which lasted longer than the surface bloom<sup>12</sup>. Likewise, in yet another BGC-Argo float TC study, the authors found a redistribution of the subsurface chlorophyll maxima following a storm overpass and suggest that this could lead to misinterpretation of Satellite based Chl-a blooms, and bloom response. They extrapolate their findings to question net increase in plankton’s responses from

global satellite estimates<sup>13</sup>. However, findings like our study, those in the North Atlantic, and a review of satellite studies indicate blooms are real (see “Introduction”, the Background section, and refs within). Subsurface and surface patterns can be different even within the same storm, and there are several variable factors between storms. The pattern across sampling types (ship, robot, and satellites), indicates individual storms are varied and extrapolating from a single study should be done with care. However, BGC-Argo studies under TCs are helping better understand these complicated phenomena.

More standardized statistical analysis of multiple floats and storms could build upon individual studies. Indeed, several studies have done so using the Core Argo floats. These studies reproduced the net temperature changes under TCs that matches a review of the related physical science literature. Cheng *et al.*<sup>14</sup>, create a TC footprint method with composites of change in temperature at depth bins, with hurricane cross-track distance and time relative to TC passage the two axes. Argo float pairs are perpendicular to the storm’s direction of motion, prior and post TC overpass. Cheng *et al.* use a TC-track coordinate system, which is a relative system based on position of floats in relation to TC track. This addresses the space time complexity that plagues TC studies, by creating a more useful frame of reference. Hu *et al.*<sup>15</sup> improve this by removing seasonality, making time a continuous variable, and incorporating improved uncertainty quantification. Combining all depth footprints gives a three dimensional footprint through time. The methods of Hu *et al.*, have also been used for tracking salinity changes in a separate study<sup>16</sup>. The above methods are promising and may be applied to BGC-Argo floats with some caveats. The BGC-Argo array is not yet mature enough to provide the spatial coverage needed, nor has it been running for as long; therefore, the sample size is smaller. Temperature changes will behave differently than biology, e.g., conduction smooths out over space and time. Finally, the diel pattern of biogeochemical variables would also need to be incorporated.

Using space for time methods several authors have been able to capture regional diel net productivity changes using BGC-Argo floats<sup>3,17</sup>. Johnson and Bif<sup>17</sup> create a ‘pseudo day’ from multiple floats in a region at hourly resolution to account for diel cycles of O<sub>2</sub>. They suggest a lower bound for oligotrophic water; twenty profiles are needed for each hour of their synthetic-day in order to reproduce the variability of high temporal sampling from oligotrophic long term ecological research stations. Since profiles are not exact integer days, subsequent profiles will not be the same diel cycle every 10 days. This kind of float density is not available in the ETNP. The pseudo day method can create a useful mean field, but any mean field would be violated by the anomalous disturbances created by TCs. That is, once the array reaches full density a combination of the above methods could be used in a satisfactory way. Despite limitations, single floats can capture important TC overpass changes, and given the mismatch in scale of TCs and our understanding of subsurface complex processes, any additional studies can help unravel the TC impacts over the global ocean.

In this study, BGC-Argo float TC interactions were investigated. (1) A statistical analysis of change of absolute, and relative depth, of the top of the OMZ (20 µmol/kg) was conducted for 171 float TC interactions in the eastern central Pacific TC zone, which is inclusive of the ETNP OMZ. (2) A single TC-float interaction that mimicked the conditions of Bud was investigated for a similar Hurricane (Chapter One). The

similarities between Olaf and Bud include, being preceded by a TC, evidence of a Chlorophyll-a bloom in satellite imagery, and occurring over the same section of the ocean as studied in the process cruise. Results indicate that subsurface profiles under Olaf captured a shoaled OMZ and disturbed oxygen profiles immediately following the TC overpass. A deep chlorophyll feature also may have been impacted by both Olaf and the preceding storm, Nora. Expanding to multiple TC BGC-float interactions, the statistical analysis suggests that individual tropical cyclones can influence the depth of the oxygen minimum zone, particularly when the OMZ is shallower. These findings align with the multidimensional nature of plankton blooms and TC overpasses observed in individual studies, emphasizing the significance of both the precondition and variability of individual storms.

## Methods

The BGC-Argo array is a popular sequel of its extremely useful older sibling the Core Argo array, a more mature array that provides CTD profiles only. Together with deep profiling floats, the three arrays are the OneArgo program<sup>1</sup>. BGC-Argo officially began in 2016<sup>2</sup>, and is currently being expanded and developed<sup>1,3,4</sup>. Core Argo began in 1998<sup>1</sup>. Because it is still in the development phase, BGC-Argo has not reached full coverage in all Ocean basins.

BGC-Argo floats typically park at 1000 meters depth for ten days, then sink to 2000 meters, where they collect data as they profile towards the surface. At the surface they transmit collected data via satellite antenna. They then sink to 1000 meters to repeat the process. An individual BGC-float's expected lifetime is negatively related to sensor load and profiling frequency because of power consumption; with a 10 day sampling equating to ca. 4 years of continuous deployment.

FLOATS of the BGC-array carry a suite of important biogeochemical state variables for a more inclusive understanding of the subsurface ocean. BGC-Argo variables<sup>3</sup> include; Chlorophyll-a, downwelling Irradiance (see the Appendix), Nitrate, PH, and optical particle measurements<sup>4</sup>. This is in addition to the core CTD functionality of all floats. The goal for the array is for 1000 floats distributed over the world's oceans. As of 2023-11-11, there were 528 floats listed as active on available repositories. At peak capacity new floats will be added at a rate of 250 a year. Because of its' active development stage not all individual floats are of the same make, conduct profiles at the same frequency, nor carry the same sensor suite. Additionally, spatial temporal coverage is not even between ocean basins, with the Southern Ocean and the Atlantic having the highest historical coverage.

Hurricane position, strength, and wind speed data are from the NE/NC Pacific HURDAT2 dataset. The HURDAT2 dataset<sup>18</sup> that was downloaded on 2023-09-13, included TCs from 1949-06 to 2022-10. While individual storm tracks are available after that end date, they have not yet been included in this systematic data product that includes spatial reanalysis of all points.

The North Eastern Pacific TC/BGC-Argo spatial domain was defined by the cardinal occurrences of TCs in the database, plus a 7 degree buffer for float and profile selection. To avoid floats and profiles that may occur in the typhoon cyclogenesis region

of the Western Pacific the western boundary was chosen to be 180 west. Additional selection used ocean basin shape files (<https://www.naturalearthdata.com/>), in order to remove TC tracks that passed over Central America.

Latitudinal data was southern skewed with the northern domain extended by a small number of anomalous storms. To constrain the meridional range of the TC zone the 99% percentile of Latitude values for all six hour eye points was selected. Boundaries for BGC-Argo profile selection are 38.5N, 3.5S, 180W, 78W. TCs were selected within a seven degree buffer within this spatial domain. For BGC-Argo match up to storm paths three spatial buffers (100km, 200km, 500km, Tables 1-3) around the hurricanes tracks in the HURDAT2 database were used. Tracks were derived from six hour eye positions per individual storm. The 7 degree/500km buffer and selection criteria were chosen following Cheng *et. al*<sup>14</sup>, who found this to be a reasonable outer bound in their analysis of subsurface temperature changes from a global analysis of Core Argo floats and TC overpass.

The 100 km and 200 km were chosen because of work in Chapters One and Two, and references within. For metadata float, and NetCDF file downloads of profiles the “BGC-Argo toolbox for R”<sup>19</sup> was used. This is an official toolbox maintained by the BGC-Argo community. Default software settings account for quality flags<sup>3</sup>, delayed mode, etc. The author used git version control to stay up to date with developments (submodules). For additional oceanographic analysis, profiles were piped to the R package “oce: Analysis of Oceanographic Data”<sup>20</sup> (see methods Ch 2).

For distance and time match up a great circle distance perpendicular to TC track line was computed between the two nearest 6-hour position locations in the HURDAT2 database. This allowed for sorting of profiles by distance and nearest time using metadata to the nearest date +- 6 hours. Time was computed to integer decimal day for analysis. Increased spatial temporal resolution would require much more detailed analysis of wind speed radii etc. That is, distance to the eye is not an exact distance from the hurricane, as storms can be 100 kms in diameter and the eye can be some time and distance away. When a float emerges, it can be under areas of high winds, despite time and space mismatch. The HURDAT2 dataset gives peak wind for each point that was used in analysis.

For a simple OMZ shoaling analysis, individual floats that met the above space and time criteria, and additionally had both before and after profiles were selected with TC overpass. These interactions were inclusive of storm strength, distance from TC, and within the greater study region. That is if three different floats interacted with the same TC, they would be counted as three different sets of observations. The pressure at which the OMZ (first occurrence of 20 µmol/kg) was used per profile. If values were higher, then the lowest oxygen value was used. Profiles contain adjusted (data reanalysis corrections) and unadjusted values. If adjusted values existed, then those were preferentially used for both oxygen and pressure. A change value for each profile after overpass (including time = 0) was calculated and then compared to the mean of all previous profiles, within the time and space selection window. Statistical analysis was a Multivariate analysis of variance (MANOVA) with absolute depth (pressure), and relative change as compared the mean of previous profiles in the same float, as dependent

variables. Very basic sensitivity analysis included multiple random resampling of N - 200, (10% of 2000 profiles) for the created dataset for post storm profiles.

Prior to analyzing the systematic selection, a single TC BGC-Argo interaction was investigated. A float TC interaction was chosen for its proximity to Station 3.5 as a case study. Conveniently, this float includes derived variables such as CDOM, a remote sensing catch-all for organic matter. The repository used was: <https://data-argo.ifremer.fr/dac/coriolis/>.

## Results and Discussion

### Oxygen BGC-Argo floats and TC overpasses

In the ETNP OMZ, using the simple selection parameters here, 39% of floats with O<sub>2</sub> sensors that have been deployed have encountered TCs, and that 27% of all O<sub>2</sub> profiles also interact (Table 1). With 21 major hurricanes interacting profiles within 100km, this dataset can be mined to better determine the most intense TC interactions in the OMZ. With over 200 tropical cyclones at the 500 km selection the lower bound is well accounted for as well (Table 2) with future sensitivity analysis possible as function of profiles and floats interacting per storm strength (Tables 3a-c).

Figure one shows spatial overlays of information in the aforementioned tables. Because float distribution is not even, the TC- float interactions are biased to land based deployment regions, e.g., near Hawaii (Fig. 1a). Selection criteria, strength of storm and distance of profiles may arbitrarily decrease sample size and spatial coverage (Fig. 1 a & b). The 30 days prior time selection window, while not necessarily for determining the impact of TC overpass, gives a useful precondition window. That precondition state could be incorporated into studies of TC overpasses that use additional sampling means.

Together this descriptive analysis gives a simple upper bound of sections of the ETNP that may be impacted for tropical cyclones. Given the use of these floats in creating spatial interpolated climatologies<sup>5</sup>, a better inclusion of these rather regular anomalies should be considered for future work.

Many float TC interactions are located near Hawaii, which is at the outer edge/outside the ETNP, thereby reducing the sample size to evaluate ETNP specific oxygen changes. However, it does allow for an understanding of oxygen changes across biogeographic regions. Additionally, profiles on the southern edge of ETNP pass over the region of equatorial upwelling (Fig 1a).

Multivariate analysis of variance (MANOVA) is shown in Table 4. The Two dependent variables are absolute depth of the top OMZ (pressure), and relative change as compared to the mean of previous profiles in the same float. Absolute depth showed many more significant confounding variables than the change in depth (pressure). ANOVA analysis of prior OMZ depth showed similar significance values, to the MANOVA of absolute depth for the same variables. Sensitivity analysis indicated that P values significance was not invariant to N-10% resampling (Methods). This prohibited further subsetting of the data to isolate variables, (e.g., only profiles within 100km of a storm).

The change in depth's most significant variables were individual storm, and the precondition minimum and mean depth. Surprisingly, wind velocity was not significant, for either of the dependent variables, nor was Longitude. This may be due to the fact the depths below 500 m were excluded, excluding some but not all profiles outside of the ETNP OMZ. Histograms showed a bi-modal pattern by Longitude, but most profiles were in the ETNP. This may explain while Longitude, which would be expected to impact the MANOV, did not.

Spatial autocorrelation may explain the many significant values of independent variables driving variance for the absolute depth. That is, independent variables may not actually be independent. From this cursory analysis of OMZ change and individual storm and precondition namely minimum OMZ depth are the two most principal factors to constrain for, and to investigate in future studies. The fact that change in depth has many fewer confounding variables as opposed to absolute depth of the OMZ, may suggest that change in OMZ depth following a TC overpass is a scalable phenomenon.

## Hurricane Olaf matchup

For the single case study of a single TC BGC-Argo match up, the overpass of Hurricane Olaf and the BGC-Argo float 6903093 was selected. Olaf was a tropical storm by the time it reached the eastern Pacific on September 2nd 2021. Olaf reached hurricane strength on 09/09 at 20.9 °N. 108.1 °W, and on the same day its eye position was 9.89 km from cycle 54 of float 6903093 (Fig. 3)—making it useful for comparison to Hurricane Bud and Station 3.5, which is located at 18.5°N 108.5°W, as well as Station 4 (Fig. 2). Like Bud, a Chlorophyll-a feature was present in the satellite imagery following the storm (Fig. 4, Ch 1 Fig. 2). This float was the primary float used for matchup and comparison; however, floats 5905068 and 6903094 also intersected Olaf (Figs 2 & 5).

Eight profiles collected close in space and time to Olaf were used to gauge the storm's impact and the delayed subsurface response to the storm. As a function of distance perpendicular to the storm track the eight profiles in order were: 2, 6, 29, 10, 5, 9, 32, 26, kms away respectively (Fig 3.). The standard profiling frequency for floats is 10 days; however, for this specific float on the dates in question, there was a mixed sampling frequency of 4, 6 and 10 days. Three profiles collected before the storm were located to the NW {(8/20, 8/24, 8/30) /(-20, -16, -10)}, (dates/days relative to the overpass). These were followed by three profiles located close to each other and the overpass, with the first of these closely coinciding with the storm's passage {(9/9, 9/13, 9/19) /(0, 4, 10)}. The second of these profiles was collected 4 days after the storm, and the third 10 days after, such that it may be better compared with two subsequent profiles. These two other profiles were located to the NE of the track and were collected several weeks after the storm's passage {(9/29, 10/3)/(20, 24)}. In sum, two profiles were used to gauge the storm's immediate effect {(9/9, 9/13)/(0, 4)}, and three used to observe the lagged response {(9/19, 9/29, 10/3)/(10, 20, 24)} (Figs 7-10).

Prior to Olaf, the weaker Hurricane Nora (Cat 1, August 28th) passed from the South to North direction farther east of Olaf (Fig. 6). It is difficult to distinguish satellite Chl-a features following the storm because of the proximity to the coast, as features may

be due to upwelling or the TC (see: <https://worldview.earthdata.nasa.gov>). The profiles prior to Olaf on float 6903093 also met the selection criteria for match up with Nora. The profile on 08/30 was 1 day after Nora at 300 km away, and also the last prior profile for Olaf, making the 11 day profile after Nora the ‘day of’ profile for Olaf (Fig 5 & 6).

The Olaf-associated profiles showed a shoaling of the OMZ that then returned to a more similar, but still different, profile (Fig 7a:c). The profiles immediately following show what appears to be an instability in the oxygen profile. The ‘day of’ profile was only 1.5 hours after the closest point on the track. (+- 6 hours accuracy) and shows a drop to 50 micromolar oxygen at 50m depth, with a secondary increase after that. Four days later, a smoothed but similar pattern is also evident. The temperature profiles show a traditional cooling from before the TC overpass to after, followed by a deepened and warmer mixed layer in the final panels (Fig. 7d:f)

A subsurface deep chlorophyll feature (DF) is not present prior to the overpass, nor the day of, but appears to last for 10 days (Fig. 8a:c). In fact, fluorescence is low throughout the profile at time equals zero, perhaps indicating mixing or reduced activity due to cloud cover. CDOM, which is a proxy for organic matter, shows similar profiles in the before and immediately after, but decreases in the final profiles along with Chl-a (Fig. 8c:f). CDOM is often a proxy for terrestrial DOC/POC, perhaps indicating the initial water mass was more coastally associated. Alternatively, loss over time may be due to biological consumption.

To complement particle analysis as conducted in Chapter Two, included is a measure of beam attenuation from a similar sensor on the float. The variable cp660 is beam attenuation for that wavelength, which provides an estimate of net particles. Figure 10 shows how the amount of matter in the profiles increases for each profile from first to last, and specifically that it approximately doubles in attenuation. It also indicates that the DF may have formed under Nora and lasted through all profiles. If using only Chl-A, the DF may be less long-lasting (Fig 9.) When comparing the three important biological indicators beam attenuation, oxygen, and Chl-a to density, the 26 [kg/m<sup>3</sup>] isopycnal surface seems to be important (Chapter 2), however it does appear that biological activity and biomass are more bifurcated above and below the isopycnal. This indicates that the strong stratification model proposed in Chapter Two only weakly fits these data. Finally, the drawdown in oxygen appears to be much higher above this density surface, but the variability is high as a function of time (Fig. 9 & Fig 8b,c).

In sum, Olaf appears like Bud to cause a short term OMZ shoaling and the creation of a deep Chlorophyll-a feature (a second chlorophyll maxima, as opposed to a DCM hence the use of DF), with temperature profiles that indicate Hurricane mixing. Aso like Bud it was preceded on the right hand side by a weaker storm that passed between its track and the coast.

## Additional floats and OMZ variability

TC overpasses and their impact on OMZ shoaling will be superimposed on top of natural temporal spatial variability. This combination of spatial and temporal variability is particularly relevant in the ETNP OMZ, where strong latitudinal and longitudinal gradients exist in productivity and oxygen. To document this variability, a simple time

series was investigated of a single float in the ENTP OMZ. This float, 6900394, was adjacent to float 6900393, and intersected Olaf's trajectory (Fig 2). Float 6900394 generally drifted offshore from the very low oxygen region affected by Bud and Olaf, and then towards Station 4 and the Baja Peninsula.

Over the multiyear deployment of float 6900394 there is high variability of dissolved oxygen at depth (Fig. 11). Oxygen levels show a better fit to the density than the temperature derived MLD. Importantly MLD depth is commonly used in many TC studies. Together with material here and within, this indicates it may be more important to use density interfaces for understanding TC subsurface biological changes.

A subsection of that time series under Nora and Olaf is shown in Figure 12. While this float was farther away than 6900393, it still shows a shoaling following the period affected by Nora and Olaf. Additionally, the one profile near October 6<sup>th</sup> with a deepening of oxygen and the density layer roughly corresponds in space and time with the TC that passed after Nora, Hurricane Pamela (albeit a few days before the eye overpass, at 150 km on its left side). Clearly, a more detailed wind analysis would be needed to explore the injection possibilities of TCs using BGC-Argo floats.

**Ch 3 - Table 1:** Total BGC-Argo floats within ETNP OMZ-Hurricane zone. Spatial temporally as defined in Methods. Floats interacting and profiles interacting are for the largest selection, All tropical cyclones, 500 km and from 30 days prior to or 45 days after TC overpass. As defined in methods, the area for BGC-Argo profile selection was 38.5N, 3.5S, 180W, 78W. TCs were selected from within a 7 degree buffer within this spatial domain. Applies to all Tables.

Total BGC-Argo Floats in area	Total profiles “”	Floats with “DOXY”	Profiles with “DOXY”	Floats interacting with TCS	Profiles interacting with TCS
136	16557	133	16173	64	4488

**Ch 3 - Table 2:** Number of TCs intersecting BGC-Argo floats. \* For floats within 30 days prior to or 45 days after TC overpass. \*\* indicates the highest category over TCs full track. Hurricanes cat 1-5, Major = Cat 4 & 5. Tropical Cyclones category is inclusive of all non-hurricane and hurricane strength storms. Hurricanes are inclusive of major and non-major Hurricanes. Designations apply to all following tables 1-3. Range indicates that an individual TC will change designation/strength over its lifetime.

Search Radius*	Tropical Cyclones	Hurricanes**	Major Hurricanes **
100 km	77-75	54 - 53	21-20
200 km	123-120	79 -77	34 -32
500 km	201-183	113 - 103	48-43

**Ch 3 - Table 3 (a):** Floats and profiles **Tropical Storms**. As table 2, for tropical cyclones only, classified as below hurricane strength.

Search Radius	Total Floats	Total Profiles
100 km	37	742 -737
200 km	46	1726 - 1719
500 km	64 - 62	4488 - 4423

**Ch 3 - Table 3 (b):** Floats and profiles **Hurricanes\*\***. As table 2, for Hurricanes only, classified as below hurricane strength, but not Major.

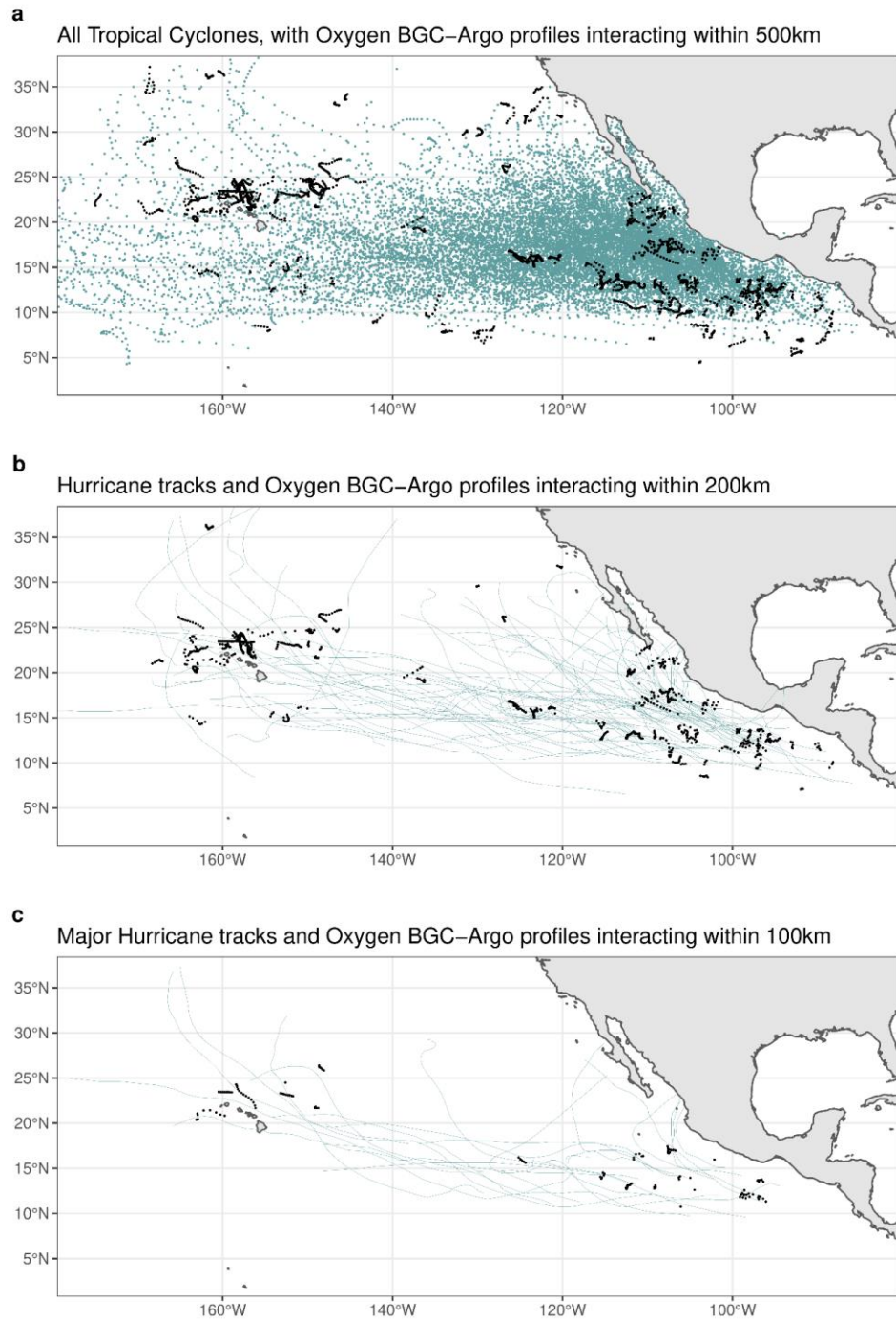
Search Radius	Total Floats	Total Profiles
100 km	35	553 -550
200 km	42	1249 - 1245
500 km	59 -57	2961 -2929

**Ch 3- Table 3 (c):** Floats and profiles **for Major Hurricanes\*\***. As table 2, for Major Hurricanes only.

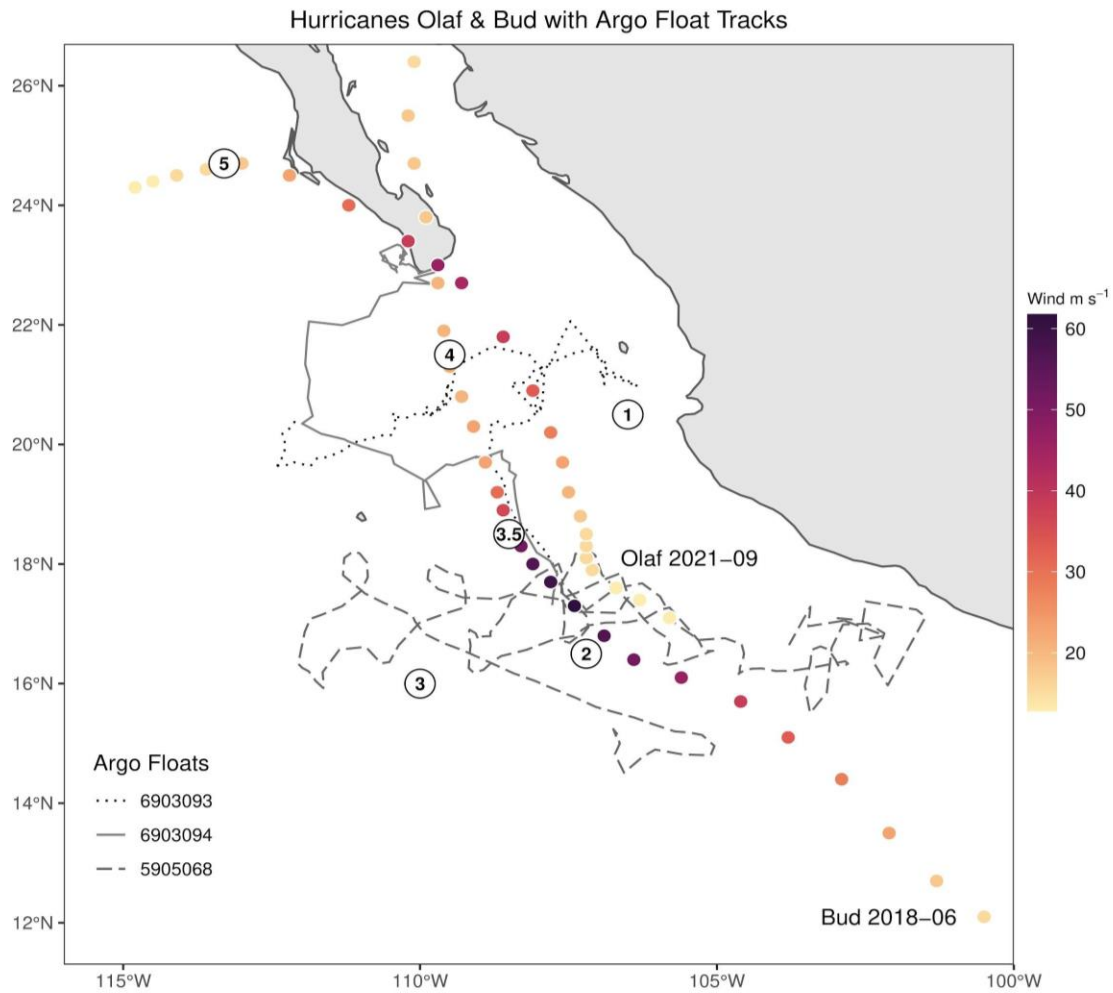
Search Radius	Total Floats	Total Profiles
100 km	16	147-144
200 km	26-25	378-274
500 km	43	1157-1137

**Ch 3 - Table 4:** MANOVA table of significance for independent variables, column one. Columns two and three are the two dependent variables. For profiles after a TC overpass. “Absolute depth of OMZ” is the value of the top of the OMZ. “Change from Pre-Strom Depth” based on the change between prior and post TC overpass for the TC-Float interactions. “Pre-storm condition profiles” indicates summary statistics for prior profiles absolute depth of the OMZ. P values are given by: \*\*\* 99%, \*\* 95%, \* 90%.

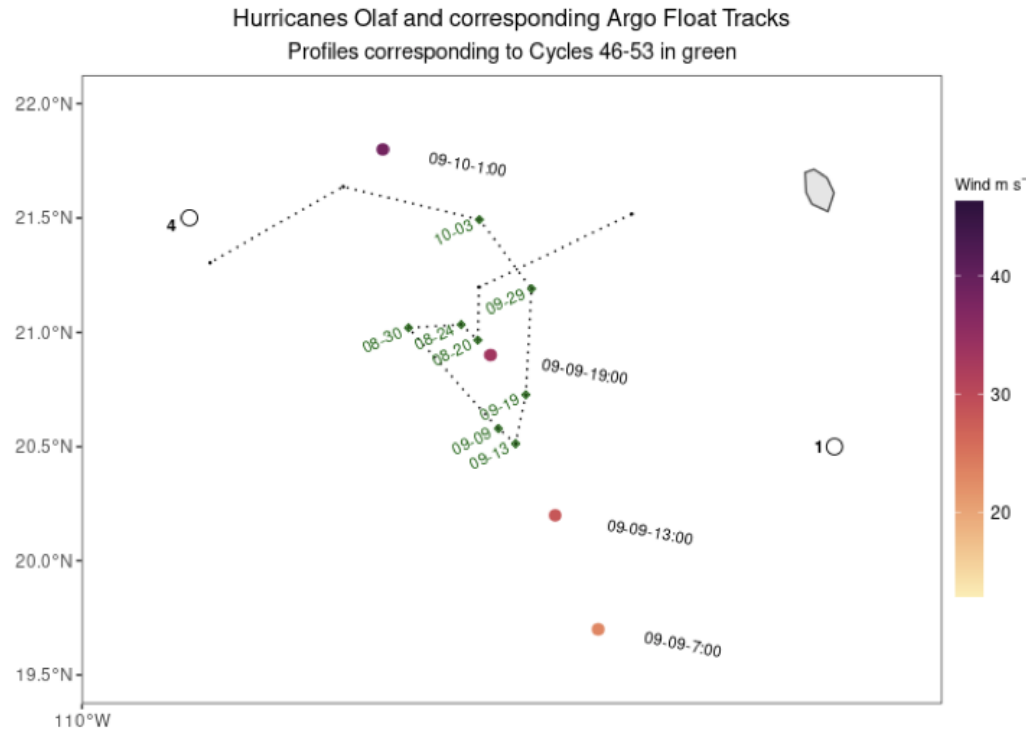
Variable	Absolute depth of OMZ	Change from Pre-Strom Depth
Relative time from Overpass	***	*
Distance From Storm	***	*
Individual Storm	***	***
Maximum TC Wind		
Storm Status	***	
Longitude		
Latitude	***	*
Pre-Storm Condition Profiles N	***	*
Pre-Storm Condition Profiles Mean	***	***
Pre-Storm Condition Profiles Variance	***	
Pre-Storm Condition Profiles Minimum Depth		***



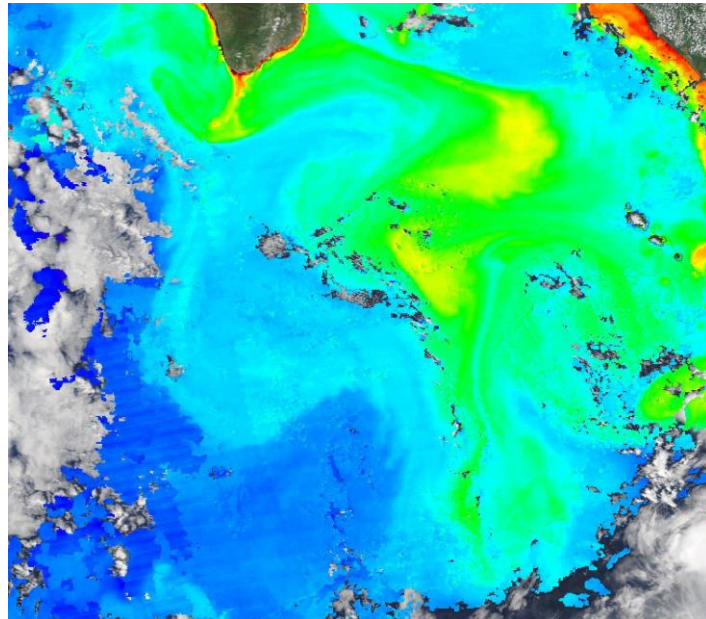
**Ch 3 - Figure 1:** Map of overlays of tropical cyclones and BGC-Argo profiles with oxygen sensors. Within the time and space selection window, see methods, Table 1. (a) All six hour positions for TC's in the database, blue dots, with profiles of a float that fell within 500 kms, black dots. (b) Hurricane tracks, blue lines, and associated profiles falling within 200km, black dots. (c) Major hurricane tracks, blue lines, and associated profiles falling within 100km, black dots. Time window is from 30 days prior to or 45 days after TC overpass.



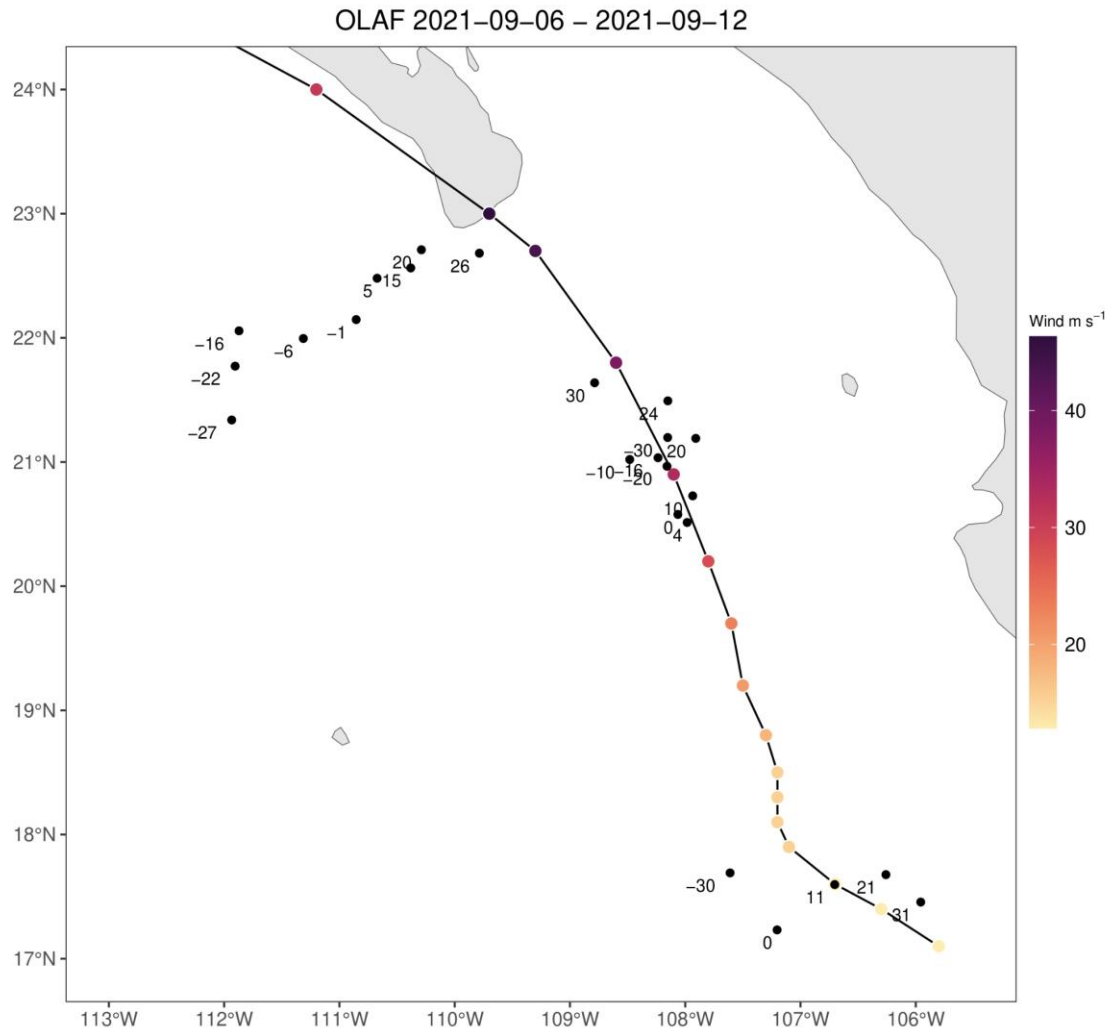
**Ch 3 - Figure 2:** Spatial overlay of Hurricanes Bud (Ch1 & 2), with cruise sampling stations (numbered circles), as well as Hurricane Olaf. Three different dashed lines are tracks of associated BGC-Argo floats with identifier numbers. Floats 6903093 and 6903094 were used for reference data for Station 3.5 (Ch 1 Fig. 4a). Color-shaded dots show maximum sustained wind speeds every six hours along Hurricane Olaf's track.



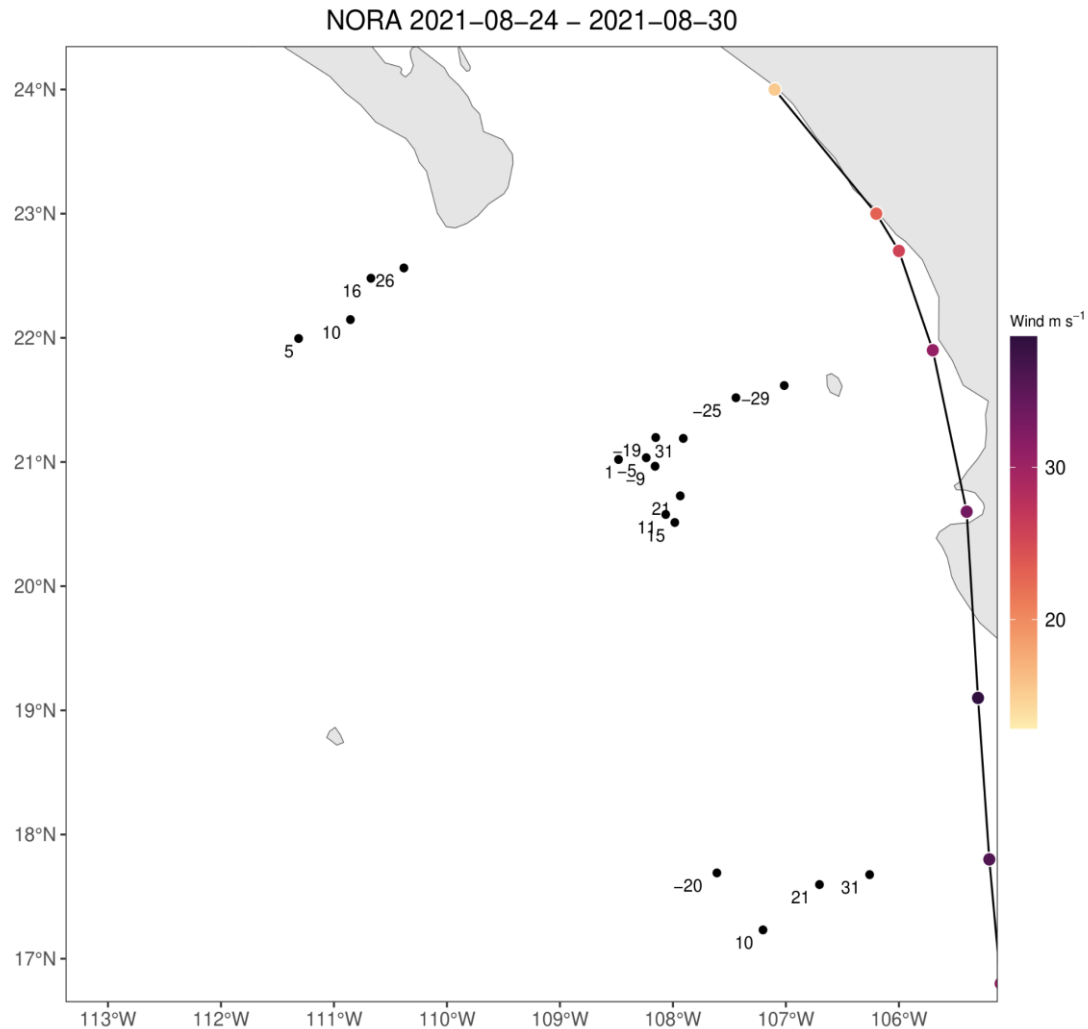
**Ch 3 - Figure 3:** Float 6903093 track under Olaf. Dates for before, during and after profiles used in following figures. Float track and dates in green. Six hour position of Hurricane Olaf with corresponding winds speeds, date and times in black. UTC-0. color-shaded dots show maximum sustained wind speeds every six hours along Hurricane Olaf's track.



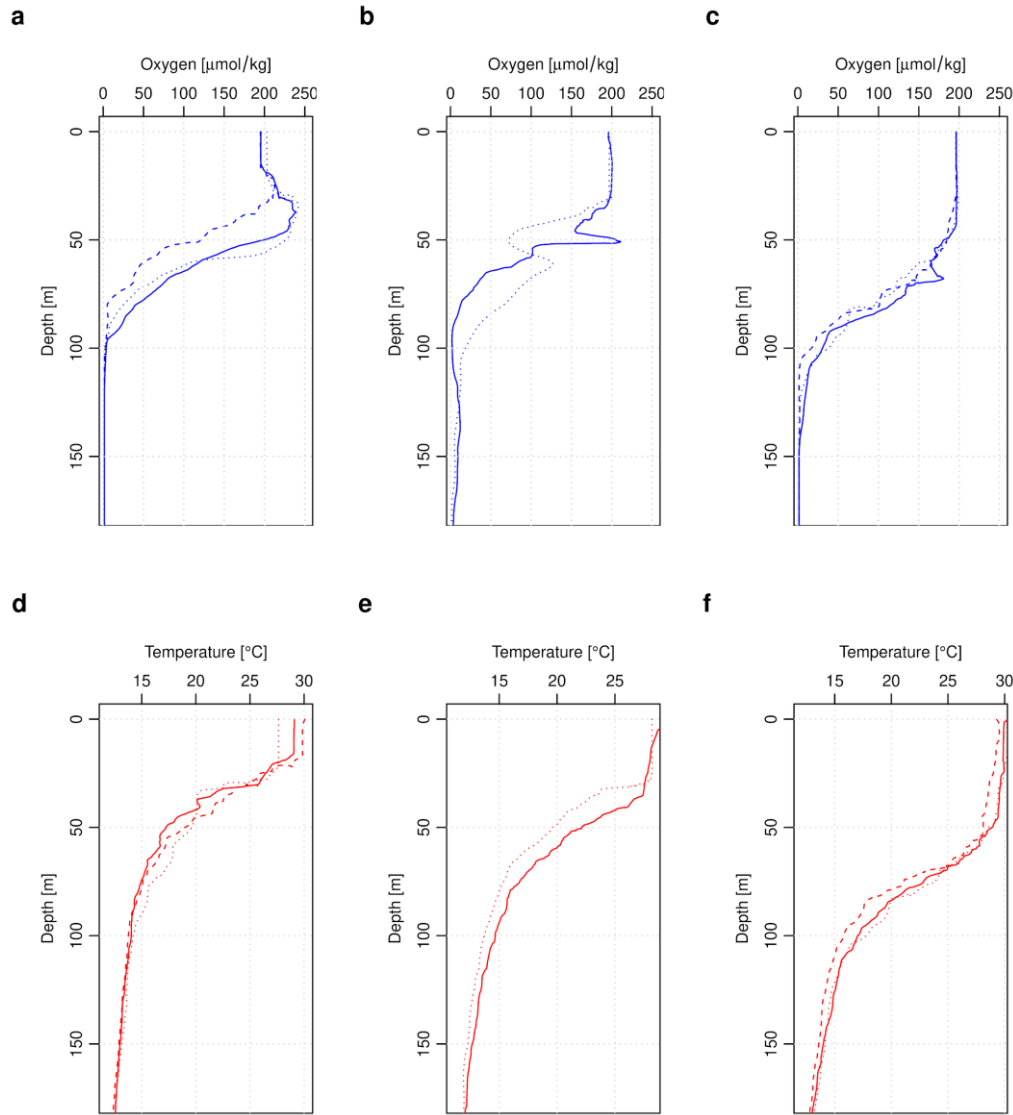
**Ch 3 - Figure 4:** Chl-a map on 2023-09-12. Olaf overpass. Multiple sensors for composite image (see Ch-1 Fig 2, and methods Ch-1) image from <https://worldview.earthdata.nasa.gov>



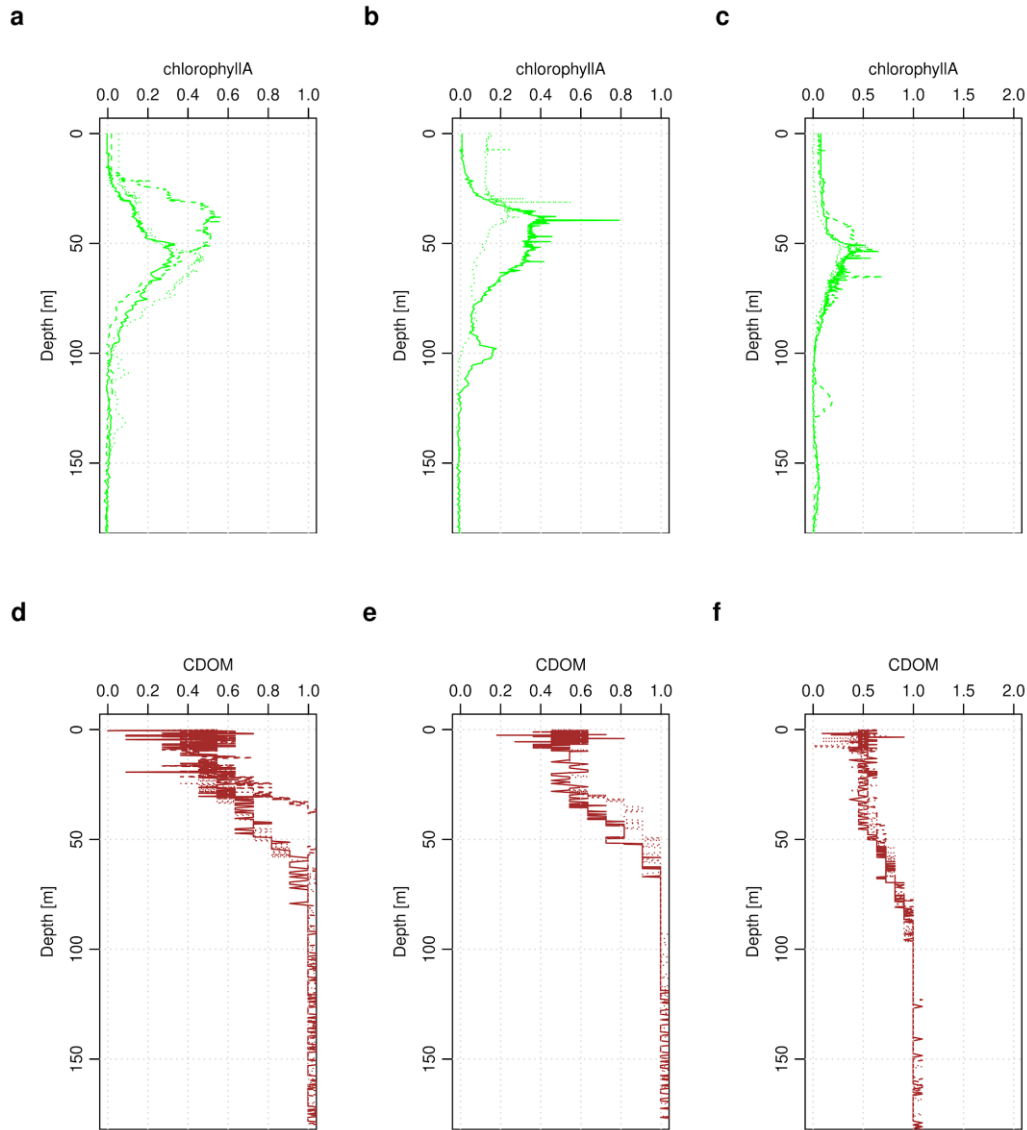
**Ch 3 - Figure 5:** Multiple floats and TC Olaf. Dates in the title give the window of six hour eye position for Olaf on the map. Three sets of dots are profiles for floats 6903094, 6903093, 5905068, from North to South, respectively. Positive and negative numbers are days after or before from closet overpass to the TC track for individual profiles. Scale is wind speed for TC at the six hour position.



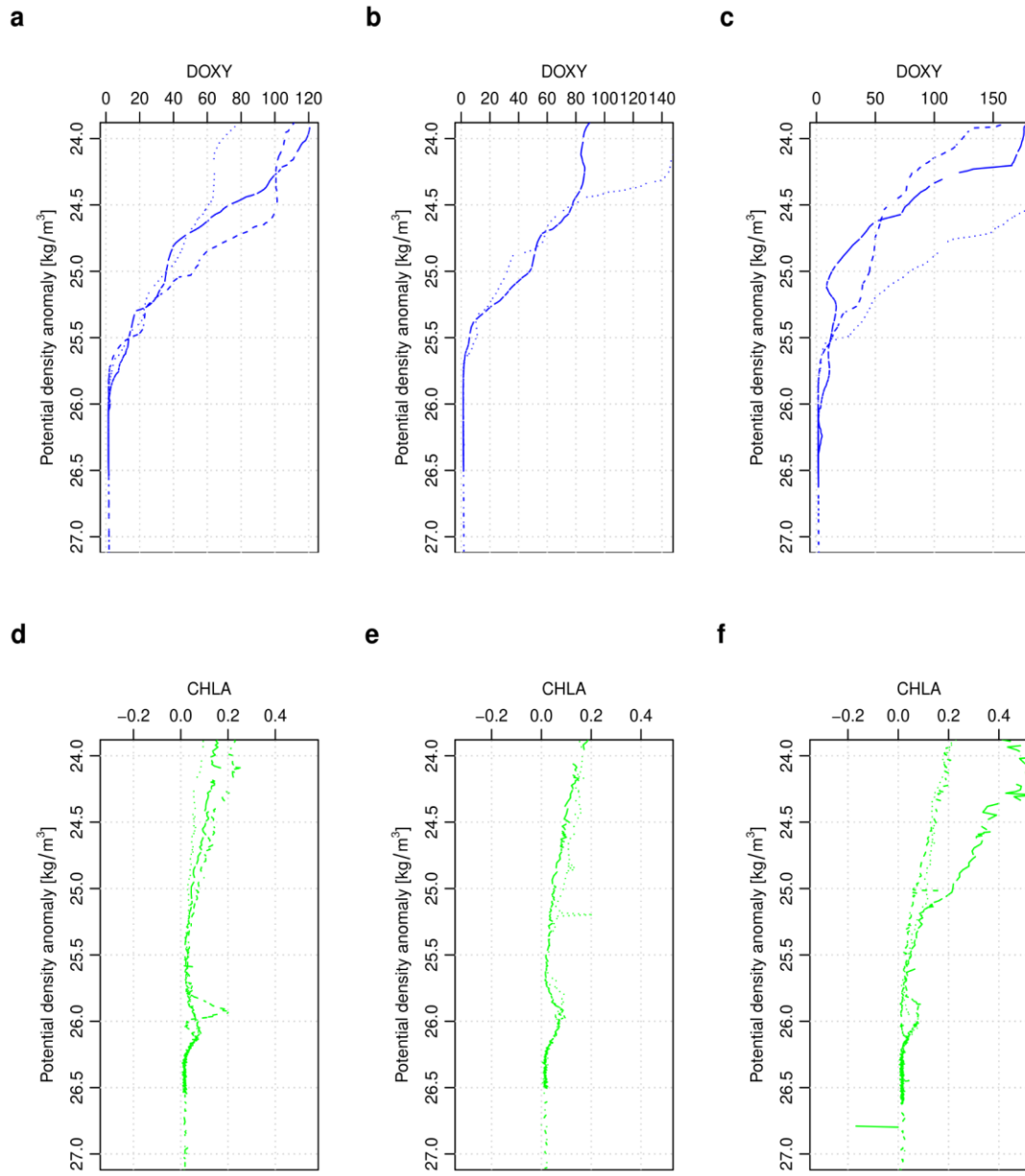
**Ch 3 - Figure 6:** Multiple floats and TC Nora .Dates in the title give the window of six hour eye position for Nora on the map. Three sets of dots are profiles for floats 6903094, 6903093, 5905068, from North to South, respectively. Positive and negative numbers are days after or before from closet overpass to the TC track for individual profiles. Scale is wind speed for TC at the six hour position.



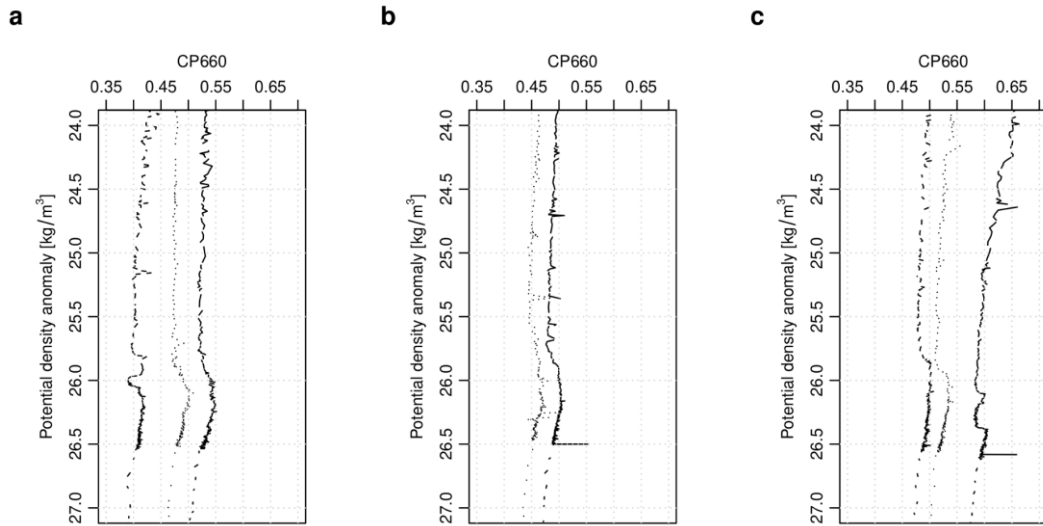
**Ch 3 - Figure 7:** Profiles of oxygen [ $\mu\text{mol}/\text{kg}$ ] (a:c), and temperature in Celsius (d:f) for float 6903093 under Olaf. Three columns (a,d; b,e; c,f), are profile groupings: prior, immediately following, and post disturbance, following sequential order corresponding time relative to TC overpass. Lines in each panel are dashed, dotted, solid in sequential order, within groupings. Days relative are: -20, -16, -10, 0, 4, 10, 20, 24.



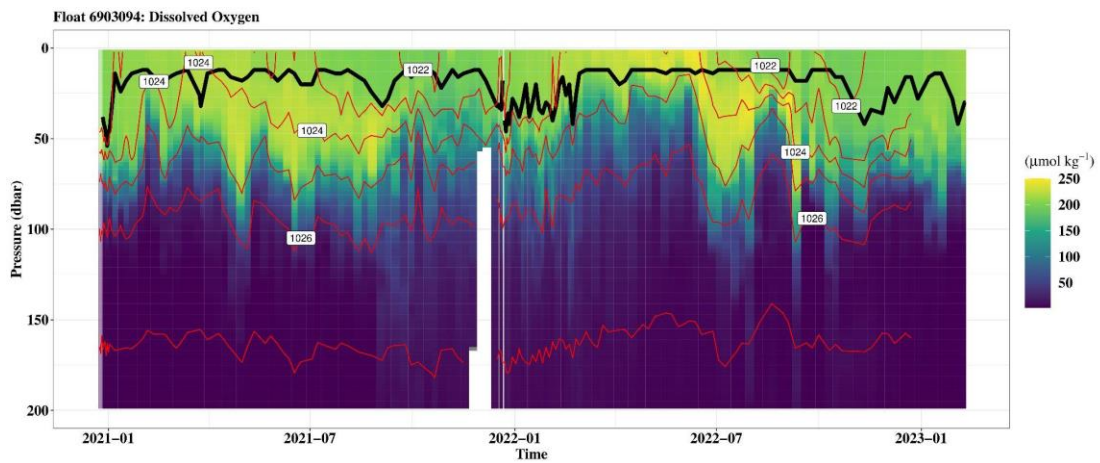
**Ch 3 - Figure 8:** Profiles of Chl-a [ $\mu\text{g L}^{-1}$ ] (a:c), and CDOM (d:f) for float 6903093 under Olaf. Three columns (a,d; b,e; c,f), are profile groupings: prior, immediately following, and post disturbance, following sequential order corresponding time relative to TC overpass. Lines in each panel are dashed, dotted, solid in sequential order, within groupings. Days relative are: -20, -16, -10, 0, 4, 10, 20, 24.



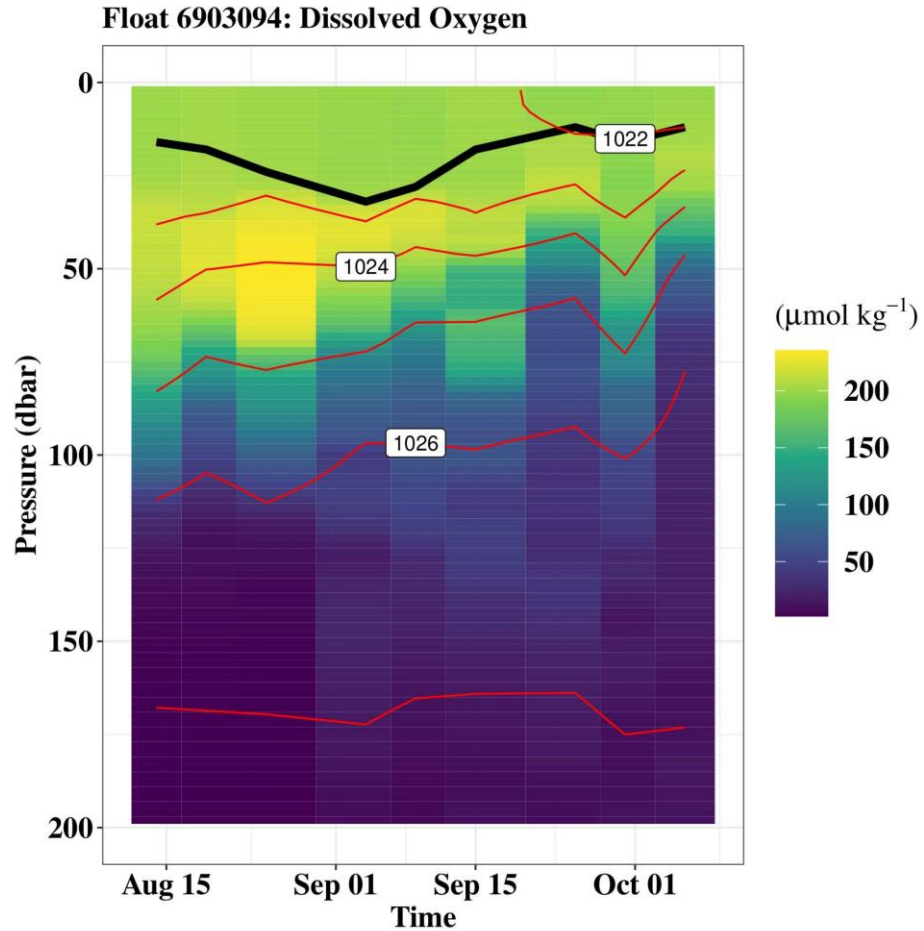
**Ch 3 - Figure 9:** Density profiles of oxygen [ $\mu\text{mol/kg}$ ] (a:c), and Chl-a [ $\mu\text{g L}^{-1}$ ] (d:f) for float 6903093 under Olaf. Three columns (a,d; b,e; c,f), are profile groupings: prior, immediately following, and post disturbance, following sequential order corresponding time relative to TC overpass. Lines in each panel are dashed, dotted, solid in sequential order, within groupings. Days relative are: -20, -16, -10, 0, 4, 10, 20, 24. y-axis being Sigma-0 , potential density anomaly [ $\text{kg/m}^3$ ], as opposed to depth.



**Ch 3 - Figure 10:** Density profiles of cp660 , beam attenuation at 660 nm [m-1] (a:c) for float 6903093 under Olaf. Three columns are profile groupings: prior, immediately following, and post disturbance, following sequential order corresponding time relative to TC overpass. Lines in each panel are dashed, dotted, solid in sequential order, within groupings. Days relative are: -20, -16, -10, 0, 4, 10, 20, 24. y-axis being Sigma-0 , potential density anomaly [ $\text{kg}/\text{m}^3$ ], as opposed to depth.



**Ch 3 - Figure 11:** Interpolated time series section of Float 69003094 from 2021-2023. Not the same float as proceeding figures of profiles. Black line is Mixed depth red lines are density isopycnals.



**Ch 3 - Figure 12:** Interpolated section of Float 69003094 for Olaf and Nora overpasses. Not the same float as proceeding figures of profiles . For Olaf Passover date (09/10), was -1 and 5 days to the closest profiles. Black line is the mixed layer depth red lines are density isopycnals.

## Conclusions

Tropical cyclones have important biological impacts and biogeochemical ramifications in the ETNP OMZ. This deserves further study and was explored using the BGC-Argo array. Floats with oxygen sensors have and will continue to interact with TCs within the spatial temporal bounds of interest here, presenting an opportunity to examine the subsurface effects of powerful storms on this important region of the ocean.

The statistical analysis here indicates that while sample size and spatial confounding factors are nontrivial, individual TCs do and can cause a change in depth of the OMZ, which is more likely when the OMZ is shallower. Results here are congruent with the multidimensional nature of plankton blooms and TC overpasses observed in single studies, but also with the fact that the precondition of the ocean, and variability of

individual storms are two of the more crucial factors explaining surface plankton blooms. Future work may be as simple as conducting methods here on a mature array with more floats in the ETNP OMZ, as this will address spatial sampling deficiencies and the limits of sample size.

The detailed analysis of Hurricane Olaf and the BGC-Argo float matchup provides valuable insights into the subsurface dynamics of biogeochemical variables in the ETNP OMZ. The proximity of a single float directly under Olaf allowed for the examination of the impact on oxygen, temperature, and optical proxies for biota. The results indicate a shoaling of the OMZ, the formation of a deep Chlorophyll-a feature, and temperature profiles consistent with hurricane-induced mixing. Samples directly under a TC overpass could not have been conducted via a research cruise and show an instability and fluctuation in the oxygen profiles immediately after the overpass, which has not been documented before.

Comparison with a weaker precursor storm (Nora) and the subsequent Hurricane Pamela suggests a pattern of short-term OMZ changes and the creation of deep biological features associated with TCs. Additionally, the examination of a multi-year deployment of a neighboring float highlights high variability in dissolved oxygen at depth, emphasizing the relevance of density interfaces over temperature-derived MLD in understanding TC-induced subsurface biological changes. Overall, this research underscores the need for further studies on the role of subsurface dynamics in biological responses to TCs, as well as the role the BGC-Argo float array may have in addressing this task.

## References

1. Owens, W. B. et al. OneArgo: A New Paradigm for Observing the Global Ocean. *Mar. Technol. Soc. J.* 56, 84–90 (2022).
2. Bittig, H. C. et al. A BGC-Argo Guide: Planning, Deployment, Data Handling and Usage. *Front. Mar. Sci.* 6, 502 (2019).
3. Stoer, A. C. et al. A census of quality-controlled Biogeochemical-Argo float measurements. *Front. Mar. Sci.* 10, 1233289 (2023).
4. Claustre, H., Johnson, K. S. & Takeshita, Y. Observing the Global Ocean with Biogeochemical-Argo. *Annu. Rev. Mar. Sci.* 12, 23–48 (2020).
5. Sharp, J. D. et al. GOBAI-O 2 : temporally and spatially resolved fields of ocean interior dissolved oxygen over nearly 2 decades. *Earth Syst. Sci. Data* 15, 4481–4518 (2023).
6. Paulmier, A. & Ruiz-Pino, D. Oxygen minimum zones (OMZs) in the modern ocean. *Prog. Oceanogr.* 80, 113–128 (2009).
7. Iwano, K., Takagaki, N., Kurose, R. & Komori, S. Mass transfer velocity across the breaking air–water interface at extremely high wind speeds. *Tellus B Chem. Phys. Meteorol.* 65, 21341 (2013).
8. Krall, K. E. & Jähne, B. First laboratory study of air–sea gas exchange at hurricane wind speeds. *Ocean Sci.* 10, 257–265 (2014).
9. Xu, H., Tang, D., Sheng, J., Liu, Y. & Sui, Y. Study of dissolved oxygen responses to tropical cyclones in the Bay of Bengal based on Argo and satellite observations. *Sci. Total Environ.* 659, 912–922 (2019).

10. Lin, J., Tang, D., Alpers, W. & Wang, S. Response of dissolved oxygen and related marine ecological parameters to a tropical cyclone in the South China Sea. *Adv. Space Res.* 53, 1081–1091 (2014).
11. Chacko, N. Chlorophyll bloom in response to tropical cyclone Hudhud in the Bay of Bengal: Bio-Argo subsurface observations. *Deep Sea Res. Part Oceanogr. Res. Pap.* 124, 66–72 (2017).
12. Ye, H. J., Sui, Y., Tang, D. L. & Afanasyev, Y. D. A subsurface chlorophyll a bloom induced by typhoon in the South China Sea. *J. Mar. Syst.* 128, 138–145 (2013).
13. Chai, F. et al. A limited effect of sub-tropical typhoons on phytoplankton dynamics. *Biogeosciences* 18, 849–859 (2021).
14. Cheng, L., Zhu, J. & Sriver, R. L. Global representation of tropical cyclone-induced short term ocean thermal changes using Argo data. *Ocean Sci.* 11, 719–741 (2015).
15. Hu, A. J., Kuusela, M., Lee, A. B., Giglio, D. & Wood, K. M. Spatio-temporal methods for estimating subsurface ocean thermal response to tropical cyclones. *ArXiv201215130 Stat* (2021).
16. Sala, J. et al. Estimating Tropical Cyclone-Induced Changes in the Upper Ocean from Argo Profiles. in 103rd AMS Annual Meeting (AMS, 2023).
17. Johnson, K. S. & Bif, M. B. Constraint on net primary productivity of the global ocean by Argo oxygen measurements. *Nat. Geosci.* 14, 769–774 (2021).
18. NOAA. NHC Data Archive. <https://www.nhc.noaa.gov/data/#hurdat>.
19. Cornec, M., Huang, Y., Jutard, Q., Sauzède, R. & Schmechtig, C. euroargodev/BGC ARGO\_R\_WORKSHOP: BGC-Argo-R v3.0. (2022) doi:10.5281/ZENODO.5028138.
20. Kelley, D. & Richards, C. oce: Analysis of Oceanographic Data. (2023).

## Chapter Four: Conclusions for tropical cyclones and OMZs

This dissertation explored the impact of tropical cyclones (TCs) on subsurface processes in the eastern tropical North Pacific (ETNP) oxygen minimum zone (OMZ). An opportunistic sampling cruise, following Hurricane Bud in 2018, provided the bulk of observations. These were complemented with a variety of above, and below water remote sensing tools.

Oxygen minimum zones are coastal and open ocean habitats with consistently low oxygen levels. They play a crucial role in biogeochemical processes, impacting microbial communities and influencing primary production. Tropical cyclones frequently form over the ETNP OMZ. Our current understanding of the impacts of these powerful storms on this important biogeochemical biome remains limited, and this work was the first of its kind to explore the connection between TCs and the ETNP OMZ.

An intense shoaling of the top of the OMZ was observed from the process cruise, above all known reference values (Chapter One). This was attributed to microbial consumption of labile organic matter, associated with the plankton bloom, itself likely a result of subsurface storm mixing and input of nutrients. Subsurface data collection was beyond thorough. It included profiles of physical and optical properties, and water sampling with an exhaustive characterization of the organic matter. Continuous sampling at two depths at the most impacted station actively detected microbial presence using RNA methods, thereby documenting active bloom biota that includes known OMZ microbes. Satellite imagery provided the space and time context for the subsurface measurements. Imagery showed a persistent Chlorophyll feature over the most impacted cruise station. The use of modeled sinking organic matter, driven by satellite input variables, suggests TCs are associated in space and time with a significant proportion of the export out of the euphotic zone. Moreover, they are also associated with extreme positive anomalies, which are more likely to either enter and be consumed within the OMZ, or sink through to the benthos below. The multidecadal satellite time series captured the common occurrence of repeat TCs over a small oceanic region. Moreover, the passage of a weaker TC before Bud highlights the importance of viewing these disturbances not only in isolation but also in sequence.

A second study of high-resolution subsurface sampling from sensors during the same cruise provided the context for developing an ecological-oceanographic theory that integrates a specific type of subsurface mixing induced by tropical cyclones (Chapter Two). This theoretical model, informed by the physics of geostrophic mixing and water density, has implications for carbon export, microbial ecology, and perhaps even the evolution of microbes that inhabit the deep chlorophyll habitats of oligotrophic TC regions in other locations around the world.

A third study used the autonomous robotic BGC-Argo float array to capture the dynamics of a similar subsurface response to a second separate hurricane (Olaf) in the same region of ocean as the primary research cruise (Chapter Three). Findings indicate increased subsurface biological activity and a shoaling of the OMZ. Differences between

storms may explain the more subtle nuances in the biological response. The oxygen profiles immediately following the storm showed incongruities that were indicative of chaotic, non-steady state conditions. The overlap in time between consecutive storms was captured in the profiles prior to Olaf, a deep chlorophyll feature briefly came into being, went away, and then reformed again after Olaf. This partially fits the conceptual model developed in the second study (Chapter Two).

The third study also looked at the scale of TC impacts in the central eastern region of the Pacific that encompasses the statistically significant bounds of TC impacts (Chapter Three). The array showed that OMZ depth change was less invariant to the multidimensional nature of the TC OMZ system than the absolute depth, when comparing post and pre profiles. Both were dependent on the precondition of the OMZ, mimicking what is known about plankton blooms and storm specific variability from that set of literature.

Tropical cyclones' numbers are inversely proportional to strength. Over the global domain, it's a geometric function. The bulk of this work explored the impact of a single strong hurricane but to understand the net impact over the OMZ future work should also look at the interplay of multiple weaker tropical cyclones. In addition, TCs are formed mostly on the southern and easterly boundary of the Northeast Central Pacific, as they travel north and westwards many pass through the equatorial upwelling zone and out into the open ocean. Potentially, entraining biota, or nutrients in the process. It is this author's educated guess that regions of the ETNP OMZ, whether coastal or open ocean, may be defined as 'hurricane alleys' with repeat TCs (days to millennia) summing to have ecological and evolutionary ramifications on the biota within.

Overall, tropical cyclones have important biological impacts and biogeochemical ramifications in the ETNP OMZ. This suggests further study.

# Appendix: Remote sensing of bioluminescent radiance: exploring the potential for increased biological information in an understudied signal

## Abstract

Bioluminescence, biologically produced light, is pervasive in the ocean, but underutilized as a remotely sensed biological state variable. This pilot study collected radiometric information at night in Tomales Bay, a coastal bay in California, known for its bioluminescent plankton. By sampling during different lunar phases (new/full moon), and environmental conditions when plankton blooms were expected to be strongest, the study successfully distinguished between water leaving radiance derived from sub-surface emission and lunar reflectance. Bioluminescence was visually apparent during the new moon but absent during the full moon. Microscopic analysis confirmed the presence of a known bioluminescent species during the new moon. Subsequent sampling indicated that several genera of bioluminescent dinoflagellates are common to the study site. The detection of elevated water leaving radiance suggests that commercially available radiometers can effectively capture radiance associated with observed bioluminescence, likely originating from known taxa of bioluminescent dinoflagellates.

## Introduction

Bioluminescence is an indicator of primary production, functional important components of ecosystems, changing biogeographic patterns due to climate change, species richness, and the vertical carbon cycling between the surface and mid-ocean depths. Nocturnal vertical migration is a major ecological event that is not sensible during the day. Despite knowledge of these relationships, bioluminescence is not widely used as an observational variable in the study and monitoring of the world's oceans.

Remote sensing methods that utilize the bioluminescent signal have the potential to provide quantitative information on biomass, and species composition of bioluminescent organisms in the ocean. Yet, we currently lack the observational tools to formalize basic relationships between aspects of the natural *in situ* bioluminescent signal and the organisms that contribute to these earth system processes. Research into the propagation of the natural signal *in situ* is needed to define the full light field for upscaling detection to sensors that rely on passive sensing via spectroscopy (e.g., ocean color satellites).

Development of a radiative transfer equation (RTE) that explicitly incorporates abundance and community composition will meet this need. Path finding field measurements designed to match up with currently active satellite assets could leverage existing infrastructure to remote sense bioluminescence. This work could inform future applications for the remote sensing community at large and provide guidance for future sensor designs.

A RTE connects information about the matter in a fluid, inclusive, to the light reflected off that fluid. Net light measured leaving the fluid will be a combination of light produced (bioluminescent organisms), and reflected light shining on that surface (lunar, solar, starlight, or anthropogenic sources) minus the light lost into the fluid. Ref.<sup>1</sup> is a useful entry point for relevant remote sensing terms and terminology.

The study set out to explore the following question: *Can passive remote sensing sensors be used to measure light produced from bioluminescent organisms?* The answer, from this study is **Yes**: The pilot study collected radiometric information at night in Tomales Bay, a coastal bay in California, known for its bioluminescent plankton.

The initial pilot study captured the two environmental states: a new moon and a full moon. Qualitatively, during those two important remote sensing states (AOPS), two different states of the plankton community were also captured. A strongly bioluminescent Dinoflagellates community during the new moon, and a non bioluminescent diatom community during the full moon. With water-leaving radiance in the visual spectrum greater during the new moon than the full moon.

Further work could translate these findings so they could be incorporated in current *in situ* sensing tools (e.g., Biogeochemical-Argo and Deep-Argo<sup>2</sup>), and planned spaced based missions (e.g., PACE<sup>3</sup>). Only focusing on measures such as Chl-a misses all the other biota in the ocean. A much more rigorous series of studies would be needed for this pilot study's results to be upscaled, but the findings here indicate that is a possibility.

All data collected during fieldwork is available upon request. The author's ORCID link contains up to date contact information: <https://orcid.org/0000-0002-8281-9620>

## Background

Bioluminescence, light emitted by living organisms, is a ubiquitous phenomenon in the oceans<sup>4</sup>, that has intrigued humankind since antiquity<sup>5</sup>. Previous research into bioluminescence has led to solid mechanistic understanding at the sub-organism scale, and a general picture of the varied ecological and biological correlations to the bioluminescent signal<sup>4</sup> (henceforth the “biolum signal”). Bioluminescence, light emitted by living organisms, appears across the tree of life in the marine realm, and is largely pangeographic<sup>6</sup>. Bioluminescence is found in major marine groups including bacteria, dinoflagellates, cnidarians, ctenophores, cephalopods, fishes, and multiple taxa of arthropods. The biolum signal is the intensity, and/or spectral shape in the visual wavelengths of the electromagnetic spectrum. The light duration pattern, flash kinetics, is also an informational component of the signal. This signal may be sensible below the water surface or above the water surface.

The intensity of light produced is a positive function of bioluminescent organism abundance, and may be a proxy for heterotrophic biomass<sup>4</sup>. *In situ* below water studies, have shown the coefficient of variation flash intensity can differentiate zooplankton from dinoflagellates<sup>7-9</sup>.

Bioluminescence is represented across marine trophic levels, yet it is unevenly distributed phylogenetically<sup>4,10,11</sup>. The heterogeneous distribution across the tree of life suggests it has evolved independently many times. Despite multiple evolutionary

emergences, the general form of chemical reaction that emits light is conserved across taxa. The secondary pathways involved may be unique to species or taxonomic lineages, yet the specific light emitting process always involves oxidation of a substrate, usually mediated by unique enzymes. In many animals, a secondary photoprotein reacts with the initial photon producing reaction to change the specific light emitted from the organism<sup>12</sup>. Species specific secondary pathways can produce species specific spectral signals.

Individual color profiles have been collected for bioluminescent taxa, and species<sup>4,9,13,14</sup>. Coupling species libraries with observations of the signal could provide an additional means to measure species diversity patterns in the oceans. However, spectral information has not been cataloged for many bioluminescent species<sup>15</sup>. Bioluminescence occurs in the visual portion of the electromagnetic spectrum. Strong convergent pressure has selected for the dominance of blue and green wavelengths, which travel best through seawater. Most known species have peak emission spectra between 440 - 505 nanometers, with an average at 470 nm. Shallower species' average peak is 490 nm and deeper species 475 nm<sup>11</sup>. Spectral shifts with depth have been documented in higher level zooplankton taxa in the Pacific, with deeper living species having shorter wavelengths than shallower species<sup>6</sup>. However, work investigating spectral shifts between surface littoral and ocean habitats is lacking, despite the known differences in the optical properties of these waters<sup>16,17</sup>. A thorough review of bioluminescence studies<sup>4</sup> shows that a strong body of work has been directed at the importance of bioluminescence in both environments.

Satellite remote sensing is an indispensable tool for observing biology in oceanic and coastal habitats<sup>16</sup>. Chlorophyll-a is the most common biological variable that is available to be remotely sensed through optical space-based methods. However, inferences based on Chlorophyll-a miss the overwhelming diversity of non-autotrophic organisms in the ocean<sup>18</sup>. Because these measurements occur during the day, they miss the important ecological dynamics that occur only at night. Novel work has shown that space-based remote sensing of naturally occurring nocturnal ocean bioluminescence is possible<sup>19,20</sup>. Passive remote sensing of bioluminescence, via *in situ* or space-based methods, can provide useful observational information about the biological, and ecological state of marine environments due to the prevalence of bioluminescence in the ocean.

There have been limited, above water radiance studies on measuring the biolum signal *in situ* e.g., refs<sup>21,22</sup>. *In situ* below water sensing, has primarily been based on the measure of bioluminescence potential (BPOT). BPOT methods induce light production through mechanical disturbance of water<sup>23</sup>. Disturbance techniques vary between studies, and identification of dominant organisms responsible for the light field may be biased by different BPOT sampling means<sup>24</sup>. This active measurement methodology does not integrate well with space-based optical remote sensing techniques that are passive, and best suited to measure the natural biolum signal over the full domain of the global ocean. Bioluminescence emission occurs naturally in the ocean largely due to physical disturbance caused by waves, and other physical oceanographic processes<sup>25-27</sup>.

Major field programs that have investigated the relationship of environmental forcing and the biolum signal find long term patterns punctuated by short term variability<sup>7,28,29</sup>. Environmental relationships include strong diel patterns in BPOT,

periodicity related to lunar cycles, shoaling above the thermocline, and community composition shifts in dominant bioluminescent organisms<sup>6,30</sup>. Heterotrophic dinoflagellates are often dominant<sup>30</sup>, although those relationships are scale dependent<sup>6</sup>. Predictive models of the BPOT based on environmental variables as input have been developed from these field studies<sup>31,32</sup>.

Environmental control of bioluminescence is not limited to eukaryotes; an in vivo study of bacterial bioluminescence showed that light production occurs at specific nutrient availability<sup>33</sup>, making it a proxy for nutrient content of water masses in oligotrophic waters. In the central Pacific gyre bioluminescence has been observed in association with thin layers<sup>34</sup>, small scale but important phenomena impacting biology in the ocean. Chlorophyll-a is one of the most important biological variables that is available to be remotely sensed through optical space-based methods. Mapping of long term datasets of BPOT, and remote sensed Chlorophyll-a show similar patterns of increased intensity along the upwelling regions of western Africa with the pattern quantitatively most similar in areas of high productivity<sup>4</sup>. This correlation varies between studies, as the relationship is dependent on spatial scale related to physical processes and biological history of larger water masses<sup>35</sup>. Known bioluminescent species occur during harmful algal blooms<sup>36</sup>.

The biolum signal may help distinguish shoaling of the poorly parameterized global diel vertical migration (DVM) through color shifts, at the surface. The DVM is a significant carbon pump between the surface and deep ocean, known to be highly bioluminescent, and currently biomass estimates vary by several orders of magnitude.

Space based remote sensing of the DVM is an exciting long term potential possibility. In the more immediate future, the scientific community could leverage the optical sensors<sup>37</sup> on the Biogeochemical-Argo array, which is already deployed and is actively being expanded and developed<sup>38,39</sup>. Integration of space based, and subsurface profiling floats is a goal of the optics community<sup>40</sup>.

To gain information from the biolum signal, we need a better quantitative understanding of the relationship between biota and the propagation of the signal. Radiative Transfer Equations (RTE) are the mathematical and theoretical models that are fundamental to remote sensing<sup>1,17</sup>, and provide this relationship. Bioluminescence is a type of internal source emission in RTE<sup>41</sup>. By knowing information about the light sources and the medium (Apparent Optical Properties, AOPs), RTE will give the solution for the sensed signal in the water column, and above the water surface. An inverse RTE gives a set of solutions, for the emission source and constituents of the medium (Inherent Optical properties, IOPs) given the sensed signal. Work on both forward and inverse RTE related to bioluminescence is reviewed by Rogovtsov *Et. al*<sup>42</sup>. A model of inverse RTE shows a spectral shift in above water radiance induced through varying the depth of emission<sup>21</sup>. Additional modeling work has shown that the biolum signal and IOPs must be considered contemporaneously for proper sensing of the biolum signal<sup>43</sup>.

Current efforts on forward and inverse RTE have not fully accounted for the identity and abundance of organisms in their equations. This is the main information to be gained in remote sensing of bioluminescence, and most relevant to the natural bioluminescence background radiation in the ocean. RTE development provides a necessary foundation for all future remote sensing of bioluminescence.

## Methods

Sampling was conducted in Tomales Bay (see “Study Area” section below). Strong bioluminescence was expected following periods of upwelling and biological activity in the open ocean north of the bay. Extensive work<sup>44-46</sup> outside of the bay has characterized the bloom dynamic shift from diatoms to dinoflagellates, a very well-known biological community shift. Additional personal communication with tour operators (who run kayak tours to see the bioluminescence at night) indicated peak bioluminescence was often observed during southerly, winds following storms, indicating a relaxation of upwelling, and inducing very calm conditions in the bay. Sampling was planned around the potential spring bloom using NOAA weather forecast for winds speeds north of the Bay.

Inclusive sampling (below and above water spectroscopy, collection of biota, and measurement of physical water variables) was conducted inside Tomales Bay with the eventual goal to construct a forward RTE. The lunar cycle was the primary determinant of field sampling in order to capture the large range of lunar irradiance and its impact on AOPs of the RTE, as well as the expected midnight peak in bioluminescence intensity<sup>6</sup>.

On the new moon the night of 2019-05-02 and, over two days and one night during the full moon 2019-06-16 and 17th, radiometric data was collected. Stations were measured inside the bay and into the open ocean. Nighttime sampling occurred in the bay only. Full sampling in June was done in order to collect reference spectra across the natural gradients of the bay out to the open ocean (open ocean profiles to a depth of 20 meters) the day before and after the full moon sampling. This data is available upon request but not presented here. It could prove helpful in future RTE development.

Three Trios RAMSES hyperspectral radiometers<sup>47</sup> were used for spectral measurements. One submersible radiance probe (ARC-VIS), one submersible irradiance probe (ACC-VIS), and an upward facing stationary irradiance probe (ACC-VIS) mounted skyward on the work vessel. Wavelengths measured were 320-950 nm. Because of noise during low light operations at the extreme ranges, and interest in the visible spectrum, only information from 400-700 nm is presented here.

Several stations were measured inside the Tomales Bay and into the open ocean. Above water and vertical profiles were conducted with radiometers. Sea water parameters were measured to a depth of 5 meters, but not analyzed here. Water samples were collected and preserved with Lugol's solution for later microscopy (40x-100x Nikon compound microscope) to identify plankton. Water samples were collected at varying depths (0-10m) per station using a custom 750ml bottle sampler. Allocated to 50 ml vials with a 1-3% Lugol's solution<sup>48</sup> (different strengths for differential preservation of diatom chains, and dinoflagellate amphiesma/thecae). Water samples were later filtered onto a Durapure membrane 0.22 µm GV filter and are currently being stored in a -80 degree freezer. Because sampling was intended for microscopy, more stringent eDNA clean methods were limited to lab processing only.

Additional water samples were collected, using a 1-liter Niskin bottle, during the night of 2023-05-03/04, ~ 2 days prior to a full moon. This sampling time was chosen because it mimicked oceanographic conditions during 2019-05-02. Five and 10 meter water bottle samples were taken at Station D2. Samples were collected for microscopic

identification of dinoflagellates, and for future environmental DNA (eDNA), and quantitative PCR (qPCR) analysis. As best as possible on a small vessel, all common eDNA clean methods<sup>49</sup> were followed for sample collection, and all laboratory work (contamination avoidance, bleach sterilization, etc.). Samples were aliquoted based on intentional replicates and sample sizes to be used for both potential qPCR and eDNA processing, with replicates, and some samples set aside for volume sensitivity analysis, as well as lugol's preservation. Environmental DNA can give site characterization between dates, where qPCR can give quantity of dinoflagellates and/or bioluminescence genes<sup>50-52</sup> at specific sites, as well as individual depth based samples. The most information over the course of the project was compiled for Station D2 with an emphasis at the 5m depth.

Microscopy was conducted within 10 days of the 2023 sampling. Samples collected in 2023 for microscopy were not preserved with Lugol's solution. This made dinoflagellate identification easier, but diatoms did not preserve well. Simple attempts were made to grow plankton from collected seawater, but did not produce viable cultures of dinoflagellates. Twenty 22x22mm slides were examined (at ~0.05 mL per drop, ~ 1 ml total volume). The ref.<sup>53</sup> was used to approximate the genera of identifiable organisms. This is a reference for common central California species that contains reference microscope images. A few samples from the 2019 sampling dates, which had been preserved by Lugol's and stored in a 4 degree refrigerator, were re-analyzed under the microscope.

## Study Area - Tomales Bay

Tomales Bay<sup>48</sup> is a narrow bay, insulated from secondary oceanographic forcing<sup>29</sup>, Located at 38.2 N 122.2W on the central California coast. Approximately 50 miles north of San Francisco Bay, a well-studied region<sup>35,54</sup>. A primary reason for choosing this enclosed bay, as it eliminates the signal to noise issues that would hamper efforts to develop a robust RTE. That is, extreme bioluminescent events are common, and are explained by well studied upwelling phenomenon, but the bay itself is protected from the long period swell, common to the surrounding coast.

Several permanent buoys that collect physical and biological data are located in close proximity to study stations. The single opening of the bay allows for sampling along a natural gradient of IOPs and physical oceanographic variables<sup>48</sup>. Previous cruises in the area provide reference spectra for water properties and plankton community composition, including known bioluminescent dinoflagellates<sup>44,55</sup>. The replicate deep and shallow pattern along the major axis of the bay is ideal for bioluminescence remote sensing validation and more traditional work on coastal remote sensing as the alternation of shallow and deep sites<sup>56</sup> creates a series of replicates to control for benthic induced noise; reflected light.

Logistically, the D2 station (Fig. 2) is less than 2 km from a well maintained boat ramp. It is adjacent to a channel marker making for easy navigation at night. A small beach in a nearby cove, could easily be used for a temporary sample processing station. The UC Davis Bodega Bay Marine lab and UC Berkeley Point Reyes Field station provide laboratory and accommodation space for traveling researchers.

Tomales bay is well suited for developing the RTE, but it is not appropriate for dependably satellite match up for open ocean work (consistent cloud cover, enclosed area/mixed pixel issues). Prior to this study and matriculation to UC Merced, the author repeatedly reconnoitered the area, recreationally.

## Results and Discussion

Water leaving radiance was stronger during the new moon than the full moon (Fig. 3) which correlates with initial microscope work that suggests higher dinoflagellate densities during that time, and greater prevalence of diatoms in June. Initial microscope work was only qualitative, and not systematic. Vertical profiles indicate a peak of 466 nm at 6 meter depth, which correlates to the above water average spectral shift of ~ ~100 nm collected here (Figure 5), and in the primary published models on depth of emission<sup>22</sup>.

The reflectance values in Fig. 3 suggest two completely different surfaces. Reflectance values are a standard way to account for variation in incoming light, while slight differences in wavelength specific reflectance are used for ocean color variables (e.g., Chl-a) the values here indicate two different surfaces, which is not the case. This is due to the bioluminescent light leaving the water surface. Values like these might otherwise be rejected as an error, if not accounting for an internal light source.

Natural environmental forcing produced visually noticeable bioluminescence inside the bay, with the water leaving radiance orders of magnitude more intense than the most similar study<sup>22</sup>. A times series buoy<sup>72</sup> in the bay (Fig. 2) showed the highest Chl-a values of the year at 30.47 ( $\mu\text{g/l}$ ), occurred on April 30th, four days before sampling, then dropped to 13.30 ( $\mu\text{g/l}$ ) by May 4th. Significant satellite chlorophyll features were present outside of the bay April 24th - May 1st.<sup>73</sup> Traditional Bakun Upwelling indices at 39N 125W were elevated starting on 04/19 and lasted past the sampling date. The peak daily integrated value of 286 occurred on 04/27. Units are cubic meters per second along each 100 meters of coastline<sup>74</sup>. Upwelling indices were lower, but still positive for June sampling. Chl-a values at the buoy were between 10.33 - 3.99 ( $\mu\text{g/l}$ ) from June 15th - 18th.

Below water profiles were not as conclusive as above water measurements, due to the preliminary nature of this study (see “Limitations” section). Figure 5 is shown to illustrate confounding factors and potential information in unfiltered subsurface radiometric profiles. Only minimal processing was conducted (removal of negative intensity values). Also, the calibration profile was set to air rather than water to facilitate quickly sampling above and below water spectra. This affects the absolute intensity values, but not associated with wavelengths in a relative sense. That is, the shape of the histogram is the same, but all values are different. Therefore, no extrapolations were made based on intensity and biomass estimates. It should be noted that even without secondary recalibration the intensity values are much lower than BPOT studies<sup>22</sup>, yet still measurable with passive radiometers.

Surface spectra patterns which may be due to a number of factors that would need further investigation. For example, the profile at Station S2-1M was likely due to bottom reflectance from lunar light, which was why that station was sampled. Whereas the peak at Station D1-6M may indeed be due to a bioluminescent organism (Fig. 5). That is even

with lower net activity (inferred lower densities), and high background illumination a deep enough probe can capture bioluminescent organisms.

The range of values in upwelling radiance during June sampling in the upper 5 meters showed high variability (Fig. 4). Intensities at known bioluminescent wavelengths are present, but noise cannot be excluded. Lack of stations and points is due to removing noise. Trends are shown for how points would influence above water spectra. Importantly high intensity may be due to lunar reflectance off of CDOM or particulate matter. Importantly all subsurface profiles should be viewed as preliminary only (see ‘Limitations’ section)

Water samples were collected in May of 2023 at Station D2 at 5m and 10m depth, to provide research closure, via additional microscopic identification. No radiative sensing was undertaken. Strong bioluminescence was visually observed at the surface through the night. Like the 2019 May sampling, Chl-a was high in satellite images. This was visible on April 30th, but continuous clouds in daily satellite images obscured the ocean area outside the bay, past the sampling date. Buoy data is not yet available. Upwelling was positive but lower. The moon phase was full.

Table 1 shows a list of dinoflagellates identified to possible genera for 2023 sampling. Genera here, match studies outside of the bay<sup>44</sup>, and inside of the bay<sup>48</sup>. With the majority known to be bioluminescent, and/or toxin producing. Species like *Lingulodinium polyedra*, (light and toxin producing) have been extensively studied in terms of mechanic stimulation, shear stress and photon production.<sup>26,27</sup> There are even studies on the spectral reflectance of daytime blooms.<sup>75</sup>

Blooms of this species are well known to cause harmful blooms/red tides in southern California<sup>67</sup>. Reanalysis of water samples collected during the night of May 2019 , that were collected in the channel between stations D1 and D2 at 10m, were found to contain *Lingulodinium sp.* and one individual appeared to be *Lingulodinium polyedra*. This author is not a dinoflagellate expert, lugol's preservation, and the small size of the organism, means this identification is cursory at best. Unarmored circular dinoflagellates were encountered, but not identified, *Dinophysis sp.* appeared in multiple slides. No attempt was made to quantify species or taxa. The cursory genera information may be useful for selection of targeted primers in future studies. That would be highly recommended to confirm findings here. Ref<sup>76</sup>. includes additional plankton species identified off the shelf near the open to Tomales Bay.

Vertical and horizontal net tows were attempted to supplement Niskin bottle water collection. Horizontal tows quickly become clogged with substantial organic matter. Much of it was seagrass material, this material was prevalent in microscope slides as well. Depth and resistance indicated strong tidal flows temporally across the slack tidal state. Current resistance could be stronger at depth, perhaps indicating tidal flows along a salt wedge. If present, a salt wedge would concentrate matter (see Chapter 2), and influence IOPS. Any high concentrations of organic matter would be important, and confounding factors in future RTE development. This would be the remote sensing variable; colored dissolved organic matter (CDOM), which absorbs in the short wavelengths visual spectrum and therefore would be expected to obscure the bioluminescent signal. It is certainly feasible that CDOM was present during May 2019 sampling, if so it did not completely obscure the above water signal.

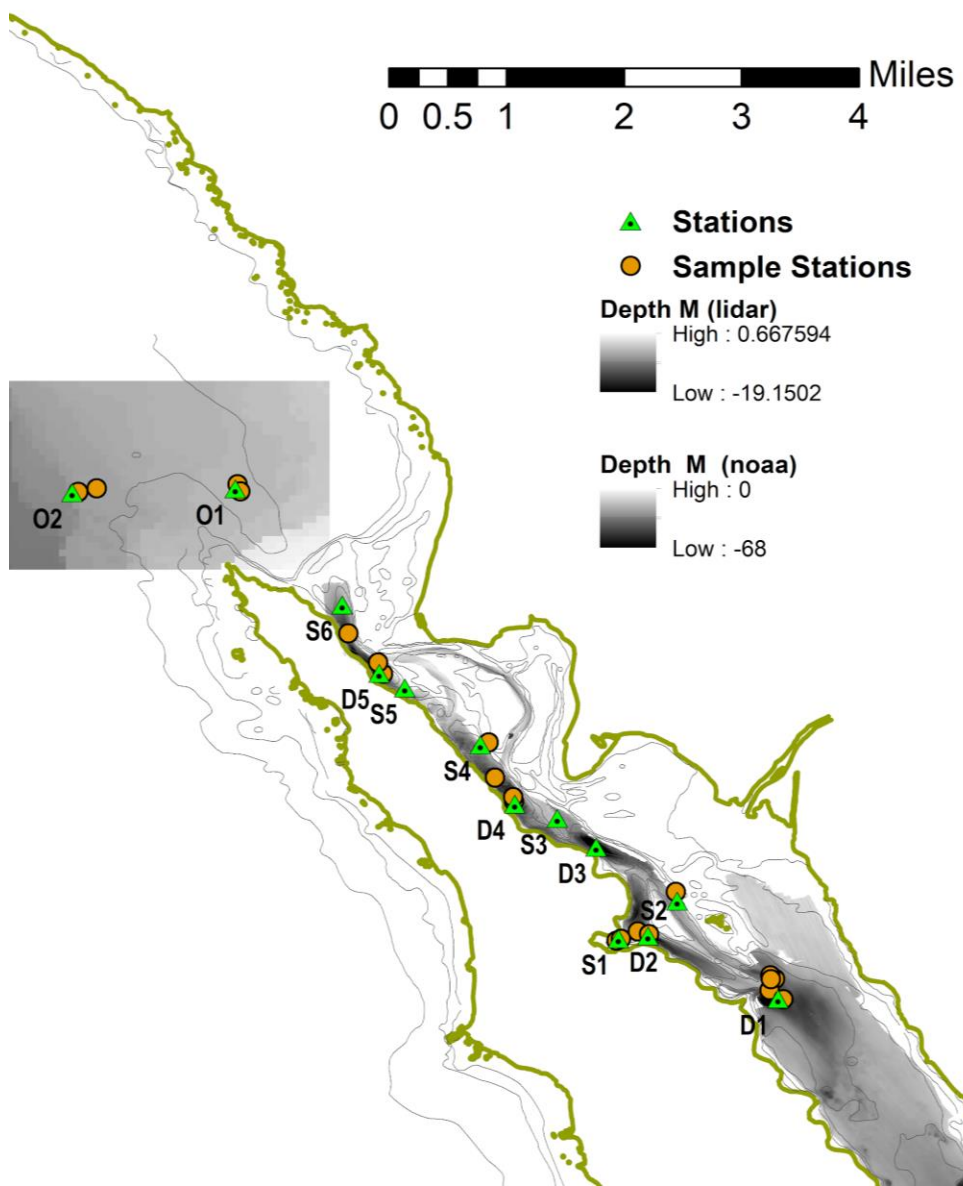
Qualitatively, bioluminescence was observed visually during the new moon and full moon in May 2019, and May 2023, but not during the Full moon in June 2019. One only has to stir their hand in the water to see this. One will notice what looks like flashes emitting from flocculent material. It may be that mixotrophic dinoflagellates are feeding on POC. Detrital matter and aggregates were common in all slides (2023 water analysis and reanalysis of 2019). Organic matters appeared to be a mix between sea grasses and macro algae.

At this juncture knowledge of IOPs, and organic matter constituents, is only vaguely speculative. Future work would need to constrain the two state variables that describe the optical properties of Tomales Bay: net absorption, and scattering. Fortunately, these methods are mature, and specialized equipment exists for this purpose. If those methods and equipment were deployed simultaneously with methods of this pilot study, then a forward RTE could be constructed. This equipment was not available during the initial sampling.

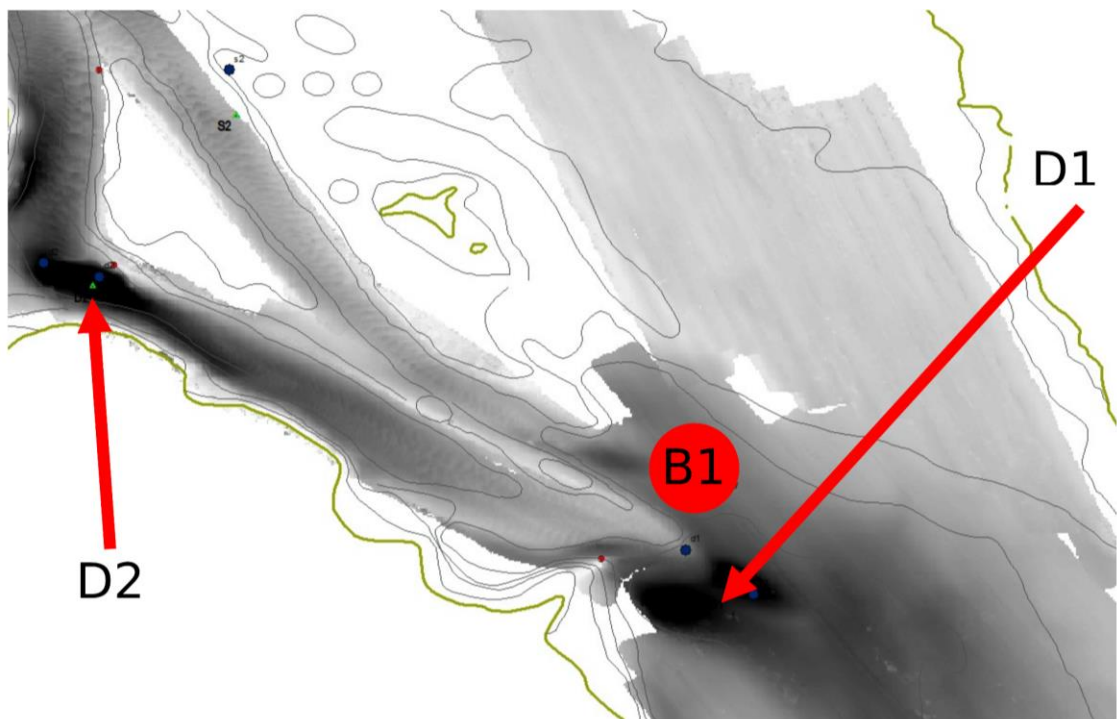
Bioluminescence is already a term that can be included in radiative transfer models, software, and equations. Common practice includes setting it to a constant or ignoring it. Another common practice is *in situ* dark calibration of radiometers at sea during the night. This pilot work suggests altering methods in the above cases when conditions apply. This dark calibration impacts multimillion dollar projects used to construct global models, for billion dollar satellites.

While the bioluminescent signal will probably have negligible impact on ocean color sampling by satellites during local solar noon (many orders of magnitude less than refinements of atmospheric corrections); It will likely have a significant impact on subsurface profile arrays such as the BGC-Argo floats equipped with radiometers. These arrays are deployed in order to better understand the carbon sequestration over the full ocean domain, and operate below the photic zone where bioluminescence occurs continually. Improving calibration and correction techniques here could help better understand the total carbon burial happening in the ocean, far more impactful than the edge case of Tomales bay biological activity.

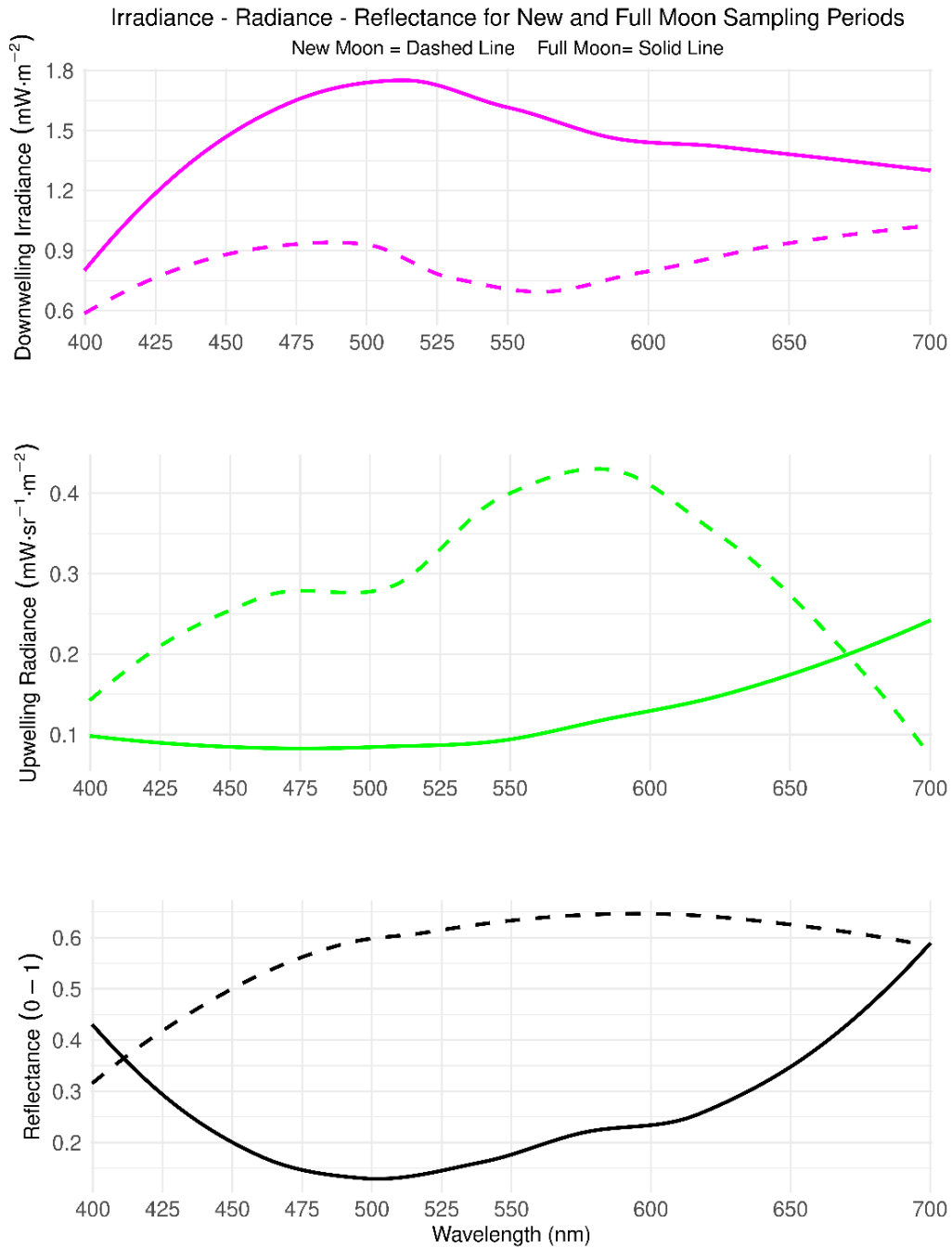
This study was first necessary step in a more complicated path-finding project; coupling available databases, global satellite products, and field reference and calibration studies to develop an inclusive Radiative Transfer Equation<sup>1</sup> (RTE) for water leaving bioluminescent radiance via the inclusion of the abundance and identify of bioluminescent organisms.



**App. - Figure 1:** Map of stations and repeat sampling. O indicates ocean, with inside the bay as either D deep (>15m) or, S shallow. High resolution lidar bathymetry was used to map the depth inside the bay, with a coarser gridded dataset for the ocean stations. Both are freely available from NOAA's Coastal Management Office. Yellow dots "Sample Stations" are averaged GPS of actual measurements. Green triangles are static station markers.

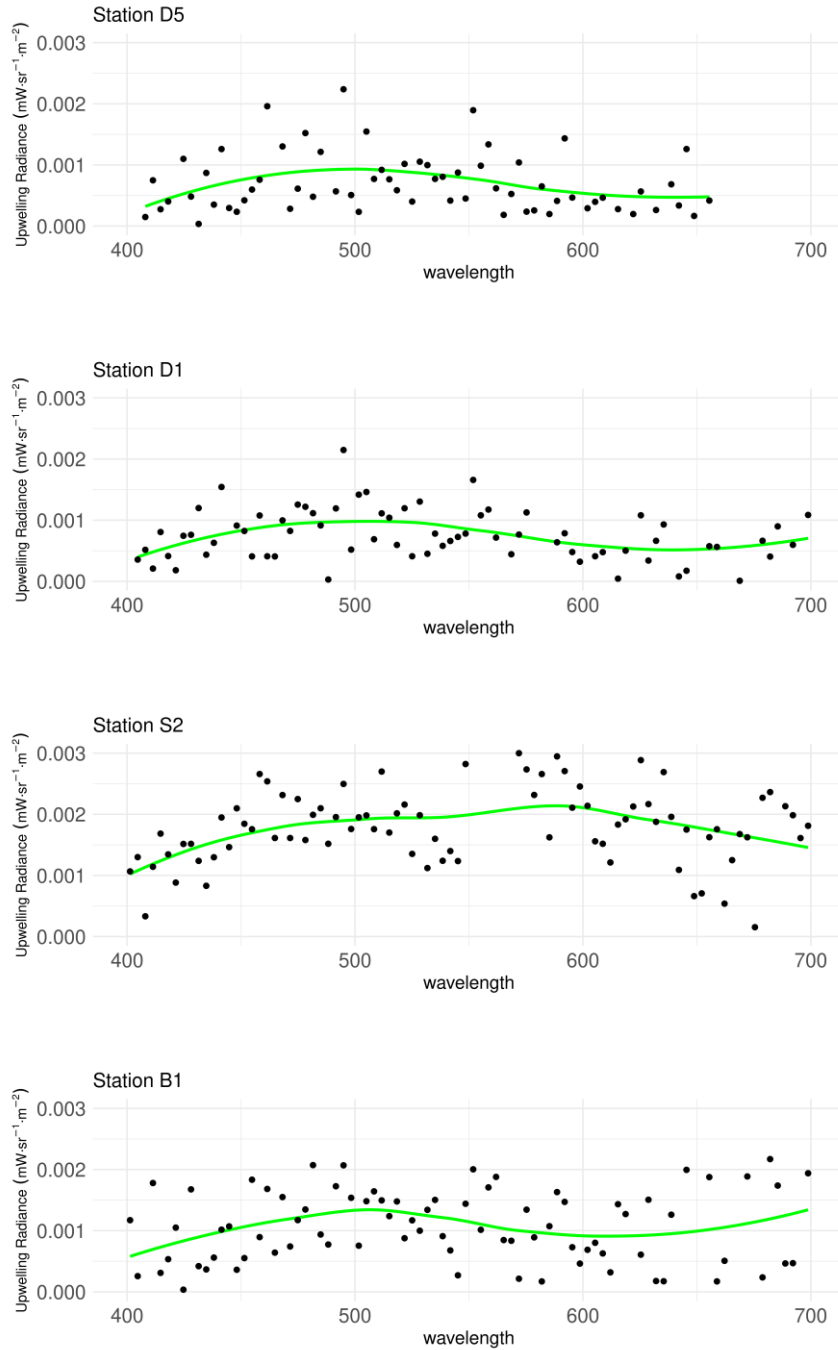


**App. - Figure 2:** Subset map from Figure 1 of stations and repeat sampling. Red arrows indicate stations D1 & D2, the most important for this study. Note sampling at B1 was added in June 2019 as it is close to a moored subsurface science buoy, operated by the Bodega Bay Marine Lab. Hog Island is the ca. center of image for reference. Gray to black in image indicates increasing depth from Lidar data used in Figure 2 (scale the same).

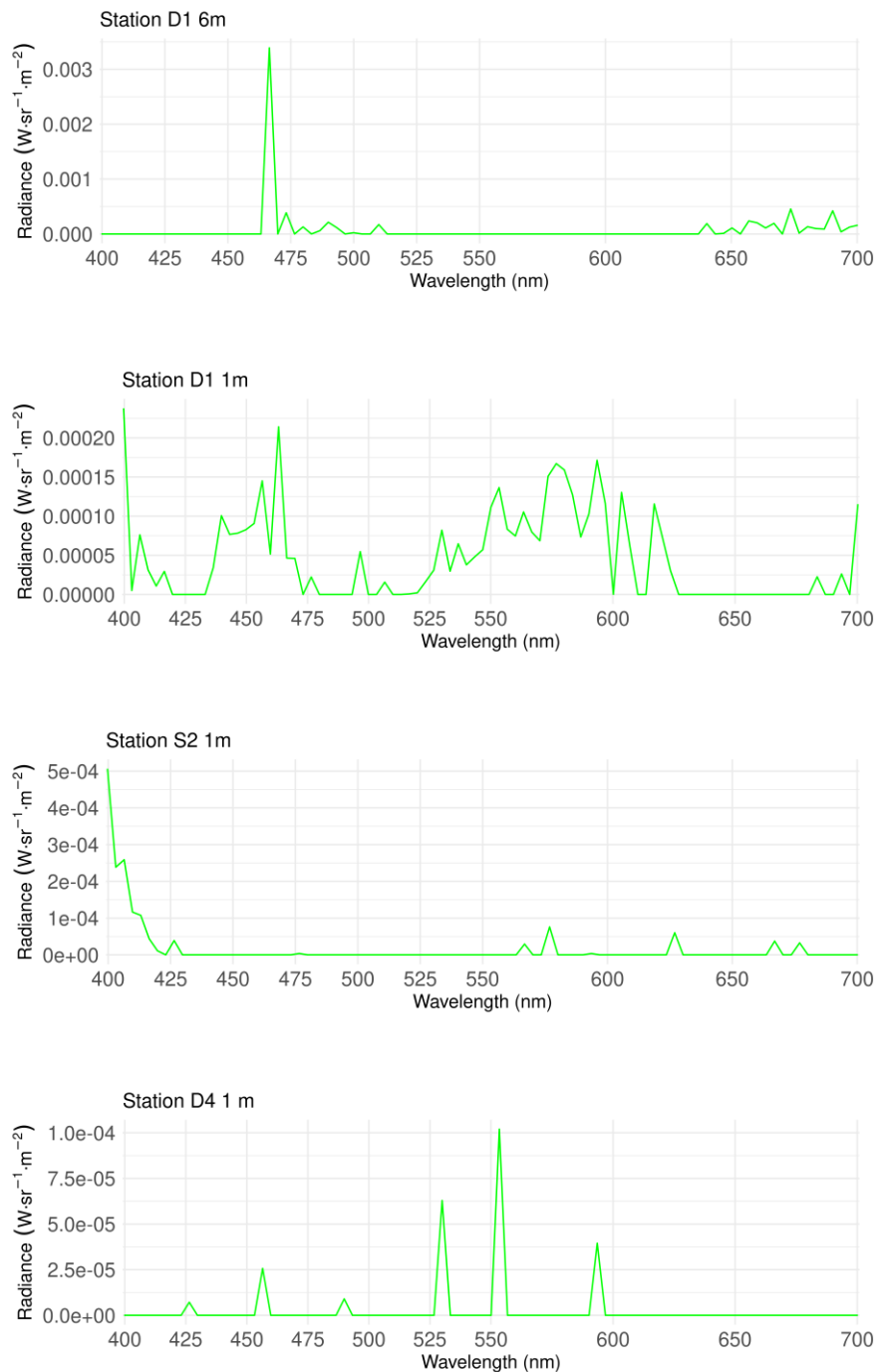


**App. - Figure 3:** Full moon indicated by solid lines, new moon dashed. Lines are mean for all sites per sampling night. Top panel is downwelling irradiance, incoming moonlight a meter above water (magenta). Middle panel is water leaving/upwelling radiance (green). Units differ. Bottom panel is reflectance (black), the ratio of upwelling energy to incoming energy ( $\pi * \text{radiance}/\text{irradiance}$ ). Does not take into account the

moon angle, assuming all angles are nadir. Reflectance values over one were excluded. X-axis is wavelength.



**App. - Figure 4:** Integrated nighttime subsurface radiometric profiles, upwelling radiance - downward facing probe, for June 2019 full moon sampling. Trends are means for integrated values (points) for 0-5m for all profiles per station. Y-axis is intensity, x axis is wavelength. From top panel:: Station D5, D1, S2, B1 (see Figure 1).



**App. - Figure 5:** Single nighttime subsurface radiometric profiles, upwelling radiance - downward facing probe, for June 2019 full moon sampling. Y-axis is intensity, x axis is wavelength. Panels are specific depths at three stations. From top panel: Station D1 6m, Station D1 1m, Station S2 1m, Station D4 1m.

Intensities at known bioluminescent wavelengths are present, but noise cannot be excluded. The strong signal @ 466nm in the upper left panel is a common wavelength for bioluminescent producing marine taxa.

**App. - Table 1:** Identified dinoflagellate genera from May 2023 sampling at Station D2. \* Slash indicates either one of the two genera, or species whose taxonomic classification have changed from the first to the second genera. HAB species indicates harmful bloom species, an inclusive term for single species, whose blooms coincide with production of toxins<sup>53</sup>. Known to be bioluminescent is largely from ref<sup>24</sup>, but also from main identification reference<sup>53</sup>.

Genera	Contains HAB species	Known to be Bioluminescent
<i>Gymnodinium</i>	Yes	No
<i>Gonyaulax/Lingulodinium*</i>	Yes/Yes	Yes
<i>Dinophysis</i>	Yes	No
<i>Protoperidinium</i>	Yes	Yes, many species
<i>Alexandrium</i>	Yes	Yes, many and common species
<i>Amphidinium</i>	No	No

## Limitations

There are many limitations to this project, and the potential future directions. Instead of fleshing them all out, *ad nauseam, ad infinitum*, below are some tractable methodological improvements for a hypothetical future next steps.

The new moon sampling of May 2019 was the first ever attempt to deploy radiometric equipment from a small zodiac at night, by all researchers involved. June sampling was deployed from a slightly larger craft which allowed for better deployment of vertical casts and quicker transits between Stations.

Subsurface profiling can inadvertently induce bioluminescence, and this observational bias will need to be adjusted for. Downcasts will create proceeding bow waves<sup>77</sup>, and shear. Upcasts will be far more disruptive because of the movement of the probe cage and attached lines. Both will increase the light produced as compared to the background signal, and then cause a time lagged depletion of light production. Sensitivity analysis will need to be conducted for both sensor integration time and time parked at depth. Moored deployment of above and/or underwater probes could address this. Deploying a moored array in congruence with the BOON observation buoy in the bay will provide co-occurrence of other important oceanographic state variables.

Use of multiple biological water sample tests, (qPCR and eDNA), can quantify dominant light producing organisms, while also accounting for secondary organisms that may contribute to full the light field<sup>4,29</sup>, (e.g., larger nekton). eDNA provides a reference point for future corrections of wavelength specific species identification, as the full diversity of bioluminescent producing organisms is not fully known.

## Future Work

### At Tomales Bay

The pilot study here, may be used to inform further studies. Future work, accounting for long term trends and seasonal changes (spring and summer biomass peaks), could deploy moored radiometric equipment<sup>3</sup>. Additional opportunistic sampling could be used to capture meteorological and upwelling events that are fundamental to shaping community composition and cause shifts in IOPs between Case 1 and Case 2 waters (winter storms, summer upwelling<sup>44</sup>). Opportunistic sampling would inform the boundary conditions of the RTE regarding wind and sea surface roughness<sup>26,57</sup>. Previous modeling of bioluminescence used an ensemble of known bioluminescent wavelengths as input for their source emission term<sup>21</sup>. *In situ* sampling could allow for relationships between species collected *in situ* and measured wavelengths as input into a RTE (for example equation 5.107 from<sup>17</sup>). Common modeling software (HydroLight) and methods<sup>17</sup> could be used for the bidirectional exploration of the RTE. With the model constrained by field measurements collected, and previous work used as guidance.

Microscopy could be used to enumerate dinoflagellates<sup>58</sup>. With bottle and vertical bongo nets used for the collection of both zooplankton and plankton. To supplement these species identification methods, collection and processing of Environmental DNA samples could be undertaken. This gives a consistent and systematic method to identify all members of the pelagic community<sup>18</sup>, allows for integration with future methods, as set out by the marine biology observing network initiative<sup>16</sup>, and can identify members of local plankton that are hard to identify using microscopy<sup>44</sup>. Once methodologies are standardized (See “Limitations” section), future workers could enlist the two kayak tour companies that operate regular excursions in Tomales, to conduct citizen science, through collection of water samples for the California eDNA project. Initial informal conversations on site with staff of tour companies suggest positive interest.

### Beyond Tomales Bay

Tomales bay is well suited for the initial development of a RTE, but it is not appropriate for dependably satellite match up (consistent cloud cover, enclosed area/mixed pixel issues). The cloud cover issues may be useful for model development; as intermittent clouds during sampling in June 2019 means that variation of instantaneous downwelling irradiance measurements may be used to tease out sources of noise. Noise could either be lunar light interacting with water constituents, or bioluminescent light interacting with the same constituents.

One possible location for satellite matchup is the HOTS/ MOBY site in the central Pacific gyre off of Hawaii. Conducting methods, (as discussed within), here provides a useful ground reference point for a large ocean biogeographic region and the biolum signal, which is needed to build satellite relationships in Case-1 waters. Additionally, the planktonic community is not dominated by dinoflagellates.

Importantly, spectral shifts caused by depth of emission are the biggest obstacle to questions on using biolum spectra shifts to identify the Diel Vertical Migration (DVM) in the open ocean, using space based sensors. Recent work has shown that day/night backscatter ratios from active lidar (CALIPSO) correlate to *in situ* ADCP biomass measurements<sup>59</sup> with the relationship most robust at the HOTS/MOBY station. Coupling spectral information from MODIS, which flies in the A-Train constellation, with CALYPSO, as well the GCOM-W1 platform that carries sensors for wind speed, which collects the full range of biophysical parameters could help resolve this obstacle.

To better explore the use of satellite match up to available biological databases, or field sites, existing datasets may be used. For example, a biomass correlation between VIIRS DNB<sup>60-62</sup> and continuous plankton recorder data<sup>63</sup>, represents a plausible path. With a regional focus on the North Atlantic (e.g., known spectra of the regional biota<sup>14</sup> can be assigned to this long term time series of planktonic species). Another avenue would be using existing MODIS data matched to diversity (e.g., OBIS records). This task could be informed based on results derived from work conducted at the HOTS/MOBY site. MODIS bands have variable signal to noise ratios, making it a useful case study for sensitivity and match-up.

Bioluminescence research dovetails with the NASA EXPORTS program<sup>64</sup>. Research started here, if expanded, could inform calibration protocols, allowing the eventual development of a derived bioluminescence product, from space based hyperspectral missions. The launch of the Plankton, Aerosol, Cloud, ocean Ecosystem (PACE) hyperspectral mission<sup>65,66</sup> is expected soon after the publication of this dissertation.

The results and conclusions of this pilot study are primarily focused on the above water radiance measurements, which translates directly to the use of similar probes at coastal regions of interest. Harmful algal blooms impact many beaches on the California coast (e.g., San Diego). One of the species potentially identified in this study is known to be both toxic and bioluminescent, and is responsible for red tides<sup>67</sup>. Normally beach closures require a day of lab testing, which introduces a time lag from collection to closure. A moored sensor could give managers the ability to make decisions in real time, and hours prior to sunrise and use by shareholders. Those few hours could make a significant public health difference. Indeed, an automatic warning system could be easily placed at high use beaches, and would only require a small power source.

Farther afield is the potential use on current and ongoing robotic research platforms. Autonomous surface drones such as the Saildrone can easily accommodate<sup>68</sup> radiometric packages for above water measurements, as a standalone sensor or for match up and calibration studies for satellite remote sensing. A core goal of the BGC-Argo program is measuring important biological variables under the surface. A subset of BGC-Argo floats do carry hyperspectral radiometers<sup>69</sup>. Trios sensors have been used on lagrangian floats in the past<sup>70</sup> and reanalysis of that data<sup>71</sup> might be useful in bioluminescent studies.

## Acknowledgments:

This spectroscopy field work was completed during a rotation in Dr. Erin Hestir's Earth Observation and Remote Sensing lab, with seed funding from the Environmental Systems graduate group. Dr. Hestir provided useful feedback on several grant submissions. June 2019 sampling was completed using a vessel loaned by Dr. Joshua Viers. Special thanks to Anna Rallings. The ES group also provided travel funding to present a poster of this work at the international workshop: "BIARRITZ (2019): Bridging International Activity and Related Research Into the Twilight Zone." in Southampton, UK. Microscope access, and helpful advice along the way, were provided by Dr. Michael N. Dawson. A very special thanks to Dr. Christiana Ade, Erik Bolch, and Daniel Gomez who volunteered to spend multiple sleepless nights drenched in the dew of Tomales Bay. But more than just fieldwork assistance I am thankful for the creative discussions on methods and research, without which it would have been impossible to try to develop this novel project.

## References

1. Mobley, C. D. Radiative transfer in the ocean. *Encycl. Ocean Sci.* **4**, 2321–2330 (2001).
2. Owens, W. B. *et al.* OneArgo: A New Paradigm for Observing the Global Ocean. *Mar. Technol. Soc. J.* **56**, 84–90 (2022).
3. Ahmad, Z. *et al.* PACE Technical Report Series , Volume 6 Consensus Document. **6**, (2019).
4. Haddock, S. H. D., Moline, M. A. & Case, J. F. Bioluminescence in the Sea. *Annu. Rev. Mar. Sci.* **2**, 443–493 (2010).
5. Carson, R. *The sea around us.* (Oxford University Press, USA, 1951).
6. Moline, M. A., Oliver, M. J., Orrico, C., Zaneveld, R. & Shulman, I. Bioluminescence in the sea. in *Subsea Optics and Imaging* 134–170 (Elsevier, 2013). doi:10.1533/9780857093523.2.134.
7. Batchelder, H. P., Swift, E. & Van Keuren, J. R. Pattern of planktonic bioluminescence in the northern Sargasso Sea: Seasonal and vertical distribution. *Mar. Biol.* **104**, 153–164 (1990).
8. Neilson, D. J., Latz, M. I. & Case, J. F. Temporal variability in the vertical structure of bioluminescence in the North Atlantic Ocean. *J. Geophys. Res.* **100**, 6591 (1995).
9. Moline, M. A. *et al.* Bioluminescence to reveal structure and interaction of coastal planktonic communities. *Deep Sea Res. Part II Top. Stud. Oceanogr.* **56**, 232–245 (2009).
10. Herring, P. J. Systematic distribution of bioluminescence in living organisms. *J. Biolumin. Chemilumin.* **1**, 147–163 (1987).
11. Widder, E. A. Bioluminescence in the Ocean: Origins of Biological, Chemical, and Ecological Diversity. *Science* **328**, 704–708 (2010).
12. Shimomura, O. *Bioluminescence: chemical principles and methods.* (World Scientific, 2006).
13. Herring, P. J. The spectral characteristics of luminous marine organisms. *Proc. R. Soc. Lond. B Biol. Sci.* **220**, 183–217 (1983).
14. Latz, M. I., Frank, T. M. & Case, J. F. Spectral composition of bioluminescence of epipelagic organisms from the Sargasso Sea. *Mar. Biol.* **98**, 441–446 (1988).
15. Widder, E. A., Latz, M. I. & Case, J. F. Marine Bioluminescence Spectra Measured With An Optical Multichannel Detection System. *Biol. Bull.* **165**, 791–810 (1983).
16. Muller-Karger, F. E. *et al.* Satellite sensor requirements for monitoring essential biodiversity

- variables of coastal ecosystems. *Ecol. Appl.* **28**, 749–760 (2018).
17. Mobley, C. D. *Light and water: radiative transfer in natural waters*. (Academic press, 1994).
  18. de Vargas, C. *et al.* Eukaryotic plankton diversity in the sunlit ocean. *Science* **348**, 1261605 (2015).
  19. Miller, S. D., Haddock, S. H. D., Elvidge, C. D. & Lee, T. F. Twenty thousand leagues over the seas: the first satellite perspective on bioluminescent ‘milky seas’. *Int. J. Remote Sens.* **27**, 5131–5143 (2006).
  20. Miller, S. D. *et al.* Honing in on bioluminescent milky seas from space. *Sci. Rep.* **11**, 15443 (2021).
  21. Oliver, M. J., Moline, M. A., Mobley, C. D., Sundman, L. & Schofield, O. M. E. Bioluminescence in a complex coastal environment: 2. Prediction of bioluminescent source depth from spectral water-leaving radiance. *J. Geophys. Res.* **112**, C11017 (2007).
  22. Moline, M. A. *et al.* Bioluminescence in a complex coastal environment: 1. Temporal dynamics of nighttime water-leaving radiance. *J. Geophys. Res. Oceans* **112**, 1–11 (2007).
  23. Herren, C. M. *et al.* A multi-platform bathyphotometer for fine-scale, coastal bioluminescence research. *Limnol. Oceanogr. Methods* **3**, 247–262 (2005).
  24. Marcinko, C. L. J., Painter, S. C., Martin, A. P. & Allen, J. T. A review of the measurement and modelling of dinoflagellate bioluminescence. *Prog. Oceanogr.* **109**, 117–129 (2013).
  25. Stokes, M. D. Bioluminescence imaging of wave-induced turbulence. *J. Geophys. Res.* **109**, C01004 (2004).
  26. Latz, M. I. & Rohr, J. Luminescent response of the red tide dinoflagellate *Lingulodinium polyedrum* to laminar and turbulent flow. *Limnol. Oceanogr.* **44**, 1423–1435 (1999).
  27. Maldonado, E. M. & Latz, M. I. Shear-stress dependence of dinoflagellate bioluminescence. *Biol. Bull.* **212**, 242–249 (2007).
  28. Marra, J. Bioluminiscence and optical variability in the ocean: An overview of the marine light-mixed layers program. *J Geophys Res* **100**, 6521–6525 (1995).
  29. Shulman, I. *et al.* A study case of bioluminescence potential dynamics in the Delaware Bay with observations and modeling. *Ocean Dyn.* **67**, 383–396 (2017).
  30. Dickey, T., Hartwig, E. & Marra, J. The Biowatt Bio-Optical and Physical Moored Program. *Eos Trans. Am. Geophys. Union* **67**, 650–650 (1986).
  31. Ondercin, D. G., Atkinson, C. A. & Kiefer, D. A. The distribution of bioluminescence and chlorophyll during the late summer in the North Atlantic: maps and a predictive model. *J. Geophys. Res.* **100**, 6575–6590 (1995).
  32. Marcinko, C. L. J., Martin, A. P. & Allen, J. T. Modelling dinoflagellates as an approach to the seasonal forecasting of bioluminescence in the north atlantic. *J. Mar. Syst.* **139**, 261–275 (2014).
  33. Ramaiah, N., Ravel, J., Straube, W. L., Hill, R. T. & Colwell, R. R. Entry of *Vibrio harveyi* and *Vibrio fischeri* into the viable but nonculturable state. *J. Appl. Microbiol.* **93**, 108–116 (2002).
  34. McManus, M. a. *et al.* Observations of Thin Layers in Coastal Hawaiian Waters. *Estuaries Coasts* **35**, 1119–1127 (2012).
  35. Lieberman, S. H., Lapota, D., Losee, J. R. & Zirino, a. Planktonic Bioluminescence in Surface Waters of the Gulf of California. *Biol. Oceanogr.* **4**, 25–46 (1987).
  36. Rogers-Bennett, L. *et al.* Dinoflagellate bloom coincides with marine invertebrate mortalities in Northern California. *Harmful Algae News* **46**, 10–11 (2012).
  37. Claustre, H. *et al.* *Bio-Optical Sensors on Argo Floats*.
  38. Stoer, A. C. *et al.* A census of quality-controlled Biogeochemical-Argo float measurements. *Front. Mar. Sci.* **10**, 1233289 (2023).
  39. Claustre, H., Johnson, K. S. & Takeshita, Y. Observing the Global Ocean with

- Biogeochemical-Argo. *Annu. Rev. Mar. Sci.* **12**, 23–48 (2020).
40. Claustre, Herve and Bishop, Jim and Boss, Emmanuel and Bernard, Stewart and Berthon, Jean-Francois and Coatanoan, Christine and Johnson, Ken and Lotiker, Aneesh and Ulloa, Osvaldo and Perry, Marie Jane and others. Bio-Optical Profiling Floats as New Observational Tools for Biogeochemical and Ecosystem Studies: Potential Synergies with Ocean Color Remote Sensing. in *Proceedings of OceanObs'09: Sustained Ocean Observations and Information for Society* 177–183 (European Space Agency, 2010). doi:10.5270/OceanObs09.cwp.17.
  41. McCormick, N. J. Inverse radiative transfer problems: A review. *Nucl. Sci. Eng.* **112**, 185–198 (1992).
  42. Rogovtsov, N. N. & Borovik, F. N. The characteristic equation of radiative transfer theory. In *Light Scattering Reviews 4: Single Light Scattering and Radiative Transfer* (ed. Kokhanovsky, A. A.) 347–429 (Springer Berlin Heidelberg, 2009). doi:10.1007/978-3-540-74276-0\_7.
  43. Tonizzo, A., Russell, B. J., Sullivan, J. M. & Twardowski, M. S. Propagation of bioluminescent signals in near-surface to mesopelagic waters. *Ocean Sens. Monit. X* **1063113**, 41 (2018).
  44. Lassiter, A. M., Wilkerson, F. P., Dugdale, R. C. & Hogue, V. E. Phytoplankton assemblages in the CoOP-WEST coastal upwelling area. *Deep-Sea Res. Part II Top. Stud. Oceanogr.* **53**, 3063–3077 (2006).
  45. Dugdale, R. C., Wilkerson, F. P., Hogue, V. E. & Marchi, A. Nutrient controls on new production in the Bodega Bay, California, coastal upwelling plume. *Deep-Sea Res. Part II Top. Stud. Oceanogr.* **53**, 3049–3062 (2006).
  46. Wilkerson, F. P., Lassiter, A. M., Dugdale, R. C., Marchi, A. & Hogue, V. E. The phytoplankton bloom response to wind events and upwelled nutrients during the CoOP WEST study. *Deep-Sea Res. Part II Top. Stud. Oceanogr.* **53**, 3023–3048 (2006).
  47. Vabson, V. et al. Field Intercomparison of Radiometers Used for Satellite Validation in the 400–900 nm Range. *Remote Sens.* **11**, 1129 (2019).
  48. Cole, B. E., Hager, S. W. & Hollibaugh, J. T. Hydrographic, biological, and nutrient properties of Tomales Bay, California, March 1985 to May 1986. *Dep. Inter. US Geol. Surv.* 1–90 (1990).
  49. Tsuji, S., Takahara, T., Doi, H., Shibata, N. & Yamanaka, H. The detection of aquatic macroorganisms using environmental DNA analysis—A review of methods for collection, extraction, and detection. *Environ. DNA* **1**, 99–108 (2019).
  50. Baker, A., Robbins, I., Moline, M. A. & Iglesias-Rodríguez, M. D. Oligonucleotide primers for the detection of bioluminescent dinoflagellates reveal novel luciferase sequences and information on the molecular evolution of this gene. *J. Phycol.* **44**, 419–428 (2008).
  51. Valiadi, M., Painter, S. C., Allen, J. T., Balch, W. M. & Iglesias-Rodriguez, M. D. Molecular detection of bioluminescent dinoflagellates in surface waters of the patagonian shelf during early austral summer 2008. *PLoS ONE* **9**, e99322 (2014).
  52. Moorthi, S. D., Countway, P. D., Stauffer, B. A. & Caron, D. A. Use of quantitative real-time PCR to investigate the dynamics of the red tide dinoflagellate *Lingulodinium polyedrum*. *Microb. Ecol.* **52**, 136–150 (2006).
  53. McGaraghan, A. *Tiny Drifters-A Guide to the Phytoplankton along the California Coast*. (Kudela Biological and Satellite Oceanography Laboratory, University of California Santa Cruz, 2018).
  54. Shulman, I. & Anderson, S. Bioluminescence potential modeling with an ensemble approach. *Ocean Dyn.* **69**, 599–614 (2019).
  55. Kudela, R. M., Garfield, N. & Bruland, K. W. Bio-optical signatures and biogeochemistry

- from intense upwelling and relaxation in coastal California. *Deep-Sea Res. Part II Top. Stud. Oceanogr.* **53**, 2999–3022 (2006).
56. Kimmerer, W. J. Distribution patterns of zooplankton in Tomales Bay, California. *Estuaries* **16**, 264–272 (1993).
  57. Mobley, C. D. Estimation of the remote-sensing reflectance from above-surface measurements. *Appl. Opt.* **38**, 7442 (1999).
  58. Paxinos, R. & Mitchell, J. G. A rapid Utermöhl method for estimating algal numbers. *J. Plankton Res.* **22**, 2255–2262 (2000).
  59. Behrenfeld, M. J. *et al.* Global satellite-observed daily vertical migrations of ocean animals. *Nature* **576**, 257–261 (2019).
  60. Elvidge, C. D., Baugh, K. E., Zhizhin, M. & Hsu, F.-C. Why VIIRS data are superior to DMSP for mapping nighttime lights. *Proc. Asia-Pac. Adv. Netw.* **35**, 62 (2013).
  61. Shi, W. & Wang, M. Ocean dynamics observed by VIIRS Day/Night Band satellite observations. *Remote Sens.* **10**, 1–10 (2018).
  62. Miller, S. D. *et al.* Illuminating the capabilities of the suomi national Polar-orbiting partnership (NPP) visible infrared imaging radiometer suite (VIIRS) day/night Band. *Remote Sens.* **5**, 6717–6766 (2013).
  63. Richardson, A. J. *et al.* Using continuous plankton recorder data. *Prog. Oceanogr.* **68**, 27–74 (2006).
  64. Siegel, D. A. *et al.* Prediction of the Export and Fate of Global Ocean Net Primary Production: The EXPORTS Science Plan. *Front. Mar. Sci.* **3**, (2016).
  65. Werdell, P. J. *et al.* The plankton, aerosol, cloud, ocean ecosystem mission status, science, advances. *Bull. Am. Meteorol. Soc.* **100**, 1775–1794 (2019).
  66. Kramer, S. J. & Siegel, D. A. How Can Phytoplankton Pigments Be Best Used to Characterize Surface Ocean Phytoplankton Groups for Ocean Color Remote Sensing Algorithms? *J. Geophys. Res. Oceans* 7557–7574 (2019) doi:10.1029/2019JC015604.
  67. Zheng, B. *et al.* Dinoflagellate vertical migration fuels an intense red tide. *Proc. Natl. Acad. Sci.* **120**, e2304590120 (2023).
  68. Gentemann, C. L. *et al.* Saildrone: Adaptively Sampling the Marine Environment. *Bull. Am. Meteorol. Soc.* **101**, E744–E762 (2020).
  69. Jemai, A., Wollschläger, J., Voß, D. & Zielinski, O. Radiometry on Argo Floats: From the Multispectral State-of-the-Art on the Step to Hyperspectral Technology. *Front. Mar. Sci.* **8**, 676537 (2021).
  70. Bagniewski, W., Fennel, K., Perry, M. J. & D'Asaro, E. A. Optimizing models of the North Atlantic spring bloom using physical, chemical and bio-optical observations from a Lagrangian float. *Biogeosciences* **8**, 1291–1307 (2011).
  71. BCO-DMO. Biofloat 48. <https://www.bco-dmo.org/>
  72. University of California, Davis, Bodega Marine Laboratory. Bodega Ocean Observing Node.
  73. NASA Goddard Space Flight Center, Ocean Ecology Laboratory, Ocean Biology Processing Group. Moderate-resolution Imaging Spectroradiometer (MODIS) Aqua Chlorophyll Data; 2018 Reprocessing. (2018) doi:10.5067/AQUA/MODIS/L3M/CHL/2018.
  74. NOAA Environmental Research Division. NOAA Fisheries - Southwest Fisheries Science Center. Bakun daily 1 degree upwelling Index.
  75. Kahru, M. & Mitchell, B. G. Spectral reflectance and absorption of a massive red tide off southern California. *J. Geophys. Res. Oceans* **103**, 21601–21609 (1998).
  76. Lassiter, Adria Marie. Inter and intra-annual patterns of phytoplankton assemblages during upwelling events off the coast of northern California. (San Francisco State University, 2003).
  77. Clark, M. R., Consalvey, M. & Rowden, A. A. *Biological sampling in the deep sea*. (John Wiley & Sons, 2016)